NOTE TO USERS

This reproduction is the best copy available.

UMI®

University of Alberta

THE OPTIMIZED DETECTION OF MYO-INOSITOL AND OTHER METABOLITES WITH STRONGLY-COUPLED SPIN SYSTEMS IN IN VIVO PROTON MAGNETIC RESONANCE SPECTROSCOPY

by

HYEONJIN KIM

©

A thesis submitted to the Faculty of Graduate Studies and Research in partial fulfillment of the requirements for the degree of DOCTOR OF PHILOSOPHY

in

MEDICAL SCIENCES-BIOMEDICAL ENGINEERING

Edmonton, Alberta

Spring 2004

Library and Archives Canada
Published Heritage Branch
395 Wellington Street
Ottawa ON K1A 0N4
Canada

Bibliothèque et Archives Canada
Direction du Patrimoine de l'édition
395, rue Wellington
Ottawa ON K1A 0N4
Canada

Your file Votre référence
ISBN: 0-612-96287-3
Our file Notre référence
ISBN: 0-612-96287-3

The author has granted a non-exclusive license allowing the Library and Archives Canada to reproduce, loan, distribute or sell copies of this thesis in microform, paper or electronic formats.

L'auteur a accordé une licence non exclusive permettant à la Bibliothèque et Archives Canada de reproduire, prêter, distribuer ou vendre des copies de cette thèse sous la forme de microfiche/film, de reproduction sur papier ou sur format électronique.

The author retains ownership of the copyright in this thesis. Neither the thesis nor substantial extracts from it may be printed or otherwise reproduced without the author's permission.

L'auteur conserve la propriété du droit d'auteur qui protège cette thèse. Ni la thèse ni des extraits substantiels de celle-ci ne doivent être imprimés ou aturement reproduits sans son autorisation.

In compliance with the Canadian Privacy Act some supporting forms may have been removed from this thesis.

Conformément à la loi canadienne sur la protection de la vie privée, quelques formulaires secondaires ont été enlevés de cette thèse.

While these forms may be included in the document page count, their removal does not represent any loss of content from the thesis.

Bien que ces formulaires aient inclus dans la pagination, il n'y aura aucun contenu manquant.

Canada

ABSTRACT

In-vivo magnetic resonance spectroscopy (MRS) enables the non-invasive extraction of biochemical information from human brain. Although MRS of the proton is the choice of nucleus to mitigate the inherent problems of low NMR sensitivity and low brain metabolite concentration, the proton resonances from many cerebral metabolites present as overlapping multiplets. The overlapping multiplets are due first to the limited range of proton chemical shifts at the field strengths available with whole body magnets, and second to the scalar-coupling interaction between the proton spins in individual metabolite molecules. The NMR pulse sequences used for biochemical analysis therefore need optimization to ensure that the target metabolite signals are maximally separated from a very cluttered background. The purpose of this Ph. D. research program was to explore and develop such optimization procedures for the brain metabolite, *myo*-inositol.

Myo-inositol, like other key brain metabolites such as glutamate, the aspartate group of N-acetylaspartate, taurine and glucose, contains strongly-coupled proton spins. Due to their complicated evolution in response to NMR pulse sequences, strongly-coupled spin dynamics are in general intractable using manual product-operator analysis. The optimization procedures mentioned above were therefore tackled by numerical methods. The actual pulse sequence designs that are specific to the strongly-coupled spin system of *myo*-inositol, together with the spin systems of its background contaminants, were then extracted from the numerical analysis.

The efficacy of the two most popular single voxel pulse sequences in ^{1}H-MRS, namely, PRESS and STEAM, was addressed first for the quantification of *myo*-Inositol in-vivo. For greater *myo*-inositol isolation from its background, the performance of a generic multiple quantum filter (MQF) was explored. To enhance the discrimination of *myo*-inositol by suppressing even weakly-coupled spin metabolites, a novel spectral editing technique was developed that enhanced both the signal yield and the discrimination of the sequence. Finally, the role of the r.f. phase of the MQ-generating pulse was explored as a potential method of metabolite discrimination. It was found that this variable was able to resolve one of the most challenging problems in ^{1}H-MRS, namely, the separation of glutamate from glutamine, far better than any technique proposed heretofore.

The Lord is my shepherd,
I shall not be in want.
He makes me lie down in green pastures,
he leads me beside quiet waters,
he restores my soul.
He guides me in paths of righteousness
for his name's sake.
Even though I walk through the valley
of the shadow of death,
I will fear no evil,
for you are with me;
Your rod and your staff,
they comfort me.

You prepare a table before me
in the presence of my enemies.
You anoint my head with oil;
my cup overflows.
Surely goodness and love will follow me
all the days of my life,
and I will dwell in the house of the Lord
forever.

- Psalm 23 -

To Jesus, *my Lord*

ACKNOWLEDGEMENTS

First of all, I would like to thank my supervisor Dr. Peter Allen whose knowledge about NMR and intuition as a physicist I respect. I also appreciate his financial support throughout my research program, which has always been more than enough for me. I wish to thank my supervisory committee members, Drs. Wayne Martin, Frances Fenrich and Alan Wilman. I would also like to thank Dr. Chris Hanstock for being one of the examiners at my defense, Dr. Richard Snyder for serving as a chairman at both my candidacy exam and defense, Dr. Peter Silverstone for being the external examiner at my candidacy exam and for his help with regards to psychiatry, and Dr. Nicholas Coupland for his smile. It was my honour to have Dr. Alex MacKay as the external examiner at my defense. I also thank Dr. Gwyn Hughes and Ms. Lynn Chandler, the former being my co-supervisor, and the latter my graduate coordinator in the department of Physics for their help and warm concern in the old days.

I must acknowledge the great amount of help I have been given in the course of my research in the BME department, without which I could not have detected even the water singlet. The previous work of Dr. Alan Wilman and Dr. Richard Thompson was a precious asset for my research, and, in particular, Dr. Richard Thompson's help in my early years was essential to my NMR background. I thank Dr. Chris Hanstock for his seriousness towards any of my questions and his willingness to help me. I also thank Dan Gheorghiu who clearly demonstrated to me what a genuine engineer is supposed to be like. I gratefully acknowledge Dr. Changho Choi for the helpful and enjoyable discussions on physics without a boundary, particularly over pitchers of beer. How can I forget Maisie, Brenda and Carol ? I sincerely appreciate their help and warm concern for me. In particular, my life in the BME department would have been more difficult without Carol's help on the manuscripts and a number of other documents.

I thank all of my friends that I met in Canada; Amir for his precision in speech and the time he takes before starting anything, Atiyah as my spoiled younger sister and

English teacher (all her family are also gratefully acknowledged), Chilo for his optimism, Jason who was the only one who ever listened to me, Jim (and his mother) for his academic help, encouragement and wonderful memories in Shefield, UK, Keith who will always be found with Mary, Yusuf who will definitely be found in the near future somewhere in Green Bay, Wisconsin, Nick as a special friend, i.e., an Italian with guns, Steven and Beau for their willingness to go see Will Ferrell anytime I wanted. So many other friends whose friendship I appreciate; Alison, Anna, Dan, Daniel (my right hand), Jacob, (Drs.) Jane and Myrlene, Lisa, Luis, Rob, Sarah, Sasha, Sherif, Osama, and so on. I must thank Keechan (and his family) for his help as my elder brother and friend throughout my days in Canada. I also thank my wonderful violin teacher, Jennifer Bustin for her effort and encouragement.

I would like to give special thanks from the deepest bottom of my heart to all of my lovely family, my father, my mother, my sister and her family, and my brother for their love, support, concern and faith in me. In particular, my mother's incessant prayer, which I will cherish for the days of my life, is what made everything possible.

Finally, I confess that the hardest part of my life in Canada was to overcome the solitude that has always been within me. However, I sometimes do realize that it is highly addictive, and more importantly it is a prerequisite to appreciating the beautiful sunset of Edmonton, the City of Champions.

TABLE OF CONTENTS

		Page
Chapter 1	***Introduction***	***1***
1.1	Introduction to the Thesis	1
1.2	Nuclear Spin and Magnetic Moment	3
1.3	Basic Concept on Resonance Phenomena	4
1.4	Preparation of Z-magnetization	5
1.5	Radio-Frequency Pulse	7
1.6	NMR Physics	8
1.6.1	Fundamental Principles in Quantum Mechanics	9
1.6.1.1	Basic Postulates in Quantum Mechanics	9
1.6.1.2	Expectation Value	10
1.6.1.3	Matrix Representation of Operators	11
1.6.2.	Spin	12
1.6.2.1	Matrix Representation of Spin	12
1.6.2.2	Eigenvalues and Eigenvectors of Spin Operator	13
1.6.2.3	Interaction of a Spin in External Magnetic Fields	14
	1.6.2.3.1 Interaction of a Spin with a B_0 Field	14
	1.6.2.3.2 Interaction of a Spin with Both B_0 and B_1 Fields	15
1.6.3	Description of the Evolution of Spin Systems in NMR Experiments	17
1.6.3.1	Density Matrix	17
1.6.3.2	Quantum Coherences	19
1.6.3.3	Calculation of the Evolution of a Spin System	21
	1.6.3.3.1 Outline of Numerical Methods	22
	1.6.3.3.2 Product Operator Formalism	24
1.7	Nuclear Spin Interaction in ^{1}H-MRS	26
1.7.1	Chemical Shift	27
1.7.2	Scalar Coupling (J-coupling)	29
1.7.2.1	Definition	29
1.7.2.2	Degree of Scalar-Coupling Interaction	30
1.7.3	Dipole-Dipole Coupling	32
1.7.4	Relaxation	32
1.7.5	Gradient Pulses	33
1.8	Spatial Localization	35
1.9	Evolution of Spin Systems and Sequence Optimization	36
1.9.1	Evolution of Weakly-coupled Spin Systems	37
1.9.2	Evolution of Strongly-coupled Spin Systems	39
1.10	Practical Example of the Evaluation of Spin Evolution in a Spin-echo Sequence	40
1.10.1	Spin-echo Sequence (General)	40
1.10.2	Evolution of an Uncoupled Spin System in Response to the Spin-echo Sequence	41
1.10.3	Evolution of a Weakly-Coupled Spin System in Response to the Spin-echo Sequence	43
1.10.4	Evolution of a Strongly-Coupled Spin System in Response to the Spin-echo Sequence	45
1.11	Pulse sequences in In-vivo ^{1}H-MRS	48
1.11.1	Voxel-Selection Phenomena	48
1.11.2	PRESS Sequence	51
1.11.3	STEAM Sequence	52
1.11.4	MQF	54

1.11.4.1 Evolution of an AX Spin System in MQF 56
1.11.4.1.1 Preparation Period and Generation of MQCs 56
1.11.4.1.2 Evolution of MQCs During TM and the Role of the First Filter Gradient 57
1.11.4.1.3 Evolution of MQCs into APCs and the Role of the Second Filter Gradient 59
1.11.4.2 Difference in Design of MQF for Strongly-Coupled Spin Systems 62
1.11.4.2.1 Preparation Period and Generation of MQCs 62
1.11.4.2.2 Evolution of MQCs during TM 62
1.11.4.2.3 Conversion of MQCs into APCs 63
1.11.5 Two-Dimensional Spectroscopy 63
1.12 References 65

Chapter 2 Myo-Inositol, Its Chemistry and Relevance to Psychiatry and Neurology; A Review of NMR Studies 68

2.1 Introduction 68
2.2 Synthesis, Regulation, and Possible Role of mI 69
2.3 In-vivo ^{1}H-MRS and ^{31}P-MRS in Psychiatric and Neurological Research 71
2.4 Psychiatric disorders Related to mI 74
2.4.1 Bipolar Disorder 74
2.4.1.1 PI-cycle and mI Depletion Hypothesis 76
2.4.1.2 Review on Inositol in BPD 78
2.4.1.2.1 Possible Etiological Role of mI 78
2.4.1.2.2 Testing the mI-depletion Hypothesis 79
2.4.1.2.2.1 Animal NMR Studies 79
2.4.1.2.2.2 Human NMR Studies 79
2.4.2 Schizophrenia 80
2.4.2.1 Review on Inositol in Schizophrenia 81
2.5 Conclusion (Psychiatric Disorders) 83
2.6 Neurological Diseases Related to mI 83
2.6.1 Alzheimer's Disease 83
2.6.1.1 mI-Hypothesis in AD 84
2.6.1.1.1 Supporting Evidence 84
2.6.1.1.2 Metabolic Change in AD Brain Measured by NMR 85
2.6.1.1.3 Possible Mechanisms Responsible for Elevated mI Level in AD Brain 86
2.6.2 Hepatic Encephalopathy 87
2.6.2.1 Review on Inositol in HE 87
2.6.2.2 Possible Consequence of the Lowered mI Level in HE Brain 88
2.7 Conclusion (Neurological Diseases) 88
2.8 References 91

Chapter 3 The Optimized Detection of Myo-Inositol In Vivo Using PRESS and STEAM Sequences at 3.0 T 96

3.1 Introduction 96
3.2 Methods 98
3.2.1 Spectral Characterization of mI and Its Neighboring Metabolites 98
3.2.2 Pulse Sequences 101
3.2.2.1 PRESS 101
3.2.2.2 STEAM 101
3.2.3 Sequence Optimization Using Numerical Methods 102

	3.2.4	Experimental Methods	104
3.3	Results		104
	3.3.1	STEAM	104
	3.3.2	PRESS	110
3.4	Discussion		114
	3.4.1	Sources of Variability	114
		3.4.1.1 STEAM	114
		3.4.1.2 PRESS	114
3.5	Summary and Conclusion		117
3.6	References		118
Chapter 4	***The Detection of Myo-Inositol In vivo Using Double Quantum Coherence Filtering at 3.0 T***		***120***
4.1	Introduction		120
4.2	Methods		122
	4.2.1	Spectral Characteristics of mI and Its Background Metabolites	122
	4.2.2	Sequence Optimization	124
	4.2.3	Phantom and In-vivo Experiments	130
4.3.	Results		132
	4.3.1	Experimental Results	132
	4.3.2	Sources of Variability During TM Period	135
4.4	Summary and Discussion		139
4.5	References		141
Chapter 5	***A Strategy For the Spectral Filtering of Myo-Inositol and Other Strongly-Coupled Spins***		***144***
5.1	Introduction		144
5.2	Theory		146
	5.2.1	The Sequence and the Multiple Quantum Filter Mechanism	146
	5.2.2	Outline of Analysis to Optimize mI Observation at ~ 3.6 ppm	148
5.3	Methods		156
	5.3.1	The Pulse Sequence	156
	5.3.2	Spectroscopy	157
5.4	Results		158
5.5	Discussion		162
5.6	References		165
Chapter 6	***In Search of the Complete Set of Optimum Sequence Parameters in the Design of MQF in In Vivo ^{1}H MRS***		***167***
6.1	Introduction		167
6.2	Methods		169
	6.2.1	Theory	169
		6.2.1.1 ZQF	171
		6.2.1.2 DQF	175
	6.2.2	Experiments	177
6.3	Results		179
6.4	Summary and Discussion		184
6.5	References		188
Chapter 7	***Conclusion***		***190***

7.1	Summary	190
7.2	Product Operator Formalism and Numerical Methods	190
7.3	LC Model -An Alternative to Spectral Editing ?	191
7.4	Spectral Editing vs. LC Model at Higher Fields	192
7.5	References	194

APPENDIX 1	***Bloch Equations***	***195***
APPENDIX 2	***Eigenvalues and Eigenvectors of Spin Operators***	***197***
APPENDIX 3	***Rotation of Spin Operators***	***199***
APPENDIX 4	***Louville-von Newman Equation***	***201***
APPENDIX 5	***Evolution of Coherences under Gradient Pulses***	***203***
APPENDIX 6a	***Transformation Equations (Weak-Coupling Approximation)***	***205***
APPENDIX 6b	***Transformation Equations for a Strongly-Coupled AB Spin System***	***207***

LIST OF TABLES

		Page
2-1	The in-vivo ^{1}H-MRS data (human brain) of mI measurements in bipolar disorder, schizophrenia, Alzheimer's disease and hepatic encephalopathy	90
3-1	The spectral characteristics of *myo*-Inositol and its background contaminants	100
4-1	The spectral characteristics of *myo*-Inositol spin system	123
4-2	The number of single quantum anti-phase coherences generated by the third 90° frequency-selective pulse for three different excitation schemes	126

LIST OF FIGURES

		Page
1-1	The polarization of the system of nuclei of spin 1/2 by the static magnetic field $\mathbf{B_o}$	4
1-2	The typical proton NMR spectra of a weakly-coupled AX spin system and a strongly-coupled AB spin system at 3.0 T using computer simulation	31
1-3	A practical example of slice selection by a shaped 90_x° r.f pulse and slice-selection gradient	36
1-4	A spin-echo pulse sequence	41
1-5	A vectorial description of the evolution of an uncoupled spin in rotating frame in a spin-echo experiment	43
1-6	A vectorial description of the scalar-coupling evolution of a weakly-coupled spin system in the rotating frame during TE	45
1-7	The coherence pathways for a strongly-coupled AB spin system in a spin-echo experiment	47
1-8	The voxel-selection phenomenon	49
1-9	A PRESS localization pulse sequence	52
1-10	A STEAM localization sequence	53
1-11	A generic MQF sequence	56
1-12	Basic two-dimensional pulse sequences	64
2-1	The molecular structure of *myo-Inositol*	69
2-2	A ^{1}H-MRS spectrum of the human brain at 3.0 T	72
2-3	A ^{31}P-MRS spectrum of the human brain at 3.0 T	74
2-4	The phosphatidylinositol (PI) signal transduction pathway	76
3-1	A diagram illustrating the mI molecule together with schematic of the proton numbers, the chemical shift values, δ ppm, and the coupling configuration, including individual interaction strengths, J Hz	98

3-2	The calculated response of *myo*-Inositol and its neighboring metabolites to a pulse-acquire experiment at 3.0 T	99
3-3	The simplified diagrams of (a) PRESS and (b) STEAM localization pulse sequences	102
3-4	The contour plots in {TE, TM} space of the response of the peak height of mI to STEAM	105
3-5	The calculated and phantom response of the target multiplet of *myo*-Inositol to STEAM at five different TEs with TM fixed at 70 ms	106
3-6	The contour plots in {TE, TM} space of the response of the peak height of (a) Tau, (b) Glu and (c) Gln to STEAM	107
3-7	The in-vivo and phantom response of myo-Inositol and its neighboring metabolites to STEAM at 3.0 T	109
3-8	The contour plots in {TE_1, TE_2} space of the response of the peak height of (a) mI, (b) Tau, (c) Glu and Gln to PRESS	110
3-9	The calculated and phantom response of the target multiplet of *myo*-Inositol in response to PRESS at six different TE_2's with TE_1 fixed at 30 ms	111
3-10	The in-vivo and phantom response of myo-Inositol and its background metabolites to PRESS at 3.0 T	113
3-11	The illustration of the rapid decay of the signal amplitude of mI in response to short-TE PRESS	115
3-12	The snapshots of the distribution of single quantum coherence (SQC) terms of mI in response to PRESS at (a) {TE_1 = 20 ms, TE_2 = 25 ms} and (b) {TE_1 = 25 ms, TE_2 = 30 ms}	116
4-1	A generic DQF sequence	124
4-2	The contour plot of the calculated signal intensity of the target peak of *myo*-Inositol in response to a DQF sequence for the determination of semi-optimum TE_1 and TE_2	128

4-3 The variation of the calculated signal intensity of the target peak of *myo*-Inositol as a function of the duration and the flip angle of the third 90° frequency selective pulse 129

4-4 The variation of the calculated signal intensity of the target peak of *myo*-Inositol as a function of TM 130

4-5 The phantom response of *myo*-Inositol and its background metabolites to a PRESS and the optimized DQF 133

4-6 The DQ-filtered spectra of the human brain 135

4-7 The snap shots of the distribution of DQCs just after the second 90° MQC-generating pulse at (a) TE_1 of 32 ms and (b) TE_1 of 62 ms 137

4-8 The generation and evolution of various DQCs of *myo*-Inositol during TM 138

5-1 A schematic illustration of a multiple quantum filter sequence including (a) the pulses and the timing definitions and (b) a representative listing made for each coupling category of the evolution of coherence terms during the individual timing periods 148

5-2 A diagram illustrating the mI molecule together with schematic of the chemical shift values, δ ppm, and the coupling configuration, including individual interaction strengths, *J* Hz 149

5-3 Specific-time snap-shots of the relative amplitudes of various coherences of the mI spin system 152

5-4 A comparison of the experimental phantom lineshapes of mI (solid lines) with the corresponding lineshapes (dashed lines) calculated using only the eight principal SQC terms of the M and N spins of mI 154

5-5 An evolutionary chart of representative coherence pathways for defining the Tau spectral response to the filter sequence 155

5-6 A comparison of the experimental phantom responses to a symmetric PRESS sequence {$TE_1 = TE_2 = 30$ ms} and to three symmetric filters with $TE_1 = TE_2 = 30$ ms, 40 ms, and 60 ms respectively, and with a mixing time TM = 9 ms for all three filters 160

5-7 A comparison of spectral responses intended to establish the efficacy of the optimized filter in vivo 161

6-1 A simplified diagram of a generic multiple quantum filter sequence 168
6-2 The φ-dependence of the representative coherence terms of citrate and *myo*-Inositol just after the MQ-pulse. 172
6-3 The response of the strongly-coupled AB spin system of Cit to ZQF at $\{TE_1 = 30$ ms, $TE_2 = 30$ ms$\}$ with varying phase of the MQ-pulse 179
6-4 The response of uncoupled Cr (methyl group) at ~ 3.0 ppm and weakly-coupled Lac (methyl group) at ~ 1.3 ppm to varying phase of the MQ-pulse in ZQF experiments taken at $\{TE_1 = 30$ ms, $TE_2 = 30$ ms$\}$ 180
6-5 The φ-dependence of the strongly-coupled spin systems of citrate, taurine and *myo*-Inositol in ZQF and DQF experiments at various representative, symmetric sequence timings 181
6-6 The practical example of the optimization of the phase of the MQ-pulse for the discrimination of mI from Tau 183
6-7 The practical example of the optimization of the phase of the MQ-pulse for the discrimination of Glu from Gln 184
6-8 The coupling networks of Glx spin systems and the J/δ-dependent oscillation amplitude of strong-coupling specific APCs of an AB spin system 187

7-1 The calculated spectra of mI and its background metabolites in response to a 90°-acquire sequence at 3.0 T, 4.7 T and 7.0 T 193

LIST OF SYMBOLS AND ABBREVIATIONS

AD	Alzheimer's disease
APC	Anti-phase coherence
Asp	Aspartate
$\mathbf{B}_1$	Radio-frequency magnetic field
$\mathbf{B}_0$	Static magnetic field
BPD	Bipolar disorder
BW	Bandwidth
Cho	Choline
Cit	Citrate
Cr	Creatine
DQC	Double quantum coherence
DQF	Double quantum coherence
E	Energy
F	Force
G	Gradient vector
GABA	γ-aminobutyric acid
Glc	Glucose
Gln	Glutamine
Glu	Glutamate
Glx	Glutamate and glutamine
Gly	Glycine
G_x, G_y, G_z	Gradients in Cartesian coordinate
$\boldsymbol{H}$	Hamiltonian
h	Planck constant
$\hbar$	Planck constant divided by 2π
HE	Hepatic encephalopathy
^{1}H-MRS	Proton magnetic resonance spectroscopy
I_x, I_y, I_z	Cartesian spin operators

I_+, I_-, I_o	Spherical spin operators
J	Angular momentum operator
j	Angular momentum quantum number
J	Scalar-coupling constant
K	Kelvin
k_B	Boltzmann constant
Lac	Lactate
mI	*Myo*-Inositol
m_j	magnetic quantum number
$\mathbf{M}_o$	Magnetic moment in a unit volume or net magnetization
MQC	Multiple quantum coherence
MQF	Multiple quantum filter
MRI	Magnetic resonance imaging
MRS	Magnetic resonance spectroscopy
m_s	Spin magnetic quantum number
M_{xy}	Transverse magnetization
M_z	Longitudinal magnetization
N	Number of spins
NAA	N-acetylaspartate
NMR	Nuclear magnetic resonance
P	Probability
PCr	Phosphocreatine
PI	Phosphatidylinositol
ppm	Parts per million
PRESS	Point REsolved SpectroScopy
r.f.	Radio-frequency
S	Spin angular momentum operator
s	Spin quantum number
S(t)	Signal
S/B	Signal to background ratio
SQC	Single quantum coherence

SQF	Single quantum filter
SQ-APC	Single quantum anti-phase coherence
S/N	Signal to noise ratio
STEAM	STimulated Echo Acquisition Mode
S_x, S_y, S_z	Cartesian spin operators
T	Tesla
t	Time
T_1	Spin-lattice relaxation time
T_2	Spin-spin relaxation time
Tau	Taurine
TE	echo time
TE_1	First echo time
TE_2	Second echo time
TM	Mixing time
U	Unitary matrix or operator
VOI	Volume Of Interest
$\vec{x}$, $\vec{y}$, $\vec{z}$	Cartesian unit vectors
$\vec{x}^{\,rot}$, $\vec{y}^{\,rot}$, $\vec{z}^{\,rot}$	Cartesian unit vectors in the rotating frame of reference
ZQC	Zero quantum coherence
ZQF	Zero quantum filter
δ	Chemical-shift
$\Delta\delta$	Chemical-shift difference between coupled spins in Hz
γ	Gyromagnetic ratio
Φ	Potential energy
φ	Phase angle of a radio-frequency pulse
λ_n	Eigenvalue
μ	Magnetic moment operator
μ_x, μ_y, μ_z	Cartesian Magnetic moment operators
ν	Frequency
ρ	Density matrix (operator)

σ	Shielding constant
$\sigma_x, \sigma_y, \sigma_z$	Pauli matrices
ω	Angular frequency
$\Delta\omega$	Bandwidth of an r.f. pulse
ω_o	Larmor frequency
Ψ	Wave function
∇	Vector Gradient operator
1	Unit matrix or operator

CHAPTER 1

Introduction

1.1 Introduction to the Thesis

Unlike clinical magnetic resonance imaging (MRI) techniques in which the signal contrast (image) comes solely from the water molecule, magnetic resonance spectroscopy (MRS) allows us to extract biochemical information from the metabolites of living organs non-invasively. Among the various nuclei species measurable using MRS, ^{1}H has been a nucleus of choice because it has the highest sensitivity. As a result, proton magnetic resonance spectroscopy (^{1}H-MRS) promises to play an important role in diagnosing and monitoring various diseases and disorders by means of the quantification of cerebral metabolites (1-10). However, the non-invasive quantification of brain metabolites using MRS is not an easy task, and as such, a great deal of effort has had to be made to tackle the inherent problems of the NMR technique for clinical applications (11-14). First of all, NMR experiments in general suffer from low sensitivity and this is exacerbated by the low concentration of brain metabolites. Moreover, the proton resonances from the many metabolites present in brain overlap each other at clinically practical field strengths due to the limited range of proton chemical shifts, i.e. the primary NMR mechanism that determines spectral resolution. The overlapping nature of the proton spectrum is made much worse because the protons within a metabolite molecule can also interact with each other through the scalar coupling (or J-coupling) interaction. This interaction causes individual molecular groups in a metabolite to exhibit not a single resonance (like uncoupled water protons), but a multiplet whose spread can easily exceed the separation between multiplets from different molecular groups or even different metabolites at clinically available field strengths. The problems, therefore, boil down to extracting a host of small signals out of the background noise and then isolating individual signals

from a very contaminated background. This process may be referred to as sequence optimization.

The so-called product operator formalism which permits a calculation of the evolution of the spin dynamics (Section 1.6.2.3) has been widely used for the purpose of sequence optimization (15-28). However, as it requires manual calculations, the application of the product operator formalism is limited to simple spin systems (15-17). As an alternative to the manual method, numerical methods prove to be a very powerful enhancement for sequence optimization, in which one solves the equation of motion of the density matrix (section 1.6.2.1) by using a computer instead of manual analysis. The evolution of very complicated spin systems can then be calculated in response to NMR pulse sequences (29-31).

Among the numerous metabolites in human brain, this thesis is mainly focused on the detection and quantification of myo-inositol (mI) by using various pulse sequences. The cerebral level of mI, which is one of the key brain metabolites, is know to be associated with various diseases and disorders such as Alzheimer's Disease, hepatic encephalopathy, diabetes mellitus, depression, and bipolar disorder (32-44). Therefore, the non-invasive quantification of mI using MRS may allow us not only to clarify the pathogenesis of such diseases and disorders, but it may also allow us to diagnose and manage patients. Since mI has a strongly-coupled system of six spins, their evolution in response to NMR pulse sequences is very complicated. Therefore, the optimization procedures are tackled by numerical methods.

Before considering the practical applications of various NMR techniques for the detection of mI *in vivo* are discussed, basic NMR theories will be reviewed first in Chapter 1 followed by a discussion on the clinical importance of the metabolite in Chapter 2 in the psychiatric and neurological domain.

1.2 Nuclear Spin and Magnetic Moment

The MRS technique takes advantage of the discrete nature of the stationary Zeeman energy states of nuclei, which originate from their intrinsic angular momentum, namely, spin angular momentum, $\mathbf{S}\hbar$, or simply spin. Among the isotopes in nature, the nucleus of hydrogen (proton) will be of interest throughout the thesis, for which the spin quantum number, s, is 1/2. Spin angular momentum, $\mathbf{S}\hbar$, is always accompanied by a magnetic moment μ and their relationship may be expressed as

$$\mu = \gamma \hbar \mathbf{S} \tag{1-1a}$$

or

$$\mu_z = \gamma \hbar S_z \tag{1-1b}$$

where $\hbar$ is the Planck constant divided by 2π and γ, the gyromagnetic ratio, is nuclear-specific constant (26.75×10^7 rad $T^{-1}s^{-1}$ for a proton).

The Stern-Gerlach experiment (45) was the first to prove that a particle possesses spin. According to classical mechanics, force is given by

$$\mathbf{F} = - \nabla \Phi \tag{1-2}$$

where Φ is a potential energy. Since a potential energy arising from the effect of magnetic field can be written as

$$\Phi = E = - \mu \cdot \mathbf{B} \tag{1-3}$$

where '$\cdot$' is dot or scalar product between two vectors, the force exerted on a particle with magnetic moment by magnetic field B_z can be expressed as

$$F \sim \mu_z \nabla B_z. \tag{1-4}$$

From Eq. (1-4), it is clear that if a beam of spin-1/2 silver atoms passes through an *inhomogeneous* magnetic field, the resulting projection is to be split into two parts according to the two possible values of μ_z of $\pm$ 1/2.

1.3 Basic Concept on Resonance Phenomena

In terms of a classical vector model (46-48), each magnetic moment of the ensemble of protons in a sample is in general randomly oriented relative to its neighbors due to thermal motion. Therefore the net magnetic moment in a unit volume or net magnetization ($\mathbf{M}_o$), which is an actual quantity measured in NMR spectroscopy, is negligible over the sample until that sample is placed in a static magnetic field $\mathbf{B}_o$. The static magnetic field then polarizes the proton magnetic moments so that they are oriented either parallel or anti-parallel to the field as illustrated in Fig. 1-1. The reason for the population difference illustrated in the figure will be explained in section 1.4. As a result of the polarization of the system by $\mathbf{B}_o$, a net magnetization $\mathbf{M}_o$ is created and the difference in energy between the two distinct states may be calculated from Eqs. (1-1) and (1-3) as

$$\Delta E = \gamma \hbar B_o. \tag{1-5}$$

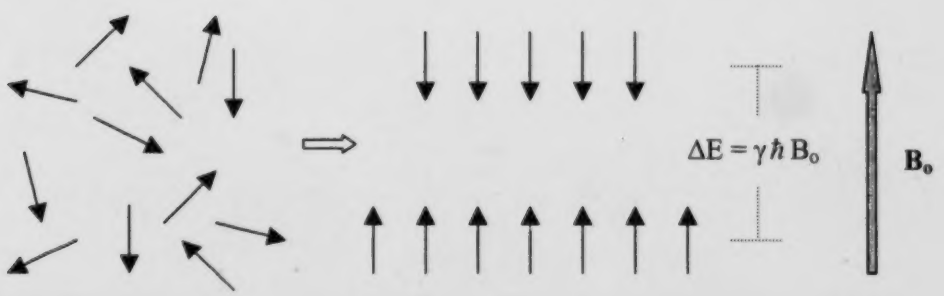

Figure 1-1 The polarization of a system of nuclei of spin-1/2 by a static magnetic field $\mathbf{B}_o$. The static magnetic field $\mathbf{B}_o$ redistributes the randomly directed dipole moment vectors in the sample into parallel or anti-parallel to the direction of $\mathbf{B}_o$ with the former slightly more probable than the latter. As a result, a net magnetization is created.

At the same time, each dipole moment in the polarized sample can be represented by a vector precessing about $\mathbf{B}_o$ with an angular frequency of ω_o, which is known as the Larmor frequency.

In NMR the magnetization vector $\mathbf{M}_o$ can be manipulated by supplying additional energy to the sample in the form of a rotating radio-frequency (r.f.) field, $\mathbf{B}_1$, which is applied orthogonal to $\mathbf{B}_o$. From a quantum mechanical point of view, the manipulation of $\mathbf{M}_o$ corresponds to perturbing a system so that the system undergoes an energy transition. Denoting the energy supplied by an r.f. pulse to the system as

$$E = h\nu = \hbar\omega, \tag{1-6}$$

then, according to Eq. (1-5), the perturbation of the system by the r.f. pulse is achieved most efficiently when

$$\omega = \omega_o = \gamma B_o. \tag{1-7}$$

In this context, ω_o is also referred to as the *resonance* frequency. According to Eq. (1-7), the resonance frequency is proportional to the magnitude of $\mathbf{B}_o$, $|\mathbf{B}_o|$, and it is ~ 128 MHz for a proton at 3 Tesla (T).

The simplified version of the interaction of spins with $\mathbf{B}_o$ and $\mathbf{B}_1$ fields discussed here will be treated again in section 1.6.2.3 with a formal quantum mechanical theory.

1.4 Preparation of Z-magnetization

As is outlined in the previous section, the first step to extract information from a sample in any NMR experiment is to create magnetization at thermal equilibrium or z-magnetization with a conventional direction of $\mathbf{B}_o$ oriented along the z-axis of a laboratory reference frame. An NMR sample is in general composed of a number of nuclei and therefore it should be dealt with as an ensemble of nuclear spins. As discussed

above, for protons, each system in the sample has two stationary energy states, ↑ and ↓, in a static $\mathbf{B}_o$ field, the energy of each of which is given as $E_\uparrow = -\gamma\hbar B_o/2$ (lower) and $E_\downarrow = +\gamma\hbar B_o/2$ (higher), respectively. It can be found in many statistical physics text books (49-51) that the ensemble of a system at thermal equilibrium has a distribution of populations, governed by the Boltzmann distribution law. Denoting $P_\uparrow$ and $P_\downarrow$ as probability of finding a spin in the state ↑ and ↓, respectively, it states that

$$P_\uparrow = \frac{\exp(-cE_\uparrow)}{\sum_{k=1}^{n}\exp(-cE_k)} \qquad (1\text{-}8)$$

where $c = 1/k_B T$, k_B = Boltzmann constant, T = temperature in Kelvin, and n = the number of energy levels, which is 2 in this case. Therefore the net magnetization M_o can be represented as

$$M_o = N\mu(P_\uparrow - P_\downarrow) \qquad (1\text{-}9)$$

where N is the number of spins in the sample and μ is the magnitude of the dipole moment vector. If the exponentials in Eq. (1-8) are expanded and only the first order terms are kept, then Eq. (1-9) is reduced into (52)

$$M_o = N\gamma^2\hbar^2 B_o / 4k_B T \qquad (1\text{-}10)$$

Eq. (1-10) offers us important information on practical NMR experiments. First, M_o is proportional to the strength of the external static magnetic field. Stronger magnetic fields therefore improve signal to noise ratio (S/N) of spectra (11-13, 52, 53). Secondly, M_o is also dependent on the sample temperature. This point may be important in *solid* NMR experiments, but not of interest in vivo, for which case T ~ 311 K. Due to the low population or probability difference, $P_\uparrow - P_\downarrow$, which is ~ 10^{-4} for protons even at as strong a field as 11.75 T (53), the attainable M_o is very small. Nevertheless, the small amount

of initial z-magnetization to be manipulated later by one or more transverse rotating magnetic fields, still provides a measurable signal.

1.5 Radio-Frequency Pulse

As recently described in section 1.3, the net magnetization vector $\mathbf{M}_o$ in a static $\mathbf{B}_o$ field can be manipulated by the irradiation of a $\mathbf{B}_1$ r.f. pulse. It was shown in Eq. (1-6) that the energy provided by an r.f. pulse is dependent on the oscillation frequency, ω, of the pulse. The oscillation of an r.f. pulse is best described by a linearly polarized magnetic field vector whose oscillation is most commonly assumed to be along the x-axis of the laboratory frame. This oscillating r.f. pulse can equivalently be described as two circularly polarized magnetic field vectors rotating at the same frequency but in opposite directions (54, 55). Among those two rotating vectors, however, the only component which interacts with spins is the one that is rotating in the same direction as the spin precession. Denoting the amplitude of the r.f pulse as $|B_1|$, that rotating r.f. component can be written as (31, 47, 56)

$$\mathbf{B}_1 = |B_1|\{\cos(\omega t)\,\vec{x} - \sin(\omega t)\,\vec{y}\} \qquad (1\text{-}11)$$

where $\vec{x}$ and is $\vec{y}$ are unit vectors along the x- and y-axis.

For simplicity, a rotating reference frame is introduced in NMR. The rotation frequency of the reference frame is commonly set to the r.f. frequency, ω (or carrier frequency). Therefore in the rotating frame a magnetization vector rotating at a frequency of ω_o will remain static if the r.f. pulse was applied to the sample *on resonance*. By incorporating the rotating reference frame, complicated evolutions of nuclei spin systems resulting from various interactions (spin-spin or spin-magnetic field interactions), which will be discussed in the following sections, can be described in a much simpler way.

A quantum mechanical approach for the description of the interaction of spins with B_o and B_1 field in the rotating frame will be given in section 1.6.2.3.

1.6 NMR Physics

There exist two methods in describing NMR phenomena. One is a classical approach in terms of the Bloch equations (Appendix 1), in which the magnetization vector is represented in the Cartesian coordinate system (46-48). The other is a quantum mechanical approach. The latter can further be divided into the so-called density matrix (or operator) formalism (section 1.6.3.1) and the product operator formalism (section 1.6.3.3.2). The classical approach provides a simple way of visualizing the temporal change of a magnetization vector from uncoupled spins in the course of its evolution in response to NMR pulse sequences. For instance, a 90° r.f. pulse, which rotates the magnetization vector by 90° around the direction of the pulse irradiation can easily be described in the classical vector model. In fact, the Bloch equations alone are sufficient to describe the evolution of the magnetization vector in MRI, which is the sum of the dipole magnetic moments of protons in water molecules with no interaction between the protons. However, when an intra-molecular spin-spin interaction is involved, such as the indirect scalar-coupling (section 1.7.2), which is the more common case for most of spin systems of key brain metabolites, the classical vector model falls short of describing various NMR phenomena such as the creation and the evolution of anti-phase coherences and multiple quantum coherence (section 1.6.3.3.2). Therefore, for more a general treatment of spin systems in in-vivo MRS, the quantum mechanical approach will be used throughout this thesis.

In the following section the basic quantum mechanics for the description of NMR experiments will be discussed. A brief discussion on the Bloch equation is given in Appendix 1.

1.6.1 Fundamental Principles in Quantum Mechanics

Quantum mechanics can be described equivalently with either matrices as was introduced by Heisenberg or with the Schrödinger equations, or with Dirac's vector (braket) method (47, 57-61). In this thesis, Dirac's method will be adopted for its brevity in notations.

1.6.1.1 Basic Postulates in Quantum Mechanics

Four fundamental postulates are described below, which are essential for understanding NMR physics (47, 52, 61).

Postulate 1 In Dirac's vector method, *the state of a physical system, which can be composed only of a single spin or of more spins, is described by a 'state vector'*. The state vector can be expressed as a matrix that is formed by basis vectors in the state space. That is to say, in *n*-dimensional space, a state vector or more commonly a 'ket' vector $|V\rangle$ is represented by a column matrix with *n* components in matrix representation, and the complex conjugate of the transposed ket vector is called a 'bra' vector and denoted as $\langle V|$ which is a row vector with *n* components.

Postulate 2 *The time variation of a state, which is determined by the Schrödinger equation* and the state vector, $|\Psi(t)\rangle$, satisfies

$$i\hbar\frac{\partial}{\partial t}|\Psi(t)\rangle = \boldsymbol{H}(t)|\Psi(t)\rangle \qquad (1\text{-}12a)$$

where $\boldsymbol{H}$ is the Hamiltonian of the system. For a time-independent Hamiltonian, the state vector at time t, $|\Psi(t)\rangle$, can be derived from the initial state vector, $|\Psi(0)\rangle$, in such a way that

$$|\Psi(t)\rangle = \exp(-i\boldsymbol{H}t/\hbar)\,|\Psi(0)\rangle. \qquad (1\text{-}12b)$$

Postulate 3 *The values obtained by a measurement of a physical quantity A take on only the eigenvalues of the related operator **A**, such as a_1, a_2, ··· ···, and the corresponding eigenvectors, $|a_1>$, $|a_2>$, ··· ··· are the states in the vector space. Therefore, the state vector $|\Psi(t)>$ can be expressed as a linear combination of the eigenvectors with weighting factors c_i's.* That is,

$$|\Psi(t)>=\sum_i c_i |a_i> \tag{1-13a}$$

and

$$c_i = <a_i|\Psi(t)> \tag{1-13b}$$

where c_i is a complex number. Those eigenvectors satisfy the so-called orthogonality condition, which can be stated as

$$< a_i | a_j > = \begin{cases} 1 & (i = j) \\ 0 & (i \neq j) \end{cases} \tag{1-14}$$

Postulate 4 *The probability of obtaining a_i by measuring a physical quantity A from a system in a state $|\Psi(t)>$ is*

$$|c_i|^2 = |<a_i|\Psi(t)>|^2. \tag{1-15}$$

1.6.1.2 Expectation Value

From the last two postulates it can be shown that when repeated measurements of a physical quantity A are made, the average value or the expectation value of the operator **A** is,

$$< \mathbf{A} >= \sum_i a_i |<a_i|\Psi>|^2$$

$$= <\Psi | \mathbf{A} \sum_i (|a_i><a_i|) | \Psi >$$

$$= <\Psi | \mathbf{A} | \Psi > \qquad (1\text{-}16)$$

where the so-called completeness theorem (56-60) was used in the last step. That is,

$$\sum_i |a_i><a_i| = \mathbf{1} \qquad (1\text{-}17)$$

where **1** is a unit vector. Eq. (1-16) states that one does not need to know the eigenvectors of **A** in order to obtain the expectation value of **A**.

1.6.1.3. Matrix Representation of Operators

An operator can be expressed as a matrix, and the form of the matrix depends upon the basis set. That is, using Eq. (1-17), an operator **A** can be written as

$$\mathbf{A} = \sum_{a'} \sum_{a''} |a''><a''| \mathrm{A} |a'><a'| \qquad (1\text{-}18)$$

where $<a''| \mathrm{A} |a'>$ is the a''th-row and a'th-column element of the matrix **A**.

As an example, for a basis set given by $|\, j, m_j>$ and $<j', m_j'|$ where j and j' are the angular momentum quantum numbers taking values j = 0, 1/2, 1, and m_j and m_j' are corresponding magnetic quantum numbers taking values $-j \sim j$, an angular momentum operator **J** can be written as (45),

$$\mathbf{J} = \begin{array}{c} \\ \langle 0,0| \\ \langle ½,½| \\ \langle ½,-½| \\ \langle 1,1| \\ \langle 1,0| \\ \langle 1,-1| \end{array} \begin{array}{c} \begin{array}{cccccc} |0,0\rangle & |½,½\rangle & |½,-½\rangle & |1,1\rangle & |1,0\rangle & |1,-1\rangle \end{array} \\ \begin{pmatrix} \blacksquare & 0 & 0 & 0 & 0 & 0 \\ 0 & \blacksquare & \blacksquare & 0 & 0 & 0 \\ 0 & \blacksquare & \blacksquare & 0 & 0 & 0 \\ 0 & 0 & 0 & \blacksquare & \blacksquare & \blacksquare \\ 0 & 0 & 0 & \blacksquare & \blacksquare & \blacksquare \\ 0 & 0 & 0 & \blacksquare & \blacksquare & \blacksquare \end{pmatrix} \end{array} . \qquad (1\text{-}19)$$

That is, the matrix component of **J** has a nonzero value only when $j = j'$.

1.6.2. Spin

1.6.2.1. Matrix Representation of Spin

For the matrix representation of a spin operator, a common choice of the basis set is $|s,m_s\rangle$ where s is the spin angular momentum quantum number and m_s is corresponding magnetic quantum number. Since m_s can take values from - s to s, for a proton (s = 1/2), the basis set consists of $|1/2, 1/2\rangle$ and $|1/2, -1/2\rangle$. Using eigenvalue equation (45) in (1-20), that is

$$S_z|\, s, m_s\rangle = m_s \hbar\, |\, s, m_s\rangle \qquad (1\text{-}20)$$

then,

$$S_z = \begin{pmatrix} \hbar/2 & 0 \\ 0 & -\hbar/2 \end{pmatrix}. \qquad (1\text{-}21a)$$

The other components S_x and S_y can also be found, which are given as (45),

$$S_x = \begin{pmatrix} 0 & \hbar/2 \\ \hbar/2 & 0 \end{pmatrix}, S_y = \begin{pmatrix} 0 & -i\hbar/2 \\ i\hbar/2 & 0 \end{pmatrix}. \qquad (1\text{-}21b)$$

Eq. (1-21a) and (1-21b) are sometimes expressed in terms of the so-called Pauli matrices, σ_i (i = x, y, or z), as

$$S_x = (\hbar/2)\sigma_x,\ S_y = (\hbar/2)\sigma_y,\ S_z = (\hbar/2)\sigma_z \qquad (1\text{-}22a)$$

where

$$\sigma_x = \begin{pmatrix} 0 & 1 \\ 1 & 0 \end{pmatrix},\ \sigma_y = \begin{pmatrix} 0 & -i \\ i & 0 \end{pmatrix},\ \text{and}\ \sigma_z = \begin{pmatrix} 1 & 0 \\ 0 & -1 \end{pmatrix}. \qquad (1\text{-}22b)$$

1.6.2.2. Eigenvalues and Eigenvectors of Spin Operator

In Appendix 2, it is shown that the eigenvalues of the spin operator **S** are $\pm \hbar/2$, regardless of the direction along which the components of **S** is measured. It was also shown in that appendix that using eigenbasis of I_z the eigenvectors of S_z, $|\uparrow>$ and $|\downarrow>$, can be written in terms of column matrices as discussed in *Postulate 1*. That is,

$$|\uparrow> = \begin{pmatrix} 1 \\ 0 \end{pmatrix},\ |\downarrow> = \begin{pmatrix} 0 \\ 1 \end{pmatrix}. \qquad (1\text{-}23)$$

Therefore, from *Postulate 3* and *Postulate 4*, an arbitrary state vector, **v**, of a proton can be described as

$$\mathbf{v} = a\begin{pmatrix} 1 \\ 0 \end{pmatrix} + b\begin{pmatrix} 0 \\ 1 \end{pmatrix} = \begin{pmatrix} a \\ b \end{pmatrix} \qquad (1\text{-}24)$$

and $|a|^2$ and $|b|^2$ represents the probability of the proton being in the state of *spin up* and *spin down*, respectively. Thus, the expectation value of S_z in the **v** state is given by Eq. (1-16) as

$$<S_z> = (a^* \ b^*)\begin{pmatrix} \hbar/2 & 0 \\ 0 & -\hbar/2 \end{pmatrix}\begin{pmatrix} a \\ b \end{pmatrix} = (\hbar/2)\,(|a|^2 - |b|^2). \qquad (1\text{-}25)$$

From Eqs. (1-21) through (1-22), it is clear that, in this eigenbasis of S_z,

$$S_x|\uparrow> = \hbar/2\,|\downarrow>,$$
$$S_y|\uparrow> = i\hbar/2\,|\downarrow>,$$
$$S_z|\uparrow> = \hbar/2|\uparrow>. \qquad (1\text{-}26)$$

1.6.2.3 Interaction of a Spin in External Magnetic Fields

1.6.2.3.1 Interaction of a Spin with a $\mathbf{B}_0$ Field

Based on Eqs. (1-1) and (1-3) the Hamiltonian for a spin **S** in a static external $\mathbf{B}_o$ ($B_o\vec{z}$) field is defined as

$$\boldsymbol{H} = -\boldsymbol{\mu}\cdot\mathbf{B}$$
$$= -\gamma\hbar B_o S_z, \qquad (1\text{-}27)$$

which is time-independent. Therefore, from Eq. (1-12b)

$$|\Psi(t)> = \exp(-i\boldsymbol{H}t/\hbar)\,|\Psi(0)>$$
$$= \exp(i\omega_o t S_z)\,|\Psi(0)> \qquad (1\text{-}28)$$

where $\omega_o = \gamma B_o$. Using Eq. (A3-1b), Eq. (1-28) can be written as

$$|\Psi(t)> = \{\mathbf{1}\cdot\cos(\omega_o t/2) + i\sigma_z\cdot\sin(\omega_o t/2)\}|\Psi(0)>$$

$$= \begin{pmatrix} \exp(i\omega_o t/2) & 0 \\ 0 & \exp(-i\omega_o t/2) \end{pmatrix}|\Psi(0)>. \qquad (1\text{-}29)$$

Assuming that the spin was in the eigenstate of S_x, i.e., **S** being aligned along the x-axis at t = 0, then from Eq. (A2-5b)

$$|\Psi(0)\rangle = (1/\sqrt{2})\begin{pmatrix}1\\1\end{pmatrix} \tag{1-30}$$

and therefore,

$$|\Psi(t)\rangle = (1/\sqrt{2})\begin{pmatrix}\exp(i\omega_o t/2)\\ \exp(-i\omega_o t/2)\end{pmatrix}. \tag{1-31}$$

Using Eq. (1-31), the expectation values of S_x, S_y and S_z are evaluated to be

$$\langle S_x\rangle = (\hbar/2)\cdot\cos(\omega_o t), \quad \langle S_y\rangle = (\hbar/2)\cdot\sin(\omega_o t), \quad \langle S_z\rangle = 0. \tag{1-32}$$

These solutions indicate that the spin placed along the x-axis in a static $\mathbf{B}_o$ field at t = 0, continuously rotates on the xy-plane at a frequency of ω_o.

1.6.2.3.2 Interaction of a Spin with Both $\mathbf{B}_0$ and $\mathbf{B}_1$ Fields

As was briefly discussed in sections 1.3 and 1.5, to manipulate spins NMR utilizes r.f. pulses ($\mathbf{B}_1$), which are applied to a sample orthogonal to $\mathbf{B}_o$. During the irradiation of $\mathbf{B}_1$, the Hamiltonian for a spin placed in a static $\mathbf{B}_o$ field takes the form of, using Eq. (1-11),

$$\boldsymbol{H} = -\gamma\hbar\,[B_o S_z + B_1\{\cos(\omega t)\cdot S_x - \sin(\omega t)\cdot S_y\}]. \tag{1-33}$$

The time-dependence of the Hamiltonian resulting from the circularly polarized $\mathbf{B}_1$can be removed by introducing a rotating frame.

Defining a wave function of the system in the rotating frame, $|\Psi(t)\rangle^{rot}$, as

$$|\Psi(t)\rangle^{rot} = \exp(-i\omega t S_z)|\Psi(t)\rangle \tag{1-34a}$$

or

$$|\Psi(t)\rangle = \exp(i\omega t S_z)|\Psi(t)\rangle^{rot}, \tag{1-34b}$$

the time-dependent Schrödinger equation (Eq. (1-12a)) in the rotating frame may be derived in such a way that

$$i\hbar\frac{\partial}{\partial t}|\Psi(t)\rangle = -\hbar\omega S_z\cdot\exp(i\omega t S_z)|\Psi(t)\rangle^{rot} + \exp(i\omega t S_z)\cdot i\hbar\frac{\partial}{\partial t}|\Psi(t)\rangle^{rot} \qquad (1\text{-}35a)$$

and

$$\boldsymbol{H}\,|\Psi(t)\rangle = -\gamma\hbar\,[B_o S_z + B_1\{\cos(\omega t)\cdot S_x - \sin(\omega t)\cdot S_y\}]\cdot\exp(i\omega t S_z)|\Psi(t)\rangle^{rot} \qquad (1\text{-}35b).$$

Combining Eqs. (1-35a) and (1-35b) together, and rearranging terms,

$$\begin{aligned} & i\hbar\frac{\partial}{\partial t}|\Psi(t)\rangle^{rot} \\ &= \hbar(\omega - \gamma B_o)S_z|\Psi(t)\rangle^{rot} - \gamma\hbar B_1\cdot\exp(-i\omega t S_z)\{\cos(\omega t)S_x - \sin(\omega t)S_y\}\exp(i\omega t S_z)|\Psi(t)\rangle^{rot} \\ &= \{\hbar(\omega - \gamma B_o)S_z - \gamma\hbar B_1 S_x\}|\Psi(t)\rangle^{rot} \end{aligned} \qquad (1\text{-}36)$$

where Eqs. (A3-2a) and (A3-2b) were used in the last step. Eq. (1-36) contains important information. First, the Hamiltonian in the laboratory frame of reference (Eq. (1-33)) transforms in the rotating frame into

$$\boldsymbol{H}^{rot} = -\gamma\hbar\,\{(B_o - \omega/\gamma)S_z + B_1 S_x\}, \qquad (1\text{-}37)$$

which is time-independent. Compared to Eq. (1-27), Eq. (1-37) indicates that when $\mathbf{B}_1$ is present the spin precesses around an effective magnetic field, $\mathbf{B}_{eff}$, instead of around $\mathbf{B}_o$, which is defined as

$$\mathbf{B}_{eff} = \{(B_o - \omega/\gamma)\,\vec{z}^{\,rot} + B_1\,\vec{x}^{\,rot}\}. \qquad (1\text{-}38)$$

where $\vec{x}^{\,rot}$ and $\vec{z}^{\,rot}$ are unit vectors in the rotating frame. Second, when the frequency of the r.f. pulse, ω, is set to γB_o, i.e., when the r.f. pulse is applied *on resonance*, the rotation of the spin takes place around x-axis of the rotating frame only. On resonance, therefore, tipping the spin on the transverse plane is achieved most efficiently.

The rotation angle or the flip angle of spins by an r.f. pulse irradiated for a time interval Δt is defined as

$$\theta_{flip} = \omega_1 \Delta t = \gamma B_1 \Delta t. \tag{1-39}$$

1.6.3 Description of the Evolution of Spin Systems in NMR Experiments

The description of the evolution of a spin system in terms of classical physics (Bloch equations, for instance) reveals its limitation when one deals with spins that are interacting with each other (or simply, coupled spins). The result of this kind of interaction is to give rise to physical quantities such as anti-phase coherences and multiple quantum coherences (section 1.6.3.3.2), which cannot be expressed meaningfully in terms of vectors in the Cartesian coordinates. Therefore, a quantum mechanical approach is necessary for the description of the spin-spin interactions in NMR. However, a direct approach to measure a physical quantity from a sample based on Eqs. (1-12), (1-13) and (1-16) requires detailed information on the individual spin systems in any ensemble of interest. However, in the following sections, we shall find that the density matrix approach offers a powerful way of extracting necessary information from the ensemble of the systems without knowing the details about the individual systems.

1.6.3.1 Density Matrix

Using Eqs. (1-13) through (1-17), the expectation value of an operator A can be written as

$$\begin{aligned} <\mathbf{A}> &= <\Psi|\mathbf{A}|\Psi> \\ &= (\sum_i c_i^* <a_i|)\mathbf{A}\sum_j c_j |a_j> \\ &= \sum_i \sum_j <a_i|\mathbf{A}|a_j> c_j c_i^* \end{aligned} \tag{1-40}$$

where ' * ' denotes the complex conjugate. Note that $\langle a_i|\mathbf{A}|a_j\rangle$ is a matrix element of the operator or matrix **A**, which can be expressed as A_{ij}. $c_j c_i^*$ can also be regarded as a component of a matrix and the matrix consisting of these elements is called a *density matrix* (47, 52, 61). Therefore, denoting the density matrix as ρ,

$$\begin{aligned}\rho_{ij} &= c_i c_j^* \\ &= \langle a_i|\Psi\rangle(\langle a_j|\Psi\rangle)^* \\ &= \langle a_i|\Psi\rangle\langle\Psi|a_j\rangle,\end{aligned} \tag{1-41}$$

and Eq. (1-40) reduces to

$$\begin{aligned}\langle \mathbf{A} \rangle &= \sum_i \sum_j (\mathbf{A})_{ij}\rho_{ji} \\ &= \mathrm{Tr}(\mathbf{A}\rho)\end{aligned} \tag{1-42}$$

where 'Tr' stands for a trace of a matrix, i.e., the sum of diagonal elements of a matrix. Eq. (1-42) states that the expectation value of an operator can be obtained by simply taking a trace of the product of a density matrix and a matrix representation of the operator in concern. Also, from Eq. (1-41), the *density operator* is defined as

$$\rho = |\Psi\rangle\langle\Psi|. \tag{1-43}$$

Note that Eq. (1-41) is applicable only for a single spin or for an ensemble of systems in a pure state (a state of an ensemble, in which all spin systems are in the same state). For the description of many spins in the sample or for an ensemble of systems in a mixed state (a state of an ensemble, in which each spin system is in a different state), the density matrix is defined as an average over the ensemble of the systems. Then, Eq. (1-41) is rewritten as

$$\rho_{ij} = \overline{c_i c_j^*}. \tag{1-44}$$

Therefore, a density operator or matrix is a mathematical tool for the description of a state function of the entire ensemble without detailed information about individual spin systems (61).

As an example, for the description of a two-spin system, there exist a total of four possible energy eigenstates. Denoting these basis vectors as $|\uparrow\uparrow>$, $|\uparrow\downarrow>$, $|\downarrow\uparrow>$ and $|\downarrow\downarrow>$, the general form of a state vector may be written, according to Eq. (1-13a), as

$$|\Psi> = c_1|\uparrow\uparrow> + c_2|\uparrow\downarrow> + c_3|\downarrow\uparrow> + c_4|\downarrow\downarrow> \tag{1-45}$$

and, from Eqs. (1-41), (1-43) and (1-44), the density matrix for the two-spin system can be found as

$$\rho = |\Psi><\Psi| = \begin{array}{c} \\ <\uparrow\uparrow| \\ <\uparrow\downarrow| \\ <\downarrow\uparrow| \\ <\downarrow\downarrow| \end{array} \begin{array}{c} \begin{array}{cccc} |\uparrow\uparrow> & |\uparrow\downarrow> & |\downarrow\uparrow> & |\downarrow\downarrow> \end{array} \\ \begin{pmatrix} \overline{c_1 c_1^*} & \overline{c_1 c_2^*} & \overline{c_1 c_3^*} & \overline{c_1 c_4^*} \\ \overline{c_2 c_1^*} & \overline{c_2 c_2^*} & \overline{c_2 c_3^*} & \overline{c_2 c_4^*} \\ \overline{c_3 c_1^*} & \overline{c_3 c_2^*} & \overline{c_3 c_3^*} & \overline{c_3 c_4^*} \\ \overline{c_4 c_1^*} & \overline{c_4 c_2^*} & \overline{c_4 c_3^*} & \overline{c_4 c_4^*} \end{pmatrix} \end{array} \tag{1-46}$$

From Eq. (1-15), it is obvious that the diagonal elements of the density matrix in Eq. (1-46) represent the ensemble average of the probabilities of the systems being in each of their eigenstates. On the other hand, the off-diagonal elements have information on the relationship between states (involved in each matrix element) over the ensemble of the systems.

1.6.3.2 Quantum Coherences

Since the c_i's in Eqs. (1-44) and (1-46) are complex numbers, each of them can be written as a product of a real number (magnitude of a complex number) and a phase factor, i.e., $c_{i(real)} \times$ [phase factor]. Then, Eq. (1-44) can be rewritten as

$$\rho_{ij} = \overline{c_i c_j^*} = \overline{c_{i(real)} c_{j(real)}} \; \overline{[\cos(\phi_i - \phi_j) + i\sin(\phi_i - \phi_j)]} \tag{1-47}$$

where $c_{i(real)}$ is real number and ϕ_i is a phase factor of a complex number. Note that from Eqs. (1-15) and (1-47) the complex coefficients c's contain both probability and phase information of a state of a system. According to Eq. (1-47), the diagonal elements (i = j) of a density matrix are not dependent on the relative phase between eigenstates. On the other hand, in order to enable the phase-dependent off-diagonal elements to have non-zero values, there must exist a phase coherence between the correlated states over the ensemble of the systems. In other words, those eigenstates must be coherently superposed (61) to take effect. This correlation between quantum states over the ensemble of the system is called *quantum coherence*. To create such coherence over an ensemble of systems, an external perturbation is required, which is capable of bringing about the phase relationship. This can be achieved by applying an r.f. pulse in NMR experiments (31, 47, 61).

Eq. (1-46) also indicates that there exist various *levels* or *orders of coherences*. For instance, $\overline{c_1 c_2^*}$ connects two states, $|\uparrow\uparrow>$ and $|\uparrow\downarrow>$, whose energy (or total quantum number) differ by one quantum that is associated with a transition of one spin from 'up' to 'down' state or vice versa. Therefore in this case, the level of coherence between these two states is defined as one, and corresponding coherence is referred to as a single quantum coherence (SQC). In the same sense, the coherence between $|\uparrow\uparrow>$ and $|\downarrow\downarrow>$, and between $|\uparrow\downarrow>$ and $|\downarrow\uparrow>$ is termed as a double quantum coherence (DQC) and zero quantum coherence (ZQC), respectively, and those coherences whose level of coherences are other than one are collectively referred to as multiple quantum coherence (MQC) (28, 47, 61). For an ensemble of N-spin systems, the maximum level of coherence possible is N.

Note that MQCs can be detected only *indirectly* by using the so-called multiple quantum filter (MQF) (18, 19, 25-27, 29, 62-72), which is one of the most effective techniques for suppressing unwanted signals from spectra. The practical applications of this sophisticated method are discussed in detail in chapters 4 through chapter 6.

1.6.3.3 Calculation of the Evolution of a Spin System

In the previous section, it was emphasized that the density matrix formalism allows one to describe the state of the entire ensemble without detailed information about individual spin systems, and subsequently to calculate the expectation value of a physical quantity by using Eq. (1-42). Therefore, to estimate the value of a physical quantity that varies in time as the ensemble of the spin systems evolves in time over an NMR pulse sequence, one needs to follow the evolution of density matrix.

The evolution of a spin system in NMR experiments is described in terms of the density operator by 'Liouville-von Neumann equation' (61) (Eq. (1-48))

$$\dot{\rho}(t) = -i[\mathbf{H}(t), \rho(t)] \qquad (1\text{-}48)$$

where $\dot{\rho}(t)$ denotes the time derivative of $\rho(t)$ and $\mathbf{H}(t)$ is a Hamiltonian of the system, and the braket, [ ], is the commutation operator. The derivation of Eq. (1-48) is given in Appendix 4. For a time-*independent* Hamiltonian, Eq. (1-48) has a general solution (45, 47, 52, 61) of

$$\rho(t) = U(t)\rho(0)U^{-1} \qquad (1\text{-}49a)$$

and

$$U = \exp(-i\mathbf{H}t/\hbar). \qquad (1\text{-}49b)$$

Here the matrix U is a unitary matrix, which satisfies $U^{\dagger} = (U^{*})^{T} = U^{-1}$ and $UU^{\dagger} = UU^{-1} = \mathbf{1}$ (" * " : complex conjugate; " T " : transpose of a matrix, which is equivalent to switching rows with columns in the matrix; **1**: a unit matrix). Eq. (1-49a) states that the density operator at time t can be calculated from the density operator of initial state at t = 0, if one knows the Hamiltonian under which the system evolved during t. Therefore, the calculation of the evolution of a spin system in response to NMR pulse sequence reduces to evaluating Eq. (1-49a).

Eq. (1-49a) can be evaluated in terms of either matrices or operators. In the matrix formalism, all the terms in the equation must be defined explicitly in terms of a matrix. The calculation of the evolution of a spin system in the matrix formalism by using a computer, namely, numerical methods, offers a powerful means of optimizing NMR pulse sequences. In the operator formalism, first, homogeneous second-order differential equations need to be solved to obtain a cohort of evolution or transformation equations for individual product operators, and thereafter the evolution of a spin system is evaluated (see Appendices 4 and 5).

Despite its limited application due mainly to the amount of manual calculations it requires, the product operator formalism is still useful in that it describes in a very intuitive way the evolution of spin systems under different kinds of Hamiltonians encountered in practical in-vivo NMR experiments. Therefore, in the following sections, the fundamental concepts in understanding ^{1}H-MRS will be introduced in terms of the product operator formalism, following an outline of the numerical methodology. The practical applications of numerical methods are given in Chapter 3 through Chapter 6 for the detection of mI *in vivo*. A detailed discussion on the numerical methodology can be found elsewhere (29, 31, 73, 74).

1.6.3.3.1 Outline of Numerical Methods

In numerical methodology, one solves the equation of motion of a density matrix, and the result is expressed in general in a two-dimensional parameter space representing an NMR pulse sequence, e.g., {TE, TM} for the STEAM sequence (chapters 3 and 4). To evaluate the unitary transformation in Eq.(1-49a) in this density matrix formalism, U(t) needs to be expressed in a matrix form, and this is possible if the Hamiltonian in the exponential function is a diagonal matrix.

An arbitrary, n × n Hamiltonian matrix, **H**, can be diagonalized by a unitary transformation using a unitary matrix, V, which can be formed from the eigenvectors, V_1, V_2, ... V_n, of **H**. That is,

$$V = (V_1, V_2, \cdots V_n). \tag{1-50}$$

Using the property of a unitary matrix of $VV^{-1} = \mathbf{1}$, Eq.(1-49a) can be rewritten as

$$\begin{aligned} \rho(t) &= V^{-1}V \exp(-i\mathbf{H}t/\hbar)\, V^{-1}V\, \rho(0)\, V^{-1}V \exp(i\mathbf{H}t/\hbar)\, V^{-1}V \\ &= V^{-1}\exp(-i\mathbf{H}_{diag}t/\hbar)V\, \rho(0)\, V^{-1}\exp(i\mathbf{H}_{diag}t/\hbar)V \end{aligned} \tag{1-51}$$

where $\mathbf{H}_{diag} = V\mathbf{H}V^{-1}$ is a diagonalized Hamiltonian matrix whose eigenvalues are $\lambda_1, \lambda_2, \ldots \lambda_n$.

Once an arbitrary Hamiltonian, **H**, is diagonalized, then, $\exp(i\mathbf{H}_{diag}t/\hbar)$ can be written in a matrix form as

$$\exp(i\mathbf{H}_{diag}t/\hbar) = \begin{pmatrix} \exp(i\lambda_1 t/\hbar) & & 0 \\ & \cdots & \\ & & \cdots \\ 0 & & \exp(i\lambda_n t/\hbar) \end{pmatrix}. \tag{1-52}$$

Now that the exponential operator becomes a diagonal matrix whose diagonal elements are scalar exponentials, Eq. (1-49a) can be evaluated.

According to Eq. (1-11), when the $\mathbf{B}_1$ field is on, the system Hamiltonian becomes time-dependent. However, by transforming it into the rotating reference frame, which rotates at a carrier frequency as discussed in section 1.6.2.3.2, the total Hamiltonian of the system becomes time-independent (45, 47, 52, 58), and Eq. (1-49a) retains its validity. As well, the actual r.f. pulses used for in-vivo MRS are shaped, soft pulses in general, and therefore, their modulation introduces a time-dependence into the total Hamiltonian. However, by decomposing them into infinitesimally narrow time-independent segments, the evaluation of Eq.(1-49a) reduces into successive evaluation of the equations.

1.6.3.3.2 Product Operator Formalism

Based on section 1.6.3.1, the density *matrix* for a proton can be formed as a 2 x 2 matrix from the two bras, $< \uparrow |$ and $< \downarrow |$, and two kets, $| \uparrow >$ and $| \downarrow >$. Equivalently, a density *operator* for a proton can be expanded in terms of operators in the Cartesian basis (31, 45, 47, 56, 61). That it,

$$\rho = a_1\mathbf{1} + a_2I_x + a_3I_y + a_4I_z \qquad (1\text{-}53)$$

where the coefficients a's are the expectation values of corresponding basis operators and **1** is a unity operator.

In general, for a system with N-spins, the corresponding density operator can be expanded in a total of 4^N basis operators and these basis operators are defined by the products of the Cartesian spin operators of each spin (28). For instance, for a system with spin I and spin S, the product of $\{\mathbf{1}, I_x, I_y, I_z\}$ and $\{\mathbf{1}, S_x, S_y, S_z\}$ forms the basis operator set as below

$$\rho = \rho\,(\mathbf{1}, I_z, S_z, I_zS_z, I_x, I_y, S_x, S_y, I_xS_z, I_yS_z, S_xI_z, S_yI_z, I_xS_x, I_xS_y, I_yS_x, I_yS_y). \qquad (1\text{-}54)$$

Note that, as will be discussed in the following section, those operators with more than two terms can only exist if there is an interaction between the spin I and the spin S. Based on the level of coherence for each operator, the terms such as I_x and I_y are called the 'in-phase SQCs of spin I', and S_x and S_y the 'in-phase SQCs of spin S'. Those operators such as I_xS_z and I_yS_x are referred to as 'single quantum anti-phase coherence (SQ-APC) of spin I', although they are sometimes dubbed somewhat differently in literature and text books. Here "in-phase" and "anti-phase" terms refers to the relative phase relationship between different energy states. For instance, from Eqs. (1-44) through (1-46), $\overline{c_1c_3^*}$ represents a coherence between $|\uparrow\uparrow>$ and $|\downarrow\uparrow>$ states, and $\overline{c_2c_4^*}$ between $|\uparrow\downarrow>$ and $|\downarrow\downarrow>$, both of which involve the transition of the first spin. In an "in-phase" mode, the two correlations

between $|\uparrow\uparrow>$ and $|\downarrow\uparrow>$, and between $|\uparrow\downarrow>$ and $|\downarrow\downarrow>$ are superposed in-phase. On the other hand, in an "anti-phase" mode, the superposition of the two correlations takes place with 180° out of phase. In a vector model, the in-phase and the anti-phase coherences are described by two parallel and anti-parallel vectors, respectively. However, it will be found later that the behavior of anti-phase coherence cannot be properly represented in the vector model in most NMR experiments.

The meaning of the operators, I_xS_x, I_xS_y, I_yS_x and I_yS_y, in Eq. (1-54) becomes clearer if they are written in terms of raising and lowering operators (57-60), which are defined as

$$I_{\pm} = I_x \pm iI_y \tag{1-55a}$$

hence

$$I_x = 1/2(I_+ + I_-),\ I_y = (1/2i)(I_+ - I_-). \tag{1-55b}$$

From Eq. (1-26), it also follows that

$$\begin{aligned} I_+|\uparrow> &= (I_x + iI_y)|\uparrow> \\ &= I_x|\uparrow> + iI_y|\uparrow> \\ &= (1/2)|\downarrow> + i(i/2)|\downarrow> \\ &= 0. \end{aligned} \tag{1-55c}$$

Similarly,

$$\begin{aligned} &I_+|\downarrow> = |\uparrow>, \\ &I_-|\uparrow> = |\downarrow>, \\ &I_-|\downarrow> = 0. \end{aligned} \tag{1-55d}$$

Using Eq. (1-55b), for instance, I_xS_x is expressed as $(1/4)(I_+S_+ + I_+S_- + I_-S_+ + I_-S_-)$. Upon using the same basis set for a system with spin I and spin S as in Eq. (1-45), the term, I_+S_+, returns non-zero values only when it operates on $|\downarrow\downarrow>$ giving in $|\uparrow\uparrow>$, and I_+S_+ returning $|\downarrow\downarrow>$ from $|\uparrow\uparrow>$. Since I_+S_+ and I_-S_- connect two eigenstates that differ in total

quantum number by two-quanta, they are classified as DQCs. Likewise, I_+S_- and I_-S_+, which connect two eigenstates that involve a simultaneous transition of two spins like I_+S_+ and I_-S_- but do not differ in total quantum number, are described as ZQCs.

The advantage of using the raising and lowering operator basis is that the index of each component directly represents the level of coherence. Another choice as a basis set in the product operator analysis is the spherical basis set (75), which is defined in terms of the Cartesian basis as

$$I_+ = -(I_x + iI_y)/\sqrt{2},$$
$$I_- = (I_x + iI_y)/\sqrt{2},$$
$$I_o = I_z. \qquad (1\text{-}56)$$

In the following section, various interactions of spins with their environment (external magnetic field or other spins) are discussed, which cause them to evolve in response to NMR pulse sequences.

1.7 Nuclear Spin Interaction in ^{1}H-MRS

The interactions of spins with their environment in in-vivo ^{1}H-MRS may be divided into two categories defined in terms of the origin of the magnetic field (external and local) to which the spin systems of interest is exposed. In addition to the two external magnetic fields, $\mathbf{B}_o$ and $\mathbf{B}_1$, the so-called $\mathbf{B}_o$ gradient pulse is also applied to a sample externally in in-vivo NMR for various purposes (section 1.7.5). Among the various types of interactions of spins with those external magnetic fields, the so-called chemical-shift effect, which results from the interaction between nuclear spins and $\mathbf{B}_o$, is introduced first in the next section.

In addition to these external magnetic fields, a local magnetic field is produced at the site of nuclear spins of interest by either a direct (the dipole-dipole coupling (section 1.7.3)) or an indirect (the scalar- (J-) coupling (section 1.7.2)) interaction between spins.

Of these two kinds of spin-spin interactions, the latter together with the chemical-shift effect constitute the major determinants of spin evolution in in-vivo ^{1}H-MRS. The role of the dipole-dipole coupling interaction in in-vivo NMR is to give rise to an irreversible signal loss, namely, relaxation, which will briefly be discussed in the following section as well.

1.7.1 Chemical Shift

The magnetic field strength, B_o, experienced for different nuclei within a molecule may differ, depending on the chemical environment of each nucleus resulting from the electronic bonding orbitals. Consequently, the resonance frequency of a particular nucleus is influenced by its chemical environment, and the magnitude of this influence is known as the 'chemical shift'. That is, chemical-shift is a difference in resonance frequency of protons in a molecule due to their different chemical environment.

A modified local magnetic field, of which the magnitude is proportional to that of the external $\mathbf{B_o}$, can be expressed as (52, 53, 76)

$$B_{local} = B_o(1 - \sigma) \tag{1-57}$$

where σ is called the shielding or screening constant, and is of the order of 10^{-6}. For the comparability of the spectra obtained with spectrometers of different B_o values, one defines the field-independent chemical shift of a spin I, δ_I, as (52, 53, 76),

$$\delta_I = 10^6 \cdot (\omega_I - \omega_{reference})/\omega_{reference} \tag{1-58}$$

where ω_I and $\omega_{reference}$ is the Larmor frequency of the spin I and a reference material, respectively, and δ_I is expressed in ppm (parts per million). As for the reference material, tetramethylsilane (TMS, $Si(CH_3)_4$) is commonly used for ^{1}H-MRS (53, 76).

The shielding constant, σ, may further be decomposed as (53, 76)

$$\sigma = \sigma_{dia} + \sigma_{para} \tag{1-59}$$

The first term (σ_{dia}) takes account of the diamagnetic effect, which comes from the precession of the electronic clouds around $\mathbf{B}_o$. According to Lenz's law (77), the electronic clouds subjected to an external $\mathbf{B}_o$ induce a secondary magnetic field, the direction of which is opposite to that of $\mathbf{B}_o$, thereby reducing the strength of the local field at a nucleus. This diamagnetic effect can be brought about in a single hydrogen atom. On the other hand, when the entire molecule is dealt with, it is also possible that other nuclei perturb the electron distribution of a nucleus, leading to a reduction in the diamagnetic effect or equivalently to the production of additional magnetic field in the same direction as $\mathbf{B}_o$, which can be termed as a paramagnetic effect (σ_{para} term in Eq. (1-59)).

Taking account of the chemical shift, the Zeeman Hamiltonian for a spin I in the rotating frame, $\boldsymbol{H}_{zeeman,I}{}^{rot}$, can be written as

$$\boldsymbol{H}_{zeeman,I}{}^{rot} = \hbar\, \omega_I{}^{rot}\, I_z \tag{1-60}$$

where $\omega_I{}^{rot}$ is the Larmor frequency of the spin I measured with respect to the rotating frame frequency of ω, i.e., $\omega_I{}^{rot} = \omega_I - \omega$. In practical in-vivo ^{1}H-MRS experiments, the frequency of the rotating frame is tuned to that of water resonance in general, in which case the range of chemical shifts of brain metabolites falls within ~ 600 Hz (~ 4.7 ppm) at 3.0 T.

Those terms defined in this section with regard to chemical-shift may be summarized by relating them to one another (for spin A and spin B) as $\omega_A{}^{rot} - \omega_B{}^{rot} = \omega_A - \omega_B = -\omega_o(\sigma_A - \sigma_B) = \omega_o(\delta_A - \delta_B)\cdot 10^{-6}$.

From here on we shall assume that we are in a rotating frame of reference (with the rotating frame frequency of ω), unless otherwise specified, and therefore the 'rot' superscript will be suppressed.

1.7.2 Scalar Coupling (J-coupling)

1.7.2.1 Definition

In usual NMR spectra, besides the change in the resonance frequency resulting from the chemical-shift effect a fine structure or multiplicity is observed. This suggests the existence of an additional magnetic interaction. Such an interaction cannot be attributed to the direct interaction between magnetic moments through the space (dipole-dipole interaction), because that is known to average to zero in liquids due to the rapid rotation of molecules in the sample (section 1.7.2.2). The additional interaction stems from the so-called hyperfine contact interaction between a nucleus and an s-electron (48), which in compliance with Pauli's exclusion principle affects the direction of polarization of the other s-electron in the covalent bond between two nuclei, thereby influencing the local magnetic field of the other nucleus. As a consequence, the two nuclei become coupled to each other and that coupling phenomenon is referred to as *scalar-coupling* or *J-coupling*. Since the mechanism requires a perturbation of the electron wave function at the location of the nucleus, only s-electrons can be involved in this interaction, because only s-electrons have a finite probability of existing at the nuclear site. As well, since the probability distribution of the s-electron is spherically symmetric, the J-interaction is independent of the direction of external magnetic field. The magnitude of the interaction, termed as J- (or coupling-) constant, for proton-proton coupling is less than ~ 20 Hz for the spin systems of brain metabolites and is independent of the spectrometer operating frequency.

For a system of two coupled spins, I and S, the J-coupling Hamiltonian, $\boldsymbol{H}_J$, can be expressed as

$$\boldsymbol{H}_J = 2\pi J \hbar\, \mathbf{I}\cdot\mathbf{S} = 2\pi J \hbar \{I_z S_z + I_x S_x + I_y S_y\}. \qquad (1\text{-}61)$$

1.7.2.2 Degree of Scalar-Coupling Interaction

Based on the scalar-coupling interaction, spin systems can be divided into two categories, namely uncoupled and coupled. Coupled spins can further be classified into weakly-coupled or strongly-coupled ones, depending on the degree of coupling, which is measured by the ratio of the coupling-constant to the chemical shift difference between the two coupled spins ($J/\Delta\delta$) both in Hz (for $J/\Delta\delta \ll 1$, weak coupling, otherwise strong coupling).

If $\boldsymbol{H}_{zeeman} \gg \boldsymbol{H}_J$, the $\boldsymbol{H}_J$ term can be treated as a perturbation with respect to $\boldsymbol{H}_{zeeman}$. In the perturbation theory in quantum mechanics (45), the *additional* energy arising from J-interaction can be written to the second order approximation as

$$E = E_1^{\,k} + E_2^{\,k} = \langle a_k | \boldsymbol{H}_J | a_k \rangle + \sum_{k \neq k'} \frac{|\langle a_k | \boldsymbol{H}_J | a_{k'} \rangle|^2}{E_k - E_{k'}} \qquad (1\text{-}62)$$

where a_k's are eigenbases and E_k's are corresponding energy eigenvalues of $\boldsymbol{H}_{zeeman}$. From Eqs. (1-26), (1-55c) and (1-55d), it follows that among the three terms, I_zS_z, I_xS_x and I_yS_y, in $\boldsymbol{H}_J$ in Eq. (1-61), only I_zS_z returns non-zero values from the first term in Eq. (1-62), and only I_xS_x and I_yS_y will contribute to the net E through the operation of the second term in the equation. Furthermore, the numerator of the second term is proportional to coupling-constant, J, whereas the denominator is proportional to the frequency difference from Eq. (1-7) or equivalently to the chemical-shift difference, $\Delta\delta$. Therefore, when $\Delta\delta \gg J$ or $J/\Delta\delta \ll 1$, the second term in Eq. (1-62) can be neglected and the J-coupling Hamiltonian can be expressed to the first approximation or to the *weak-coupling approximation* as

$$\boldsymbol{H}_J^{weak} = 2\pi J \hbar I_z S_z. \qquad (1\text{-}63)$$

The consequence of the scalar-coupling interaction is to split a single resonance peak into multiplet(s). As an example, illustrated in Fig. 1-2 is the calculated spectrum of

a weakly-coupled two-spin system denoted as AX. It consists of two doublets, each of which is centered at the resonance frequency of spin A and spin X, respectively. The splitting of each doublet is equal to the coupling-constant, J_{AX}. In general, for weakly-coupled spin systems, the number of peaks in a multiplet is equal to n +1 where n is the number of neighboring interacting protons. For instance, consider a weakly-coupled AX_3 spin system, for which the chemical-shift of the three X spins are identical and the coupling-constant between the three X-spins and the A-spin are all the same (in which case, the three X spins are referred to as *magnetically–equivalent* (78)). Due to the J-coupling interaction, the spin A is observed as four resonance peaks (*3*+1) or a quartet, while the spin X as a doublet (*1*+1).

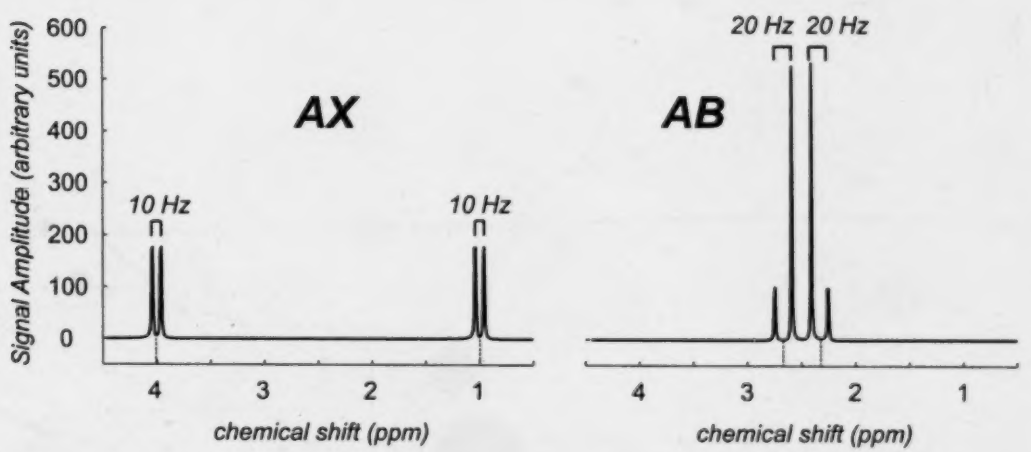

Figure 1-2 The typical proton NMR spectra of a weakly-coupled AX spin system and a strongly-coupled AB spin system at 3.0 T obtained by computer simulation. For the AX spin system, the chemical-shift of the A spin and the X spin is 4.0 and 1.0 ppm, respectively, and the coupling-constant, J_{AX}, was assumed to be 10 Hz ($J/\Delta\delta \sim 0.03$). For the AB spin system, the chemical-shift of A and B spins was assumed to be 2.65 ppm and 2.35 ppm, respectively, with J_{AB} of 20 Hz ($J/\Delta\delta \sim 0.5$). The peak-to-peak separation in each multiplet corresponds to the coupling constant, J.

In Fig. 1-2, the two peaks in each of the two multiplets of an AB spin system are no longer symmetric unlike with an AX spin system. In general, the structure of the spectra of more complicated strongly-coupled spin systems may include more lines or increased multiplicity and consequently tends to be unpredictable (52, 53, 76).

1.7.3 Dipole-Dipole Coupling

Another source of variation in the local magnetic field at the sites of nuclei can result from the 'dipole-dipole coupling' or (to distinguish it from the electron cloud-mediated indirect-coupling) 'direct-coupling' through the space between nuclei. Due to fast molecular motions in a liquid sample, however, the dipole-dipole interaction is averaged to zero and in general its effect is manifested in a weak form in in-vivo NMR spectra as signal loss or 'relaxation', although some exceptions have recently been reported (31, 79-83).

A detailed discussion on the dipole-dipole interaction can be found in typical NMR text books (47, 48, 52, 61).

1.7.4 Relaxation

We have seen in the previous sections that it is transverse magnetization or SQC that actually gives rise to the NMR signal, and that the transverse magnetization is brought about by supplying energy to the sample in the form of a $\mathbf{B}_1$ field. The energy thus provided is not permanently possessed by the spins in the sample. Instead, it is dissipated slowly into the environment of the local spins. This mechanism is called the 'relaxation', and the related time constant is termed as 'relaxation time' (46, 47, 52, 53, 76). Although the relaxation phenomenon is an essential element for delivering contrast in MRI, it is primary source of signal loss in MRS.

Both longitudinal (M_z) and transverse magnetization (M_{xy}) undergo the relaxation process which can be approximated as a first order rate process, thereby giving rise to an exponential recovery of M_z to its thermal equilibrium state where $M_z = M_o$, and an exponential decay of M_{xy} to its thermal equilibrium state of zero. As a result, two time constants are introduced in this approximation, namely T_1 and T_2, the former termed as the longitudinal relaxation time which M_z takes to recover back into ~ 63 % of its original

value of M_o, while the latter dubbed as the transverse relaxation time, the time when M_{xy} diminishes down to ~ 37 % of its maximum value.

T_1 relaxation is mainly attributed to the energy dissipation from the excited nuclei into the surrounding lattice, for instance, the nearby molecules. For this reason, T_1 relaxation is also referred to as 'spin-lattice relaxation'.

In the vector model, the observation of the net transverse magnetization requires phase coherence among the individual magnetic dipole moment vectors precessing at the resonance frequency in the sample. The phase coherence, which can be brought about by a 90° r.f. pulse is gradually lost due mainly to interactions among the excited protons in the sample. In this context, the transverse relaxation is also termed as 'spin-spin relaxation'.

An inhomogeneous local magnetic field over the sample resulting from the imperfection of the magnet and the magnetic susceptibility effect also induces transverse relaxation (46, 47, 52, 53, 76). However, the transverse relaxation of this kind is distinguished from that arising from the spin-spin interaction in that the former takes place time-independent (neglecting diffusion effect) and the resultant loss of phase coherence among the spins in the sample can be retrieved by applying a 180° pulse. This refocusing of the dephased spins in the sample, namely, the spin-echo (section 1.11.1), however, cannot recover the decay of the transverse magnetization induced by the time-dependent spin-spin interactions.

1.7.5 Gradient Pulses

In in-vivo MRS, spatial localization is achieved by incorporating 'gradient pulses' (84, 85) in conjunction with bandwidth limited r.f. pulses. A gradient pulse spatially encodes the spins in the sample by making the local magnetic field vary in a controlled manner over the sample, and the simultaneous irradiation of a band-limited r.f. pulse selectively excites a 'slice' in the sample (section 1.8). In addition to these 'slice-

selective' gradients, gradient pulses are also utilized to destroy unwanted transverse magnetization, in which case they are termed as 'spoiler' or 'crusher' gradients (sections 1.11.3 and 1.11.4). Another important application of gradient pulses in in-vivo MRS is as a 'filtering' gradient to filter out a specific order of coherence in MQF sequences (section 1.11.4).

The local magnetic field strength during the application of a gradient pulse can be expressed as

$$B(r) = B_o + \mathbf{G}\cdot\mathbf{r} \tag{1-64}$$

where $\mathbf{r}$ is a displacement vector measured from the isocenter of the magnet where the static field $\mathbf{B}_o$ exists, and $\mathbf{G}$ is a gradient vector that can be written as $|G|\,\bar{z}$ ($\bar{z}$: unit vector along the z-direction in the Cartesian coordinate system; $|G|$: the magnitude of the gradient vector), i.e., the direction of the gradient field is always parallel to the $\mathbf{B}_o$. From Eq. (1-64), the net Larmor precession frequency ω in the presence of the gradient pulse can also be written as

$$\begin{aligned}\omega &= \omega_o + \omega_G \\ &= -\gamma(B_o + \mathbf{G}\cdot\mathbf{r})\end{aligned} \tag{1-65}$$

where ω_G ($= -\gamma\mathbf{G}\cdot\mathbf{r}$) is an additional angular frequency resulting from the gradient field. Therefore, in the rotating frame, the phase angle accumulated on spins by the application of the gradient pulse for a time t is given by

$$\theta_G = \omega_G \cdot t = -\gamma\mathbf{G}\cdot\mathbf{r}\,t \tag{1-66a}$$

or

$$\theta_G = -\gamma \int \mathbf{G}\cdot\mathbf{r}\,dt\,. \tag{1-66b}$$

In the practical implementation of a gradient pulse into NMR pulse sequences, a finite ramp time is required before the gradient attains its maximum amplitude, due to limited performance of the hardware. In this context, Eq. (1-66b) more precisely defines the amount of phase accumulation during a gradient pulse than Eq. (1-66a), which assumes an ideal, rectangular gradient pulse.

From Eq. (1-65), the gradient Hamiltonian, $\boldsymbol{H}_G$, can be written in the rotating frame as

$$\boldsymbol{H}_G = \hbar\,\omega_G\,\mathrm{I}_z = -\,\gamma\hbar\,\mathbf{G}\cdot\mathbf{r}\mathrm{I}_z. \qquad (1\text{-}67)$$

1.8 Spatial Localization

In in-vivo MRS, a shaped, band-limited r.f pulse (or *soft* r.f. pulse) is used predominantly rather than a rectangular (hard) pulse for selective excitation of a volume of interest (VOI) in the sample (slice selection). It is also used to selectively excite particular resonance lines in a frequency domain (frequency-selectivity).

A soft r.f. pulse can be characterized by the length and the shape of the pulse modulation envelope. In particular, the shape of the pulse envelope determines the spatial distribution of the excitation envelope. As illustrated in Fig. 1-3, the gradient causes the local magnetic field to vary linearly in space. Consequently the local resonance frequency in the sample has a corresponding variation.

The irradiation of a shaped r.f pulse with a limited bandwidth, $\Delta\omega$, enables a selective excitation of the sample to take place. Due to the change in local resonance frequency, however, the net location of the transverse components of the dipole vectors immediately after the selective excitation are distributed on the transverse plane in the rotating frame. To refocus these dephased components to recover maximal transverse magnetization, another gradient pulse referred to as a refocusing lobe is required, the polarity of which is opposite to the preceding slice-selection gradient.

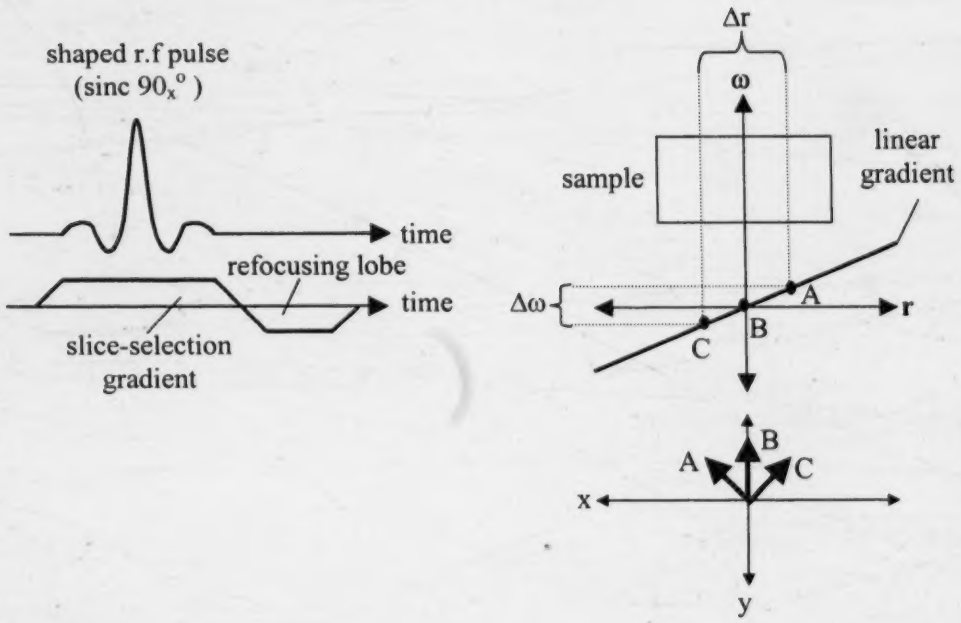

Figure 1-3 A practical example of slice selection by a shaped 90_x° r.f pulse and a slice-selection gradient. The slice-selection gradient encodes local magnetic field resulting in a distribution of linearly varying resonance frequency in one dimension. By applying an r.f pulse with a limited bandwidth of $\Delta\omega$ concurrently with the gradient, selective spatial excitation (Δr) is achieved. A refocusing lobe refocuses dipole vectors (A and C) that have been dephased just after the selective excitation.

1.9 Evolution of Spin Systems and Sequence Optimization

In general the spin system of each key brain metabolite has its own characteristic chemical-shift and J-constant values, giving rise to different evolutionary pathways and subsequently different spin responses to a particular NMR pulse sequence. Nonetheless, due to the lack of uniqueness in spectral characteristics of a variety of spin systems found *in vivo*, and to the multiplicity of resonances arising from J-coupling interaction, one needs to maximize a target signal(s) and to minimize its contamination from background unwanted signals. This procedure, which is essential for identifying and ultimately quantifying a targeted metabolite using MRS technique is called sequence optimization.

To achieve this goal, the evolution of a density operator in response to an NMR pulse sequence must be evaluated for each spin system, and, as discussed in section 1.6.3.3, this can be done by solving Eq. (1-49a), provided that the total Hamiltonian of the spin system is known.

1.9.1 Evolution of Weakly-coupled Spin Systems

For a weakly-coupled two-spin system with spin I and spin S, the total Hamiltonian, $\boldsymbol{H}_{total}$, in the rotating frame can be written as

$$\begin{aligned}\boldsymbol{H}_{total} &= \boldsymbol{H}_{r.f.} + \boldsymbol{H}_G + \boldsymbol{H}_{Zeeman} + \boldsymbol{H}_J^{weak} \\ &= -\gamma\hbar B_1 (I_x + S_x) - \gamma\hbar \mathbf{G}\cdot\mathbf{r}(I_z + S_z) + \hbar(\omega_I I_z + \omega_S S_z) + 2\pi J \hbar I_z S_z \end{aligned} \qquad (1\text{-}68)$$

where the irradiation of the r.f. pulse was assumed to be polarized along the + x-axis of the rotating frame.

Using Eq. (1-49a), it is possible to calculate the evolution of the density operator under each of the Hamiltonians in Eq. (1-68) in terms of product operators. The derivation of the evolution equations from Eq. (1-49a) reduces to solving a cohort of homogeneous second order differential equations. As an example, the derivation of the evolution (or transformation) equations under the gradient Hamiltonian, $\boldsymbol{H}_G$ is given in Appendix 5.

Note that each Hamiltonian in Eq. (1-68) is nothing but energy expressed quantum mechanically in terms of an operator. Since $E = \hbar\omega$, each Hamiltonian component in Eq. (1-68) can be viewed as $\hbar\omega\cdot$*operator*. Therefore in this context, a generalized angular frequency, ω, can be defined for $\boldsymbol{H}_{r.f.}$, $\boldsymbol{H}_G$, $\boldsymbol{H}_{Zeeman}$ and $\boldsymbol{H}_J^{weak}$ as $-\gamma B_1$, $-\gamma\mathbf{G}\cdot\mathbf{r}$, ω_I (or ω_S), and $2\pi J$, respectively. Since rotation angle = angular frequency × time, a generalized rotation angle, θ, can also be defined as $\omega \times t$ (t: time during which a Hamiltonian applies to the system). Therefore, using in Eq. (1-69) below a notation for

the description of the evolution of a density operator under the action of each Hamiltonian

$$\rho(0) \xrightarrow{\theta \cdot operator} \rho(t), \tag{1-69}$$

the evolution equation for I_y under the r.f. Hamiltonian is derived as

$$I_y \xrightarrow{-\gamma B_1 t \cdot I_x} I_y\cos(-\gamma B_1 t) + I_z\sin(-\gamma B_1 t) \tag{1-70a}$$

and under the chemical-shift Hamiltonian,

$$I_y \xrightarrow{\omega t \cdot I_z} I_y\cos(\omega_I t) - I_x\sin(\omega_I t), \tag{1-70b}$$

and finally under the scalar-coupling Hamiltonian,

$$I_y \xrightarrow{2\pi J t \cdot I_{1z}I_{2z}} I_y\cos(\pi J t) - 2I_{1x}I_{2z}\sin(\pi J t). \tag{1-70c}$$

In particular, during a period without an r.f and a gradient pulse, namely, a free evolution period, $\boldsymbol{H}_{total}$ in Eq. (1-68) simplifies to $\boldsymbol{H}_{total} = \boldsymbol{H}_{Zeeman} + \boldsymbol{H}_J$, and Eq. (1-49a) takes the form of

$$\begin{aligned}\rho(t) &= \exp(-i\boldsymbol{H}_{total}t/\hbar)\rho(0)\exp(i\boldsymbol{H}_{total}t/\hbar) \\ &= \exp\{-i(\boldsymbol{H}_{Zeeman} + \boldsymbol{H}_J^{weak})t/\hbar\}\rho(0)\exp\{i(\boldsymbol{H}_{Zeeman} + \boldsymbol{H}_J^{weak})t/\hbar\}.\end{aligned} \tag{1-71}$$

Since $[\boldsymbol{H}_{Zeeman}, \boldsymbol{H}_J^{weak}] = 0$, Eq. (1-58) can be rewritten as

$$\begin{aligned}&\rho(t) = \\ &\exp\{-i(\boldsymbol{H}_{Zeeman})t/\hbar\}\exp\{-i(\boldsymbol{H}_J^{weak})t/\hbar\}\rho(0)\exp\{i(\boldsymbol{H}_J^{weak})t/\hbar\}\exp\{i(\boldsymbol{H}_{Zeeman})t/\hbar\}.\end{aligned} \tag{1-72}$$

Eq. (1-72) contains a significant point, namely, that for a weakly-coupled spin system, for which the J-coupling Hamiltonian and the Zeeman Hamiltonian commute, one can evaluate the evolution of the spin system during a free evolution period *interaction by interaction*. Since the gradient Hamiltonian also commutes with both the Zeeman and the J-coupling Hamiltonians in Eq. (1-68), the interaction-by-interaction evaluation of the evolution of a density operator still holds for the gradient Hamiltonian. The r.f pulse Hamiltonian on the other hand does not commute with any of the other Hamiltonians in Eq. (1-68). However, in typical NMR experiments the duration of r.f. pulses is much shorter than a free evolution period or an inter-pulse period. For this reason any intra-pulse evolution of spin systems is neglected in the product operator calculation approach and, in fact, this is one of the shortcomings of the method.

A set of transformation equations under each of the Hamiltonians is given in Appendix 6a for a weakly-coupled two-spin system.

1.9.2 Evolution of Strongly-coupled Spin Systems

For strongly-coupled spin systems, the full scalar-coupling Hamiltonian in Eq. (1-61) needs to be incorporated in evaluating Eq. (1-49a) instead of Eq. (1-63). In this case, since $\boldsymbol{H}_{Zeeman}$ and $\boldsymbol{H}_J$ no longer commute, the reduction of Eq.(1-71) into (1-72) is not possible. Nonetheless, the total Hamiltonian that applies during any free evolution period can be rearranged into two groups that do commute with each other, and consequently some simplification of the calculation of the density operator can be exploited (86). That is, for a strongly-coupled AB spin system, the Hamiltonian in the absence of both r.f. and gradient pulses can be written as

$$\begin{aligned}\boldsymbol{H} &= \{\boldsymbol{H}^{weak}\} + \{\boldsymbol{H}^{strong}\} \\ &= \{\hbar \cdot \varpi \cdot (A_z + B_z) + 2\pi J_{AB} \hbar (A_z B_z)\} + \{\hbar \cdot \delta\omega \cdot (A_z - B_z) + 2\pi J_{AB} \hbar (A_x B_x + A_y B_y)\} \quad (1\text{-}73)\end{aligned}$$

where $\varpi = (\omega_A + \omega_B)/2$ and $\delta\omega = (\omega_A - \omega_B)/2$, and ω_A and ω_B is the Larmor frequency of spin A and spin B, respectively, measured with respect to the rotating frame frequency of

ω. Note that H^{weak} is similar but not identical to H_J^{weak} defined in section 1.9.1. Since $[H^{weak}, H^{strong}] = 0$, the density operator at time t can be obtained by evaluating separately the evolution of the spin system under H^{weak} and H^{strong}. In Appendix 6b the evolution equations for an AB spin system are summarized in terms of the Cartesian basis operators. These equations are used extensively in Chapter 6.

In this way, the evolution of spin systems in response to NMR pulse sequences can be calculated using the product operator formalism. However, since it requires manual calculations, its application is limited to strongly-coupled spin systems with restricted number of spins in the system. Moreover, in the product operator analysis, shaped r.f. pulses are approximated as a rectangular hard pulse whereby any intra-pulse evolution of a spin system is neglected. This hard-pulse approximation used in the product operator analysis can lead to a significant error, which becomes even worse when the soft r.f. pulse is slice-selective. This exacerbation of mismatch between the calculated and the experimental response of a spin system to pulse sequences in in-vivo MRS is ascribed mainly to the so-called "voxel displacement effect" (87, 88), which is much more significant for weakly-coupled spin systems due to the larger chemical-shift dispersion between the coupled spins. The analytical consideration of this effect is given in section 1.11.1.

1.10 Practical Example of the Evaluation of Spin Evolution in a Spin-echo Sequence

In this section, an actual calculation of spin evolution is given for an uncoupled IS, a weakly-coupled AX and a strongly-coupled AB spin systems in response to a spin-echo sequence.

1.10.1 Spin-echo Sequence (General)

A hard pulse spin-echo sequence is illustrated in Fig. 1-4. The first 90° r.f. pulse excites a spin system in the thermal equilibrium state to create a net transverse

magnetization or in-phase SQCs. In the rotating frame an uncoupled-spin system will evolve under the chemical-shift Hamiltonian during the inter-pulse delays, TE/2.

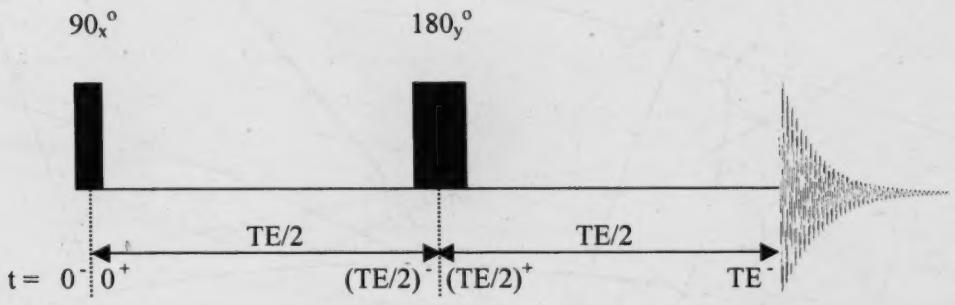

Figure 1-4 A spin-echo pulse sequence. It consists of one 90° and one 180° r.f. pulses. The first and the second inter-pulse delays together are called an echo time.

For a coupled-spin system the evolution will take place under the J-coupling Hamiltonian as well. The chemical-shift evolution is refocused by the 180° r.f. pulse for uncoupled and weakly-coupled spin systems but not for a strongly-coupled ones. After these evolutions, the in-phase SQCs are detected during the acquisition period as a final signal output.

1.10.2 Evolution of an Uncoupled Spin System in Response to the Spin-echo Sequence

In the rotating frame, just before the first 90° pulse, the density operator of the system is described as

$$\rho(0^-) = I_z + S_z. \tag{1-74}$$

Just after the excitation by the 90° pulse, the density operator upon the right-hand side rotation takes the form of

$$\rho(0^+) = -(I_y + S_y), \tag{1-75}$$

which contains the in-phase SQCs of spin I and spin S. Since no coupling exists between the two spins, the spin system evolves independently under the chemical-shift Hamiltonian alone, during two inter-pulse delays. The evolution of spin S is symmetric with that of spin I for this uncoupled IS spin system. Therefore, only the evolution of spin I will be considered henceforth. Just before the 180° pulse, the density operator has become

$$\rho(TE/2^{-})_I = -I_y \cos(\omega_I \cdot TE/2) + I_x \sin(\omega_I \cdot TE/2) \tag{1-76}$$

where ω_I is the relative Larmor frequency of the spin I, which is calculated with respect to the operating frequency of the magnet system. Since the 180° pulse is irradiated along the y-axis, that is, the phase of the pulse is set to y, it has no effect on the I_y term and simply changes the sign of the I_x term in Eq. (1-76). Thus after the 180° pulse the density operator for spin I merely reduces into

$$\rho(TE/2^{+})_I = -I_y \cos(\omega_I \cdot TE/2) - I_x \sin(\omega_I \cdot TE/2). \tag{1-77}$$

After the second TE/2 period the density operator evolves into

$$\begin{aligned}\rho(TE^{-})_I &= -\{I_y \cos(\omega_I \cdot TE) - I_x \sin(\omega_I \cdot TE)\}\cos(\omega_I \cdot TE) \\ &\quad - \{I_x \cos(\omega_I \cdot TE) + I_y \sin(\omega_I \cdot TE)\}\sin(\omega_I \cdot TE) \\ &= -I_y. \end{aligned} \tag{1-78}$$

According to Eq. (1-78), the coherence of the uncoupled spin I at the onset of acquisition takes the same form that it had just after the 90° excitation pulse in Eq. (1-75), and this recovery of the spin I (as well as spin S) takes place independently of both the sequence timing (TE) and ω_I, i.e., the spin I is *refocused*. From an analytical point of view, this is because the chemical-shift evolution of spin I during the first and the second TE/2 were cancelled out by the 180° *refocusing* pulse. This mechanism that refocuses chemical-shift evolution of a spin system by 180° r.f. pulse encapsulated with a pair of symmetric free evolution period, is referred to as the *spin-echo* and the total timings of the evolution

periods is dubbed as the *echo time* (TE). The spin-echo resulting from 180° pulse greatly simplifies the analysis of spin evolution in response to NMR pulse sequences.

In Fig. 1-5, the spin-echo mechanism is illustrated in the vector model, which is sufficient for the description of the evolution of uncoupled spin systems.

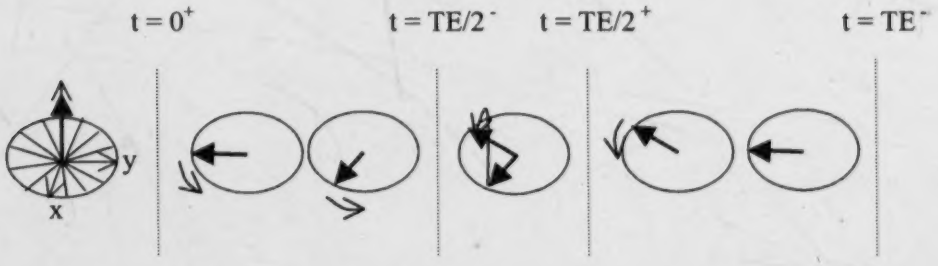

Figure 1-5 A vectorial description of the evolution of an uncoupled spin in the rotating frame in a spin-echo experiment. In the initial thermal equilibrium state, no net transverse magnetization exists due to the arbitrarily-phased transverse components of dipole moment vectors in the sample. A 90° pulse renders the transverse components of the dipole moment vectors possess coherent phases, thereby giving rise to a net transverse magnetization. During the first TE/2 period the transverse magnetization evolves under the chemical-shift effect, which is a rotation about z-axis. This rotation is reversed in direction by the 180° pulse and subsequently refocused just before the onset of acquisition. A right-hand side rotation was assumed.

1.10.3 Evolution of a Weakly-Coupled Spin System in Response to the Spin-echo Sequence

The refocusing of the chemical-shift evolution by a 180° r.f. pulse also holds for weakly-coupled spin systems. Therefore the chemical-shift effect will be neglected in the following analysis for the evolution of a weakly-coupled AX spin system in response to the spin-echo sequence.

Just before the 180° refocusing pulse, using Eq. (A6a-3) in Appendix 6a, the density operator for spin A of a weakly-coupled AX spin system becomes

$$\rho(TE/2^{-})_A = -A_y \cos(\pi J_{AX} \cdot TE/2) + 2A_x X_z \sin(\pi J_{AX} \cdot TE/2) \qquad (1\text{-}79)$$

where J_{AX} is the scalar-coupling constant between spin A and spin X.

After a 180_y° pulse that has no net effect on the coherence terms in Eq. (1-79) (see Eq. (A6a-1) in Appendix 6a), the spin system continues to evolve and at the onset of acquisition the density operator takes the form of

$$\rho(TE^{-})_A = -A_y \cos(\pi J_{AX} \cdot TE) + 2A_x X_z \sin(\pi J_{AX} \cdot TE). \qquad (1\text{-}80)$$

Upon symmetric consideration, the density operator for spin X at time $t = TE^{-}$ can also be written as

$$\rho(TE^{-})_X = -X_y \cos(\pi J_{AX} \cdot TE) + 2X_x A_z \sin(\pi J_{AX} \cdot TE). \qquad (1\text{-}81)$$

Note that Eqs. (1-80) and (1-81) contain not only in-phase SQCs but also anti-phase SQCs terms, which are created from coupled spins only as a result of scalar-coupling interaction. According to Eqs. (1-80) and (1-81), the amount of in-phase SQC or APC at the end of the spin-echo period can be controlled by adjusting TE. For instance, a choice of TE set to $1/J_{AX}$ maximizes the amount of A_y, while the choice of TE of 1/2J maximizes that of $2A_xX_z$. This temporal weighting of either of the two types of coherence by optimizing TE becomes of special importance in the design of an MQF (section 1.11.4), in which the amount of APC is proportional to the signal yield of the sequence.

In NMR experiments, a complex signal is acquired using a quadrature detection. Assuming the real part of the complex signal is collected along the y-axis of the rotating frame, then, in product operator analysis taken in the Cartesian operator basis, the actual signal acquired during the detection period is proportional to the sum of the coefficients of SQCs with y-phase such as I_y, which is equivalent to taking the real part of the sum of the coefficients of I_- in the spherical operator basis (89) defined in Eq. (1.43). Therefore, the signal from spin A, $S(t)_A$, after the spin-echo period is proportional to

$$S(t)_A \sim \cos(\pi J_{AX} \cdot TE). \qquad (1\text{-}82)$$

A pseudovectorial description of the evolution of a weakly-coupled AX spin system is illustrated in Fig. 1-6.

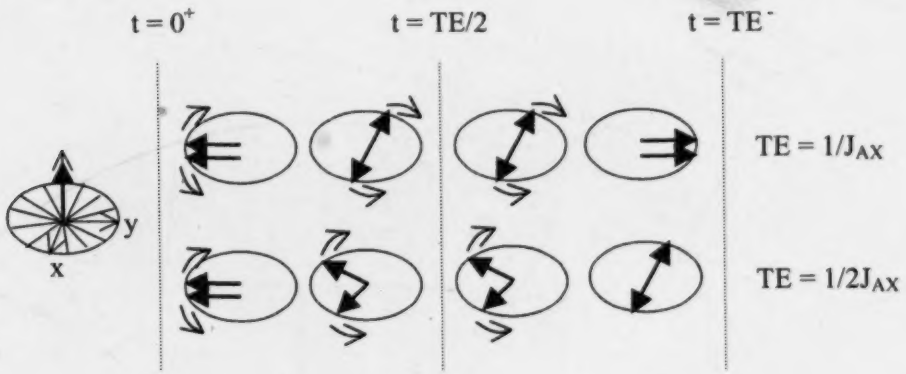

Figure 1-6 A vectorial description of the scalar-coupling evolution of a weakly-coupled spin system in the rotating frame during TE. To illustrate the creation of APC, two vectors are used, which are coupled to each other. Immediately after the 90° pulse, each vector starts rotating in opposite direction on the xy-plane of the rotating frame. Depending on the choice of TE, the coupled two vectors can form either in-phase or anti-phase just before the onset of acquisition. No chemical-shift effect was considered as it is refocused by the 180° pulse. A right-hand side rotation was assumed.

1.10.4 Evolution of a Strongly-Coupled Spin System in Response to the Spin-echo Sequence

As discussed in section 1.9.2, due to the additional terms in the strong-coupling Hamiltonian, one can no longer evaluate the evolution of the strongly-coupled spin systems under the Zeeman Hamiltonian and the scalar-coupling Hamiltonian, separately. As described in section 1.9.2 and Appendix 6b, however, the calculation can be simplified by separating the total Hamiltonian in the absence of an r.f. pulse and a gradient pulse into $\boldsymbol{H}^{weak}$ and $\boldsymbol{H}^{strong}$, each of which contains both chemical-shift and scalar-coupling interaction terms.

Assuming for brevity of analysis that only A_y exists just after the first 90° pulse, then after the spin-echo period the density operator for a strongly-coupled AB spin system is calculated, using the evolution equations in Appendix 6b, to be

$$\begin{aligned}\rho(TE^-)_A = \; & A_y \cdot\{-\cos(\pi J\cdot TE)\cos^2(\Lambda\cdot TE/2) \\ & - [(\delta\omega/\Lambda)^2-(\pi J/\Lambda)^2]\cos(\pi J\cdot TE)\sin^2(\Lambda\cdot TE/2)\} \\ & + 2A_xB_z\cdot\{\sin(\pi J\cdot TE)\cos^2(\Lambda\cdot TE_1/2) \\ & \quad + [(\delta\omega/\Lambda)^2-(\pi J/\Lambda)^2]\sin(\pi J\cdot TE)\sin^2(\Lambda\cdot TE/2)\} \\ & + B_x\cdot\{-2(\delta\omega/\Lambda)(\pi J/\Lambda)\sin(\pi J\cdot TE)\sin^2(\Lambda\cdot TE/2)\} \\ & + B_y\cdot\{-(\pi J/\Lambda)\sin(\pi J\cdot TE)\sin(\Lambda\cdot TE)\} \\ & + 2B_xA_z\cdot\{-(\pi J/\Lambda)\cos(\pi J\cdot TE)\sin(\Lambda\cdot TE)\} \\ & + 2B_yA_z\cdot\{2(\delta\omega/\Lambda)(\pi J/\Lambda)\cos(\pi J\cdot TE)\sin^2(\Lambda\cdot TE/2)\} \qquad (1\text{-}83)\end{aligned}$$

where $\Lambda = [(\delta\omega)^2 + (\pi J)^2]^{1/2}$ and $\delta\omega = (\omega_A - \omega_B)/2$.

In weak-coupling approximation ($\delta\omega >> \pi J$, $\Lambda \sim \delta\omega$, $\delta\omega/\Lambda \sim 1$, and $\pi J/\Lambda \sim 0$), Eq. (1-83) reduces to,

$$\rho(TE^-)_A^{weak} \sim A_y\cdot\{-\cos(\pi J\cdot TE)\} + 2A_xB_z\cdot\{\sin(\pi J\cdot TE)\}, \qquad (1\text{-}84)$$

which is equal to Eq. (1-80). Therefore, the evolution of a weakly-coupled AX spin system during a spin-echo period can be regarded as a special case of that of a strongly-coupled AB spin system.

The density operator for spin B, $\rho(TE^-)_B$, can also be obtained from Eq. (1-83) by symmetric consideration, in which a sign change is required for the terms with $\delta\omega$, as was shown in Appendix 6b. Note that in Eq. (1-83), SQCs of spin B are also created during the spin-echo period, despite the initial state at $t = 0^+$ consisting exclusively of spin A. This transfer of transverse magnetization between different spin species, e.g., from A_y to B_y in this example, is referred to as the *coherence transfer*. Although different

definitions are found elsewhere (52, 78), the term 'coherence transfer' found in the thesis will be used in this sense.

Among those four SQCs of spin B in Eq. (1-83), which are created from initial A_y during TE, terms such as B_x and B_yA_z are produced solely from strongly-coupled spin systems, whereas B_y and B_xA_z are ordinary coherence terms that are common for all coupled spin systems. This becomes clear if Eq. (1-83) is compared with Eqs. (1-80) and (1-82). The significance of these specifically strong-coupling terms, which was originally pointed out by Trabesinger et al (90), will be discussed extensively in Chapters 5 and 6. Figure 1-7 summarizes the origin of these two distinct groups of SQCs created from an AB spin system after a spin-echo.

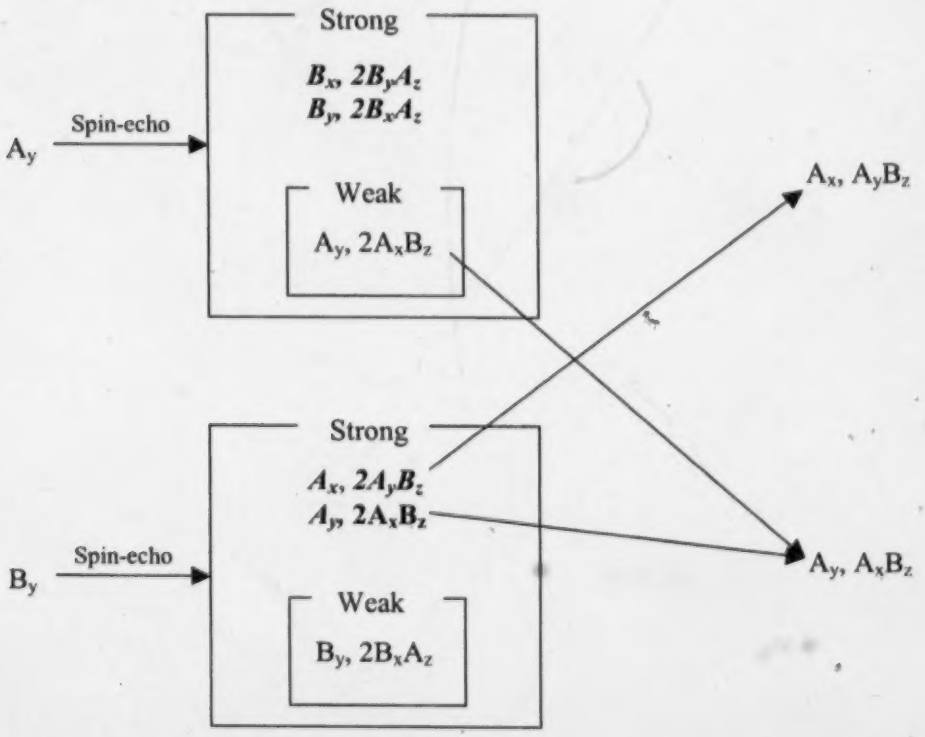

Figure 1-7 The coherence pathways for a strongly-coupled AB spin system in a spin-echo experiment. Unlike a weakly-coupled spin system, additional terms (bold-italic) are created through coherence transfer that is facilitated by the strong-coupling Hamiltonian. As a result, there exist strong-coupling specific SQCs at the end of the spin-echo period such as A_x and A_yB_z, which are distinguished from A_y and A_xB_z terms.

In Eq. (1-83), the density operator for the spin A of the strongly-coupled AB system is still a function of ω_A and ω_B even after the spin-echo period. This is because the chemical-shift effect was not fully refocused, in contrast to the uncoupled and weakly-coupled spin systems. For this reason, together with the creation of the strong-coupling specific coherence terms through coherence transfer, the vectorial description of the evolution of a AB spin system during the spin-echo period is not straightforward.

1.11 Pulse sequences in In-vivo ^{1}H-MRS

In practical human studies, any NMR pulse sequence requires at least three soft r.f. pulses in conjunction with gradient pulses to define a VOI or a single voxel. PRESS (Point-REsolved SpectroScopy) (91, 92) and STEAM (STimulated Echo Acquisiton Mode) (93, 94) are the two most popular single voxel localization pulse sequences in in-vivo ^{1}H-MRS. The superiority of one over the other relies on the spin systems of a target metabolite to be observed. For instance, for the quantification of metabolites with uncoupled spin system(s), PRESS sequence with long sequence timings is a better choice for higher signal yield of the sequence, by a factor of 2 in principle, relative to STEAM. The use of long sequence timings facilitates the suppression of unwanted signals, in particular, from broad macromolecule resonances. For metabolites with coupled spin system(s), however, due mainly to the voxel-shift effect (87, 88), the status of PRESS needs to be reconsidered. The voxel-shift effect, which is introduced during slice-selection by the combined use of an r.f. and a gradient pulse, plays a significant role in quantitative analysis of metabolites with coupled spins. In the following section, therefore, a discussion on this issue is given prior to proceeding to the practical pulse sequences for human studies such as PRESS, STEAM and MQF.

1.11.1 Voxel-Selection Phenomena

Due to the chemical-shift effect and the limited bandwidth of soft r.f pulses, the actual spatial slices selected for the different spin species by each combination of r.f. pulse and gradient pulse are shifted relative to each other in space. This phenomenon,

which is manifested as the accumulated shifts of slices in three orthogonal dimensions, is called the voxel-shift (or -displacement) effect. It is illustrated in Fig. 1-8, and for uncoupled spins results in different spectral lines originating from different (but usually overlapping) locations in space.

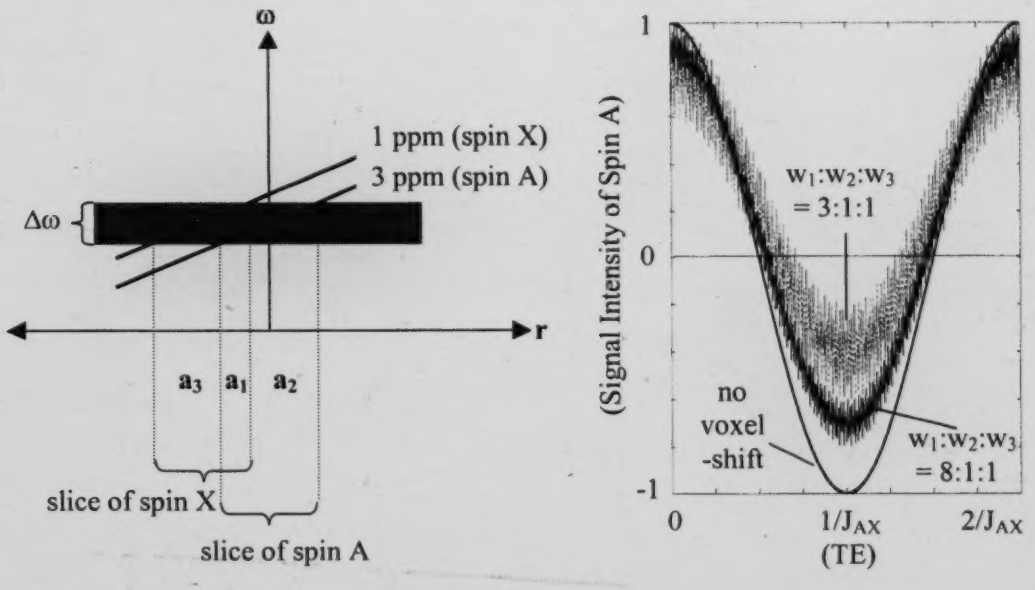

Figure 1-8 The voxel-selection phenomenon. Due to the chemical-shift the actual slices selected by the combination of an r.f pulse (bandwidth $\Delta\omega$) and a gradient pulse are defined differently for different spin species in a molecule. As a result, the actual r.f pulse experienced by the spin A and the spin X in three regions, a_1, a_2 and a_3 is different from one another. Also illustrated in the right panel is a loss of signal of spin A in the spin-echo experiment resulting from the voxel-shift effect at 3.0 T. The amount of signal loss is dependent not only on the ratio of w_1, w_2 and w_3, which are weighting factors proportional to the area and the spin density of each region, but on TE (or scalar-coupling constant, J_{AX}) as well. The relative Larmor frequency of the A spin, ω_A, and J_{AX} was assumed to be 766π rad/sec (at 3.0 T) and 5 Hz, respectively. No field inhomogeneity effect was assumed.

The amount of voxel-shift, Δr, can be written as (87)

$$\Delta r = r_{voxel} \times (\Delta\delta/\Delta\omega) = \Delta\delta/\gamma G \qquad (1\text{-}85)$$

where r_{voxel} is a voxel dimension, $\Delta\delta$ is a chemical-shift difference between two coupled spins measured in Hz with respect to the carrier frequency, BW is a bandwidth of an r.f pulse in Hz, and G is a gradient strength. Hence, the amount of voxel displacement is more significant for coupled spins that have a large chemical-shift difference and therefore tend to be weakly-coupled. It is mitigated by a wider bandwidth of the r.f. pulse or a stronger gradient strength.

For coupled spins, the consequence of shifted voxels becomes more complicated. Consider the response of a weakly-coupled AX spin system to a spin-echo sequence similar to that shown in Fig. 1-4, but equipped with soft r.f pulses. As described in Fig. 1-8, only in region a_1 do both spin A (3 ppm) and spin X (1 ppm) of the same coupled pair experience the band-limited 180_y° refocusing pulse. Just after the spin-echo period, the density operator for spin A in region $\mathbf{a_1}$, $\rho(TE^-)_A^{a1}$, takes the same form as in Eq. (1-80). In contrast, only spin A will experience the 180_y° refocusing pulse in region a_2, and only spin X in region a_3. That is to say, the 180° r.f. pulse works as a frequency-selective pulse due to the voxel-shift effect. Neglecting field inhomogeneity effect, the density operator for spin A in each region can be shown to become,

$$\begin{aligned}
\rho(TE^-)_A^{a1} &= -A_y\cos(\pi J_{AX}\cdot TE) + 2A_xX_z\sin(\pi J_{AX}\cdot TE) && \text{(region } a_1\text{)} \\
\rho(TE^-)_A^{a2} &= -A_y && \text{(region } a_2\text{)} \qquad (1\text{-}86) \\
\rho(TE^-)_A^{a3} &= -A_y\cos(\omega_A\cdot TE) && \text{(region } a_3\text{)}
\end{aligned}$$

where ω_A is the relative Larmor frequency of the spin A. The ω_A-dependence of $\rho(TE^-)_A^{a3}$ results from the fact that the spin A in region a_3 did not experience the 180_y° refocusing pulse and therefore the chemical-shift evolution of that spin was not refocused in that region. Since the final output is the sum of signal from all three regions, the signal for A spin, after the spin-echo period becomes

$$\begin{aligned}
S(TE)_A &\sim \cos(\pi J_{AX}\cdot TE) && \text{(without voxel-shift effect)} \\
S(TE)_A &\sim w_1\cdot\cos(\pi J_{AX}\cdot TE) + w_2 + w_3\cdot\cos(\omega_A\cdot TE) && \text{(with voxel-shift effect)} \qquad (1\text{-}87)
\end{aligned}$$

where w_1, w_2 and w_3 are weighting factors that are proportional to the area and the spin density in each region. Eq. (1-87) demonstrates that for coupled spins the severity of the voxel-shift effect is also dependent on the sequence timing (TE in this example) or equivalently on the scalar-coupling constant, J_{AX}. The change in signal intensity of spin A at two different ratios of $w_1 : w_2 : w_2$ (8:1:1 and 3:1:1) is illustrated in the right panel of Fig. 1-8 where the high-frequency oscillations of the signal intensity of the spin A results from the chemical-shift evolution of that spin in region a_3.

In conclusion, the desired signal from a coupled spin system comes only from that region in the sample in which the three slices defined by three spatial localization r.f pulses overlap. For this reason, the acquired signal (lineshape and peak amplitude) of more complicated spin systems can be significantly different from what can be derived using product operator analysis in which all soft pulses are approximated as rectangular hard pulses.

1.11.2 PRESS Sequence

A generic PRESS sequence is shown in Fig. 1-9. The VOI is defined by three slice-selection gradients in each of the x, y and z directions in conjunction with three soft r.f. pulses. The first 90° pulse creates SQCs, which evolve during the first and the second echo time (TE_1 and TE_2, respectively) under the chemical-shift and scalar-coupling Hamiltonians. The two 180° pulses refocus the chemical-shift evolution of uncoupled and weakly-coupled spin systems during TE_1 and TE_2 period. Therefore, a PRESS sequence is a double spin-echo sequence. These spin-echoes also refocus time-independent dephasing of the transverse magnetization arising from field inhomogeneities. The spoiler gradient pairs that encapsulate each 180° pulse, dephase "or spoil" coherences that do not experience the intended flip angle of 180°, in principle. To minimize the voxel-selection phenomenon, the bandwidth of the two 180° pulses and the slice-selection gradients in the sequence need to be efficiently designed (see Eq. (1-85)).

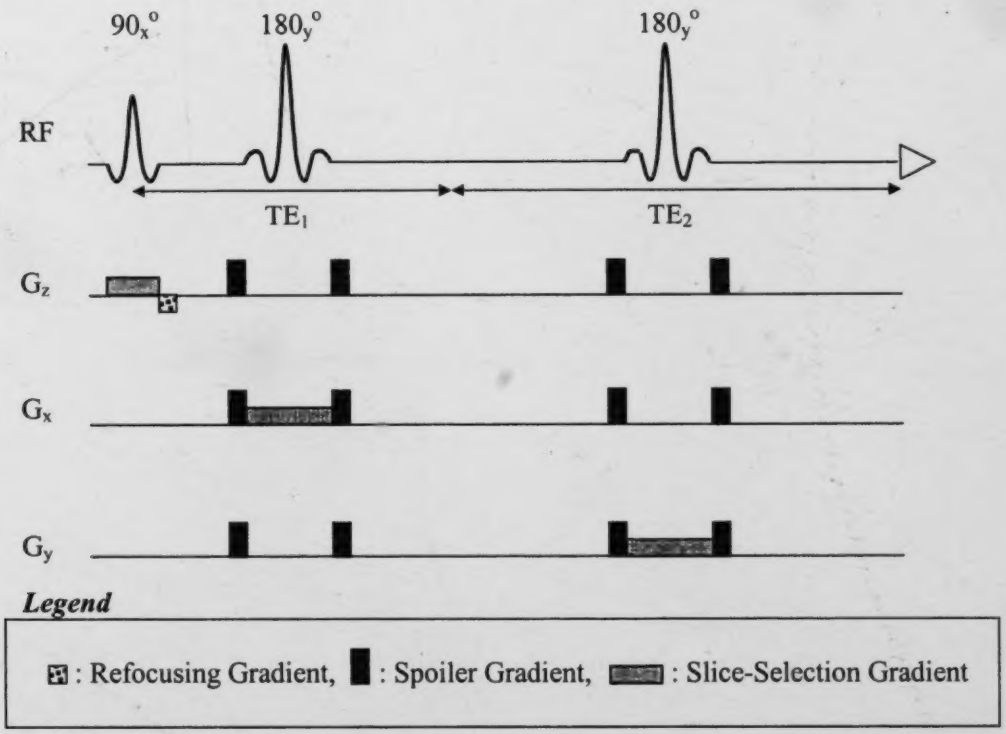

Figure 1-9 A PRESS localization pulse sequence. It consists of one 90° pulse and two 180° refocusing pulses, all of which are spatially selective. The dotted gradient refocuses the dephased transverse magnetization, which results from the first slice selective excitation. The dark-shaded gradients spoil any coherences, which are not refocused by the 180° pulses. The light-shaded gradients spatially encode the sample to define VOI in conjunction with r.f. pulses.

In PRESS experiments, the response of metabolites depends mainly on the choice of TE_1 and TE_2 due to the J-evolution of spin systems, and the coherences that contribute to the final signal acquired during a detection period remain as SQCs throughout the sequence.

1.11.3 STEAM Sequence

Fig. 1-10 illustrates the STEAM sequence. The sequence is composed of three 90° pulses, which define a voxel in conjunction with the slice-selection gradients. In general, the bandwidth of a soft 90° r.f. pulse can be designed wider than that of a soft

180° pulse (or equivalently, with a shorter pulse duration). Therefore, STEAM is much less vulnerable to the voxel-selection phenomenon than PRESS.

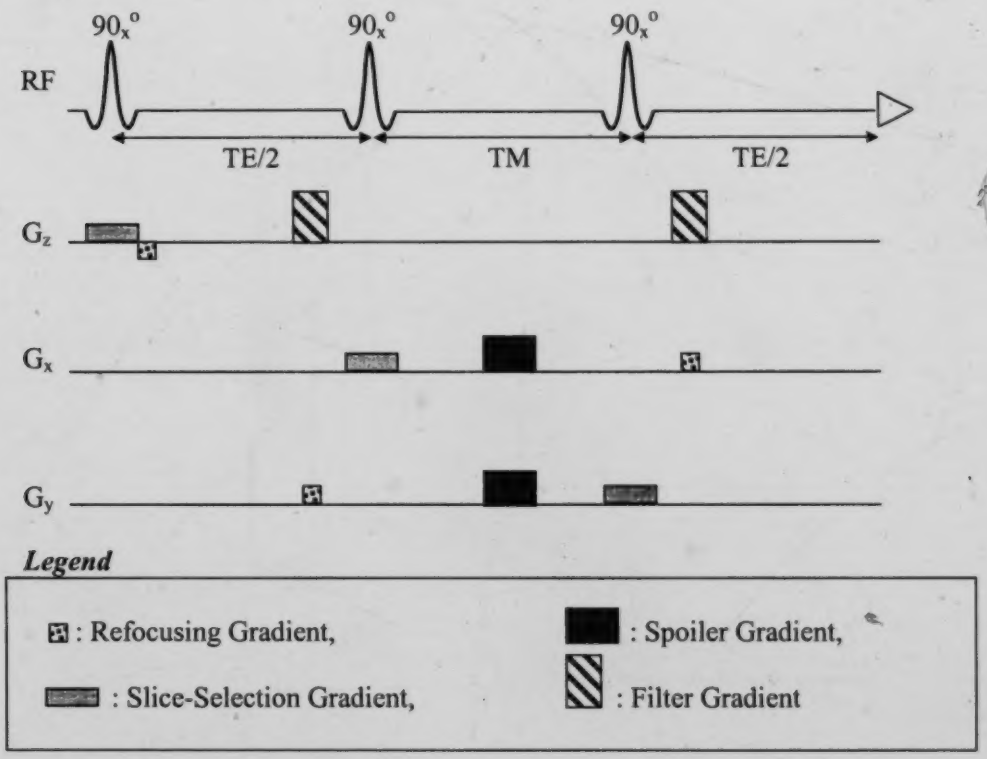

Figure 1-10 A STEAM localization sequence. A total of three slice selective 90° pulses is implemented with coherent r.f phases. In addition to the three kinds of gradients found in a PRESS sequence, filter gradients are also used to ensure that the signal acquired originate from the SQCs during the first TE/2 period. The spoiler gradient during TM period dephases all gradient-sensitive coherences.

The second 90° pulse converts in-phase SQCs and APCs created during the first TE/2 into longitudinal magnetization and MQCs. During TM, the spoiler gradient completely dephases all the gradient-sensitive coherence terms, thereby leaving only longitudinal magnetization and ZQCs, both of which have the order of coherence of zero and are therefore gradient-insensitive (See Appendix 5). The final 90° pulse converts longitudinal magnetization and ZQCs back into SQCs. These SQCs continue to evolve

during the second TE/2 period and are finally detected as signal during acquisition period.

For STEAM, the refocusing of spins takes place at the end of the sequence by the last two 90° pulses and this spin echo is called a stimulated-echo in distinction from the spin-echo achieved by a single 180° pulse in PRESS. In principle, a stimulated-echo has only 50 % efficiency with respect to a spin-echo due to the fact that only half the coherences present at the end of the first TE/2 period are converted into gradient-insensitive terms by the second 90° pulse and the other half are to be completely dephased by the spoiler gradient during TM (93, 94).

In contrast to PRESS, the coherences detected during the acquisition period have undergone changes in coherence order during a STEAM sequence. The detailed discussion on the generation, the evolution and the indirect detection of longitudinal magnetization and ZQCs is given in the following section 1.11.4 together with selective filtering of specific coherences by filter gradients.

1.11.4 MQF

A generic MQF sequence is shown in Fig. 1-11. The VOI is defined by the first 90° pulse and the two 180° pulses as in PRESS. The second 90° pulse generates MQCs and longitudinal magnetization from the pool of APCs and in-phase SQCs, respectively. A short rectangular pulse is usually used for this purpose to minimize the intra-pulse evolution of coherences. The first filter gradient following the second 90° pulse encodes MQCs according to their *levels of coherences* (Appendix 5). Therefore, for the gradient-insensitive terms such as longitudinal magnetization and ZQCs, the filter gradient is not significant. The third 90° pulse reverses those MQCs back into APCs, which will evolve into in-phase SQCs during TE_2 period under the J-coupling Hamiltonian. A *frequency-selective* soft pulse is used in general for the third 90° pulse in order to achieve selective excitation in the frequency domain for maximal performance of the sequence (Chapter 4).

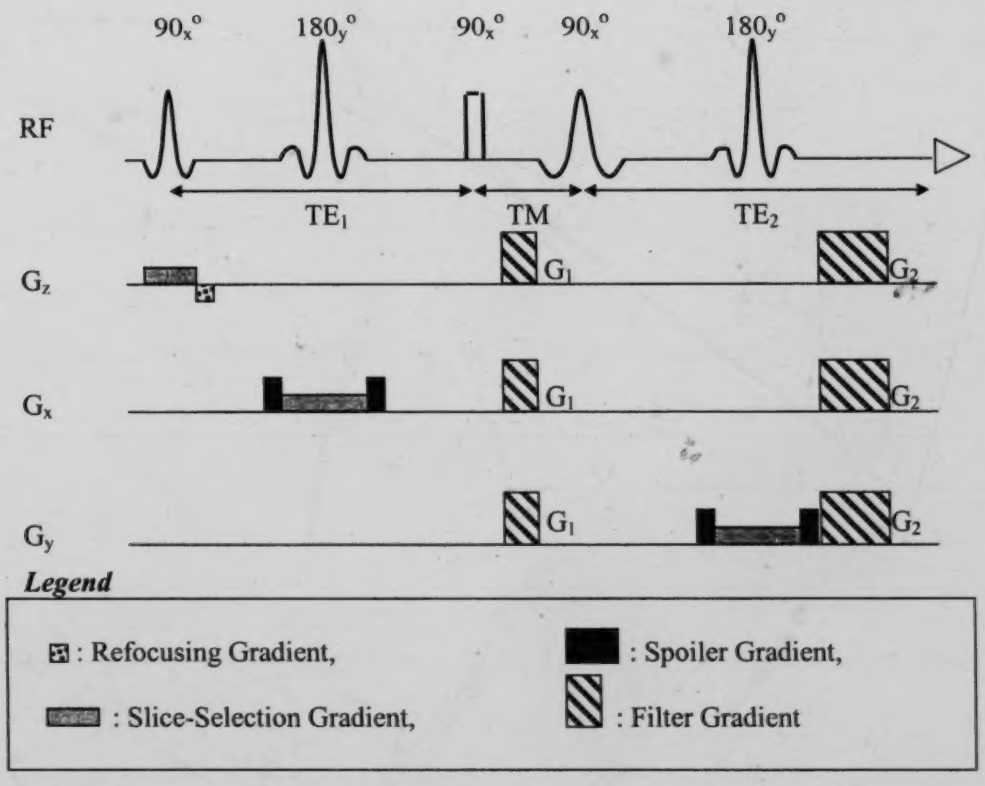

Figure 1-11 A generic MQF sequence. The filtering of specific coherences is achieved by the second and the third 90° pulse in conjunction with a pair of filter gradients. The area of the second filter gradient is adjusted with respect to the first one, according to the level of coherence to be filtered out. The second 90° rectangular hard pulse generates MQCs. The third 90° pulse is frequency-selective in general and converts MQCs back into APCs.

The relative areas of the two filter gradients is adjusted according to the level of coherence to be allowed through the filter. In contrast ZQF does not require the second filter gradient for coherence rephrasing, because it is not encoded by the first filter gradient during TM period.

The spin systems evolutionary response to a MQF is far more complicated than their response to PRESS or STEAM. Therefore, to understand the basic concepts of the sequence a detailed discussion is given in the following section with a weakly-coupled

AX spin system. The difference between weakly- and strongly-coupled spin systems in the design of MQF is also discussed briefly at the end of the section.

1.11.4.1 Evolution of an AX spin system in MQF

1.11.4.1.1 Preparation Period and Generation of MQCs

Retaining only SQCs of spin A, the density operator immediately after the second 90^{o} pulse takes the form of (see Eq. (1-80))

$$\rho(TE^{+})_{A} = - A_{z}\cos(\pi J_{AX}\cdot TE_{1}) - 2A_{x}X_{y}\sin(\pi J_{AX}\cdot TE_{1})$$
$$= - A_{z}\cos(\pi J_{AX}\cdot TE_{1}) - (1/2i)\{(A_{+}X_{+} - A_{-}X_{-}) - (A_{+}X_{-} - A_{-}X_{+})\}\sin(\pi J_{AX}\cdot TE_{1}) \quad (1\text{-}88)$$

where the raising and lowering operators were used as defined in Eqs. (1-55a) and (1-55b). As was discussed in section (1.6.3.2), $(A_{+}X_{+} - A_{-}X_{-})$ in Eq. (1-88) are DQCs with the level of coherence of two, and $(A_{+}X_{-} - A_{-}X_{+})$ are ZQCs with the level of coherence of zero. That is, MQCs are created from APCs that were present just before the application of the MQC-generating hard 90^{o} pulse. For more complicated spin systems with more than three coupled spins involved, higher orders of coherences can also be generated at this stage such as a triple quantum coherence. Since MQC are created exclusively from APC, which is a unique state of coupled spins, MQF can in general effectively suppress signal from uncoupled spins except for ZQF (section 1.11.4.1.3).

From Eq. (1-80) it is clear that, for this simple AX spin system, adjusting TE_1 equal to 1/2J maximizes the amount of APCs leading to maximum generation of MQCs. For this reason, TE_1 needs to be optimized in the design of MQF. For more complicated spin systems, however, in which the target signal originates from various APC terms (or various coherence pathways) thereby involving multiple J values from different coupled pairs in the spin system, the optimization of TE_1 is not straightforward and an optimal TE_1 for maximum signal yield can significantly deviate from 1/2J (section 1.11.4.2).

As well, since longitudinal magnetization terms also contribute to the final signal in ZQF (section 1.11.4.1.3) in addition to ZQCs, maximizing APCs during TE_1 does not necessarily maximize the final filter yield in ZQF experiments.

The coherence terms in Eq. (1-88) can be rearranged according to their order of coherence as

$$\rho(TE^+)_A^{DQC} = -(1/2i)\{(A_+X_+ - A_-X_-)\}\sin(\pi J_{AX}\cdot TE_1) \quad (1\text{-}89a)$$

and

$$\rho(TE^+)_A^{ZQC} = -A_z\cos(\pi J_{AX}\cdot TE_1) + (1/2i)\{(A_+X_- - A_-X_+)\}\sin(\pi J_{AX}\cdot TE_1) \quad (1\text{-}89b)$$

where the longitudinal magnetization was also included in the density operator for ZQC, and the reason will be clear in the following sections.

1.11.4.1.2 Evolution of MQCs During TM and the Role of the First Filter Gradient

As in Appendix 6a, A_xX_y in Eq. (1-88) and other MQC terms such as A_xX_x, A_yX_x and A_yX_y are invariant under the weak-coupling Hamiltonian. However, they do evolve under the zeeman Hamiltonian. For instance, using the transformation equations in Appendix 6a, the DQC term $(1/2i)(A_+X_+ - A_-X_-)$ $(= A_xX_y + A_yX_x)$ in Eq. (1-88) transforms, after successive operations of the Zeeman Hamiltonian of spin A and spin X, into

$$(1/2i)(A_+X_+ - A_-X_-) \xrightarrow{\omega_A t \cdot A_z} \xrightarrow{\omega_X t \cdot X_z} (1/2i)\{(A_+X_+ - A_-X_-)\cos\{(\omega_A + \omega_X)TM\} - (1/2)(A_+X_+ + A_-X_-)\sin\{(\omega_A + \omega_X)TM\}, \quad (1\text{-}90a)$$

or equivalently,

$$A_xX_y + A_yX_x \rightarrow (A_xX_y + A_yX_x)\cos\{(\omega_A + \omega_X)TM\} - (A_xX_x - A_yX_y)\sin\{(\omega_A + \omega_X)TM\}. \quad (1\text{-}90b)$$

Eq. (1-90) shows that the DQC, $A_xX_y + A_yX_x$, oscillate during TM between two DQC states, $A_xX_y + A_yX_x$ and $A_xX_x - A_yX_y$, under the action of the Zeeman Hamiltonian, and the oscillation frequency is equal to the *sum* of the chemical-shifts of the two coupled spins in Hz. The first term in Eq. (1-90), which involves *i* when expressed in terms of raising and lowering operators, is dubbed as an *imaginary* DQC term, while the second term as a *real* DQC term. As will be discussed in section 1.11.4.1.3, it is these oscillations of DQCs that necessitate the optimization of TM.

Similar to DQCs, ZQCs also oscillate between the real ($A_xX_x + A_yX_y$) and imaginary ($A_xX_y - A_yX_x$) state under the Zeeman Hamiltonian, but the oscillation frequency is equal to the *difference* in chemical-shift of the two coupled spins, i.e., ($\omega_A - \omega_X$). Since such evolution of ZQCs takes place during TM of STEAM in the same mode, the adjustment of the sequence timing should be included in the optimization procedure of the sequence as well.

As shown in Appendix 5, gradient pulses dephase coherence according to order of coherence. Since ZQCs and longitudinal magnetization are gradient-insensitive, they are not dephased or encoded by the first gradient pulse. However, those DQCs in Eq. (1-89) will evolve under the gradient Hamiltonian. For example, the evolution of A_+X_+ in Eq. (1-89) by the first filter gradient can be written as

$$A_+X_+ \xrightarrow{p\theta_{G1}\cdot A_z} \xrightarrow{p\theta_{G1}\cdot X_z} A_+X_+ \exp(-i\cdot 2\cdot\theta_{G1})$$
$$= (A_xX_x + iA_xX_y + iA_yX_x - A_yX_y)\exp(-i\cdot 2\cdot\theta_{G1}) \qquad (1\text{-}91a)$$

and similarly,

$$A_-X_- \xrightarrow{p\theta_{G1}\cdot A_z} \xrightarrow{p\theta_{G1}\cdot X_z} A_-X_- \exp(i\cdot 2\cdot\theta_{G1})$$
$$= (A_xX_x - iA_xX_y - iA_yX_x - A_yX_y)\exp(i\cdot 2\cdot\theta_{G1}) \qquad (1\text{-}91b)$$

where p is the order of coherence and θ_{G1} was defined in Eq. (1-66).

1.11.4.1.3 Evolution of MQCs into APCs and the Role of the Second Filter Gradient

The third 90° pulse converts MQCs into APCs, which will continuously evolve during TE_2 into observable in-phase SQCs. For ZQF, it will convert longitudinal magnetization directly into in-phase SQC.

Note that among the resultant four terms in Eqs. (1-91a) and (1-91b) only the second and the third terms are converted by the third 90_x° into APCs. That is,

$$iA_xX_y \exp(-i\cdot 2\cdot\theta_{G1}) \rightarrow iA_xX_z \exp(-i\cdot 2\cdot\theta_{G1}) \quad (1\text{-}92a)$$

and

$$iA_yX_x \exp(-i\cdot 2\cdot\theta_{G1}) \rightarrow iA_zX_x \exp(-i\cdot 2\cdot\theta_{G1}). \quad (1\text{-}92b)$$

The first terms in Eq. (1-91) is invariant by the third 90_x°, thereby remaining as a non-observable MQC. The fourth term is transformed by that pulse into a product of two longitudinal magnetization terms, A_zX_z, which is referred to as a "longitudinal-scalar-order", and is also non-observable.

Therefore, neglecting the evolution of MQCs under the chemical-shift Hamiltonian during TM and retaining only SQC of spin A, the reduced density operator for DQC in Eq. (1-89a) transforms just after the third 90° pulse into

$$\rho(TE + TM^+)_A^{DQC}$$
$$\sim -(1/2)A_xX_z\{\exp(-i\cdot 2\cdot\theta_{G1}) + \exp(i\cdot 2\cdot\theta_{G1})\}\sin(\pi J_{AX}\cdot TE_1)$$
$$= -(1/4)(A_+X_z + A_-X_z)\{\exp(-i\cdot 2\cdot\theta_{G1}) + \exp(i\cdot 2\cdot\theta_{G1})\}\sin(\pi J_{AX}\cdot TE_1). \quad (1\text{-}93)$$

The second gradient, which is located after the second 180° refocusing pulse during TE_2 period in Fig. 1-11, can be thought of equivalently as placed just after the third 90° pulse with a negative polarity. Thus, by the second filter gradient, SQCs in Eq. (1-93) reduce into

$$\rho(TE + TM^{+})_A^{DQC} \sim$$
$$- (1/4)< A_+X_z [\exp\{i(\theta_{G2} - 2\cdot\theta_{G1}) + \exp\{i(\theta_{G2} + 2\cdot\theta_{G1})\}]$$
$$+ A_-X_z [\exp\{- i(\theta_{G2} + 2\cdot\theta_{G1}) + \exp\{- i(\theta_{G2} - 2\cdot\theta_{G1})\}] >\sin(\pi J_{AX}\cdot TE_1). \quad (1\text{-}94)$$

Note that, for $\theta_{G2} = 2\cdot\theta_{G1}$, only one-half of the APCs in Eq. (1-94) will be rephrased, while the other half will be further dephased, and for $\theta_{G2} = - 2\theta_{G1}$, vice versa. Due to this signal loss mechanism DQ-filtering technique suffers from a poor signal yield in general. Therefore, for $\theta_{G2} = 2\cdot\theta_{G1}$,

$$\rho(TE + TM^{+})_A^{DQC} \sim - (1/4)(A_+X_z + A_-X_z)\sin(\pi J_{AX}\cdot TE_1)$$
$$= - (1/2)A_xX_z \sin(\pi J_{AX}\cdot TE_1). \quad (1\text{-}95)$$

Again, neglecting the evolution of ZQCs under the chemical-shift Hamiltonian during TM, similar calculation can be made for $\rho(TE + TM^{+})_A^{ZQC}$, and Eq. (1-89b) reduces after the second gradient into

$$\rho(TE + TM^{+})_A^{ZQC} \sim (1/2i)\{A_+ \exp(i\cdot\theta_{G2}) - A_- \exp(- i\cdot\theta_{G2})\}\cos(\pi J_{AX}\cdot TE_1)$$
$$- (1/2)\{A_+X_z \exp(i\cdot\theta_{G2}) + A_-X_z \exp(- i\cdot\theta_{G2})\}\sin(\pi J_{AX}\cdot TE_1). \quad (1\text{-}96)$$

Since ZQC and longitudinal magnetization were not encoded by the first filter gradient, all terms in Eq.(1-96) will be dephased by the second filter gradient. Therefore without the second filter gradient, or for $\theta_{G2} = 0$,

$$\rho(TE + TM^{+})_A^{ZQC} \sim (1/2i)(A_+ - A_-)\cos(\pi J_{AX}\cdot TE_1) - (1/2)(A_+X_z + A_-X_z)\sin(\pi J_{AX}\cdot TE_1)$$
$$= A_y\cos(\pi J_{AX}\cdot TE_1) - A_xX_z \sin(\pi J_{AX}\cdot TE_1). \quad (1\text{-}97)$$

Note that as pointed out earlier the SQC, A_y, which was present just before the second 90^o pulse (Eq. 1-80), has passed through the ZQF, although in this case of *weakly-coupled* spin system it can be removed in principle by setting TE_1 to 1/2J, thereby maximizing the amount of APC, (see Eq. (1-97)). However, this is not possible with in-

phase SQCs from *uncoupled* spins, as they do not evolve and subsequently have no coupling to trigonometric functions unlike those in-phase SQCs or APCs from coupled spins. Due to this property of a generic ZQF being permeable to longitudinal magnetization, DQF has been more popular than ZQF for human studies. However, it will be found in chapters 5 and 6 that this drawback in the nature of a generic ZQF can be tackled by modifying one of the components of the sequence.

The APC term, A_xX_z, in Eq. (1-95) and Eq. (1-97) will continue to evolve during TE_2 into in-phase SQC and will ultimately be detected. Note, however, that the amount of that APC term in response to ZQF (Eq. (1-97)) is twice as much as that in response to DQF (Eq. (1-95)). This is due to the fact that only one-half of the DQC terms are rephrased by the second filter gradient. Note also that those APC terms under comparison originate from the one present just before the MQC-generating second 90° pulse (Eq. (1-80)), which was then converted into ZQC and DQC at the same proportion as clearly illustrated in Eq. (1-88). Therefore in this context a ZQF has signal efficiency of 50%, while a DQF only 25%. Nonetheless, due to the flaw of a generic ZQF being unable to suppress uncoupled spins, a DQF is more popularly used in in-vivo MRS.

To overcome the intrinsic poor signal yield of MQF, several signal enhancement techniques have been reported for simple spin systems (25, 95). For instance, by making the third 90° pulse frequency-selective, one can improve the signal yield of either spin A or spin B (but not both) of an AX spin system by a factor of 2 (25). However, for more complicated spin systems, this technique is not as profitable. As well, when the third 90° pulse is frequency-selective, the duration of that pulse becomes no longer negligible, during which considerable spin evolution may take place. Therefore, the duration of the pulse also needs to be optimized for better performance of the filter (29). Whenever gradient pulses are used as a means of filtering DQCs, adjusting the flip angle of the third 90° pulse may also be helpful for enhancing the signal yield of a DQF (95). For instance, depending on the polarity of the second filter gradient with respect to the first encoding gradient, the maximum signal occurs at 60° or 120° for an AX spin system.

1.11.4.2. Difference in Design of MQF for Strongly-Coupled Spin Systems

1.11.4.2.1 Preparation Period and Generation of MQCs

For strongly-coupled spin systems, adjusting TE_1 to 1/2J for a maximum APC generation no longer holds even for a simple AB spin system (96). This is due mainly to the fact that the chemical-shift evolution of SQCs of such spin systems during a TE_1 cannot be treated separately from J-evolution. For instance, in Eq. (1-83), the coefficient of an APC term, $2A_xB_z$, of an AB spin system after TE_1 includes additional terms such as $\cos^2(\Lambda \cdot TE_1/2)$ and $\sin^2(\Lambda \cdot TE/2)$, in which Λ is a function of both chemical-shift and J-constant. As such, the chemical-shift evolution of such spin systems is not fully refocused after a spin-echo period, and subsequently the optimum TE_1 for maximum APC generation can considerably differ from the conventional 1/2J.

The phase of the second 90° pulse plays an important role in the design of MQF for strongly-coupled spin systems (97) due to the additional coherence terms as in Eq. (1-83) arising from coherence transfer under the strong-coupling Hamiltonian. A detailed discussion on this issue is given in chapters 5 and 6 where it is shown that by adjusting the phase of the MQC-generating pulse a generic MQF can be made responsive to strongly-coupled spin systems only.

1.11.4.2.2 Evolution of MQCs during TM

A major difference in evolution of coherences during TM between strongly-coupled spin systems and weakly-coupled ones is that, for the former, the transfer between longitudinal magnetization and ZQC is possible via the strong-coupling Hamiltonian, $\boldsymbol{H}^{strong}$ (15, 17). Therefore this additional mixing of coherence also needs to be considered in the optimization of TM in addition to ZQC's oscillation between real and imaginary state during that period. Unlike the transfer between longitudinal magnetization and ZQC, in which the order of coherence is conserved, no such additional transfer mechanism takes place for DQCs.

1.11.4.2.3 Conversion of MQCs into APCs

Due to the active proliferation of coherences of strongly-coupled spin systems discussed above, the choice of both TM and the duration of the third 90° pulse becomes more influential to the final filter output (lineshape and peak amplitude). As well, for strongly-coupled spins, the coherence transfer during TE_2 similar to that taking place during TE_1 illustrated in Fig. 1-7 makes it difficult to choose the spectral region to be excited by the frequency-selective third 90° pulse for maximum signal yield.

In fact, for the most part, strongly-coupled spin systems do not allow a realistic opportunity for selective excitation due to the spectral proximity of their resonance lines.

1.11.5 Two-Dimensional Spectroscopy

Two-dimensional magnetic resonance spectroscopy (2D-MRS) methods (61) have been used to identify the J-coupling network of spin systems (peak assignment) and, to a lesser extent, to improve spectral resolution (peak separation). The extension of the dimension of spectra is achieved by incorporating an additional time variable (typically denoted as t_1) as a parameter in the sequence design, which is chosen to be independent of the other time variable (t_2) that runs during the detection period.

The performance of 2D techniques depends on the types of evolution of spin systems during the t_1 period. For instance, the so-called correlation spectroscopy (COSY) and J-resolved spectroscopy techniques (61, 98, 99) are commonly used for the purpose of peak assignment and peak separation, respectively. Basic pulse sequences for these techniques are shown in Fig. 1-12. In 2D experiments signal is acquired during the t_2 period as in one-dimensional (1D) spectroscopy, but repetitively with different t_1 values. The resulting spectra are expressed on a 2D frequency space $\{f_1, f_2\}$ via the two-dimensional fast Fourier transformation (2D FFT) of the signal, $S(t_1, t_2)$, and the resolution of the spectra is determined not only by the number of data points during t_2 period, but also by the number of experiments with different t_1 values.

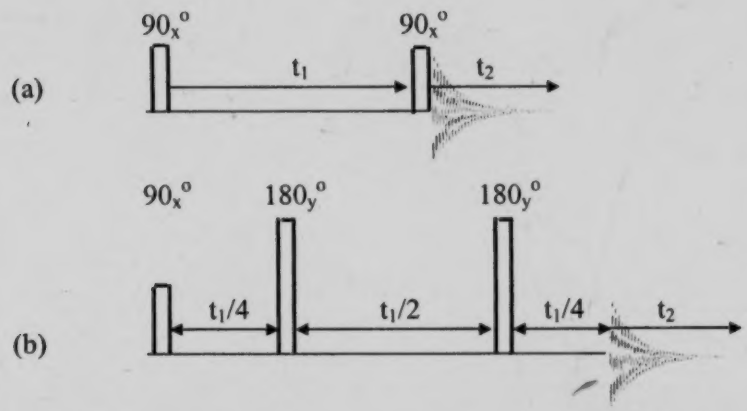

Figure 1-12 Basic two-dimensional pulse sequences. The COSY sequence in (a) consists of two 90° r.f. pulses. Signal is acquired during t_2 period with t_1 as a parameter. In 2D J-resolved spectroscopy experiments using the pulse sequence shown in (b), a double spin-echo period (= total TE = t_1) refocuses the chemical-shift evolution of spin systems, and as a consequence, the corresponding frequency axis, f_1, of a resultant spectrum contains J-coupling information only.

In a typical COSY experiment (98) (Fig. 1-12(a)), both the f_1- and the f_2-axis contain information on the chemical-shift and the J-coupling of spin systems. Among the peaks observed in a 2D COSY spectrum (diagonal ($f_1 = f_2$) and off-diagonal peaks), those off-diagonal peaks or cross-peaks provide information about correlations (J-coupling) between peaks, which is not available in 1D spectra, and therefore allow for unambiguous assignment of peaks. In a J-resolved spectroscopy experiment, for instance, using the pulse sequence (99) shown in Fig. 1-12(b), the chemical-shift evolution of spin systems is refocused at $t = t_1$ (= total TE in this example), and as a consequence, the f_1-axis of resultant spectra contains J-coupling information only, while the f_2-axis possesses both J-coupling and chemical-shift information. Therefore, the projection of a cross-section at a certain f_1 value onto the f_2-axis yields a *decoupled* 1D spectrum (99), and different peak separations are obtained at different f_1 values. This homonuclear decoupling technique, in particular, can be very useful when a target spectral region is crowded with background resonances.

Nevertheless, due to the long acquisition times (resulting from the large number of experiments with different t_1 values) required to obtain reasonable spectral resolution along the f_1-axis, the application of 2D MRS is in general not feasible in-vivo.

1.12 References

1. R. G. Shulman, A. M. Blamire, D. L. Rothman, and G. McCarthy, *Proc. Natl. Acad. Sci.*, **90**, 3127, 1993
2. J. Vion-Dury, D. J. Meyerhoff, P. J. Cozzone, and M. W. Weiner, *J. Neurol.*, **241**, 354, 1994
3. T. Ernst, R. Kreis, and B. D. Ross, *J. Magn. Reson.*, **B102**, 1, 1993
4. P. J. Pouwels and J. Frahm, *Magn. Reson. Med.*, **39**, 53, 1998
5. T. Michaelis, K. D. Merboldt, H. Bruhn, J. Frahm, *Radiology*, **187**, 219, 1993
6. S. W. Provencher, *Magn. Reson. Med.*, **30**, 672, 1993
7. R. Kreis, T. Ernst, and B. D. Ross, *Magn. Reson. Med.*, **30**, 424, 1993
8. B. D. Ross, R. Kreis, and T. Ernst, *Euro. J. Radiology*, **14**, 128, 1992
9. C. G. Choi and J. Frahm, *Magn. Reson. Med.*, **41**, 204, 1999
10. D. J. Meyerhoff, *Magn. Reson. Med.*, **42**, 417, 1999
11. R. M. Henkelman, *Med. Phys.*, **12(2)**, 232, 1985
12. C. N. Chen and D. I. Holt, *Biomedical magnetic resonance technology*, Adam Hilger, 1989
13. W. A. Edelstein, G. H. Glover, C. J. Hardy, and R. W. Redington, *Magn. Reson. Med.*, **3**, 248, 1986
14. J. D. De Certaines, W. M. Bovee, and F. Podo, *Magnetic resonance in biology and medicine*, Pergamon Press, 1992
15. A. H. Wilman and P. S. Allen, *J. Magn. Reson.*, **B107**, 25, 1995
16. A. H. Wilman and P. S. Allen, *J. Magn. Reson.*, **B113**, 203, 1996
17. L. E. Kay and R. E. D. McClung, *J. Magn. Reson.*, **77**, 258, 1988
18. J. F. Shen and P. S. Allen, *J. Magn. Reson.*, **92**, 398, 1991
19. J. F. Shen and P. S. Allen, *J. Magn. Reson.*, **92**, 550, 1991
20. L. Braunschweiler and R. R. Ernst, *J. Magn. Reson.*, **53**, 521, 1983
21. R. Bowtell, R. M. Bowley, and P. Glover, *J. Magn. Reson.*, **88**, 643, 1990
22. F. J. M. van de Ven, and C. W. Hilbers, *J. Magn. Reson.*, **54**, 512, 1983
23. H. K. Lee, A. Yaman, and O. Nalcioglu, *Magn. Reson. Med.*, **34**, 253, 1995
24. A. H. Wilman and P. S. Allen, *J. Magn. Reson.*, **B101**, 102, 1993
25. L. A. Trimble, J. F. Shen, A. H. Wilman, and P. S. Allen, *J. Magn. Reson.*, **86**, 191, 1990
26. A. H. Wilman and P. S. Allen, *J. Magn. Reson.*, **B101**, 165, 1993
27. A. H. Wilman and P. S. Allen, *J. Magn. Reson.*, **B109**, 169, 1995
28. O. W. Sorensen, G. W. Eich, M. H. Levitt, G. Bodenhausen and R. R. Ernst, *Prog. NMR Spect.*, **16**, 163, 1983
29. R. B. Thomson and P. S. Allen, *Magn. Reson. Med.*, **39**, 762, 1998
30. R. B. Thomson and P. S. Allen, *Magn. Reson. Med.*, **41**, 1162, 1999
31. R. B. Thomson, *Ph.D. Thesis*, Univ. of Alberta, 1999

32. R. A. Moats, T. Ernst, T. K. Shonk, and B. D. Ross, *Magn. Reson. Med.*, **32**, 110, 1994
33. B. L. Miller, R. A. Moats, T. K. Shonk, T. Ernst, S. Woolley, and B. D. Ross, *Radiology*, **187**, 433, 1993
34. R. Kreis, B. D. Ross, N. A. Farrow, and Z. Ackerman, *Radiology*, **182**, 19, 1992
35. R. A. Moat, Y. H. Lien, D. Filippi, and B. D. Ross, *Biochem. J.*, **295**, 15, 1993
36. R. Kreis and B. D. Ross, *Radiology*, **184**, 123, 1992
37. R. H. Lenox and D. G. Watson, *Clin. Chem.*, **40(2)**, 309, 1994
38. S. R. Nahorski, C. I. Ragan, and R. A. Challiss, *TiPS*, **12**, 297, 1991
39. H. Bruhn, G. Stoppe, J. Staedt, K. D. Merboldt, and J. Frahm, *Proc. ISMRM*, New York, 1993, p. 1543
40. T. Shonk and B. D. Ross, *Magn. Reson. Med.*, **33**, 858, 1995
41. C. E. Stokes and J. N. Hawthorne, *J. Neurochem.*, **48**, 1018, 1987
42. B. R. Fruen and B. R. Lester, *Biochem. J.*, **270**, 119, 1990
43. N. E. Preece, S. Amor, D. Baker, D. G. Gadian, J. K. O'Neill, and J. Urenjak, *Magn. Reson. Med.*, **32**, 692, 1994
44. T. Kato, T. Shioiri, S. Takahashi, and T. Inubushi, *J. Affec. Disor.*, **22**, 185, 1991
45. H.S. Song, *Quantum Mechanics*, Kyo-Hak, 1989
46. E. M. Haacke, R. W. Brawn, M. R. Thomson, and R. Venkatesan, *Magnetic Resonance Imaging*, Wiley-Liss, 1999
47. C. P. Slichter, *Principles of magnetic resosnance*, Spring-Verlag, 1978
48. A. Abragam, *Principles of nuclear magnetism*, Oxford Univ. Press, 1961
49. F. Reif, *Berkeley physics course, v. 5, Statistical Physics*, McGraw-Hill, 1965
50. F. Reif, *Fundamentals of statistical and thermal physics*, McGraw-Hill, 1965
51. K. Huang, *Statistical mechanics*, John Wiley & Sons, 1987
52. D. Canet, *Nuclear magnetic resonance-concepts and methods*, John Wiley & Sons, 1991
53. F. A. Bovey, *NMR spectroscopy*, Academic Press, 1988
54. J. R. Reitz, F. J. Milford, and R. W. Christy, *Fundamentals of electromagnetic theory*, Addison-Wesley, 1979
55. J. D. Jackson, *Classical electrodynamics*, John Wiley & Sons, 1975
56. A. H. Wilman, *Ph.D. Thesis*, Univ. of Alberta, 1994
57. D. Park, *Introduction to the quantum theory*, McGraw-Hill, 1992
58. E. E. Anderson, *Modern physics and quantum mechanics*, McGraw-Hill, 1971
59. J. L. Powell and B. Crasemann, *Quantum mechanics*, Addison Wesley, 1984
60. P. A. M. Dirac, *The principles of quantum mechanics*, Oxford Univ. Press, 1981
61. R. R. Ernst, G. Bodenhausen, and A. Wokaun, *Principles of nuclear magnetic resonance in one and two dimensions*, Oxford Univ. Press, 1987
62. C. H. Sotak, D. M. Freeman, and R. E. Hurd, *J. Magn. Reson.*, **78**, 355, 1988
63. Y. Sharf, U. Eliav, H. Shinar, and G. Navon, *J. Magn. Reson.*, **B107**, 60, 1995
64. K. Kanamori, B. D. Ross, and J. Tropp, *J. Magn. Reson.*, **B107**, 107, 1995
65. Q. He, Z. M. Bhujwalla, R. J. Maxwell, J. R. Griffiths, and J. D. Glickson, *Magn. Reson. Med.*, **33**, 414, 1995
66. Q. He, Z. M. Bhujwalla, and J. D. Glickson, *J. Magn. Reson.*, **B112**, 18, 1996
67. L. Jouvensal, P. G. Carlier, and G. Bloch, *Magn. Reson. Med.*, **36**, 487, 1996

68. J. R. Keltner, L. L. Wald, B. B. Frederick, and P. F. Renshaw, *Magn. Reson. Med.*, **37**, 366, 1997
69. J. A. Kmiecik, C. D. Gregory, Z. P. Liang, D. E. Hrad, P. C. Lauterbur, and M. J. Dawson, *Magn. Reson. Med.*, **37**, 840, 1997
70. J. R. Keltner, L. L. Wald, P. J. Ledden, Y. I. Chen, R. T. Matthews, J. R. Baker, B. R. Rosen, and B. G. Jenkins, *Magn. Reson. Med.*, **39**, 651, 1998
71. A. H. Trabesinger, O. M. Weber, C. O. Duc, and P. Boesiger, *Magn. Reson. Med.*, **42**, 283, 1999
72. H. Lei and J. Peeling, *Magn. Reson. Med.*, **42**, 454, 1999
73. K. Young, V. Govindaraju, B. J. Soher, and A. A. Maudsley, *Magn. Reson. Med.*, **40**, 812, 1998
74. K. Young, B. J. Soher, and A. A. Maudsley, *Magn. Reson. Med.*, **40**, 816, 1998
75. Bodenhausen, *J. Magn. Reson.*, **58**, 370, 1984
76. Gunther, *NMR Spectroscopy*, John Wiley & Sons, 1980
77. E. M. Purcell, Berkeley Physics Course, v. 2, Electricity and Magnetism, McGraw-Hill, 1985
78. M. H. Levitt, *Spin dynamics*, John Wiley & Sons, 2001
79. C. C. Hanstock, R. B. Thomson, M. E. Trump, D. Gheorghiu, P. W. Hochachka, and P. S. Allen, *Magn. Reson. Med.*, **42**, 421, 1999
80. R. Kreis and C. Boesch, *J. Magn. Reson.*, **B104**, 189, 1994
81. R. Kreis, J. Slotboom, J. Felblinger, B. Jung and C. Boesch, *Proc. ISMRM*, Vancouver, 1997, p. 1338
82. I. Asllani, E. Shankland, T. Pratum, and M. Kushmerick, *J. Magn. Reson.*, **139**, 213, 1999
83. R. Bowtell, *J. Magn. Reson.*, **100**, 1, 1992
84. A. A. Maudsley, A. Wokaun, and R. R. Ernst, *Chem. Phys. Lett.*, **55**, 9, 1978
85. A. Bax, P. G. De Gong, A. F. Mehlkoph, and J. Smidt, *Chem. Phys. Lett.*, **69**, 567, 1980
86. L. E. Kay and R. E. D. McClung, *J. Magn. Reson.*, **77**, 258, 1988
87. J. Slotboom, A. F. Mehlkopf, and W. M. M. J. Bovee, *J. Magn. Reson.*, **A108**, 38, 1994
88. D. A. Yablonskiya, J. J. Neil, M. E. Raichle, and J. J. H. Ackerman, *Magn. Reson. Med.*, **39**, 169, 1998
89. T. T. NaKashima and R. E. D. McClung, *J. Magn. Reson.*, **70**, 187, 1986
90. A. H. Trabesinger, D. C. Mueller, and P. Boesiger, *J. Magn. Reson.*, **145**, 237, 2000
91. P. A. Bottomley, *US Patent 4*, **480**, 228, 1984
92. R. J. Ordidge, M. R. Bendall, R. E. Gordon, and A. Connelly, *Magnetic resonance in biology and medicine*, McGraw-Hill, 1985
93. J. Frahm, K. D. Merboldt, and W. Hanicke, *J. Magn. Reson.*, **72**, 502, 1987
94. J. Frahm, H. Bruhn, M. L. Gyngell, K. D. Merboldt, W. Hanicke, and R. Kaptein, *Magn. Reson. Med.*, **9**, 79, 1989
95. J. F. Shen and P. S. Allen, *J. Magn. Reson.*, **90**, 606, 1990
96. A. H. Willman and P. S. Allen, *J. Magn. Reson.*, **B105**, 58, 1994
97. H. Kim, J. M. Wild, and P. S. Allen, *Proc. ISMRM*, Glasgow, 2001, p. 621
98. W. P. Aue, E. Bartholdi, and R. R. Ernst, *J. Chem. Phys.*, **64**, 2229, 1976
99. W. Dreher and D. Leibfritz, *Magn. Reson. Med.*, **34**, 331, 1995

CHAPTER 2

Myo-Inositol, Its Chemistry and Relevance to Psychiatry and Neurology; A Review of NMR Studies

2.1. Introduction

Myo-inositol (mI) is a precursor in the phosphatidylinositol (PI) second messenger system (PI-cycle) and an important osmolyte in brain. A growing body of evidence suggests that brain mI may be associated with psychiatric disorders such as bipolar disorder and schizophrenia, and to a lesser extent with neurological diseases such as Alzheimer's disease and hepatic encephalopathy. The purpose of this review is to examine the evidence that alterations in the chemistry, the regulation and the production of mI are related to the etiology, or to the treatment of, specific psychiatric disorders and neurological diseases. These suggestions come from animal studies (1) as well as human volunteer and patient studies.

As well as having a theoretical interest, the advent of magnetic resonance spectroscopy (MRS) has also allowed measurement of mI concentrations *in vivo*. This has allowed more detailed examination of many of these hypotheses in patient groups.

In terms of this review, as noted the focus is on studies in psychiatric patients. Most work has been done in the area of bipolar disorder. This has followed the suggestion by Berridge and his colleagues (2), more than 20 years ago, that the mechanism of action of lithium may be related to its effects on inositol monophosphatase (IMPase). This led to them proposing the mI hypothesis.

2.2 Synthesis, Regulation, and Possible Role of mI

In trying to understand why mI could be involved in multiple psychiatric conditions, it is important to have some understanding of its metabolism and possible roles. Inositol is a carbohydrate that has a ring conformation with 6 carbons (Fig. 2-1), and its biologically active stereoisomer is called mI (3, 4). Since it was isolated from muscle for the first time, it is also sometimes referred to as muscle sugar (5, 6).

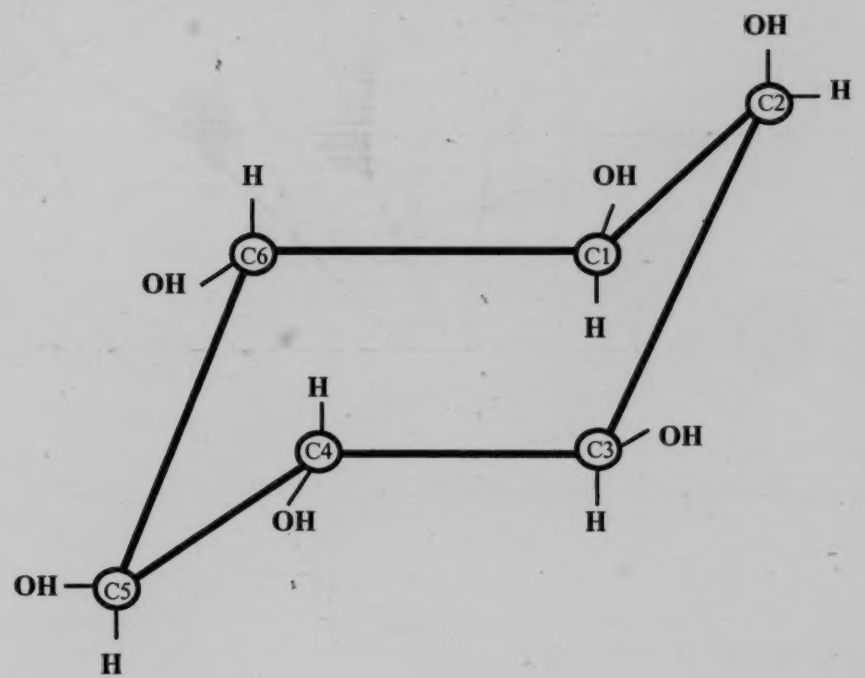

Figure 2-1 The molecular structure of *myo-Inositol*. It has a symmetric ring structure with six carbons.

There are three ways cells gain a supply of mI for the synthesis of membrane phospholipids and for the maintenance of intracellular free mI, namely, synthesis, recycling and uptake by transport. It is synthesized *de novo* from glucose-6-phosphate (G-6-P) into inositol-1-monophosphate (I-1-P) by the action of I-1-P synthase, and subsequently into mI by IMPase. In a study on rabbits it was reported that about one half of the total unbound inositol in brain was synthesized from glucose and the rest transported from blood (7). It was also reported that slices of rat brain, kidney, liver and

testis were all capable of synthesizing mI (7). The recycling pathway of mI is complex, and is commonly named the PI-cycle because of the inositol lipid involved in that pathway. Phosphoinositol is the primary inositol-containing phospholipid present in mammalian cells and subcellular membranes (7). The hydrolysis of phosphoinositol also occurs in peripheral tissue through the stimulation of receptors by agonist, such as smooth muscle, the pancreas, or the salivary glands (2).

Although the relative concentrations of mI in each organ are not fully clear, the highest concentrations are found in brain, stomach, kidney, intestine, and liver (5, 7-9). In particular, the concentration of free inositol in the mammalian brain, and cerebrospinal fluid (CSF) is found to be at a higher concentration than in plasma (7, 9). A major part in regulating plasma inositol concentrations in the human body is carried out by the kidney (7).

As for the distribution in brain, mI was initially found only in astrocytes and was not observed in the neuronal cells of rat brain measured by proton- (^{1}H-) and carbon- (^{13}C-) MRS, thereby suggesting mI is a glial marker (10). In this study, less than 0.5 mM was observed in neuronal cells in comparison with ~ 6 mM of total mI in brain. Thus, it has been suggested that mI is stored in glial cells before its consumption in the PI-cycle (3). Astrocytes might take the role of regulating extracellular inositol concentrations (11). However, in a temporal pole biopsy study (12), no differences in mI concentrations were reported between gray and white matter. Cerebral mI level was not found to be affected by age or sex in any brain region in a postmortem human brain study (13).

Inositol is actively transported from the blood into organs such as the intestine, the kidney, and into nerve tissue, and astrocytes except for in the brain where the transfer rate was relatively low due to the presence of the blood-brain barrier (5, 7, 14). On the other hand, it is transported non-actively or through carrier-mediated diffusion in the liver and in skeletal muscle (14). Since the human brain probably obtains its inositol supply mainly from resynthesis through the PI-cycle and *de novo* synthesis from G-6-P with the ratio of ~ 7:1 (8) or 9:1 (2), it is likely to be very sensitive to any perturbation in the PI-

cycle (15). For these reasons it is possible that a large range of psychiatric conditions could theoretically involve alterations in mI metabolism.

The function of mI in the body is not fully understood. However, some studies support its role as a long-term osmolyte, an osmotically active solute (4), and a volume regulator of astrocytes in the brain (3, 4, 10, 14, 16) and the kidney (14). The role of mI as an osmolyte in brain glial cells (4) is supported by the observation that intracellular mI concentrations are controlled according to plasma osmolality. Regulation of the volume of brain cells is brought about by the influx and efflux (rather than *de novo* synthesis (17)) of organic osmolytes such as amino acids as well as mI in response to hyper- or hypo-tonic media without affecting cell functioning (14, 16-18). Inorganic osmolytes also contribute to this cell homeostasis, most likely for relatively acute volume regulation (14, 17). This is important since changes in cell volume and ultimately brain volume can result in neurological dysfunction and mortality (14). In the case of hepatic failure, for instance, the concentration of glutamine in glial cells becomes high as a process of ammonia detoxification. In response to the increased glutamine in glial cells, which may result in brain edema (astrocytes are known to be a primary cell type related in brain edema (14)), the mI level is decreased, thereby regulating the osmolality of cells (16). It is also reported that in peripheral tissues, unlike in the brain where the transport of mI across the blood-brain barrier is limited, the plasma level of mI is increased in order to protect its depletion in response to lithium treatment, which is known to inhibit mI synthesis (2). Moreover, mI is also known to be an important growth factor for human cells (4, 7), and it is a nutritional supply for brain cells (19). Nonetheless, probably most importantly for its psychiatric relevance, it is a precursor in the intracellular second messenger system PI-cycle (19, 20).

2.3 In-vivo ^{1}H-MRS and ^{31}P-MRS in Psychiatric and Neurological Research

Much of our recent understanding of the possible role of mI has been gained by using MRS. Both ^{1}H-MRS and ^{31}P-MRS have been used to explore alterations in the PI-cycle in psychiatric patients.

Among the various nuclei detectable by using MRS, ^{1}H-MRS has been most widely used for quantifying key brain metabolites. In a typical ^{1}H-MRS spectrum of the human brain (Fig. 2-2), four singlets are prominent. These arise from the two peaks of creatine (Cr) + phosphocreatine (PCr), choline (Cho) and N-acetylaspartate (NAA) + N-acetylaspartylglutamate (NAAG).

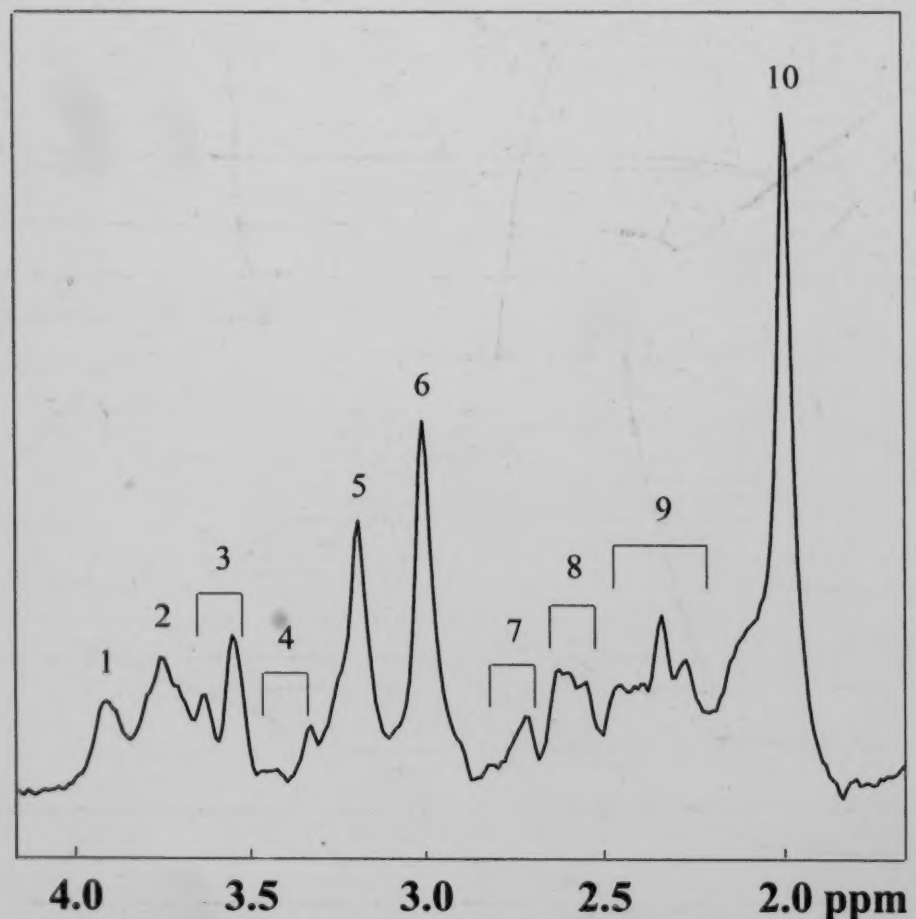

Figure 2-2 A ^{1}H-MRS spectrum of the human brain at 3.0 T. For data acquisition, a stimulated echo sequence was used with the voxel size of 2.5×2.5×2.5 cm^3 localized in the occipital cortex (1: creatine (methylene) + phosphocreatine, 2: glutamate + glutamine, 3: *mI* + glycine, 4: taurine, 5: total choline compounds, 6: creatine (methyl) + phosphocreatine + γ-aminobutyric acid, 7: aspartate, 8: N-acetylaspartate, 9: glutamate + glutamine + γ-aminobutyric acid, 10: N-acetylaspartate + N-acetylaspartylglutamate).

The resonance from the methyl group of Cr (~ 3.0 ppm) is a common choice as a reference peak for metabolite quantification. The signal of mI, which has been the target of most interest resides between the two Cr peaks. However, this signal is subject to contamination at typical low magnetic field strengths of clinical scanners by resonances from background metabolites such as glycine, glutamate, glutamine, taurine and macromolecules. Due to low concentration and spectral characteristic very similar to that of mI, I-1-P cannot be measured in practice and simply plays as an additional background signal of mI in ^{1}H-MRS.

Using ^{31}P-MRS, the phosphomonoester (PME) peak can be measured. This peak contains I-1-P, and gives information on the synthesis of membrane phospholipids (21). At a field strength of 3.0 T, there are seven peaks in a human in-vivo ^{31}P-MRS spectrum that are clearly spectrally resolved (fig. 2-3). These include PME, phosphodiester (PDE), inorganic phosphate (Pi), Phosphocreatine (PCr), and α-, β-, γ- adenosine triphosphate (ATP). As was Cr in ^{1}H-NMR spectra, PCr and β-ATP are often chosen as concentration references in ^{31}P-NMR spectra. Analyses at high magnetic field strengths have shown that the PME peak is contributed mainly by phosphoethanolamine (PE) (most prominently), phosphocholine (PC), and sugar phosphates including I-1-P and G-6-P with the ratio of PE + PC to sugar phosphates approximately 3 - 8 (22). Since PC and PE are precursors of membrane phospholipids (23), the PME region may be used to examine membrane phospholipid metabolism. It should be noted that while the PME peak is used to estimate change in the concentration of I-1-P, this compound is only a minor component of this peak (inositol monophosphates constituting 10 % - 15 % of the total PME peak area (24)). Another limitation of existing MRS literature is the use of ratio methods to determine metabolite changes. Thus, for example, changes in mI concentrations may be inferred from changes in the peak-area ratio of mI and a reference molecule, such as NAA. However, it is by no means certain that these reference metabolites remain unchanged, and this limitation needs to be recognized (25).

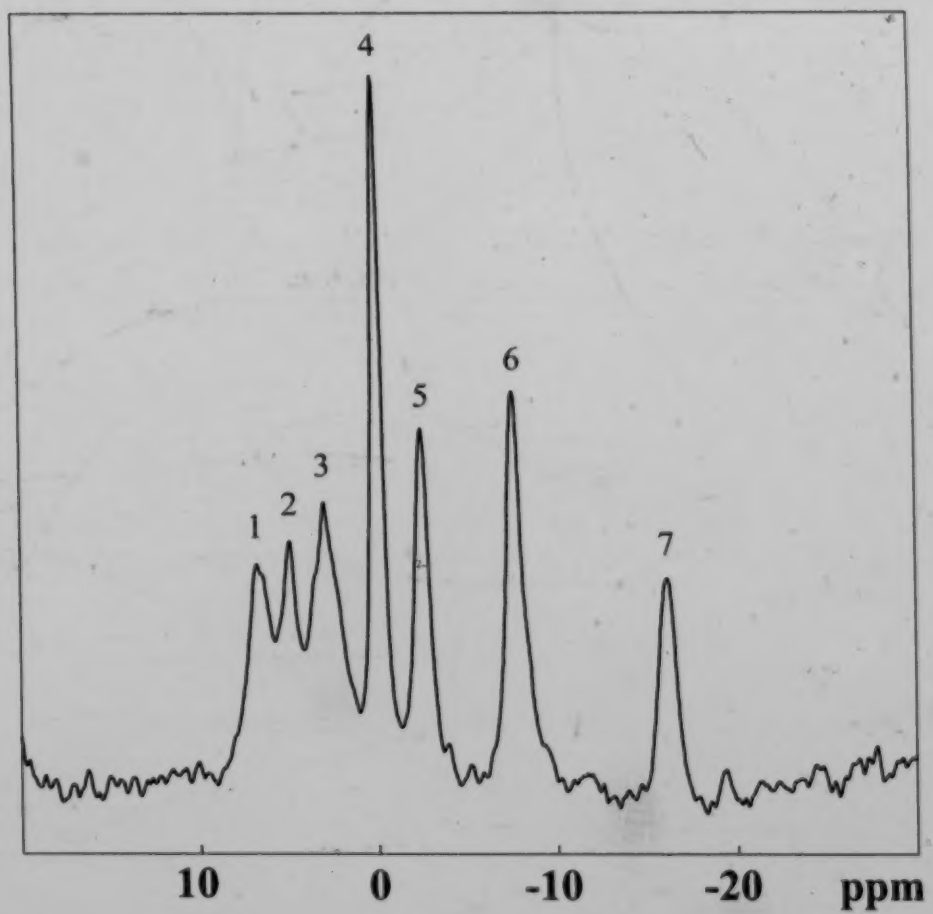

Figure 2-3 A ^{31}P-MRS spectrum of the human brain at 3.0 T. For data acquisition, a 90°-pulse-acquire sequence was used in combination with 1D-image selected *in-vivo* spectroscopy (ISIS) for a 20 cm slice selected from temporal lobe (1: phosphomonoesters, 2: inorganic phosphate, 3: phosphodiesters, 4: phosphocreatine, 5: γ-ATP, 6: α-ATP, 7: β-ATP). (Courtesy from Dr. Christopher C. Hanstock)

2.4 Psychiatric Disorders Related to mI

2.4.1 Bipolar Disorder

Bipolar disorder (BPD) is characterized by mood swings between episodes of major depression and mania, often separated by periods of normal mood (26). Major depression is defined as having at least five symptoms during the same 2-week period,

with marked change in function. One of the symptoms must be a depressed mood or a loss of interest or pleasure. In addition, changes in at least three of the following must be present: weight, sleep, activity level, energy, ability to think or concentrate, or suicidal ideation (27). It usually accompanies physical symptoms such as backache, headache, fatigue, loss of appetite, or insomnia (26). Mania is defined as a distinct period of abnormally elevated, expansive, or irritable mood lasting at least 1 week, with symptoms such as grandiosity, decreased need for sleep, racing thoughts, or excessive involvement in activities that have a high potential for painful consequences (27). BPD can be classified into two subtypes, Bipolar type I and Bipolar type II. Patients with bipolar type I have both major depression and mania. Those with bipolar type II have major depression and hypomania (mood elevations with less severity in impairing the individual's functioning) (27). BPD is distinguished from unipolar disorder in which the patients suffer from major depression only. At least about 1 % of general population is affected by the BPD type I. BPD type II may be more prevalent (~ 4 % of population) (26, 27).

Significant effort has been made to elucidate the pathophysiology of such a mood disorder with brain imaging, autopsies, and the action of a variety of mood stabilizers and antidepressants. However, the fundamental cause of BPD still remains unclear (20, 28-30). Some abnormality in brain structure may be associated with BPD, such as atrophy in the frontal cortex and the hippocampus, and enlargement of the amygdala (28). Ventricular enlargement may also be related to BPD (31). A relatively small size of the hippocampus/amygdala complex and the cerebellum could also be implicated in that disorder (31). These findings are non-specific, however. It has also been reported that both neuronal and glial cell abnormalities were found in the frontal lobes of patients with BPD (32). It is also believed that BPD is associated with family history or heredity. Roughly one-half of the patients with BPD have relatives with similar mood swings (28).

Although its mechanism of action is yet to be clarified, lithium has been a major treatment for BPD (30).

2.4.1.1 PI-cycle and mI Depletion Hypothesis

In the PI-cycle (Fig. 2-4), receptor binding by agonists stimulates hydrolysis of phosphatidylinositol 4,5-bisphosphate (PIP_2), into the second messengers diacylglycerol (DAG) and inositol 1,4,5-trisphosphate (IP_3), which in turn initiate separate cascades of cellular events.

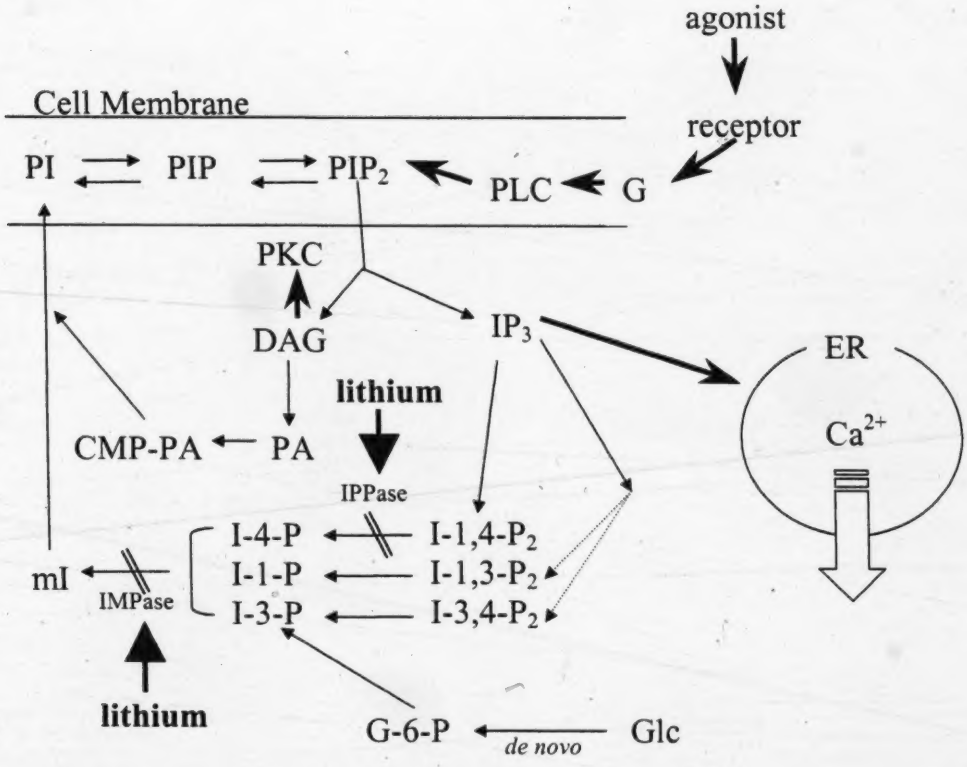

Figure 2-4 The phosphatidylinositol (PI) signal transduction pathway. (PIP: phosphatidylinositol 4-phosphate, PIP_2: phosphatidylinositol 4,5-biphosphate, G: G-protein, PLC: phospholipase C, PKC: protein kinase C, DAG: diacylglycerol, PA: phosphotidate acid, CMP-PA: cytidine monophosphate-phosphatidate acid, Glc: glucose, G-6-P : glucose 6-phosphate, ER : endoplasmic reticulum, IP_3 : I-1,4,5-P_3, IMPase : inositol monophosphatase, IPPase : inositol polyphosphate 1-phosphatase).

The most widely accepted hypotheses for lithium's mechanism of action in BPD is the inositol depletion hypothesis involving the PI-cycle (2, 19). This hypothesis is based on findings that lithium inhibits IMPase, and thus inhibits the recycling of inositol

monophosphates to mI in the PI second messenger system (33, 34). The availability of mI is consequently decreased, which results in a decrease in its incorporation into membrane phospholipids such as PIP_2.

The peculiarity of the action of lithium lies in the uncompetitive nature of its inhibition of IMPase and inositol polyphosphatase (2, 19, 20). That is to say, the inhibitory action of lithium on the PI-cycle is more pronounced in the system when it is over-activated. In such a system, the presence of lithium will ultimately induce depletion of the PI-cycle components in membranes, leading to decreased receptor sensitivity in that system, which may be another expression of the therapeutic efficacy of the lithium (2).

The inositol-depletion hypothesis further assumes that brain cells have limited access to plasma inositol, and as a result, the brain inositol supply mainly relies on the recycling from inositol lipid turnover as well as *de novo* synthesis from G-6-P. On the other hand, although the hydrolysis of mI occurs in various receptors in peripheral tissues as well, they are protected from the inhibitory action of lithium by the mI supply from plasma (2). For instance, the effect of lithium is much greater in the brain than in the kidney, despite the fact that the lithium level in the kidney is approximately 3 times higher than that in the brain (8). For these reasons, it is suggested that altered PI-cycle function can have far reaching implications for cell activity. This would then underlie the clinical efficacy of lithium.

Certain testable predictions emerge from the hypothesis. It would be predicted that the inhibition of IMPase and inositol polyphosphatase by lithium may lower not only mI but also inositol triphosphate (IP_3) concentrations, and elevate I-1-P concentrations. Despite much research into this hypothesis (19, 20, 29, 30, 35-38), it remains unproven. Additionally, although lithium does alter the PI-cycle, it is still uncertain if these effects on mI concentrations are related to its therapeutic efficacy (29, 30). The purpose of this review is to examine these points using current evidence, particularly recent MRS studies. The possible wider relationships between mI and BPD are also to be examined.

2.4.1.2 Review on Inositol in BPD

2.4.1.2.1 Possible Etiological Role of mI

In addition to the possible effects of lithium on mI concentrations, there exist several reports on changes in concentrations of mI in unmedicated (lithium-free) BPD patients. This suggests that mI changes may be involved in the etiology of BPD. In a postmortem brain study, Shimon et al (13) reported significantly reduced mI concentrations in the frontal cortex of unmedicated bipolar patients in comparison to normal subjects. However, no significant differences were found in the occipital region. In another study, low inositol levels were found in CSF from both unipolar and bipolar patients (39). On the other hand, no difference in mI/Cr ratios were found in the frontal lobe of drug-free, unipolar or bipolar patients in the depressive phase (3) compared to controls measured by ^{1}H-MRS. Interestingly, using ^{1}H-MRS, Davanzo and his colleagues found a higher mI/Cr ratio in the anterior cingulate cortex of children with BPD during the manic phase, compared to normal controls (40).

Using ^{31}P-MRS, a significantly lower PME value was found in the frontal lobe (41) and temporal lobe (42) of unmedicated, euthymic bipolar patients in comparison with normal subjects. In contrast, however, no difference in PME level was found (43) in ^{31}P-MRS spectra taken from the frontal cortex of drug-free patients with BPD in the euthymic state compared with the control group, although the size of the patient group was relatively small in this study (n = 7).

It should be noted that not all of the brains of the patients were completely lithium-free in Shimon et al's study (13) and that metabolite concentration in CSF may be significantly different from that in brain tissue (44). Nonetheless, these findings raise the intriguing possibility that abnormal phospholipid metabolism or membrane abnormalities in the frontal and temporal lobe could be involved in the pathophysiology and/or etiology of BPD (41).

2.4.1.2.2 Testing the mI-depletion Hypothesis

2.4.1.2.2.1 Animal NMR Studies

The PME peak was observed to be elevated *in vivo* both in cat (43) and rat brains (46, 47) following both chronic and acute lithium injection. Subsequently it was shown that the increased PME was from an increase in I-1-P concentration. In these studies the lithium-induced reduction in mI level was observed only in the spectra from brain extract using a high field magnet but not *in vivo*. In a study in which both decreased mI concentrations and increased I-1-P concentrations were found after chronic lithium injection (25), the use of a high field magnet (11.5 T) allowed for the observation of mI peaks without contamination from that of glycine. This is important since glycine has also been reported to be affected by lithium (48), and there is a spectral overlap between mI and I-1-P at lower field strengths. However, no effect of lithium on glycine level was found in this study.

2.4.1.2.2.2 Human NMR Studies

Most of the key recent research examining this hypothesis has involved in-vivo MRS. A reduced mI/Cr ratio was observed in the anterior cingulate cortices of children with BPD following acute lithium administration (40). In addition, a trend towards a higher mI/Cr ratio during the manic phase was found in bipolar patients compared to controls in the same study. In a well-conducted study in which absolute concentrations were measured, a reduction of mI concentrations was reported by Moore et al (32) in the frontal lobe of bipolar patients in the depression phase, but not in the occipital, parietal or temporal region, after both acute and chronic lithium administration. In contrast, in a smaller study no changes in temporal and parietal mI ratios were seen following chronic lithium treatment (49). In two studies in which healthy volunteers were administered lithium for 1 week no significant effect of lithium on mI/Cr ratios was observed (24, 44).

Several studies by the same group utilizing ^{31}P MRS (21, 23, 31, 50-52) suggested that euthymic bipolar patients treated with lithium have PME concentrations that are either reduced or not significantly different from controls, although it should be noted that in some of the studies results are presented for groups of patients where only some of them were receiving lithium, and in one study (21) patients had discontinued lithium during a wide range of days (from 11 – 365 days) before the ^{31}P-MRS examination. Consistent with these findings no difference in PME level was found between controls, lithium-treated and valproate-treated bipolar patients in the euthymic phase (53).

In contrast to a lack of findings in euthymic patients, in two studies Kato et al reported higher I-1-P in the frontal lobe of bipolar patients in the manic phase with chronic lithium treatment, compared to bipolar patients in the euthymic phase and to drug-free controls (50, 51). No correlation was found between cerebral lithium concentrations and PME levels, thereby suggesting the change in PME levels in bipolar patients cannot be ascribed exclusively to the elevation of I-1-P in response to lithium, at least, in manic patients. They also reported higher PME/total peak in the frontal lobe of bipolar patients in the depressive state than in the euthymic state (23). Since 70 % of the bipolar patients in the depression phase were lithium-free in this study, they proposed in combination of their former findings (50, 51) that the change in PME value may reflect the pathophysiology of BPD but less likely from the effect of lithium.

2.4.2 Schizophrenia

Schizophrenia has a lifetime prevalence estimated to be 1 ~ 1.5 % (27, 54, 55). Nevertheless, little is known about the illness, and currently no accurate biological test or animal model is available (54, 55). The symptoms seen in schizophrenia patients are largely divided into positive symptoms and negative symptoms (27, 54, 55). The positive symptoms include psychotic features such as delusions and hallucinations, while the negative symptoms refer to a lower level of social functioning (social isolation and loss of emotional expression and curiosity) and cognitive impairment (confused thought and speech) (27, 54). While BPD is referred to as a disorder of mood, schizophrenia is

categorized as a disorder of thought (27). When the symptoms include both mood and thought symptoms, it is referred to as schizoaffective disorder (27, 54).

Although many studies have shown structural and functional abnormalities in various brain regions of schizophrenia patients, particularly in the frontal region, the pathophysiological mechanism remains unknown (56-58). Frontal lobe dysfunction (hypofrontality and reduced metabolic rate) may be responsible for the deficit in higher cognitive functioning such as lack of judgment, creativity and planning (56). A breakdown in communication between frontal lobe and other regions of the brain may result in failure in the coordination of mental activity leading to poor decision-making, erratic behavior, and hallucination (54). This disturbed neuronal circuitry may be caused by excitotoxic glutamate (54, 55, 57, 59). Excessive dopamine activities were also found in some schizophrenia patients (54, 60).

2.4.2.1 Review on Inositol in Schizophrenia

It has been suggested that anti-psychotic drugs may be clinically effective via a dampening action on an overactive PI-cycle (61), although it remains uncertain if any such actions are via effects on second messenger systems (62) or possibly via increased PI-cycle activity (60). Nonetheless, studies to date have not consistently suggested that the PI-cycle is altered in patients with schizophrenia. In platelet studies one group found no differences in the accumulation of IP_3 in blood platelets between drug-free patients and controls (63), while others have reported an increase in IP_3 production (64). A postmortem study of patients with chronic schizophrenia found a reduction in mI concentrations in the frontal and the occipital cortex as well as in the cerebellum, but the activity of IMPase did not differ from that of controls (65), while, in another post-mortem study, a higher IMPase activity was reported in the CSF taken from schizophrenia patients (66).

The effect of oral administration of mI has also been examined in schizophrenia patients (1, 66, 67). However, no significant effect was found on the CSF IMPase

activity in patients with schizophrenia (66). Apomorphine challenge, which may be used to induce stereotypy as a model of schizophrenia was not altered either by acute inositol administration (1). This lack of effect of increasing mI level by oral administration was also reported in a study with chronic schizophrenia patients receiving anti-psychotics (67). Thus, taken together these findings do not give consistent support to suggestions of altered PI-cycle in schizophrenia.

MRS studies in schizophrenic patients have not suggested altered PI-cycle activity. Thus, although increased concentrations of mI in parietal matter was reported in one study (68), no significant changes in mI concentrations was observed in several brain regions of schizophrenic patients in two other studies (57, 69). While the possible effects of medication cannot be excluded in these studies, and all patients were receiving anti-psychotics, in another study no changes in mI concentrations was observed in the parietal cortex in both medicated and drug-free patients (70). In contrast to the ^{1}H-MRS studies, a decrease in PME concentrations was reported in the prefrontal cortex of both drug-free (56, 62) and chronically medicated patients (71). On the other hand, no changes in PME concentrations were observed in the same region of the brains of medicated chronic schizophrenia patients (72). Interestingly, an increase in PME concentration was also reported in the basal ganglia of medicated patients (73) and in the parietal cortex of both drug-receiving and drug-free schizophrenic patients (70). Similar inconsistencies have also been reported in PDE concentrations in patient studies. An increase in PDE levels was observed in the prefrontal cortex of drug-free and treated patients (56, 62, 74), and in the temporal region of medicated patients (73). In contrast, no alteration in the concentration of PDE was reported in the parietal cortex of both medicated (70, 71) and drug-free schizophrenic patients (70), while a decrease in concentration was also reported in the prefrontal region of chronic patients (72). Taken together, therefore, MRS findings do not suggest consistent changes in PI-cycle activity in schizophrenic patients.

2.5. Conclusion (Psychiatric Disorders)

Taken together, the research to date is consistent with the suggestion that in patients with BPD there may be an abnormality in PI-cycle functioning or activity that leads to altered concentrations of mI and PME. This can then be detected in the manic and depressed stages, and possibly also at times in the euthymic state. Based upon this, it is hypothesized that chronic treatment with lithium will act to normalize these abnormalities in PI-cycle functioning, probably acting via the mechanism of inositol depletion. Supporting evidence from animal studies is fairly strong, at least for lithium, but there have been some contradictory findings. Human studies have been less clear-cut, but overall the evidence is still supportive. Clearly, however, more research needs to be done to try and determine if this hypothesis is correct. The other point to note is that there are likely multiple factors involved in the pathogenesis and the development of BPD, as well as multiple factors explaining why some patients respond clinically to lithium while others do not. Therefore, even if future studies continue to be supportive of this hypothesis, it is highly unlikely to be the single answer explaining how this disease develops and how treatments are clinically effective.

Compared to BPD, not many studies have been reported with regard to the direct measurement of mI concentration in schizophrenic patients, and they do not suggest consistent alteration in PI-cycle.

2.6 Neurological Diseases Related to mI

2.6.1 Alzheimer's Disease

Alzheimer's disease (AD) is a progressive degenerative disease characterized by the impairment of memory (75-77) and progressive loss of cognitive functions (deficiency in attention, language, and so on (76, 77)), leading to dementia (78, 79). AD afflicts 5-11 % of the population over the age of 65 (77). Despite this relatively high

prevalence of the disease, no methods for effective prevention and treatment of the disease are available to date (78).

Pathological abnormalities in AD brain include synaptic loss, the accumulation of neurofibrillary tangles (NFT) and the formation of neuritic plaques that contain the β-amyloid peptides (Aβ). In particular, NFT is known to be associated with cognitive dysfunction in AD patients (75) and Aβ may be neurotoxic leading to the dysfunction and death of neurons (77, 79, 80).

The etiology of AD is still unknown. However, there exist mainly three hypotheses on the pathogenesis of the disease, namely the genetic hypothesis, the β-amyloid hypothesis, and the cholinergic theory, among which the first two are closely related. In addition, recent findings suggest possible implication of mI in the pathogenesis of AD.

The detailed discussion on those three major hypotheses is beyond the scope of this review, and can be found elsewhere (77, 79-88). Therefore, the discussion in the following sections is focused on the possible involvement of mI in AD brain.

2.6.1.1 mI-Hypothesis in AD

2.6.1.1.1 Supporting Evidence

Several line of evidence support a role of mI in AD (81). First, an alteration in the formation of inositol phospholipids has been reported. For example, a 50 % reduction in PIP formation was reported in the cortex of AD brain, thereby suggesting possible involvement of the PI-cycle in the pathogenesis of AD (89). Reduced synthesis of PIP may affect the level of PIP_2, which is a key substance for the generation of the second messengers such as DAG and IP_3. A significantly lowered PI concentration was also observed in the temporal cortex of AD brain (90). The concentrations of PIP and PIP_2 were also lower (but not statistically significant) in the same study, but the concentration

of free mI was slightly higher. This implies that the reduced PI is not from a lack of mI. Since inositol lipids may play an important role in the initiation and propagation of nerve impulses, and ultimately in neuronal and brain functioning (89), these abnormal concentrations of inositol lipids might be responsible in part for lesions in AD patients.

Secondly, reduced binding of IP_3 was observed in the parietal cortex and the hippocampus (91). The binding of this second messenger is believed to take place in endoplasmic reticulum (ER) and the plasma membrane, the former being known as a storage of intracellular Ca^{2+} and the latter as activating transmembrane Ca^{2+} influx (91). Therefore, this altered binding of IP_3 may give rise to inhibited cellular Ca^{2+} mobilization via dysfunction of the second messenger system. This mechanism may be partially responsible for the cognitive dysfunction in AD brain (79, 91).

Thirdly, an increase in cerebral mI concentrations may be the most remarkable evidence for the putative involvement of mI in the pathogenesis of AD. The elevation of cerebral mI level may affect the PI system, affecting the phosphorylation state of cellular protein or alterations in membrane structure (82).

2.6.1.1.2 Metabolic Change in AD Brain Measured by NMR

Reduced NAA and elevated mI concentrations are common spectroscopic abnormalities in AD (75, 79, 82, 92-95). The reduced NAA concentrations may be due to actual death of neurons in affected brain regions or, at least, the decreased function of neurons that are still viable (75, 79, 82, 92). In addition, a higher concentration of PME is frequently reported in AD brain measured by ^{31}P-MRS (76). This may be due to the abnormal phosphorylation of proteins in AD brain, which may influence the activity of the enzyme that converts PME into phospholipids, thereby making neurons weak in structure and consequently vulnerable to toxicity and death (79).

Using ^{1}H MRS, higher mI concentrations were reported in the posterior cingulate (75), the temporoparietal region (93, 96), the parietal cortex (82), the parietal white

matter and the occipital gray matter (95) of AD brain. However, no change was observed in the frontal region (96) in AD patients.

Discrimination of AD from other diseases as well as from normal brains is an important issue (79). Although the specificity and sensitivity are yet to be established, the combined observation of NAA and mI using ^{1}H-MRS may be promising as a non-invasive diagnostic tool for AD patients (82, 97, 98). A significant correlation was found between NAA/mI ratio and mental status as well as the extent of atrophy in AD patients (94). For instance, Shonk et al reported that the use of mI/NAA ratio allowed for discriminating AD from other dementias with 83 % accuracy (98). In this study both AD and other types of dementia showed a reduction in NAA concentrations but the elevated mI levels were observed only in AD brains. As well, based on mI/NAA ratio, the differentiation of AD from multi-infarct dementia (MID) could readily be made (99) where significantly higher mI concentrations were observed in the occipital region of the AD patients relative to MID patients.

2.6.1.1.3 Possible Mechanisms Responsible for Elevated mI Level in AD Brain

Although further studies are required to explain the abnormal mI concentrations observed in AD brain, possible mechanisms underlying these findings are summarized (81) as: 1) mI could be a marker of those substances observed in AD, such as amyloid, plaques, and tangles (81, 82, 100, 101); 2) mI could also be a marker of a cell type that replaces neurons (gliosis) (81, 101) upon the assumption that mI is a glial marker (3, 10, 11, 101); 3) Increased mI and decreased PI levels suggest that there may be abnormalities in PI cycle in AD brain (89, 101), such as an inhibition of the conversion of mI into PI (81, 82, 100) or into IP_3 (6, 100); 4) the hyperactive conversion of I-1-P into mI by IMPase (81); 5) an increase in mI concentrations in AD brain may also result from abnormalities in local cell volume homeostasis (101).

2.6.2. Hepatic Encephalopathy

Hepatic encephalopathy (HE), also known as portal-systemic encephalopathy (102), is a complication of a chronic liver disease that accompanies metabolic disturbance in the brain (103, 104). It can cause a variety of neuropsychiatric symptoms such as drowsiness, altered sleep pattern, changing mood or behavior, tremor, loss of consciousness, seizures and dementia (102-107).

The pathogenesis of HE is not clearly known, but there is a widely accepted role of ammonia, which is neurotoxic when present at excessive concentration in the brain (102-104). For instance, an excessive amount of ammonia in the brain can cause functional alterations of blood-brain barrier permeability (103, 108, 109), and can increase synaptic inhibition (107). Using MRS, both reduced mI and elevated Gln concentrations are the most common characteristics of HE brain (16, 103-105). Although the role of mI and Gln in HE brain is not completely known, it is hypothesized that the decrease in cerebral mI concentration is a compensatory response of the brain to the increased Gln concentrations in astrocytes, which result from the synthesis of the metabolite from Glu and ammonia as a primary ammonia detoxification process in the brain (16, 103, 105, 108, 110, 111).

2.6.2.1 Review on Inositol in HE

No direct involvement of mI in the pathogenesis of HE has been established to date. However, the detection of mI using ^{1}H-MRS may provide for a means of early diagnosis and differentiation of HE from other types of liver diseases. For instance, based on mI concentrations measured by ^{1}H-MRS, a precise diagnosis of HE was made with the sensitivity of ~ 80 % (104, 112). As well, in other studies, the concentration of mI was proposed as a potential marker of chronic HE (108, 113). Elevated Gln (65 %), lowered mI (54 %) and total Cho (23 %) concentrations were observed in the parietal cortex of HE patients (102). A concomitant reduction in mI and Cho levels, and an elevation in both Glu and Gln (collectively referred to as Glx) levels were also reported

in the occipital lobe (112) as well as in the parietal white matter (WM) and gray matter (GM) (110) of HE patients. In one study, reduced Cho level was observed in the parietal WM and the occipital GM of the patients with liver disease *without* HE, but a remarkable decrease in mI levels and an increase in Glx levels were observed only in the patients *with* HE (104). The reduced Cho peak in ^{1}H-MRS may be due to a reduction in glycerophosphocholine concentrations, which is also know as an osmolyte in the brain (110), in response to the increased Gln. It is difficult to separate Gln from Glu by ^{1}H-MRS at the field strengths of clinical scanners, and as a result, the findings of decreased Gln may be controversial. However, in other studies with human brain extracts analyzed by using high resolution MRS (114) and with autopsied brain (115), the increased Glx complex was confirmed to be from that of Gln.

2.6.2.2 Possible Consequence of the Lowered mI Level in HE Brain

To date, it is not clear whether the reduced mI concentration takes a significant role in the development of the diseases and the neuropsychiatric symptoms in HE. However, the resultant down-regulation of mI in HE may influence aspects such as membrane phospholipid turnover, cell signaling and release of neurotransmitters (16, 104, 108).

In addition, mI may be a precursor of glucuronic acid, which is known to be involved in the detoxification process in the brain, the liver and the kidney (102, 114). Therefore, reduced availability of glucuronate caused by the depletion of mI in chronic HE-affected brain may be associated with a variety of symptoms in HE (102, 114). Interestingly, it may also be possible that the reduced mI content results from an excessive detoxification process rather than from its role as an osmolyte (102, 114).

2.7 Conclusion (Neurological Diseases)

In this review, two neurological diseases were considered in association with the concentration of mI in the brain. At present, the observation of elevated mI

concentrations in AD brain cannot directly be related to the pathology of AD. However, together with NAA, the quantification of the metabolite using ^{1}H-MRS may be beneficial in the diagnosis of AD as well as in the differentiation of the disease from normal and other dementias.

Likewise, no clear evidence has been reported, which supports direct involvement of mI in the etiology of HE. Nonetheless, the consequence of the reduced mI concentrations in HE should not be neglected because abnormal concentrations of the metabolite in the brain are also implicated with some mood disorders. The reduction in mI level in HE distinguishes this disorder from other liver diseases or other types of encephalopathy. The quantification of mI using ^{1}H-MRS, therefore, appears to hold more promise for the diagnosis of HE than for AD. Future studies may clarify the implication of the abnormal mI concentrations observed in those diseases.

The in-vivo ^{1}H-MRS data (human brain) of mI measurements reviewed in this chapter are summarized in Table 2-1 below.

Diseases/disorders reviewed	References	mI changes	Brain regions	Subjects/phase (medication)
Bipolar disorder	3	-	frontal lobe	BPDP/depressed (Li free)
				UPDP (Li free)
	38	↑	anterior cingulate cortex	BPDP/manic (Li free)
				BPDP/manic (Li medicated)
	30	↓	frontal lobe	BPDP/depressed (Li medicated)
		-	occipital lobe	
			parietal lobe	
			temporal lobe	
	47	-	temporal region	BPDP (Li medicated)
			parietal region	
	42, 48	-	·	healthy (Li medicated)
Schizophrenia	67	↑	parietal region	SPP (·)
	56, 68	-	·	SPP (medicated)
	69	-	parietal cortex	SPP (medicated)
				SPP (drug free)
Alzheimer's disease	74	↑	posterior cingulate	ADP (·)
	92, 95		temporoparietal	
	81		parietal cortex	
	94		parietal WM	
			occipital GM	
	95	-	frontal region	
	97	↑	·	
	98		occipital region	
Hepatic encephalopathy	111	↓	occipital lobe	HEP (·)
	109		parietal WM	
			parietal GM	
	103		·	

Table 2-1 The in-vivo ^{1}H-MRS data (human brain) of mI measurements in bipolar disorder, schizophrenia, Alzheimer's disease and hepatic encephalopathy. (BPDP: bipolar disorder patients, SPP: schizophrenia patients, ADP: Alzheimer's disease patients, HEP: hepatic encephalopathy patients, Li: lithium, GM: gray matter, WM: white matter).

2.8 References

1. H. Einat and R. H. Belmaker,. *J. Affect. Disord.*, **62**, 113, 2001
2. M. J. Berridge, C. P. Downes, and M. R. Hanley, *Biochem. J.*, **206**, 587, 1982
3. R. Frey, D. Metzler, P. Fischer, A. Heiden, J. Scharfetter, E. Moser, and S. Kasper, *J. Psychiatr. Res.*, **32**, 411, 1998
4. B. D. Ross BD, *NMR Biomed.*, **4**, 59, 1991
5. A. Cantarow and B. Schepartz, *Biochemistry,* W. B. Saunders Company, 1962, p. 216
6. E. A. Doisy Jr., *The encyclopedia of biochemistry,* Reinhold Publishing Corporation, 1967, p. 443
7. B. J. Holub, *Adv. Nutr. Res.*, **4**, 107, 1982
8. W. R. Sherman, L. Y. Munsell, B. G. Gish, and M. P. Honchar, *J. Neurochem.* **44**, 798, 1985
9. W. Greil, R. Steber, and D. van Calker D, *Biol. Psychiatry*, **30**, 443, 1991
10. A. Brand, C. Richter-Landsberg, and D. Leibfritz, *Dev. Neurosci.* **15**, 289, 1993
11. M. Wolfson, Y. Bersudsky, E. Zinger, M. Simkin, R. H. Belmaker, and L. Hertz, *Brain Res.*, **855**, 158, 2000
12. O. A. Petroff, D. D. Spencer, and J. R. Alger, *Neurology,* **39**, 1197, 1989
13. H. Shimon, G. Agam, R. H. Belmaker, T. M. Hyde, and J. E. Kleinman, *Am. J. Psychiatry*, **154**, 1148, 1997
14. R. E. Isaacks, A. S. Bender, C. Y. Kim, N. M. Prieto, and M. D. Norenberg, *Neurochem. Res.*, **19**, 331, 1994
15. D. L. Vaden, D. Ding, B. Peterson, and M. L. Greenberg, *J. Biol. Chem.*, **276**, 15466, 2001
16. J. Cordoba, J. Gottstein, and Blei AT, *Hepatology,* **24**, 919, 1996
17. A. Paredes, M. McManus, H. M. Kwon, and K. Strange, *Am. J. Physiol.*, **263**, C1282, 1992
18. R. E. Isaacks, A. S. Bender, C. Y. Kim, and Y. F. Shi, *J. Neurosci. Res.*, **57**, 866, 1991
19. M. J. Berridge and R. F. Irvine, *Nature*, **341**, 197, 1989
20. M. J. Berridge, C. P. Downes, and M. R. Hanley, *Cell,* **59**, 411, 1989
21. T. Kato, T. Inubushi, and N. Kato, *J. Neuropsychiatry Clin. Neurosci.*, **10**, 133, 1998
22. L. Gyulai, L. Bolinger, J. S. leigh Jr., C. Barlow, and B. Chance, *FEBS Lett.*, **178**, 137, 1984
23. T. Kato, S. Takahashi, T. Shioiri, and T. Inubushi, *J. Affect. Disord.* **26**, 223, 1992
24. P. H. Silverstone, S. Rotzinger, A. Pukhovsky, and C. C. Hanstock, *Biol. Psychiatry,* **46**, 1634, 1999
25. T. O'Donnell, S. Rotzinger, T. T. Nakashima, C. C. Hanstock, M. Ulrich, and P. H. Silverstone, *Brain Res.*, **880**, 84, 2000
26. Anonymous, *Harv. Ment. Health Lett.* **17,** Article 41, 2001, p. NA
27. I. D. Glick, T. Supples, C. de Battista, R. J. Hu, and S. Marder, *Ann. Intern. Med.* **134**, 47, 2001
28. Anonymous, *Harv. Ment. Health Lett.* **17**, Article 36, 2001, p. NA

29. G. Chen, K. A. Hasanat, J. M. Bebchuk, G. J. Moore, D. Glitz, and H. K. Manji, *Psychosom. Med.* **61**, 599, 1999
30. H. K. Maji, G. J. Moore, and G. Chen, *Br. J. Psychiatry*, **Suppl 41,** 107, 2001
31. T. Kato, T. Shioiri, J. Murashita, H. Hamakawa, T. Inubushi, and S. Takahashi, *Psychiatry Res.*, **55**, 41, 1994
32. G. J. Moore, J. M. Bebchuk, J. K. Parrish, M. W. Faulk, C. L. Arfken, J. Strahl-Bevacqua, and H. K. Manji, *Am. J. Psychiatry*, **156**, 1902, 1999
33. L. M. Hallcher and W. R. Sherman, *J. Biol. Chem.*, **25**, 10896, 1980
34. P. W. Majerus, T. M. Connolly, V. S. Bansal, R. C. Inhorn, T. S. Ross, and D. L. Lips, *J. Biol. Chem.*, **5**, 3051, 1988
35. C. J. Phiel and P. S. Klein, *Annu. Rev. Pharmacol. Toxicol.*, 41, 789, 2001
36. J. M. Baraban, P. F. Worley, and S. H. Snyder, *Am. J. Psychiatry,* **146**, 1251, 1989
37. R. H. Lenox and D. G. Watson, *Clin. Chem.*, **40**, 309, 1994
38. S. R. Nahorski, C. I. Ragan, and R. A. J. Challiss, *Trends Pharmacol. Sci.*, **12**, 297, 1991
39. A. I. Barkai, D. L. Dunner, H. A. Gross, P. Mayo, and R. R. Fieve, *Biol. Psychiatry*, **13**, 65, 1978
40. P. Davanzo, M. A. Thomas, K. Yue, T. Oshiro, T. Belin, M. Strober, and J. McCracken, *Neuropsychopharmacology,* **24**, 359, 2001
41. R. F. Deicken, G. Fein, and M. W. Weiner, *Am. J. Psychiatry,* **152**, 915, 1995
42. R. F. Deicken, M. W. Weiner, and G. Fein, *J. Affect. Disord.* **33**, 195, 1995
43. T. Kato, J. Murashita, A. Kamiya, T. Shioiri, N. Kato, and T. Inubushi, *Eur. Arch. Psychiatry Clin. Neurosci.* **248**, 301, 1998
44. P. H. Silverstone, C. C. Hanstock, J. Fabian , R. Staab, and P. S. Allen, *Biol. Psychiatry*, **40**, 235, 1996
45. P. F. Renshaw, J. J. Summers, C. E. Renshaw, K. G. Hines, and J. S. Leigh Jr., *Biol. Psychiatry,* 21, 694, 1986
46. N. E. Preece, D. G. Gadian, J. Houseman, and S. R. Williamson, *Lithium,* **3**, 287, 1992
47. N. E. Preece, D. G. Gadian, J. Houseman, and S. R. Williams, *proc. ISMRM, San Francisco,* 1991, p. 428
48. S. I. Deutsch, M. Stanley, E. D. Peselow, and M. Banay-Schwartz, *Neuropsychobiology,* **9**, 215, 1983
49. H. Bruhn, G. Stoppe, J. Staedt, K. D. Merboldt, W. Hanicke, and J. Frahm, *Proc. ISMRM, New York,* 1993, p. 1543
50. T. Kato, T. Shioiri, S. Takahashi, and T. Inubushi, *J. Affect. Disord.*, **22**, 185, 1999
51. T. Kato, S. Takahashi, T. Shioiri, and T. Inubushi, *J. Affect. Disord.*, **27**, 53, 1993
52. T. Kato, S. Takahashi, T. Shioiri, J. Murashita, H. Hamakawa, and T. Inubushi, *J. Affect. Disord.*, **31**, 125, 1994
53. P. H. Silverstone, S. Rotzinger, T. O'Donnell, M. Ulrich, S. Asghar, P. Tibbo, and C. C. Hanstock, Unpublished.
54. Anonymous, *Harv. Ment. Health Lett.*, **15,** Article 172, 1999, p. HARV99141001
55. Anonymous, *Harv. Ment. Health Lett.*, **15,** Article 166, 1999, p. ITEM00143001
56. J. W/ Pettegrew, M. S. Keshavan, K. Panchalingam, S. Strychor, D. B. Kaplan, M. G. Tretta, and M. Allen, *Arch. Gen. Psychiatry,* **48**, 563, 1991

57. W. Block, T. A. Bayer, R. Tepest, F. Traber, M. Rietschel, D. J. Muller, T. G. Schulze, W. G. Honer, W. Maier, and H. H. Schild, *Neurosci. Lett.*, **289**, 147, 2000
58. J. A. Stanley, P. C. Williamson, D. J. Drost, T. J. Carr, R. J. Rylett, A. Malla, and R. T. Thompson, *Arch. Gen. Psychiatry*, **52**, 399, 1995
59. P. F. Buckley, and J. L. Waddington, *Biol. Psychiatry*, **36**, 789, 1994
60. J. K. Yao, P. Yasaei P, and D. P. van Kammen, *Prostaglandins Leukot. Essent. Fatty Acids*, **46**, 39, 1992
61. R. S. Jope, L. Song, C. A. Grimes, M. A. Pacheco, G. E. Dilley, X. Li, H. Y. Meltzer, J. C. Overholser, and C. A. Stockmeier, *J. Neurochem.*, **70**, 763, 1998
62. J. W. Pettegrew, M. Keshavan, and K. Panchalingam, *Biol. Psychiatry*, **25**, 14A, 1989
63. M. A. Essali, I. Das, J. de Belleroche, and S. R. Hirsch, *Biol. Psychiatry*, **28**, 475, 1990
64. I. Das, M. A. Essali, J. de Belleroche, and S. R. Hirsch, *Prostaglandins Leukot. Essent. Fatty Acids*, **46**, 65, 1992
65. H. Shimon, Y. Sobolev, M. Davidson, V. Haroutunian, R. H. Belmaker, and G. Agam, *Biol. Psychiatry*, **44**, 428, 1998
66. J. R. Atack, J. Levine, and R. H. Belmaker, *Biol. Psychiatry*, **44**, 433, 1998
67. J. Levine, R. Umansky, G. Ezrielev, and R. H. Belmaker, *Biol. Psychiatry*, **33**, 673, 1993
68. D. P. Auer, M. Wilke, A. Grabner, J. O. Heidenreich, T. Bronisch, and T. C. Wetter, *Schizophr. Res.*, **52**, 87, 2001
69. P. Delamillieure, J. M. Constans, J. Fernandez, P. Brazo, K. Benali, P. Courtheoux, F. Thibaut, M. Petit, and S. Dollfus, *Schizophr. Bull.*, **28**, 329, 2002
70. S. Bluml, J. Tan, K. Harris, N. Adatia, A. Karme, T. Sproull, and B. Ross, *J. Comput. Assist. Tomogr.*, **23**, 272, 1999
71. P. Williamson, D. Drost, J. Stanley, T. Carr, S. Morrison, and H. Merskey, *Arch. Gen. Psychiatry*, **48**, 578, 1991
72. H. P. Volz, R. Rzanny, S. May, H. Hegewald, B. Preubler, M. Hajek, W. A. Kaiser, and H. Sauer, *Biol. Psychiatry*, **41**, 644, 1997
73. T. Fujimoto, T. Nakano, T. Takano, Y. Hozazono, T. Asakura, and T. Tsuji, *Acta. Psychiatr. Scand.*, **86**, 455, 1992
74. R. F. Deicken, G. Calabrese, E. L. Merrin, D. J. Meyerhoff, W. P. Dillon, M. W. Weiner, and G. Fein, *Biol. Psychiatry*, **36**, 503, 1994
75. K. Kantarci, C. R. Jack Jr., Y. C. Xu, N. G. Campeau, P. C. O'Brien, G. E. Smith, R. J. Ivnik, B. F. Boeve, E. Kokmen, E. G. Tangalos, and R. C. Petersen, *Neurology*, **55**, 210, 2000
76. D. G. M. Murphy, P. A. Bottomley, J. A. Salerno, C. de Carli, M. J. Mentis, C. L. Grady, D. Teichberg, K. R. Giacometti, J. M. Rosenberg, C. J. Hardy, M. B. Schapiro, S. I. Rapoport, J. R. Alger, and B. Horwitz, *Arch. Gen. Psychiatry*, **50**, 341, 1993
77. B. A. Yankner, and M. M. Mesulam, *N. Engl. J. Med.*, **325**, 1849, 1991
78. G. G. Brown, S. R. Levine, J. M. Gorell, J. W. Pettegrew, J. W. Gdovski, J. A. Bueri, J. A. Helpern, and K. M. A. Welch, *Neurology*, **39**, 1423, 1989
79. J. G. Nicholls, A. R. Martin, and B. G. Wallace, *From neuron to brain*, Sinauer Associates Inc., 1992

80. J. H. Growdon, *Arch. Neurol.*, **56**, 281, 1999
81. B. D. Ross, S. Bluml, R. Cowan, E. Danielsen, N. Farrow, and R. Gruetter, *Biophys. Chem.*, **68**, 161, 1997
82. B. L. Miller, R. A. Moat, T. Shonk, T. Ernst, S. Woolley, and B. D. Ross, D, *Radiology*, **187**, 433, 1993
83. L. Missiaen, W. Robberecht, L. van den Bosch, G. Callewaert, J. B. Parys, F. Wuytack, L. Raeymaekers, B. Nilius, J. Eggermont, and H. de Smedt, *Cell. Calcium*, **28**, 1, 2000
84. D. J. Meyerhoff, S. MacKay, J. M. Constans, D. Norman, C. van Dyke, G. Fein, and M. W. Weiner, *Ann. Neurol.*, **36**, 40, 1994
85. D. J. Selkoe, *J. Neuropathol. Exp. Neurol.*, **53**, 438, 1994
86. A. M. Saunders, W. J. Strittmatter, D. Schumechel, P. H. St. George-Hyslop, M. A. Pericak-Vance, S. H. Joo, B. L. Rosi, J. F. Gusella, D. R. Crapper-MacLachlan, and M. J. Alberts, *Neurology*, **43**, 1467, 1993
87. H. Arai, M. Terajima, M. Miura, S. Higuchi, T. Muramatsu, N. Machida, H. Seiki, S. Takase, C. M. Clark, and V. M. Y. Lee, *Ann. Neurol.*, **38**, 649, 1995
88. H. F. Bradford, *Chemical Neurobiology: An introduction to neurochemistry*, W. H. Freeman and Company, 1986.
89. J. Jolles, J. Bothman, M. Markerink, and R. Ravid, *J. Neurochem.*, **58**, 2326, 1992
90. C. E. Stokes and J. N. Hawthorne, *J. Neurochem.*, **48**, 1018, 1987
91. L. T. Young, S. J. Kish, P. P. Li, and J. J. Warsh, *Neurosci. Lett.*, **94**, 198, 1988
92. F. Jessen, W. Block, F. Traber, E. Keller, S. Flacke, A. Papassotiropoulos, L. Lamerichs, R. Heun, and H. H. Schild, *Neurology*, **55**, 684, 2000
93. L. Parnetti, D. T. Lowenthal, O. Presciutti, G. P. Pelliccioli, R. Palumbo, G. Gobbi, P. Chiarini, B. Palumbo, R. Tarducci, and U. Senin, *J. Am. Geriatr. Soc.*, **44**, 133, 1996
94. S. E. Rose, G. I. de Zubicaray, D. Wang, G. J. Galloway, J. B. Chalk, S. C. Eagle, J. Semple, and D. M. Doddrell, *Magn. Reson. Imaging*, **17**, 291, 1999
95. R. A. Moats, T. Ernst, T. K. Shonk, and B. D. Ross, *Magn. Reson. Med.*, **32**, 110, 1994
96. T. Ernst, L. Chang, R. Melchor, and C. M. Mehringer, *Radiology*, **203**, 829, 1997
97. R. A. Moats and T. Shonk, *AJNR Am. J. Neuroradiol.*, **16**, 1779, 1995
98. T. K. Shonk, R. A. Moat, P. Gifford, T. Michaelis, J. C. Mandigo, J. Izumi, and B. D. Ross, *Radiology*, **195**, 65, 1995
99. G. S. Rai, J. R. McConnell, A. Waldman, D. Grant, and M. Chaudry, *Lancet*, **353**, 1063, 1999
100. M. J. Valenjuela and P. Sachdev, *Neurology*, **56**, 592, 2001
101. T. Shonk and B. D. Ross, *Magn. Reson. Med.*, **33**, 858, 1995
102. R. Kreis, B. D. Ross, N. A. Farrow, and Z. Ackerman, *Radiology*, **182**, 19, 1992
103. D. Haussinger, G. Kircheis, R. Fischer, F. Schliess, and S. vom Dahl, *J. Hepatol.*, **32**, 1035, 2000
104. B. D. Ross, S. Jacobson, F. Villamil, J. Korula, R. Kreis, T. Ernst, T. Shonk, and R. A. Moats, *Radiology*, **193**, 457, 1994
105. C. Zwingmann, A. Brand, C. Richter-Landsberg, and D. Leibfritz, *Dev. Neurosci.*, **20**, 417, 1998

106. M. A. Thomas, A. Huda, B. Guze, J. Curran, M. Bugbee, L. Fairbanks, Y. Ke, T. Oshiro, P. Martin, and F. Fawzy, *AJR Am. J. Roentgenol.*, **171**, 1123, 1998
107. A. H. Lockwood, E. W. H. Yap, and W. H. Wong, *J. Cereb. Blood Flow Metab.*, **11**, 337, 1991
108. D. Haussinger, J. Laubenberger, S. vom Dahl, T. Ernst, S. Nayer, M. Langer, W. Gerok, and J. Hennig, *Gastroenterology,* **107**, 1475, 1994
109. L. J. Haseler, W. L. Sibbitt Jr., H. N. Mojtahedzadeh, S. Reddy, V. P. Agarwal, and D. M. McCarthy, *AJNR Am. J. Neuroradiol.*, **19**, 1681, 1998
110. S. Bluml, E. Zuckerman, J. Tan, and B. D. Ross, *J. Neurochem.*, **71,** 1564, 1998
111. H. Yamamoto, H. Konno, T. Yamamoto, K. Ito, M. Mizugaki, and Y. Iwasaki, *J. Neurochem.*, **49,** 603, 1987
112. T. Naegele, W. Grodd, R. Viebahn, U. Seeger, U. Klose, D. Seitz, S. Kaiser, I. Mader, J. Mayer, and W. Lauchart, *Radiology,* **216**, 683, 2000
113. R. Kreis, N. Farrow, and B. D. Ross, *Lancet,* **336**, 635, 1990
114. R. A. Moats, Y. H. Lien, D. Filippi, B. D. Ross BD, *Biochem. J.*, **295**, 15, 1993
115. J. Lavoie, J. F. Giguere, G. P. Layrargues, R. F. Butterworth, *J. Neurochem.*, **49**, 692, 1987

CHAPTER 3

The Optimized Detection of *Myo*-Inositol *In Vivo* Using PRESS and STEAM Sequences at 3.0 T

3.1 Introduction

Myo-Inositol (mI) is a cerebral metabolite, which is involved in osmoregulation, nutrition, and detoxification of brain cells (1). The concentration of mI is known to vary with the progression of various diseases and disorders such as Alzheimer's disease (2-5), diabetes mellitus (6), hepatic encephalopathy (7-10), depression (11) and bipolar (manic-depressive) disorder (1, 12-15). A precise and non-invasive quantification of the metabolite *in vivo* using magnetic resonance spectroscopy (MRS) will therefore, not only help diagnose and monitor patients with such diseases and disorders, but will also facilitate the research on the related pathogenesis.

PRESS (Point REsolved SpectroScopy) (16, 17) and STEAM (STimulated Echo Acquisition Mode) (18) are the two most commonly used spatial localization methods for single voxel ^{1}H-MRS. Of these methods STEAM has been more popular for mI quantification (3, 5-7, 19-22) due both to the attainability of shorter echo times (TEs) and its superior water suppression performance. Water suppression is a significant concern given the spectral proximity of the water and mI resonances. The typical TEs used in the literature are 30 ms at 1.5 T (3, 5-7, 22) and 20 ms at 2.0 T (19-21), all of which fall into a shorter TE regime. However, while shorter TEs do tend to increase the yield of mI, they can permit severe background contamination of the target spectral region, first, from broad macromolecular resonances (22-25) and secondly from neighboring metabolite peaks, such as glutamate, glutamine (Glu, Gln, respectively, or Glx jointly), taurine (Tau), and glycine (Gly), which are relatively well-defined contaminators compared with macromolecules.

While the overlap of the mI signal with the Gly singlet (26) cannot be avoided with conventional unedited pulse sequences such as PRESS and STEAM, the spectral clarity of mI can, nevertheless, be greatly improved by establishing optimum *longer* sequence timings that mitigate all background contamination, but at a price of some trade-off in signal to noise ratio. Optimization of the timing requires a calculation of the evolution of the spin dynamics, not only of mI, but also of all its contaminants. In the case of weakly-coupled or even strongly-coupled spin systems with a very restricted number of spins, that optimization may be attempted using evolution equations derived through product operator analyses (27, 28). However, the complexity of the spin systems of mI (a strongly-coupled AM_2N_2P 6-spin system at 3.0 T (29)) and its Glx contaminants makes this analytical approach quite impractical. Instead, by means of numerical solutions of the equation of motion of the density matrix (30-32) the prediction of the optimum-clarity sequence timings can be made.

Optimizing spectral clarity is not trivial when both the target metabolite and the background contaminants arise from coupled spins. Lineshapes as well as intensities can change in an irregular fashion with sequence timing, and these changes have different timing characteristics for different metabolites. However, what at first sight might seem a hopeless complication, does in fact provide an opportunity to suppress the signal of one metabolite relative to another, if only we can find the right sequence design. Although we do not claim to eliminate the background, this process makes the application of post-processing spectral filtering routines far more robust and much more accurate, than when applied to substantially contaminated spectra.

In this report we evaluate optimum-clarity sequence timings for the quantification of mI in-vivo, using either PRESS or STEAM at 3.0 T. The optimization criteria are the effective suppression of signal from the A multiplets of Glx at ~ 3.8 ppm and from Tau at ~ 3.4 ppm, together with the retention of signal from mI at ~ 3.6 ppm. The optimal sequence timings should also be long enough to permit the transverse decay of macromolecular signal to be largely completed. The optimum-clarity spectra from PRESS and STEAM experiments were tested both in phantoms and *in vivo* at 3.0 T.

3.2 Methods

3.2.1 Spectral Characterization of mI and Its Neighboring Metabolites

The chemical shifts (δ) and scalar-coupling constants (J) of the protons in the mI spin system, together with the estimates of the degree of the coupling at 3.0 T, are as follows (29): H(1){M_1}, H(3){M_2} = 3.54 ppm; H(2){A} = 4.06 ppm; H(4){N_1}, H(6){N_2} = 3.62 ppm; H(5){P} = 3.28 ppm; J(1,2), J(2,3) = 2.7 Hz; J(3,4) = 9.9 Hz; J(4,5), J(5,6) = 9.2 Hz; J(1,6) = 9.8 Hz; $[J/\delta]_{AM} \sim 0.04$, $[J/\delta]_{MN} \sim 0.97$ and $[J/\delta]_{NP} \sim 0.21$, where the protons are identified in Fig. 3-1.

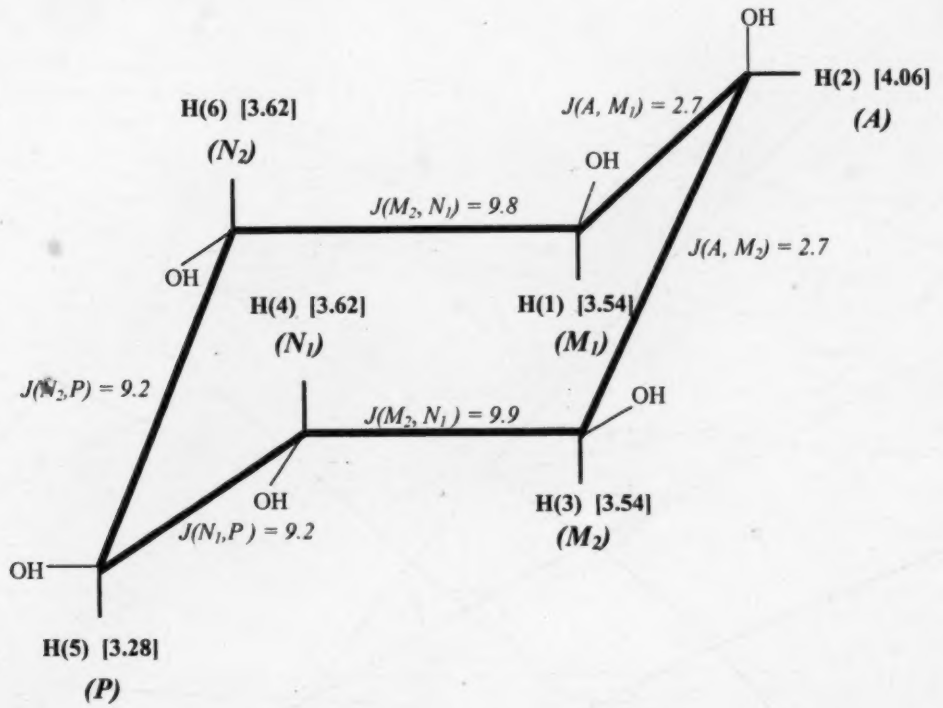

Figure 3-1 A diagram illustrating the mI molecule together with schematic of the proton numbers, the chemical shift values, δ ppm, and the coupling configuration, including individual interaction strengths, *J* Hz.

Due to the symmetry in the molecular structure (33, 34) only four different chemical shifts exist and it can therefore be classified as an AM_2N_2P spin system at 3.0 T. To

characterize the spectral discrimination problem when quantifying mI at 3.0 T, Fig. 3-2 illustrates the calculated response to a 90°-pulse-acquire sequence of mI and its contaminating background metabolites.

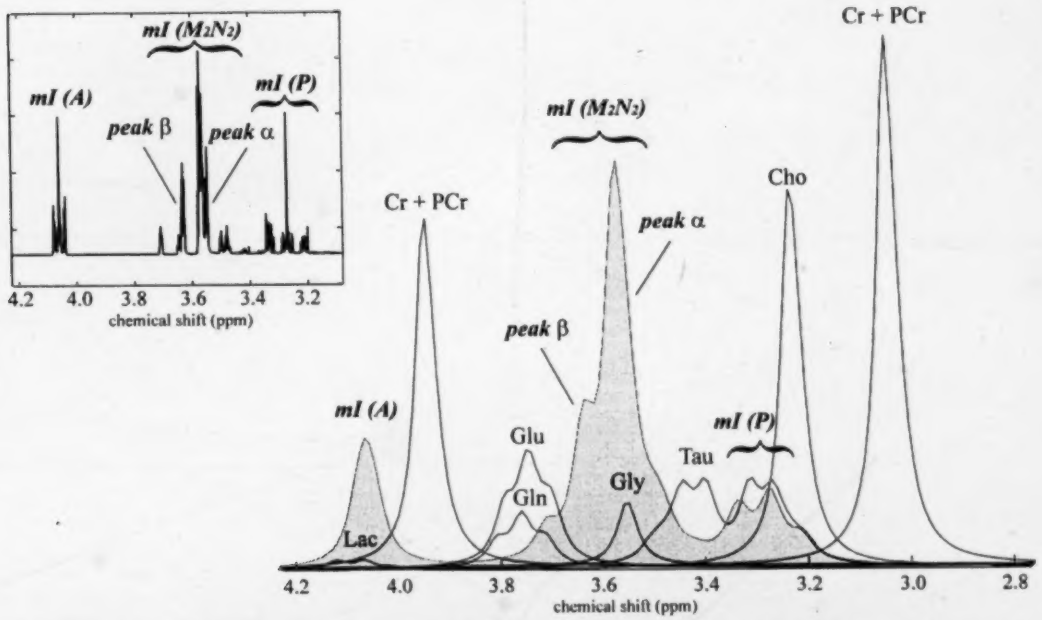

Figure 3-2 The calculated response of *myo*-Inositol and its neighboring metabolites to a pulse-acquire experiment at 3.0 T. Due to their negligible concentrations relative to mI, alanine, glucose, and syllo-Inositol are not shown. The linewidth in the spectra was artificially broadened to ~ 6 Hz to simulate the in-vivo environment. (Cho: choline, Cr + PCr: creatine + phosphocreatine, Glu: glutamate, Gln: glutamine, Gly: glycine, Lac: lactate, mI: *myo*-Inositol, Tau: taurine). A highly resolved (0.1 Hz) *myo*-Inositol spectrum is also shown in the separate panel.

It must be borne in mind, however, and will be demonstrated later, that in response to a single voxel localization sequence, the lineshapes of the coupled spin systems can be very variable. Under typical experimental conditions at 3.0 T only the α and β peaks in the central M_2N_2 multiplet of mI are usually used for mI quantification *in vivo*. The spectral characteristics of those background metabolites are summarized in Table 3-1 as well as that of mI. The weaker mI A multiplet at ~ 4.06 ppm overlaps lactate (~ 4.09 ppm) and creatine (~ 3.94 ppm), and is uncomfortably close to the strong water resonance (~ 4.7

ppm). The mI (P) multiplet (~ 3.28 ppm) overlaps with choline compounds (~ 3.22 ppm) and Tau (~ 3.35 ppm). That is not to say that the central M_2N_2 multiplet of mI is uncontaminated. Multiplets of Glx and Tau in addition to the Gly singlet, centered at ~ 3.76 ppm, ~ 3.35 ppm and at ~ 3.56 ppm, respectively, all contaminate the target mI multiplet.

Compound Name	Spin Group	Chemical Shift (ppm)	Scalar Coupling (Hz)
Cho	A_3	$\delta_A = 3.22$	N/A
Cr	A_2, A_3	$\delta_{A2} = 3.94$, $\delta_{A3} = 3.02$	N/A
Glu	AMNPQ	$\delta_A = \mathbf{3.75}$, $\delta_M = 2.06$, $\delta_N = 2.14$, $\delta_P = 2.35$, $\delta_Q = 2.37$	$J_{AM} = 7.33$, $J_{AN} = 4.65$, $J_{MN} = -14.85$, $J_{MP} = 6.43$, $J_{NP} = 8.47$, $J_{MQ} = 8.39$, $J_{NQ} = 6.89$, $J_{PQ} = -15.89$
Gln	AMNPQ	$\delta_A = \mathbf{3.76}$, $\delta_M = 2.13$, $\delta_N = 2.15$, $\delta_P = 2.45$, $\delta_Q = 2.47$	$J_{AM} = 6.53$, $J_{AN} = 5.84$, $J_{MN} = -14.45$, $J_{MP} = 6.33$, $J_{NP} = 9.16$, $J_{MQ} = 9.25$, $J_{NQ} = 6.35$, $J_{PQ} = -15.55$
Gly	A_2	$\delta_A = \mathbf{3.56}$	N/A
Lac	AX_3	$\delta_A = 4.09$, $\delta_X = 1.31$	$J_{AX} = 6.93$
mI	$\boldsymbol{AM_2N_2P}$	$\boldsymbol{\delta_A = 4.06}$, $\boldsymbol{\delta_M = 3.54}$, $\boldsymbol{\delta_N = 3.62}$, $\boldsymbol{\delta_P = 3.28}$	$\boldsymbol{J_{AM} = 2.7}$, $\boldsymbol{J_{M1N2} = 9.8}$, $\boldsymbol{J_{M2N1} = 9.9}$, $\boldsymbol{J_{NP} = 9.2}$
Tau	A_2B_2	$\delta_A = \mathbf{3.44}$, $\delta_B = 3.27$	$J_{AB} = 6.7$

Table 3-1 The spectral characteristics of *myo*-Inositol and its background contaminants. Among those background metabolites, Glu, Gln, Gly, and Tau have resonances that overlap with the central target multiplet of mI at ~ 3.6 ppm.

Moreover, at shorter echo times a broad macromolecular band distorts the baseline over the entire region (23, 25, 35, 48). Although the characteristics (connectivities and J-coupling constants) of some of those background macromolecules are known to some

extent (23, 48), they cannot be precisely modeled. Finally, because of their very small spectral contributions, we have chosen to neglect the contamination from alanine (~ 3.78 ppm), glucose (between ~ 3.2 and ~ 3.9 ppm) and syllo-Inositol (~ 3.35 ppm).

3.2.2 Pulse Sequences

3.2.2.1 PRESS

A generic PRESS sequence (Fig. 3-3(a)) was used both for calculation and experiment, i.e., $\{90^{\circ}_{x} - (TE_1)/2 - 180^{\circ}_{y} - (TE_1)/2 - (TE_2)/2 - 180^{\circ}_{y} - (TE_2)/2 -$ acquisition$\}$ (16, 17), where the 90° excitation pulse was a sinc-Gaussian pulse with a length of 3.5 ms and a bandwidth of ~ 3000 Hz, and the 180° refocusing pulses were numerically optimized sinc pulses (by using the MATPULSE software (37) written in MATLAB™) with a length of 5.5 ms and a bandwidth of ~ 770 Hz. The numerical optimization of the r.f. pulses minimized the spatial extent of the tip-angle transition region (37). Water suppression was achieved by means of a spectrally selective hyperbolic-secant inversion recovery pulse designed to have minimal effects on the A multiplet of mI at ~ 4.06 ppm.

3.2.2.2 STEAM

A generic STEAM sequence (Fig. 3-3(b)) was also used for calculation and experiment, i.e., $\{90^{\circ}_{x} - (TE)/2 - 90^{\circ}_{x} - (TM) - 90^{\circ}_{x} - (TE)/2 -$ acquisition$\}$ (18), where numerically optimized sinc pulses with a length of 3.7 ms and a bandwidth ~ 2000 Hz was employed coherently for all three 90° r.f. pulses. Water suppression followed the same routine as that exercised for PRESS sequence.

To encourage the suppression of unwanted outer volume signals, the r.f pulses were phase-cycled in both PRESS (4-steps) and STEAM (8-steps) sequences as shown in Fig. 3-3.

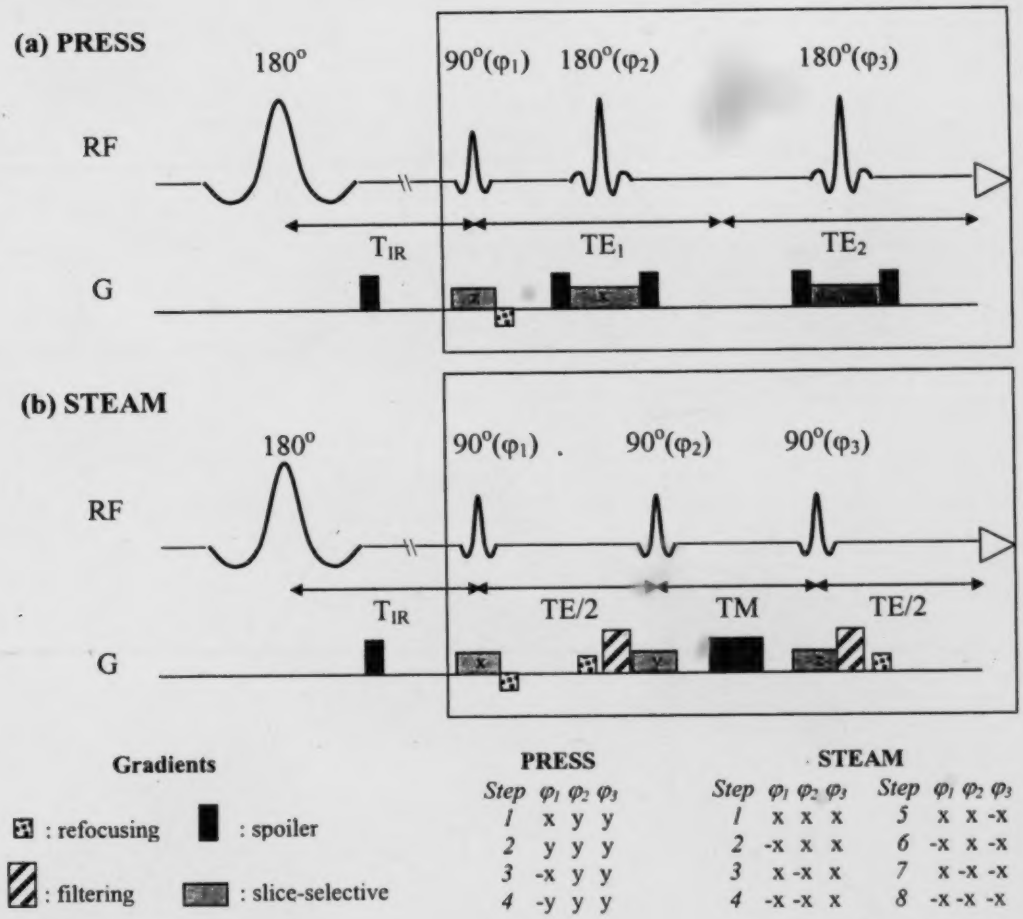

PRESS

Step	φ_1	φ_2	φ_3
1	x	y	y
2	y	y	y
3	-x	y	y
4	-y	y	y

STEAM

Step	φ_1	φ_2	φ_3	*Step*	φ_1	φ_2	φ_3
1	x	x	x	*5*	x	x	-x
2	-x	x	x	*6*	-x	x	-x
3	x	-x	x	*7*	x	-x	-x
4	-x	-x	x	*8*	-x	-x	-x

Figure 3-3 The simplified diagrams of (a) PRESS and (b) STEAM localization pulse sequences. For water suppression a hyperbolic-secant 180° pulse and an inversion-recovery delay (T_{IR}) precede the main sequences. To minimize unwanted signals the r.f. pulses were phase-cycled as summarized on the bottom for both sequences.

3.2.3 Sequence Optimization Using Numerical Methods

As described in Reference 30, numerical methods provide an efficient means of prospective sequence design. They are especially valuable for sequences that use spatially selective pulses and for metabolites that contain large or strongly-coupled spin systems that prove intractable with a conventional product operator approach. In particular, numerical methods enable the intra-pulse evolution of the spin systems to be

determined in response to the actual pulse envelopes and magnetic field gradients. A convenient way to display the variability of the predicted metabolite responses is a contour plot in which the variation of any signal parameter, e.g. the intensity of a targeted peak, is represented as a function of key sequence parameters, e.g., two of the sequence timings (TE_1 and TE_2 in PRESS or TE and TM in STEAM) (30). When a target peak intensity was the variable displayed in a contour plot, the value of that intensity, i.e. yield, was normalized to the value corresponding to the yield with no inter-pulse delays. The effects of transverse relaxation are not represented in this analysis and they will lead to additional modification of signal yield.

To determine the optimum sequence timing for discriminating a target peak from its contaminating background, i.e. maximizing the signal to background ratio, S/B, it is necessary to evaluate the intensity contour diagrams for all the metabolites contributing to the target spectral region. Therefore, the contour plots of the central target multiplet of mI centered at ~ 3.6 ppm, the A multiplets of Glx and the A_2B_2 multiplet of Tau were all obtained for both PRESS and STEAM. For the PRESS simulations the $\{TE_1, TE_2\}$-space ranges from 0 ms to 200 ms with the step size of 4 ms, and for STEAM the TE values range from 0 ms to 200 ms and the TM values range from 0 ms to 100 ms with step sizes of 4 ms and 2 ms, respectively. In our preliminary studies, we found that the responses of the α peak and the β peak of mI were significantly different from each other in the short TE range of both PRESS and STEAM. To examine that observation further the contour plots of the response of the individual peaks of mI to each of the sequences were also separately obtained (not shown).

Contamination from macromolecular signal can be dealt with on an ad-hoc basis (35) and relaxation losses are assumed to be not too different for the target and all contaminating resonances.

3.2.4 Experimental Methods

A total of six spherical phantoms (~ 6-cm in diameter) were made using distilled water. For all phantoms pH was adjusted to 7.1 ± 0.1 using hydrochloride and sodium hydroxide. Phantoms #1 through #4 contained mI, Glu, Gln and Tau, individually in aqueous solution, each at a concentration of 50 mM. In these phantoms 10 mM of Cr was also included as a reference for the behavior of an uncoupled spin system. Phantom #5 contained mI (at 50 mM) and Glu, Gln, Tau, Cr at the appropriate concentration to produce an aqueous mixture at the relative physiological ratios of normal human brain {1 : 1.3 : 0.6 : 0.5 : 1.1} (26, 35, 38). In phantom #6, Gly was added to the same mixture as phantom #5, in the relative concentration ratio mI : Gly = 5 : 1. All chemicals (purity ≥ 98%) were purchased from Sigma Chemical Co. (St. Louis, USA) except for Cr (ICN Biomedicals Inc, Aurora, USA).

For the PRESS experiments, a single 2 × 2 × 3 cm^3 voxel was employed both for phantom and *in vivo* experiments, using a total of 8 and 128 averages, respectively. For the STEAM experiments, the voxel dimensions were 2.5 × 2.5 × 2.5 cm^3 and the phantom and in vivo averaging was 16 and 256 respectively. For all acquisitions the bandwidth was 2.5 kHz with the collection of 2048 data points and the repetition time (TR) was 3 s. A linewidth broadening function of ~ 6 Hz was applied to all phantom spectra in order to simulate the in-vivo environment. All experiments were carried out at 3.0 T in an 80-cm bore magnet (Magnex Scientific PLC, Abingdon, UK) using a home-built 28-cm diameter quadrature birdcage coil for both transmission and reception, and spectrometer control was provided by a SMIS (Surrey Medical Imaging System) console.

3.3 Results

3.3.1 STEAM

A contour plot of the peak amplitude of the combined response of the α and β peaks of mI to the STEAM sequence is shown in Fig. 3-4. Although the initial decay is

rapid as TE increases to ~ 80 ms, it is not monotonic and increases to about half of the maximum signal at ~ 200 ms. In contrast, the variation of the mI signal is not sensitive to the choice of TM when TE ≤ 60 ms.

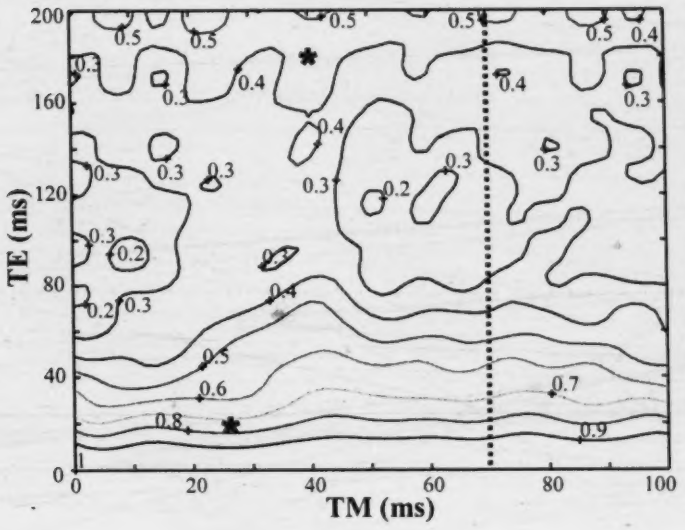

Figure 3-4 The contour plots in {TE, TM} space of the response of the peak height of mI to STEAM. All indices were normalized to the maximum peak height, which occurs at both TE and TM equal to zero. No relaxation loss was assumed in the calculation. A step size of 4 ms and 2 ms was used for TE and TM, respectively.

To validate the calculations, the spectral variations along a one-dimensional cut through the contour plot of Fig. 3-4 at TM = 70 ms were compared with experimental data from phantom #1. The result, shown in Fig. 3-5, demonstrates spectral agreement between the calculated and the phantom response at five different TEs. In the phantom spectra, Cr was used as a reference.

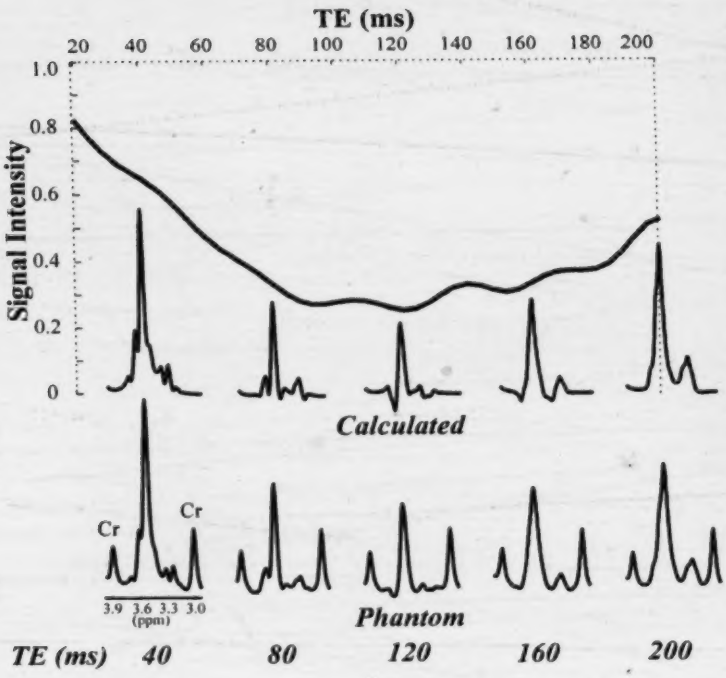

Figure 3-5 The calculated and phantom response of the target multiplet of *myo*-Inositol to STEAM at five different TEs with TM fixed at 70 ms. In phantom spectra, the two creatine singlets are also observed. The signal intensity was normalized to the maximum value, which occurs at both TE and TM equal to zero. All spectra were artificially broadened to ~ 6 Hz. No relaxation loss was assumed in the calculation.

Similar contour plots, for the background contaminants Tau (Fig. 3-6(a)), Glu (Fig. 3-6(b)) and Gln (Fig. 3-6(c)) suggest that an optimum sequence for mI quantification using STEAM might be {TE = 180 ms, TM = 40 ms}. With this design a significant reduction in the Glx (~ 30 %) and Tau (~ 33 %) signals brought them to 20 % and 23 % respectively of the not-so-reduced mI target peak. This sequence timing was also favored because it engineers a marked reduction in the background signal from macromolecules due to transverse-relaxation. For comparison a short TE/TM STEAM design denoted by '*' in each contour plot of Figs. 3-6(a) through (c) i.e., {TE = 20 ms, TM = 25 ms}, was also tested.

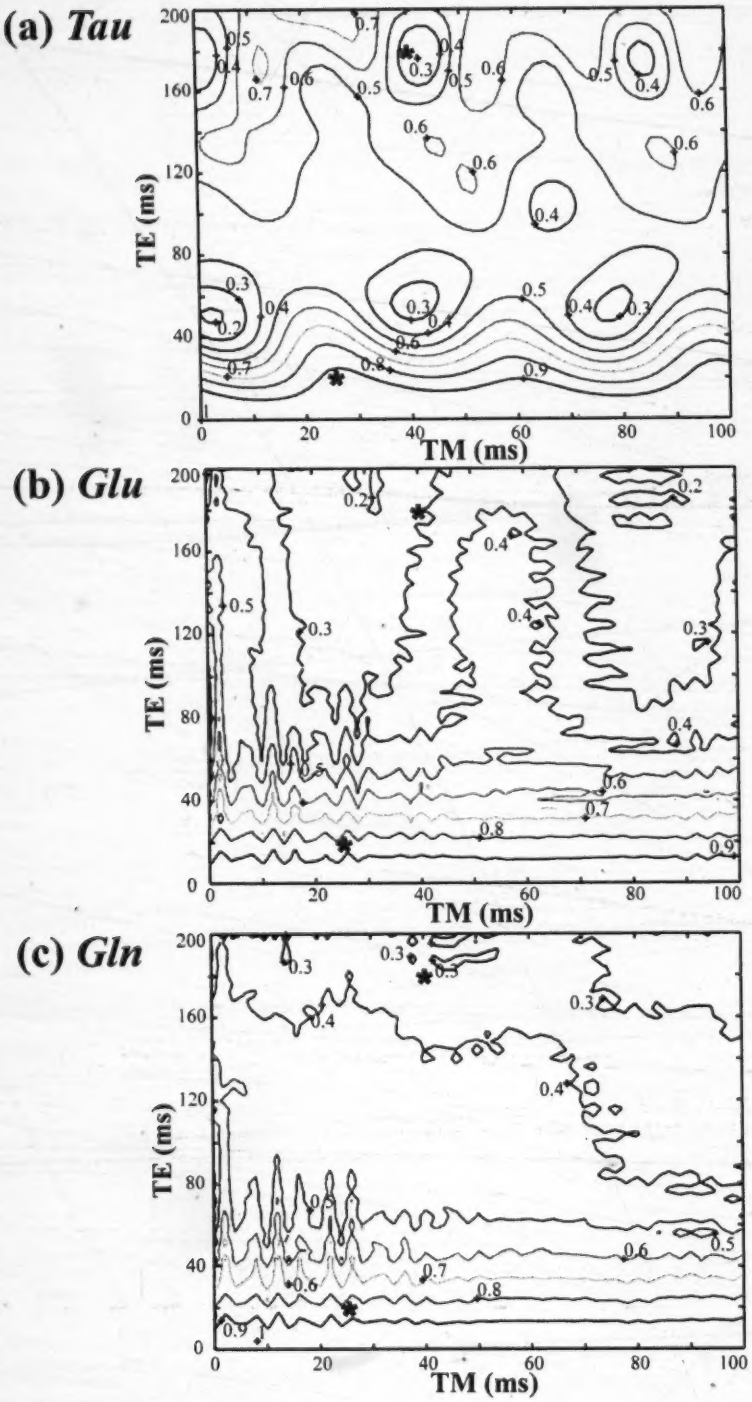

Figure 3-6 The contour plots in {TE, TM} space of the response of the peak height of (a) Tau, (b) Glu and (c) Gln to STEAM. All indices were normalized to the maximum peak height, which occurs at both TE and TM equal to zero. No relaxation loss was assumed in the calculation. A step size of 4 ms and 2 ms was used for TE and TM, respectively.

Experimental (in-vivo and phantom) and calculated spectra arising from each of the two sequence designs marked on the contour figures 3-4 and 3-6 (a) through (c) are

compared in Fig. 3-7. The spectra of Glu, Gln and Tau were scaled according to their relative *in vivo* concentration ratio with respect to that of mI using the amplitude of Cr singlet at ~ 3.9 ppm as the calibration standard. In Fig. 3-7(b) acquired with the shorter timing design, the relative amplitude of peak α of mI is observed to be more than twice that of the amplitude of peak β. As the sequence timings change, the relative behaviour of the α and β peaks evolves. These two peaks tend to coalesce at the optimized sequence timings due to the J-modulation effect and form a single band (peak α+β) with the *in vivo* linewidth shown in Fig. 3-7(i). Clearly then by measuring the 3.6 band peak height one is measuring different quantities at different echo times. This makes inter-laboratory comparisons vulnerable to misinterpretation if their timing design is much different from each other. At 1.5 T, no publications to our knowledge have reported the resolution of the α and β peaks and hence at that field strength any variation in the proportion of the total mI intensity contributing to the band peak at ~ 3.6 ppm, is transparent to the researchers.

The background signals from Glu, Gln and Tau are all suppressed more than mI by going to the optimized sequence timings. Theoretically the signal yields under the optimal conditions (at TE = 180 ms and TM = 40 ms) are ~ 55%, ~ 40%, ~ 45%, ~ 35% of their short echo values for mI, Glu, Gln and Tau, respectively. Phantom results are in close agreement. Note that the effect of transverse relaxation is not significant *in vitro* due to the relatively long transverse relaxation times of them (apparent T_2 estimated to be ~ 1000 ms).

In-vivo, spectral resolution enhancement provided by the optimized STEAM experiment is even more striking due to the elimination of macromolecular resonances by transverse relaxation. It should nevertheless be noted, in the calculations and phantom verifications the impact of transverse relaxation is either neglected or negligible, respectively. Without accurate T_2 measurements on all the metabolites the quantitative effect of transverse relaxation on our in-vivo spectra is not known.

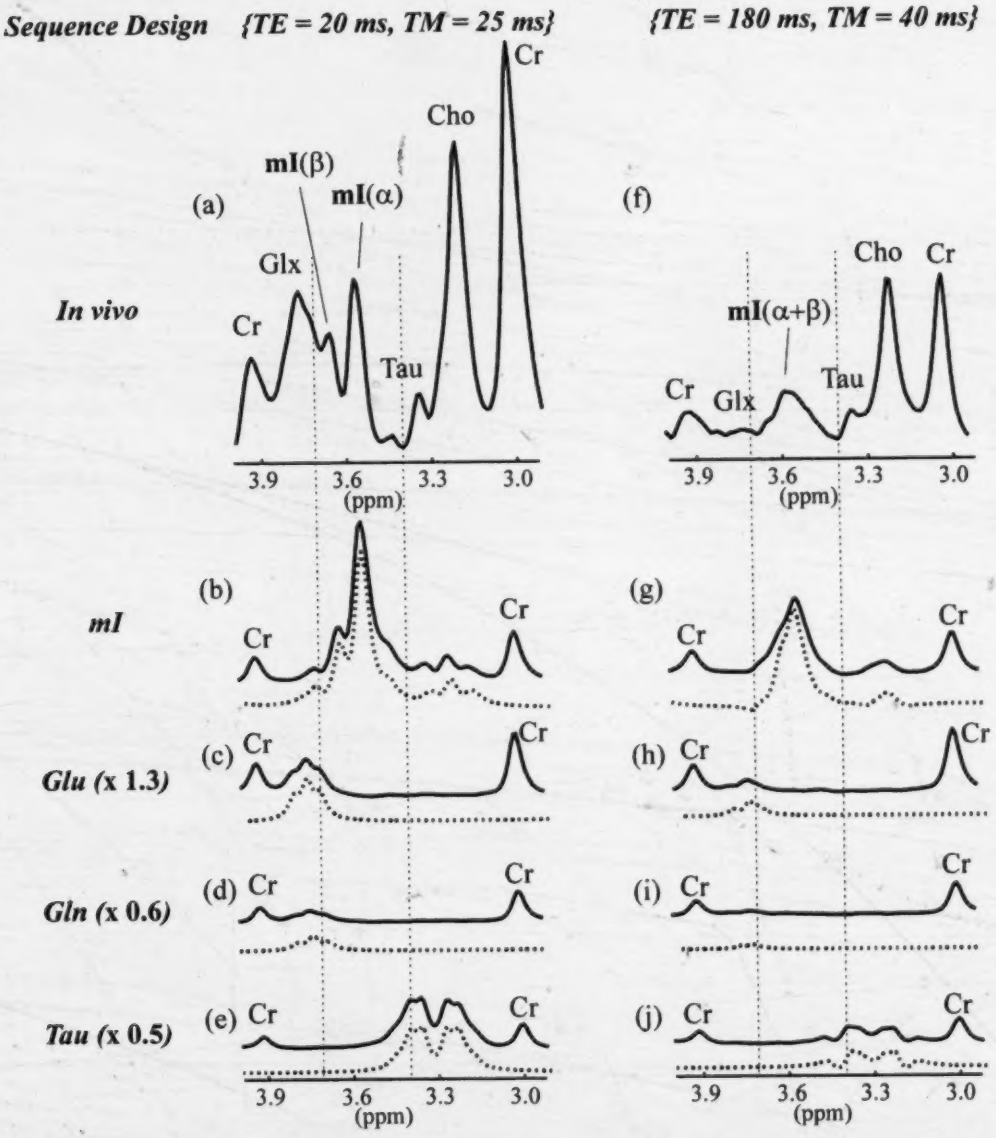

Figure 3-7 The in-vivo and phantom response of *myo*-Inositol and its neighboring metabolites to STEAM at 3.0 T. The phantom spectra of (b) mI, (c) Glu, (d) Gln and (e) Tau as well as (a) their in-vivo spectrum taken at {TE = 20 ms, TM = 25 ms} are compared to those ((f) thorugh (j)) acquired by using the suggested optimum sequence timings of {TE = 180 ms, TM = 40 ms}. The spectra of Glx and Tau were all scaled with respect to mI according to their relative concentration ratio in normal human brain. The calculated spectra are also shown below phantom spectra as dotted lines. All phantom and calculated spectra were artificially broadened to ~ 6 Hz.

3.3.2 PRESS

Similar contour plots, but in $\{TE_1, TE_2\}$ space, of the signal intensity response to PRESS of the multiplets of (a) mI, (b) Tau, (c) Glu and (d) Gln are shown in Fig. 3-8.

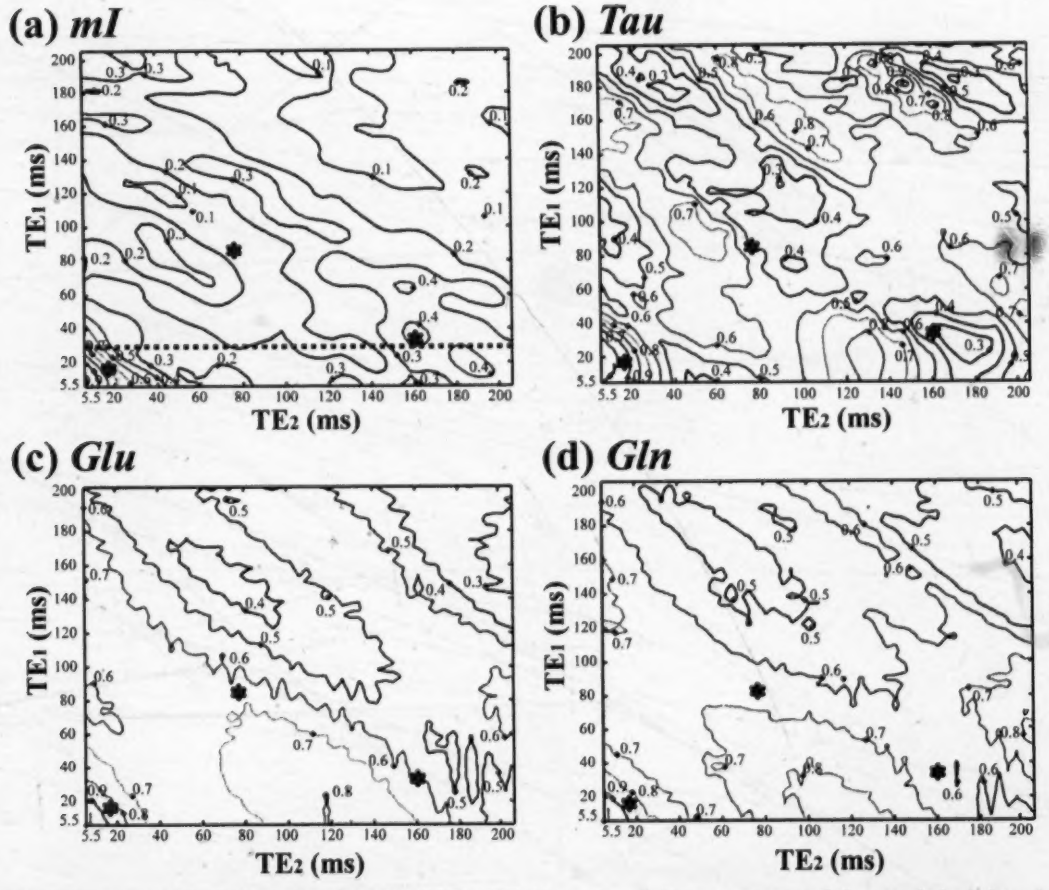

Figure 3-8 The contour plots in $\{TE_1, TE_2\}$ space of the response of the peak height of (a) mI, (b) Tau, (c) Glu and (d) Gln to PRESS. All indices were normalized to the maximum peak height, which occurs at both TEs equal to 5.5 ms (the duration of the 180° pulse). No relaxation loss was assumed in the calculation. A step size of 4 ms was used for both TEs.

The reduction in mI intensity is even more rapid for PRESS than was observed by increasing the echo time in the STEAM sequence (c.f. Figs. 3-4 and 3-8(a)).

Again a cut through the mI contour plot of Fig. 3-8(a) at TE_1 = 30 ms was explored to demonstrate agreement between calculation and phantom measurement for the strongly-coupled mI AM_2N_2P spin system, and the results are shown in Fig. 3-9. The marked recovery of the ~ 3.6 ppm band at long echo times is to be noted.

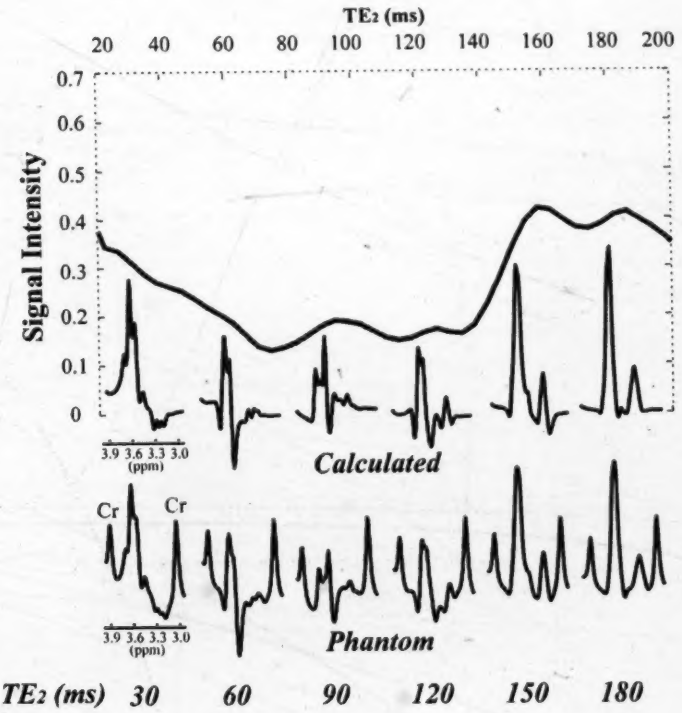

Figure 3-9 The calculated and phantom response of the target multiplet of *myo*-Inositol in response to PRESS at six different TE_2's with TE_1 fixed at 30 ms. In phantom spectra, the two creatine singlets are also observed. The signal intensity was normalized to the maximum value, which occurs at both TE_1 and TE_2 equal to 5.5 ms. All spectra were artificially broadened to ~ 6 Hz. No relaxation loss was assumed in the calculation.

To evaluate spectral discrimination, we calculated the response of mI and its contaminating background metabolites at three pairs of {TE_1, TE_2} times, the objective being to compare short TEs {TE_1 = 18 ms, TE_2 = 16 ms}, with both desirable {TE_1 = 36 ms, TE_2 = 160 ms} and undesirable {TE_1 = 83 ms, TE_2 = 76 ms} long TEs. The short values of TE_1 and TE_2 were chosen to be typical of in-vivo literature and were comparable to those used for the STEAM demonstration. The location in {TE_1, TE_2} space regarded as optimal, gave rise to 45 % reduction of mI, but to a suppression of Glx and Tau by only 30 % and 70 % respectively. This is not as promising as the STEAM optimum. Nevertheless, the total TE of 196 ms ensures a substantial reduction of

macromolecule resonances and much greater clarity around ~ 3.6 ppm. The third location in $\{TE_1, TE_2\}$ space, namely, {83 ms, 76 ms}, was chosen to demonstrate the possibility of loosing the mI signal completely by an inappropriate choice of echo times. This emphasizes the importance of prospective sequence design.

A breakdown of the overall spectral response to PRESS in the 3.6 ppm region is illustrated in Fig. 3-10, in a manner that corresponds to the treatment of STEAM. Again the α and β mI peaks are resolved at 3.0 T using the shortest echo times (see Fig. 3-10(b)) but coalesce to form a single peak at the optimal timing (Fig. 3-10(g)). The contamination of the macromolecular band is also clearly apparent in the *in vivo* spectra taken with the short PRESS sequence (as it was for STEAM). The elevation of the Glx-mI(β) region demands a precise knowledge of the macromolecular lineshape if contamination of the mI target signal is to be offset by post-processing, e.g., LC modeling (35). With the optimized PRESS (Fig. 3-10(f)), however, the *in vivo* lineshape and the signal amplitude of mI relative to that of Glx and Tau are in good agreement with those in phantom, which indicates a negligible amount of the macromolecular contamination, as well as minimized metabolite contaminants. This means that post-processing only needs to use the well defined metabolite lineshapes from the density matrix analysis and is likely to be more robust and accurate.

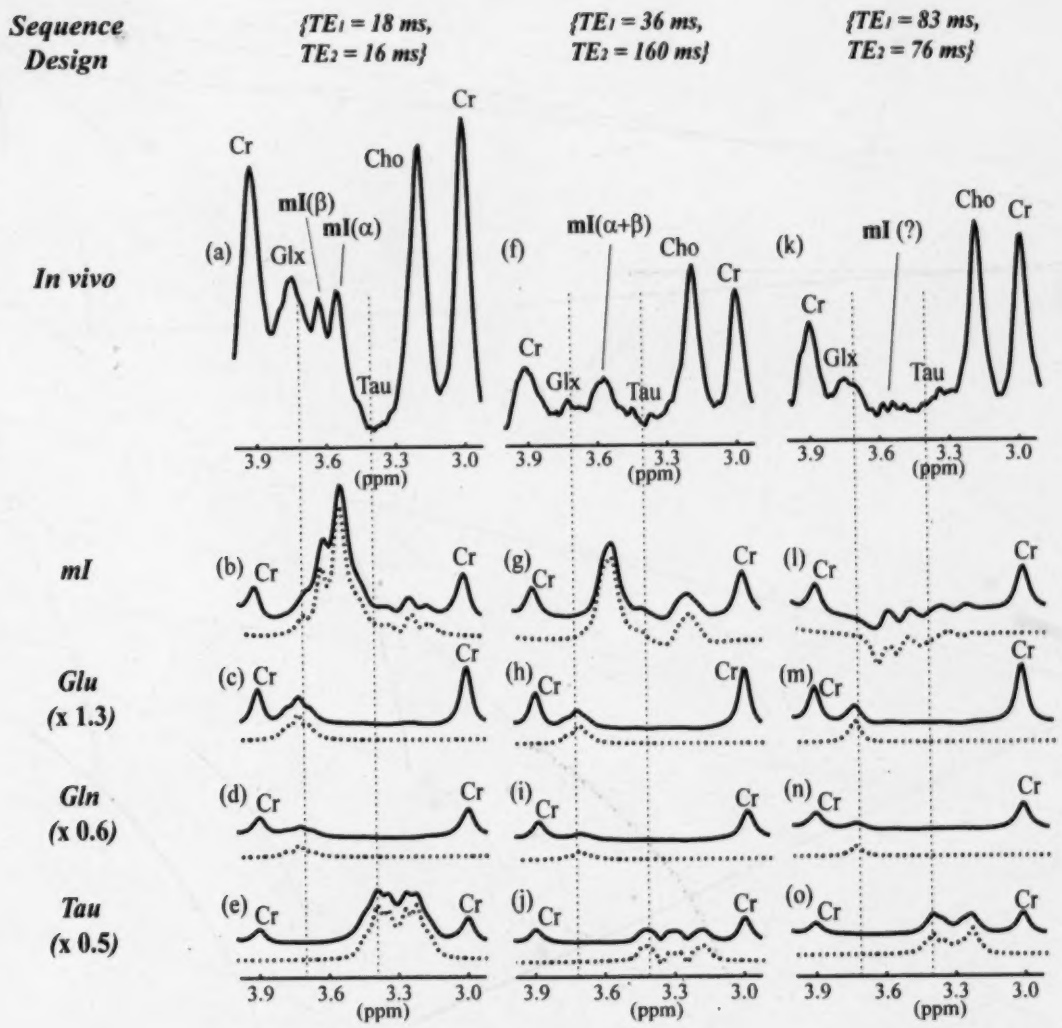

Figure 3-10 The in-vivo and phantom response of *myo*-Inositol and its background metabolites to PRESS at 3.0 T. The phantom spectra of (b) mI, (c) Glu, (d) Gln and (e) Tau as well as (a) their in-vivo spectrum taken at {TE_1 = 18 ms, TE_2 = 16 ms} are compared to those ((f) thorugh (j)) acquired by using the suggested optimum sequence timings of {TE_1 = 36 ms, TE_2 = 160 ms}, and to those ((k) thorugh (o)) taken at the mI-nulling timings of {TE_1 = 83 ms, TE_2 = 76 ms}. The phantom spectra of Glu, Gln and Tau were all scaled with respect to mI according to their relative concentration ratio in normal human brain. The calculated spectra are also shown below each phantom spectrum as dotted lines. All spectra were artificially broadened to ~ 6 Hz.

3.4 Discussion

3.4.1 Sources of Variability

According to the contour plots in the previous sections, the mI target signal drops very rapidly as TE increases in both PRESS and STEAM. In particular with PRESS, it reduces to ~ 20 % of its maximum at the total TE of ~ 60 ms. In this section a mechanism is examined for the fast signal decay of the target multiplet of mI in response to short-TE PRESS, using the numerical method (30). First, a brief discussion is given on the sources of variability in the response of mI to STEAM.

3.4.1.1 STEAM

The rapid decay in signal during the two TE phases of the STEAM sequence results from the rapid evolution (which is typical of multispin strongly-coupled systems) of the in-phase and anti-phase SQC. Not only does this evolution cause oscillation between in-phase and anti-phase terms of the same spin (as occurs with weakly-coupled spins) but it gives rise to the transfer of polarization to other members of the coupled spin system, which can then also evolve. The resultant proliferation of coherences steals intensity from the M derived α resonance at a rate that is faster than one would expect for simple in-phase to anti-phase evolution alone.

3.4.1.2 PRESS

In order to examine the fast decay of the mI signal in the short TE range in response to PRESS, two sequence timing pairs, $\{TE_1 = 20$ ms, $TE_2 = 25$ ms$\}$ and $\{TE_1 = 25$ ms, $TE_2 = 30$ ms$\}$, were chosen. Over 10 ms difference between these two sequences, more than 30 % of the mI signal is lost as predicted in the contour plot shown in Fig. 3-8(a). The phantom and calculated spectra are shown in Fig. 3-11, which clearly demonstrates that the decay of α peak alone accounts for the rapid loss of a broadened target multiplet of mI. The β peak remains robust over that 10 ms interval.

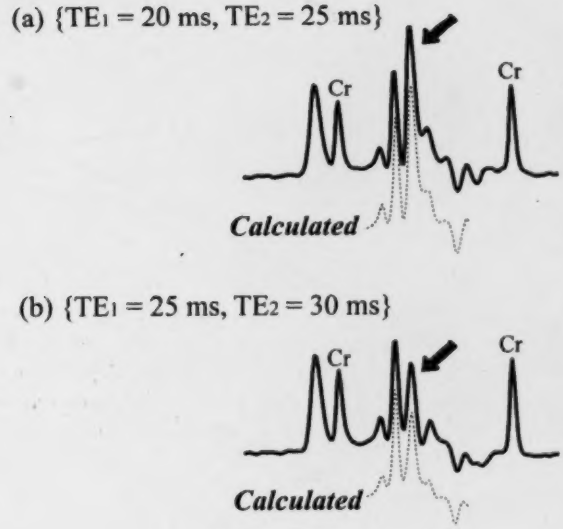

Figure 3-11 The illustration of the rapid decay of the signal amplitude of mI in response to short-TE PRESS. Over the 10 ms interval between the two sequence timings of (a) {TE_1 = 20 ms, TE_2 = 25 ms} and (b) {TE_1 = 25 ms, TE_2 = 30 ms}, the signal of the target multiple of mI is reduced by ~ 30 % , which is attributed mainly to the decay of the amplitude of peak α. The calculated spectra are also shown below the experimental ones as dotted lines. For better separation of the α and β peaks from each other, the linewidth of those spectra was adjusted to ~ 4 Hz.

To identify the coherences that are responsible for the rapid decay of the α peak, snapshots of the distribution of coherences at the onset of data acquisition were obtained at each of those two sequence timing pairs under comparison, and the results are shown in Fig. 3-12. Among the 384 single quantum coherence (SQC) terms available for the 6-spin system of mI, only the 128 SQC terms from M_1 and M_2 are primary contributors to the α resonance. The temporal evolutions of the M_1 and M_2 spins are identical due to the symmetry of the mI molecule. Of the 64 SQCs corresponding to each of these spins, only six terms are critical to the α peak decay. For the M_1 spin they are $2M_{1x}A_z$, $2M_{1x}N_{2z}$, $2M_{1x}P_z$, M_{1y}, $2M_{1y}N_{2z}$ and $2M_{1y}P_z$, and they are labeled in the coherence amplitude snapshot shown in Fig. 3-12. Each of the SQC terms has a unique lineshape, and all of the SQC term lineshapes available for the mI spin system, form a lineshape basis set. A linear combination of the components of that basis set with time-dependent weighting coefficients, e.g., the amplitudes of the M_1 SQC terms shown in Fig. 3-12 determines a final lineshape. The lineshape panels of Fig. 3-12 show the calculated weighted sum of the six M_1 SQC terms (solid line) as well as the full lineshape obtained with all of the 384 SQC terms (dotted line). The reduction of the α peak illustrated by the difference between the two panels during that 10 ms interval is well demonstrated with the six representative SQC terms only.

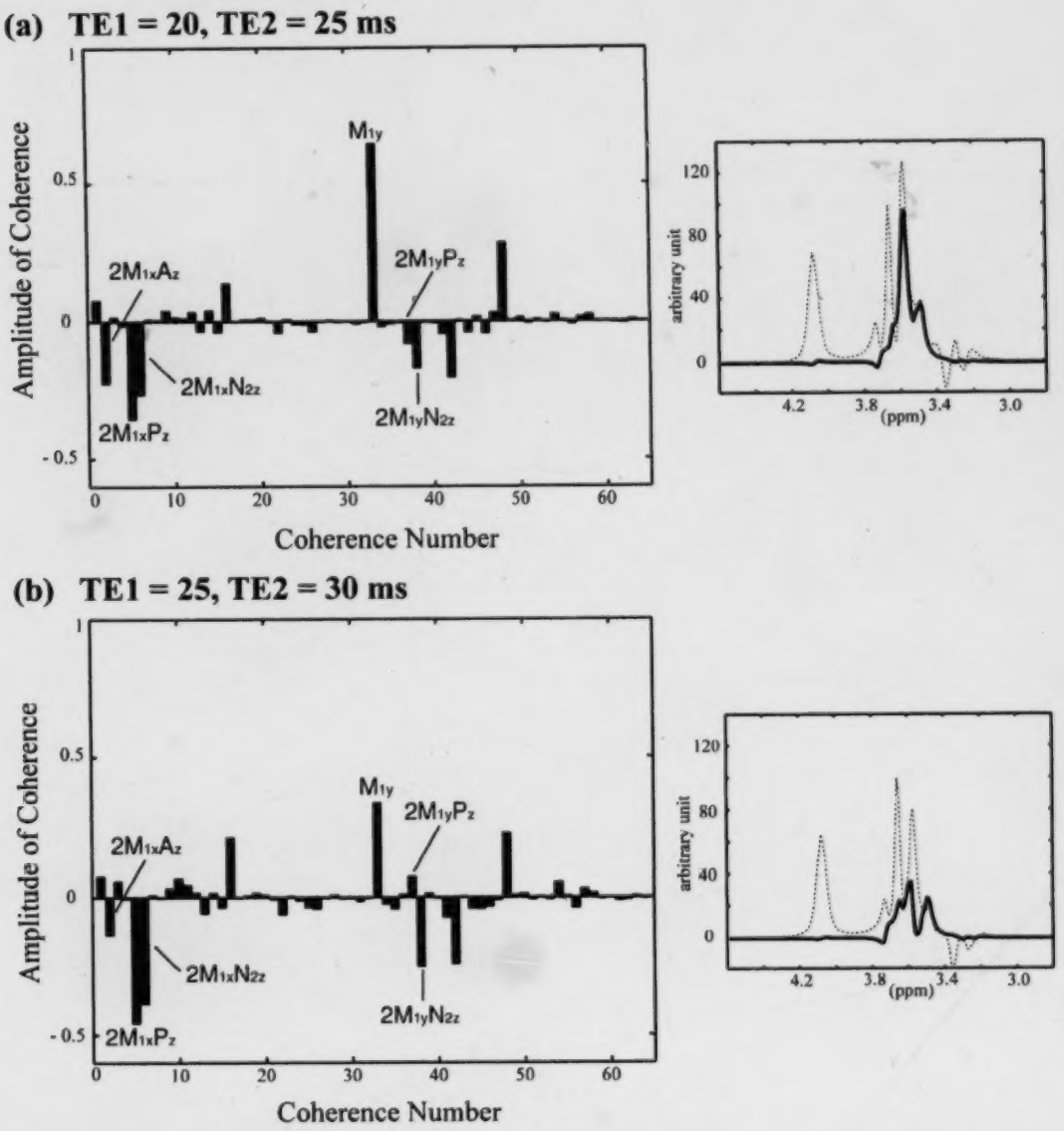

Figure 3-12 The snap shots of the distribution of single quantum coherence (SQC) terms of mI in response to PRESS at (a) {TE_1 = 20 ms, TE_2 = 25 ms} and (b) {TE_1 = 25 ms, TE_2 = 30 ms}. Among 384 SQCs available for the mI spin system, only those 64 terms of M_1-spin are shown, which make up major contribution to the α peak of mI. A total of six terms were indexed, which show relatively large change in amplitude, and are therefore mainly responsible for the drastic signal loss between the two sequence timings. The spectra at each sequence timing pair are shown in the right column, which were obtained from the weighted sum of the basis spectra of those six representative terms only (solid line). The full lineshape of mI including all coherence terms is also shown in each spectrum (discrete line).

3.5 Summary and Conclusion

The purpose of this study was to establish the best conditions for the *in vivo* quantification of mI using PRESS or STEAM at 3.0 T. It was motivated by the recognition that the short-TE-STEAM recipe, which has been the most popular choice by researchers for mI quantification, results in a significant contamination of the target mI signal not only by its neighboring metabolites, but also by a broad macromolecular resonance as well. Surprisingly, far less attention has been paid to the macromolecular contamination of mI signal, than to the similar contamination of γ-aminobutyric acid (GABA), which is a major inhibitory neurotransmitter in the central nervous system (39-41).

By incorporating a prospective numerical analysis of the response to the sequence into the optimization procedure, the establishment of optimum long sequence times was made possible. These sequence times are {TE_1 = 36 ms, TE_2 = 160 ms} for PRESS and {TE = 180 ms, TM = 40 ms} for STEAM at 3.0 T. With this sequence design the contribution of the macromolecular resonances to the mI baseline is negligible and the interference of Glx and Tau is significantly mitigated.

In comparing the two pulse sequences for mI quantification, the optimized STEAM may be a better choice. First, a higher mI signal is retained with that sequence relative to its background metabolites such as Glx, Tau and Gly. Secondly, STEAM's better performance in water suppression cannot be underestimated in view of the proximity of the target mI signal to water resonance. Thirdly, STEAM provides more flexibility in the choice of the optimum sequence timings. For instance, our preliminary phantom studies showed that a {TE = 160 ms, TM = 40 ms} pair can be a good alternative to the one proposed as an optimum in this study. Although PRESS gives a better S/N and subsequently requires a shorter scan time, the ratio of the S/N of PRESS to that of STEAM is less than 2 due to the imperfect, nominal 180° refocusing pulses of PRESS (37, 42, 43). One beneficial aspect of PRESS in mI quantification at 3.0 T may be a potential use of the mI-nulling sequence timing pair to clarify the reported sensitivity

of Gly to lithium (44). In combination with the optimum sequence timing pair, this use may prove helpful in testing the mI-depletion hypothesis (15).

Finally, since the degree of coupling between the coupled spins not only in the spin system of mI but also in its contaminating background metabolites is dependent on the field strength, their evolution in response to PRESS and STEAM will differ at different field strengths. Therefore, the optimum sequence timings proposed herein are optimum only at 3.0 T.

3.6 References

1. M. J. Berridge and R. F. Irvine, *Nature*, **341**, 197, 1989
2. R. A. Moats, T. Ernst, T. K. Shonk, and B. D. Ross, *Magn. Reson. Med.*, **32**, 110, 1994
3. B. L. Miller, R. A. Moats, T. K. Shonk, T. Ernst, S. Woolley, and B. D. Ross, *Radiology*, **187**, 433, 1993
4. B. D. Ross, S. Bluml, R. Cowan, E. Danielsen, N. Farrow and R. Gruetter, *Biophys. Chem.*, **68**, 161, 1997
5. T. Shonk and B. D. Ross, *Magn. Reson. Med.*, **33**, 858, 1995
6. R. Kreis and B. D. Ross, *Radiology*, **184**, 123, 1992
7. R. Kreis, B. D. Ross, N. A. Farrow and Z. Ackerman, *Radiology*, **182**, 19, 1992
8. T. Naegele, W. Grodd, R. Viebahn, U. Seeger, U. Klose, D. Seitz, S. Kaiser, I. Mader, J. Mayer, W. Lauchart, M. Gregor and K. Voigt, *Radiology*, **216**, 683, 2000
9. B. D. Ross, S. Jacobson, F. Villamil, J. Korula, R. Kreis, T. Ernst, T. Shonk and R. A. Moats, *Radiology*, **193**, 457, 1994
10. R. A. Moat, Y. H. Lien, D. Filippi and B. D. Ross, *Biochem. J.*, **295**, 15, 1993
11. R. Frey, D. Metzler, P. Fisher, A. Heiden, J. Scharfetter, E. Moser and S. Kasper, *J. Psyc. Res.*, **32**, 411, 1998
12. H. Shimon, G. Agam, R. H. Belmaker, T. M. Hyde and J. E. Kleinman, *Am. J. Psyc.*, **154**, 1148, 1997
13. G. J. Moore, J. M. Bebchuk, J. K. Parrish, M. W. Faulk, C. L. Arfken, J. Strahl-Bevacqua and H. K. Manji, *Am. J. Psyc.*, **156**, 1902, 1999
14. R. H. Lenox and D. G. Watson, *Clin. Chem.*, **40**, 309, 1994
15. M. J. Berridge, C. P. Downes, and M. R. Hanley, *Biochem. J.*, **206**, 587, 1982
16. P. A. Bottomley, *US Patent*, **4(480)**, 228, 1984
17. R. J. Ordidge, M. R. Bendall, R. E. Gordon, and A. Connelly, *Magnetic resonance in biology and medicine*, McGraw-Hill, 1985, p. 387
18. J. Frahm, K. D. Merboldt, and W. Hanicke, *J. Magn. Reson.*, **72**, 502, 1987
19. H. Bruhn, G. Stoppe, J. Staedt, K. D. Merboldt, and J. Frahm, *Proc. ISMRM*, New York, 1993, p. 1543
20. C. G. Choi and J. Frahm, *Magn. Reson. Med.*, **41**, 204, 1999
21. T. Michaelis, K. D. Merboldt, H. Bruhn, and J. Frahm, *Radiology*, **187**, 219, 1993

22. R. Kreis, T. Ernst, and B. D. Ross, *Magn. Reson. Med.*, **30**, 424, 1993
23. K. L. Behar, D. L. Rothman, D. D. Spencer and O. A. C. Petroff, *Magn. Reson. Med.*, **32**, 294, 1994
24. U. Seeger, I. Mader, T. Nagele, W. Grodd, O. Lutz and U. Klose, *Magn. Reson. Med.*, **45**, 948, 2001
25. L. Hofmann, J. Slotboom, C. Boesch and R. Kreis, *Magn. Reson. Med.*, **46**, 855, 2001
26. B. D. Ross, *NMR in Biomed.*, **4**, 59, 1991
27. R. R. Ernst, G. Bodenhausen, and A. Wokaun, *Principles of Nuclear Magnetic Resonance in One and Two Dimensions*, Oxford Univ. Press, 1987
28. L. E. Kay and R. E. D. McClung, *J. Magn. Reson.*, **77**, 258, 1988
29. R. B. Thompson, *Ph.D Thesis*, University of Alberta, 1999
30. R. B. Thomson and P. S. Allen, *Magn. Reson. Med.*, **39**, 762, 1998
31. K. Young, V. Govindaraju, B. J. Soher, and A. A. Maudsley, *Magn. Reson. Med.*, **40**, 812, 1998
32. K. Young, B. J. Soher, and A. A. Maudsley, *Magn. Reson. Med.*, **40**, 816, 1998
33. J. C. Linden, D. J. Baker, R. D. Farrant, and J. M. Williams, *Biochem. J.*, **233**, 275, 1986
34. S. Cerdan, C. A. Hansen, R. Johanson, T. Inubushi, and J. R. Williamson, *J. Biol. Chem.*, **261**, 14676, 1986
35. S. W. Provencher, *Magn. Reson. Med.*, **30**, 672, 1993
36. K. L. Behar and T. Ogino, *Magn. Reson. Med.*, **30**, 38, 1993
37. G. B. Matson, *Magn. Reson. Imag.*, **12**, 1205, 1994
38. R. Kreis, T. Ernst and B. D. Ross, *J. Magn. Reson.*, **B102**, 9, 1993
39. D. L. Rothman, O. A. C. Petroff, K. L. Behar, and R. H. Mattson, *Proc. Natl. Acad. Sci. USA*, **90**, 5662, 1993
40. J. R. Keltner, L. L. Wald, J. D. Christensen, L. C. Maas, C. M. Moore, B. M. Cohen, and P. F. Renshaw, *Magn. Reson. Med.*, **36**, 458, 1996
41. H. P. Hetherington, B. R. Newcomer, and J. W. Pan, *Magn. Reson. Med.*, **39**, 6, 1998
42. D. A. Yablonskiy, J. J. Neil, M. E. Raichle, and J. J. Ackerman, *Magn. Reson. Med.*, **39**, 169, 1998
43. J. Slotboom, A. F. Mehlkopf, and W. M. M. J. Bovee, *J. Magn. Reson.*, **A108**, 38, 1994
44. S. I. Deutsch, M. Stanley, E. D. Peselow, and M. Banay-Schwartz, *Neuropsychobiology*, **9**, 215, 1983

CHAPTER 4

The Detection of *Myo*-Inositol *In vivo* Using Double Quantum Coherence Filtering at 3.0 T

4.1 Introduction

The cerebral level of *myo*-Inositol (mI) is known to vary with the progression of various diseases and disorders such as Alzheimer's disease (1-4), diabetes mellitus (5), Hepatic encephalopathy (6-9), depression (10) and bipolar (manic-depressive) disorder (11-14). Therefore the precise quantification of the metabolite *in vivo* using nuclear magnetic resonance (NMR) technique may help diagnose and monitor patients with such diseases and disorders.

PRESS and STEAM are the two most commonly used single voxel localization pulse sequences in in-vivo proton magnetic resonance spectroscopy (^{1}H-MRS). Of these two sequences STEAM has been more popular for the measurement of the metabolite as a result of the shorter echo times (TEs) attainable (2, 4, 5-8, 15-17). The use of short TEs, however, enhances not only the mI target multiplet at ~ 3.6 ppm, but it also enhances its background resonances such as the A multiplets of the AMNPQ spin systems of glutamate (Glu) and glutamine (Gln) (collectively referred to as Glx) at ~ 3.78 ppm, uncoupled glycine (Gly) at ~ 3.55 ppm and taurine (Tau) at ~ 3.45 ppm. An enhancement of other source of unwanted background signal such as macromolecules (18-20) is an additional disadvantage of using short sequence timings. Therefore, an enhanced signal yield resulting from shortening the sequence timings tends to be compensated with the poor integrity of a target peak.

It is possible to establish optimum *long* sequence timings for both PRESS and STEAM to minimize signal from those background contaminators, while retaining an

observable amount signal of mI (21). The suppression of macromolecule resonances is an additional benefit of using such long sequence timings as the T_2 of macromolecules is known to be significantly shorter than that of metabolites (18, 20). In the case of weakly-coupled spin systems or strongly-coupled ones with a restricted number of spins, the prediction of such optimum long pulse sequence timings may be achieved by referring to the product operator formalism (22), but as mI has a strongly-coupled 6-spin system such an manual analysis is impractical. By numerical solutions of density matrix (23), the establishment of such optimum long sequence timings can be achieved. Nonetheless, the problem of uncoupled Gly, which is the closest neighbor of the target peak of mI, cannot be resolved by optimization of conventional pulse sequences such as PRESS and STEAM. Although it is found at a very low concentration with respect to that of mI in the normal human brain (mI : Gly ~ 5 : 1 (24)), the removal of the Gly resonance in the target spectral region can significantly improve the measurement precision of mI *in vivo*.

A difference spectra method might be an option for suppressing uncoupled spin resonances from a spectrum (25, 26). Although this post-data-processing method can potentially retrieve a greater signal yield in the target peak, it has an intrinsic problem of sensitivity to the subject motion during acquisitions, which causes cancellation errors (27, 28). Moreover, the complicated mI spin system exhibits a rapid change in both the lineshape and the signal amplitude of the target multiplet in response to any NMR pulse sequences. This intractable evolution pattern of the spin system, which is facilitated by the strong-coupling Hamiltonian makes the use of such a post-data-processing technique not feasible.

A double quantum filter (DQF) (23, 27, 28, 30-37) has been useful for background suppression for the following reasons. First, combined (most commonly) with the PRESS sequence for the purpose of spatial localization, DQF becomes a single-shot method for data acquisition with less susceptibility to subject motion. Secondly, it provides a unique way of suppressing uncoupled metabolites by taking advantage of the fact that uncoupled spin systems cannot evolve into multiple quantum states. However, due to the intrinsic problem of poor signal yield with the technique, a variety of sequence

parameters needs to be precisely optimized (23), such as TEs, mixing time (TM), and the tip angle, the frequency offset and the duration of the third 90° pulse, which converts multiple quantum coherences (MQCs) during TM back into anti-phase coherences (APCs). Combined with the complexity of the mI spin system, therefore, the optimal design of a DQF for mI detection is not a trivial task. Based on the previous analytic solutions derived for the AB spin system of citrate in terms of product operators (38), Lei et al optimized a DQF for Tau (29), which has a strongly-coupled A_2B_2 spin system. However, to the best of our knowledge, such an analytic basis is not available for the complicated mI spin system.

In this report, we tackle the complexity of designing a DQF for the detection of mI *in vivo* by incorporating numerical methods (23) into the sequence optimization procedure. We believe it is the first application of a double quantum coherence (DQC) filter to the detection of mI. Of special importance in the optimization procedure are the effective removal of uncoupled Gly and other neighboring metabolites with coupled spins such as Glx and Tau, while retaining an observable amount of filtered mI signal. The efficacy of the filter is demonstrated both in phantom and *in vivo*.

4.2 Methods

4.2.1 Spectral Characteristics of mI and Its Background Metabolites

The mI molecule has a chair conformation with a symmetry about the axis that connects A spin (H(2)) and P spin (H(5)) (11, 39). The mI spin system can be termed as AM_2N_2P at 3 T, based on the ratio of the coupling constant to the difference in chemical shift in Hz (J/δ) between coupled spins, e.g., $[J/\Delta\delta]_{AM} \sim 0.04$ (weak-coupling), $[J/\Delta\delta]_{MN} \sim 0.97$ (strong-coupling) and $[J/\Delta\delta]_{NP} \sim 0.21$ (intermediate-coupling). Summarized in Table 4-1 are the chemical shifts and the coupling constants of the mI spin system (40).

Proton No.	H(2)	H(1),H(3)	H(4),H(6)	H(5)
Spin Species	A	$\mathbf{M_1,M_2}$	$\mathbf{N_1,N_2}$	P
Chemical Shift (ppm)	4.06	3.54	3.62	3.28
J-Coupling Constant (Hz)	$J_{M_1A} = J_{AM_2} = 2.7$ $J_{M_2N_1} = 9.9$ $J_{M_1N_2} = 9.8$ $J_{N_1P} = J_{PN_2} = 9.2$			

Table 4-1 The spectral characteristics of *myo*-Inositol spin system.

The resonances of mI are grouped into three multiplets. Among them, a triplet at ~ 3.3 ppm, which is contributed by P spin, is almost completely overlapped by resonances from Tau and choline (Cho). Therefore, together with its low signal amplitude with respect to the central multiplet at ~ 3.6 ppm, the possibility of using the P spin resonance as a target multiplet is excluded. Similarly, the A spin resonance at ~ 4.1 ppm overlaps with Cr and lactate (Lac). This peak is usually unobservable *in vivo* with unedited pulse sequences such as PRESS and STEAM due to its spectral proximity to the strong water signal. The quartet-like, central multiplet at ~ 3.6 ppm (M_2N_2 spin resonances) is assigned to be the target peak for its dominance in amplitude over the two other multiplets, although it does have overlaps with Glx and Tau as well as with Gly. Due to low concentrations relative to mI in normal human brain, some of the background metabolites whose resonances lie between the A and the P multiplets of mI are not considered in this study. They are alanine (~ 3.78 ppm), glucose (~ 3.75 ppm and 3.4 ppm) and syllo-Inositol (~ 3.35 ppm).

4.2.2 Sequence Optimization

A generic DQF sequence is shown in Fig. 4-1, in which PRESS was incorporated into the sequence for the purpose of spatial localization. It is comprised of three 90° r.f pulses and two 180° pulses. The optimization of each r.f. pulse in the sequence was achieved by using MATPULSE software written in MATLAB™ (41). The first 90° pulse is an optimized sinc pulse which is ~ 3 ms in duration and ~ 4000 Hz in bandwidth.

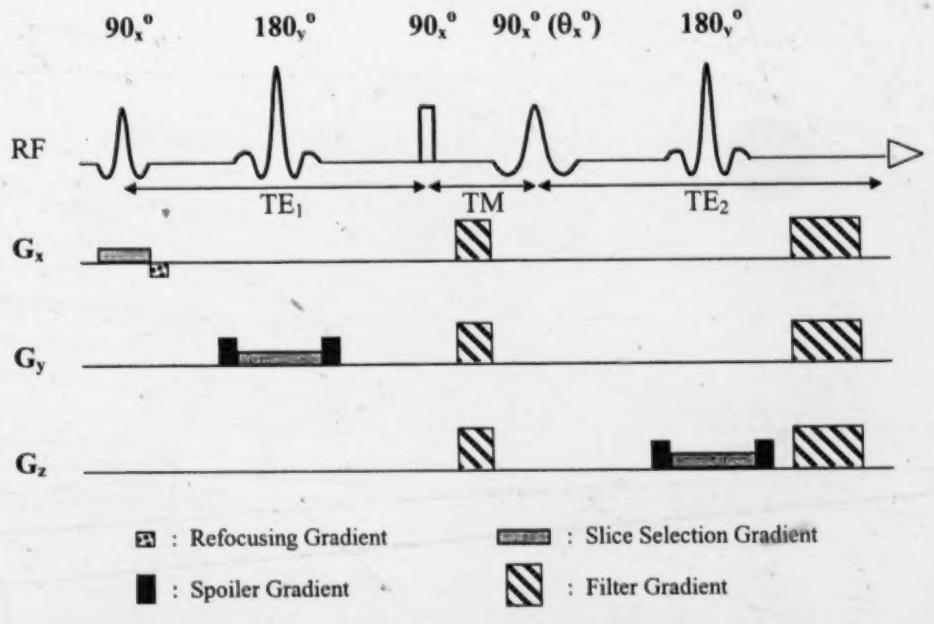

Figure 4-1 A generic DQF sequence. It consists of three 90° and two 180° r. f. pulses. The filtering of a specific order of coherence is achieved by the second and the third 90° pulse in conjunction with a pair of filter gradients. The area of the second filter gradient is adjusted with respect to the first one, according to the level of coherence to be filtered out.

For the second 90° pulse that generates MQCs, a rectangular hard pulse was chosen with its duration as short as 250 μs. It should be noted that any unnecessary increase in the width of this pulse may result in a loss of efficiency of the optimally chosen TM by allowing additional intra-pulse evolution of coherences, namely, the mixing of

coherences (23). Shortening this pulse becomes more important for strongly-coupled spin systems for their rapid coherence transfer mechanisms (42, 43). The optimization of the third 90° read pulse, a numerically optimized sinc-Gaussian pulse, includes consideration of the frequency offset, the duration and the tip-angle of the pulse, which will be discussed below in detail. As for the two 180° pulses, an optimized sinc pulse was used for both slice selection and chemical shift refocusing with a duration of 3.5 ms and a bandwidth of ~ 1200 Hz. The length and amplitude of each slice selection gradient was calculated according to the voxel size. The duration of spoiler gradients for each 180° refocusing pulses was 2 ms with the maximal amplitude of 20 mTm^{-1}. The filter gradients were implemented in all three directions with the length of G_1 = 3 ms and G_2 = $2\times G_1$ for double quantum coherence selection, and the maximal amplitude of 20 mTm^{-1} for both G_1 and G_2. The net gradient vector, therefore, was oriented at the magic angle (54.74°) to facilitate the suppression of residual water signal resulting from the demagnetizing dipole-dipole interaction between water molecules in conjunction with a 16 step phase-cycling (23).

The determination of the optimum values for the offset frequency and the bandwidth (or duration) of the third 90° read pulse preceded the optimization of TEs and TM. As for those metabolites with two well-separated resonances such as a simple AX spin system, the excitation of a target multiplet by the third 90° pulse is avoided to enhance signal yield by a factor of two with respect to that obtainable by exciting all resonances. In the case of mI, however, it is not straightforward which multiplet(s) are to be excited for maximum signal of the target peak due to the complex spectral characteristics of the spin system. Minimizing the excitation of water resonance by the read pulse is another issue to be considered simultaneously. Therefore, an analysis was made by using the product operator formalism (22) to determine the most appropriate excitation scheme by the read pulse, which produces the largest number of single quantum APCs (SQ-APCs) with at least one transverse magnetization of M or N spin that ultimately contributes to the target signal. The result is summarized in table 4-2. The additional double-order terms (DQCs with more than one passive spin involved, e.g., $A_xM_{1x}N_{2z}$), which are produced during TM, were not considered in the analysis for their

negligible contribution to the final signal yield (see section 4.3.2). As will be discussed in section 4.3.2, each DQC term oscillates between a real and an imaginary state during TM under the action of the Zeeman Hamiltonian. Using raising and lowering operators these two components of a DQC during TM may be represented more clearly. For instance, the DQC term involving A and M_1 spins denoted as $DQC(AM_1)$ can be decomposed as

$$\begin{aligned} DQC(AM_1) &\rightarrow 2(A_xM_{1x} - A_yM_{1y}) \rightarrow \quad (A_+M_{1+} + A_-M_{1-}) : DQC(AM_1)_{real} \\ &\rightarrow 2(A_xM_{1y} + A_yM_{1x}) \rightarrow -i(A_+M_{1+} - A_-M_{1-}) : DQC(AM_1)_{imag} \end{aligned} \quad (4\text{-}1a)$$

where

$$A_\pm = A_x \pm iA_y. \quad (4\text{-}1b)$$

Note from Eq. (4-1a) that real and imaginary components of DQC terms are converted by the third 90° frequency-selective pulse into different APCs. Therefore, they were separately considered in Table 4-2 for all DQCs available for the mI spin system.

Spin species excited by 3rd 90° pulse	**DQC (*imag.*) ⇓ APC**	**DQC (*real*) ⇓ APC**	**Total number of APCs**
P	4	4	**8**
M, N, P	16	0	**16**
A, M, N, P	20	0	**20**

Table 4-2 The number of single quantum anti-phase coherences converted by the third 90° frequency-selective pulse for three different excitation schemes. Only those APC terms with transverse M or N magnetization were counted, which ultimately contribute to the target peak of mI at ~ 3.6 ppm.

As well, due to the strong-coupling interaction, those DQCs that involve two spins with no direct J-coupling between them but have a common coupling partner, e.g., DQC(AN) are also created during TM (42-44). Therefore, such DQC terms were also considered in the analysis. According to Table 4-2, exciting all spin species yields the largest number of SQ-APCs with at least one transverse magnetization of M or N spin. Therefore, the third 90° frequency selective pulse was tuned to excite all spin species of mI, while leaving water resonance intact. However, it should be noted that, for strongly-coupled spin systems, the optimal choice of the spectral region to be excited by the third 90° pulse for maximum signal yield is also influenced by the choice of TE_2 due to the active coherence transfer facilitated by the strong-coupling Hamiltonian during that period of time. Therefore, the analysis given above should be used only as a guideline. Another excitation scheme may be possible such as the excitation of A and P spins by using a composite pulse (45, 46). But for the same reason as above, it does not necessarily enhance the filter yield. Moreover, that method may cause unwanted perturbation of other spectral region such as the excitation of water resonance. Therefore it was not considered in this study.

As a next step in the design of a DQF for mI editing, the optimization of TE_1 and TE_2 was carried out. With an initial value of 5 ms for TM, and 90° and 5 ms for the flip angle and the duration of the third 90° read pulse, respectively, a contour plot of the signal intensity of the target multiplet of mI was produced (23) as shown in Fig. 4-2. It visualizes the variation in the signal intensity of the targeted peak as a function of TE_1 (vertical axis) and TE_2 (horizontal axis) in ms, which will be denoted as $\{TE_1, TE_2\}$ henceforth. No transverse relaxation was assumed in the calculation and all indices were normalized to the maximum signal intensity appearing at ~ {100, 100} in the figure.

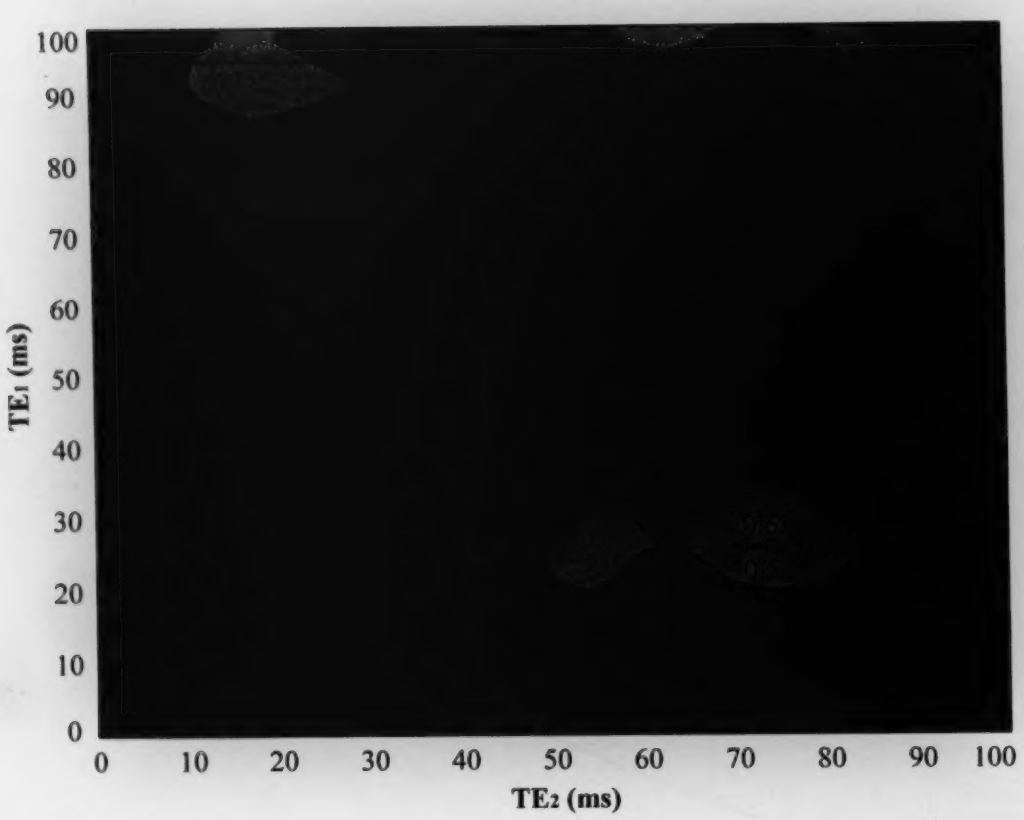

Figure 4-2 The contour plot of the calculated signal intensity of the target peak of *myo*-Inositol in response to a DQF sequence for the determination of semi-optimum TE_1 and TE_2. Initially, TM was set to 5 ms. Also, the flip angle and the duration of the frequency selective r.f. pulse was set to 90° and 5 ms, respectively. No relaxation loss was assumed in the calculation. All indices were normalized to the maximum signal found at both TE_1 and $TE_2 \sim 100$ ms. A step size of 2 ms was used in the calculation for both TE_1 and TE_2.

Based on this preliminary contour plot and an initial TM of 5 ms, the optimization of the tip angle and the duration of the third 90° read pulse was achieved by producing another contour plot as a function of those two sequence parameters as illustrated in Fig. 4-3. According to Fig. 4-3, the optimal flip angle is found to be ~ 65°, and the filter yield can be enhanced by designing the pulse as short as possible. However, to achieve the bandwidth required for the optimal excitation scheme found in the previous analysis, the initial duration of 5 ms was retained.

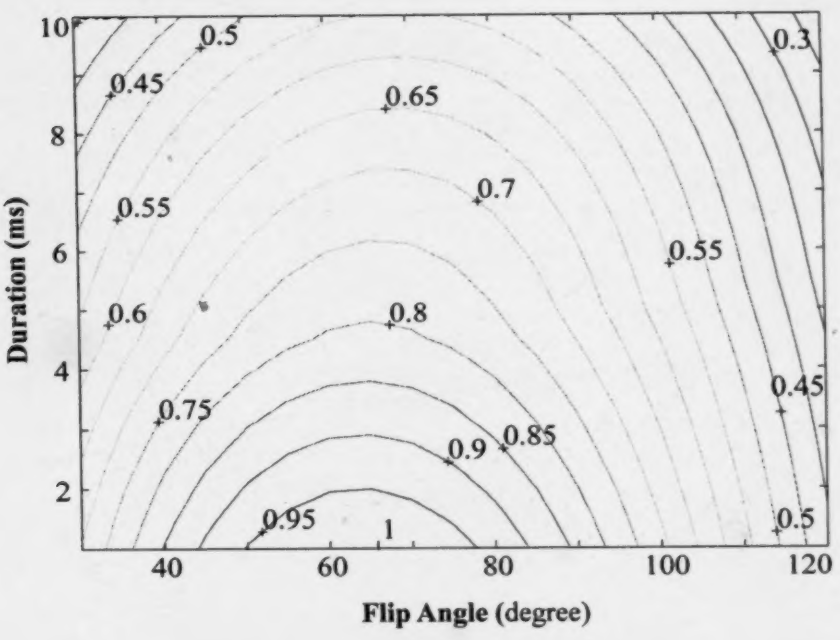

Figure 4-3 The variation of the calculated signal intensity of the target peak of *myo*-Inositol as a function of the duration and the flip angle of the third 90° frequency selective pulse. No relaxation loss was assumed in the calculation. Also, the indices were normalized to the maximum signal found at the duration of 1 ms and the flip angle of ~ 65°.

The optimization of TM was also made by producing Fig. 4-4, which illustrates the TM-dependence of the filter yield. Although the maximum signal occurs at ~ 5.5 ms, the actual TM was set to 7 ms to accommodate the filter gradient during the mixing period. As a last step, all the parameters found to be optimal were combined together to produce another contour plot for the reoptimization of TE_1 and TE_2 (23). For effective background suppression, such contour plots were also calculated for the A multiplets of Glx and for Tau.

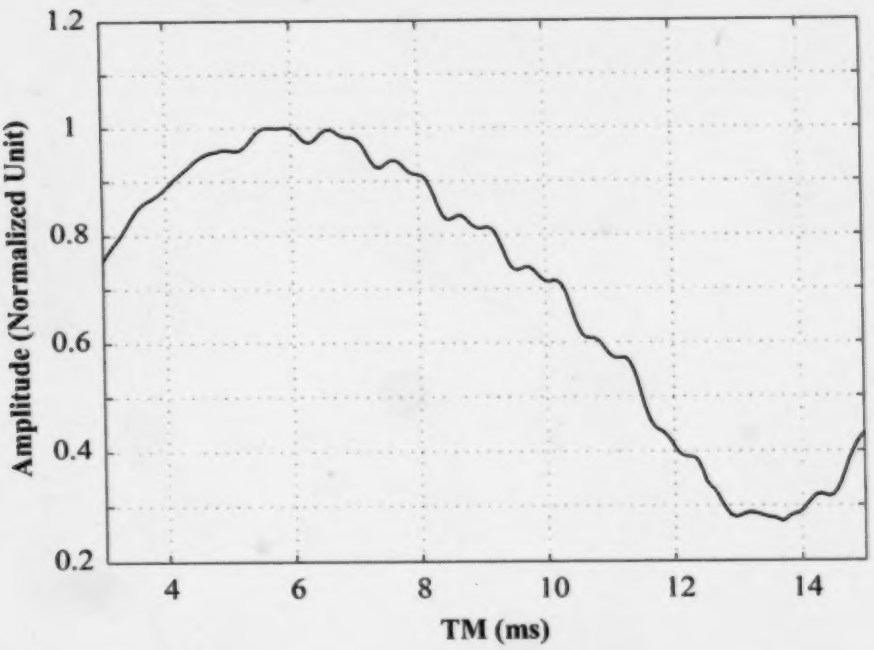

Figure 4-4 The variation of the calculated signal intensity of the target peak of *myo*-Inositol as a function of TM. The amplitude was normalized to the maximum value that occurs at ~ 5.5 ms of TM. No relaxation loss was assumed in the calculation.

4.2.3 Phantom and In-vivo Experiments

Two spherical phantoms (~ 5 cm in diameter; pH ~ 7) of aqueous solutions (distilled water) were manufactured, with pH adjusted to 7.1 ± 0.1 using hydrochloride and sodium hydroxide. One (phantom #1) contains mI and Cr, and the other (phantom #2) comprises mI, Cr, Glu, Gln, Gly and Tau at the relative physiological concentration ratio of normal human brain (1 : 1.1 : 1.3 : 0.6 : 0.2 : 0.5) (24, 47, 48). For both phantoms the concentration of mI was maintained at 50 mM. In phantom #1, Cr (10 mM) was included to be used as a reference peak. All chemicals (purity ≥ 98%) were purchased from Sigma Chemical Co. (St. Louis, USA) except for Cr (ICN Biomedicals, Inc, Aurora, USA).

An 80-cm bore magnet (Magnex Scientific PLC, Abingdon, UK) was used for all tests with a home-built 28-cm diameter quadrature birdcage coil for both transmission and reception. The spectrometer control was provided by a SMIS console (Surrey Medical Imaging Systems PCL, Guilford, UK).

A total of 2048 data points were used for data acquisition. A linewidth broadening of ~ 7 Hz was applied for all spectra throughout this study. A 2.5 × 2.5 × 2.5 cm^3 voxel was located at the isocenter of the phantoms for all phantom experiments and in the occipital region of the brain for *in vivo* experiments. In order to improve signal to noise ratio (S/N), a larger voxel size of 3.5 × 3.5 × 3.5 cm^3 was also used for another *in vivo* study. As well, the repetition time (TR) of 3 s was used for all experiments.

As will be discussed in detail in Chapters 5 and 6, the phase of the MQC-generating, second 90° r.f. pulse needs to be precisely tuned to obtain a desired outcome. For conventional even order filtering, it should be tuned to a phase of x as shown in Fig. 4-1. A phase error can result in a significant loss of signal and unexpected lineshape of a target peak (Chapters 5 and 6). A mismatch between the phase of an r.f. pulse coded in an NMR pulse program and the actual phase of that pulse is mainly due to phase accumulation during the switching of the synthesizer frequency, which is necessary when slice-selective pulses are used with non-zero offset frequencies (27, 28, 35). The phase error of this kind can be compensated, for instance, by comparing the response of the water resonance acquired with and without an additional 180° pulse (35). However, imperfect hardware performance such as instability of the r.f. and/or the gradient amplifiers can also potentially give rise to phase errors, which could be intractable. Such an additional phase error can be identified by acquiring data from a voxel located at the isocenter. To cope with these phase errors as a whole, the phase of the MQC-generating, second 90° pulse was calibrated manually by resorting to the behaviour of the Cr methyl singlet at ~ 3.0 ppm in response to a zero quantum filter (ZQF). This was based on the fact that when the phase of the second 90° pulse is tuned identically to that of the first excitation pulse the amplitude of resonances from uncoupled (and weakly-coupled) spin systems in response to a ZQF is maximized (Chapters 5 and 6). After optimizing the

phase of the MQC-generating pulse in this manner, DQ filtering experiments were carried out by turning on the second filtering gradient, which is the only component of a DQF that differs from a ZQF.

4.3. Results

4.3.1 Experimental Results

Based on the contour plots obtained for the M_2N_2 multiplet of mI, the A multiplets of Glx and for Tau, the optimized sequence parameters for the DQF were determined to be: TE_1 = 32 ms, TE_2 = 58 ms, TM = 7 ms, and the duration and the flip angle of the third 90° being 5 ms and ~ 65°, respectively, with the frequency offset of that pulse tuned to excite all spin species of mI. The total TE of the optimized filter also facilitates the suppression of macromolecule resonances in the target spectral region.

The optimized filter for mI was tested first in the phantoms and the results are shown in Fig. 4-5 together with those taken with PRESS at {32, 58}. Fig. 4-5 (a) and (b) compares the response of mI in phantom #1 to PRESS with that in phantom #2, which includes those background metabolites as well. At this sequence timing pair, the mI peak at ~ 3.6 ppm in response to PRESS is observed as an anti-phase doublet, and as a result, Gly signal, which lies in the transition region of the two peaks of mI, appears as a tiny spike. The filtered spectra of mI are shown in (d) without, and in (e) with, its background metabolites along with the calculated response in (c). The lineshape and the signal amplitude of the mI target peak in Fig. 4-5 (c) through (e) are all in close agreement with one another, and comparing (d) with (e), both the A multiplets of Glx and Tau are effectively suppressed, while the MNPQ multiplets of Glx still persist over the range of 2.0 ppm through 2.5 ppm in (e). The efficacy of a DQF in suppressing uncoupled spin resonances is clearly demonstrated by comparing Fig. 4-5 (b) with (e) where the strong Cr resonances at ~ 3.0 ppm and ~ 3.0 ppm in response to PRESS (Fig. 4-5 (b)) are completely removed from the filtered spectrum shown in (e). This observation also guarantees an effective removal of the uncoupled Gly from the target spectral region.

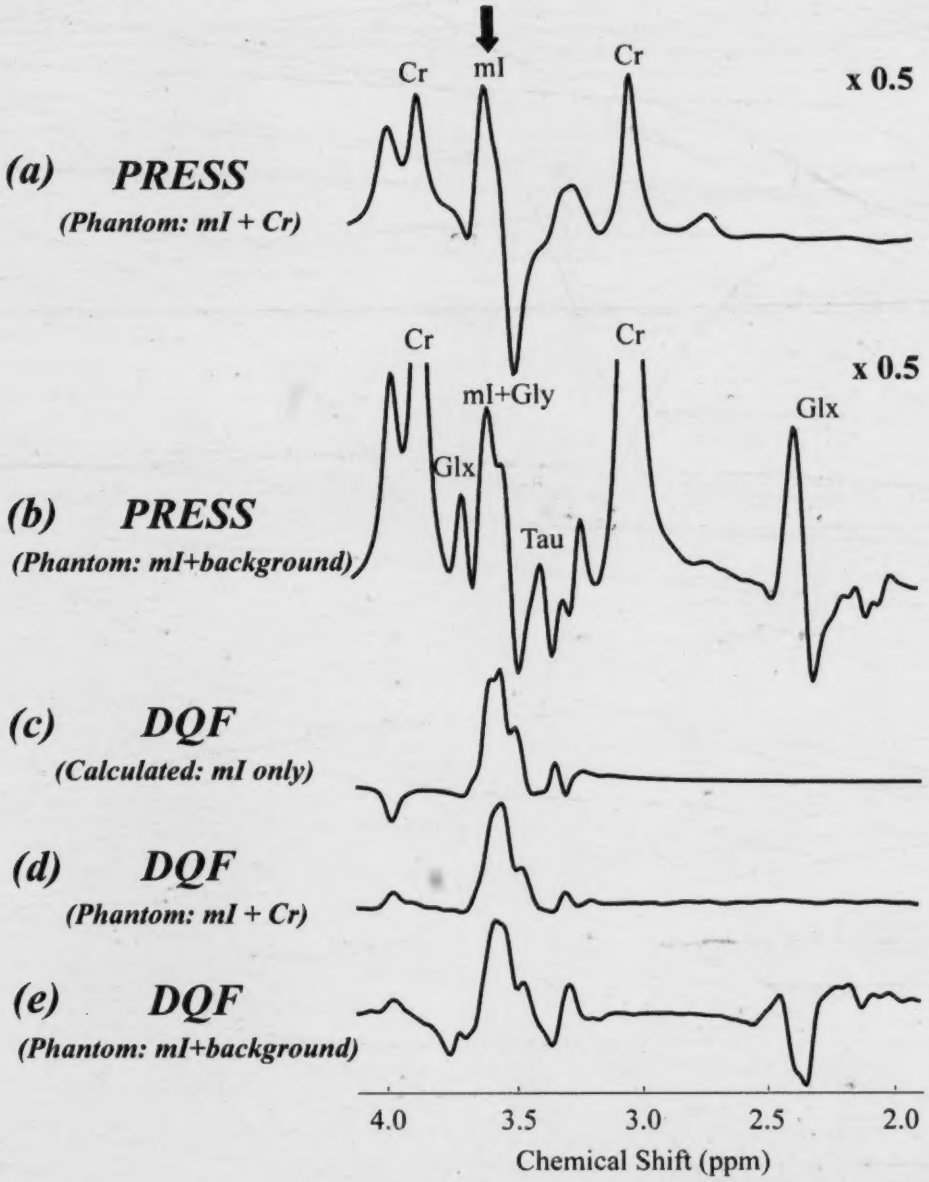

Figure 4-5 The phantom response of *myo*-Inositol and its background metabolites to a PRESS and the optimized DQF. The response of mI to a PRESS at {TE_1=32 ms, TE_2=58 ms} is shown (a) without, and (b) with, background metabolites. The filtered mI signal is also shown (d) without, and (e) with, its background metabolites. The calculated spectrum is also shown in (c). The lineshape of the mI target multiplet matches close to one another in all filtered spectra. For all spectra, the linewidth was artificially broadened to ~ 7 Hz.

The signal yield of mI in response to the optimized filter is estimated to be ~ 15 % of that obtainable in PRESS experiment with the shortest timings of TE_1 = 18 ms and TE_2 = 16 ms in the limit of a pulse sequence programming (21). Although a theoretical signal yield of a DQF is predicted to be 25 % with respect to unfiltered signal, which originates from the fact that only 50 % of the DQCs are refocused by the second filter gradient after their reversion back into APCs by the third 90° frequency selective pulse, this simple algebra for estimating a theoretical filter output does not apply for complicated spin systems such as mI. This is because final DQ-filtered signal of strongly-coupled spin systems is contributed by a variety of coherence terms whose evolution pathways can be significantly different from one another due to the complicated coherence proliferation under the strong-coupling Hamiltonian. It should be noted that although the DQ-filtered outputs in the literature range from ~ 25 to ~ 45 % (23, 27, 28, 30-32, 34, 35), some of those values (27, 28, 30, 35) were estimated with respect to that obtained with a PRESS or a STEAM sequence at the same sequence timings used for DQF experiments, which is not an appropriate means of estimating filter yield.

The performance of the optimized DQF was further tested *in vivo* and the results are shown in Fig. 4-6 along with that obtained in phantom for comparison purpose. Both in-vivo spectra in (b) and (c) were taken from the occipital region of the brain from two different volunteers. The lineshapes of the target peak of mI in all three spectra match close to one another. In Fig. 4-6(c), the MNPQ multiplet of Glx at ~ 2.3 ppm (negative peak) is also well identified as in the phantom spectrum in (a). As well, no uncoupled resonances are observed in the spectra such as water, Cr and N-acetylaspartate (NAA; ~ 2.0 ppm). Therefore, taking account of much higher concentrations of those metabolites with respect to that of Gly in the normal human brain, the suppression of Gly in the target spectral region can be assured. Finally, since the total TE of the optimized filter is as long as 90 ms, the contamination of the target peak of mI by macromolecule resonances can be neglected (18, 20).

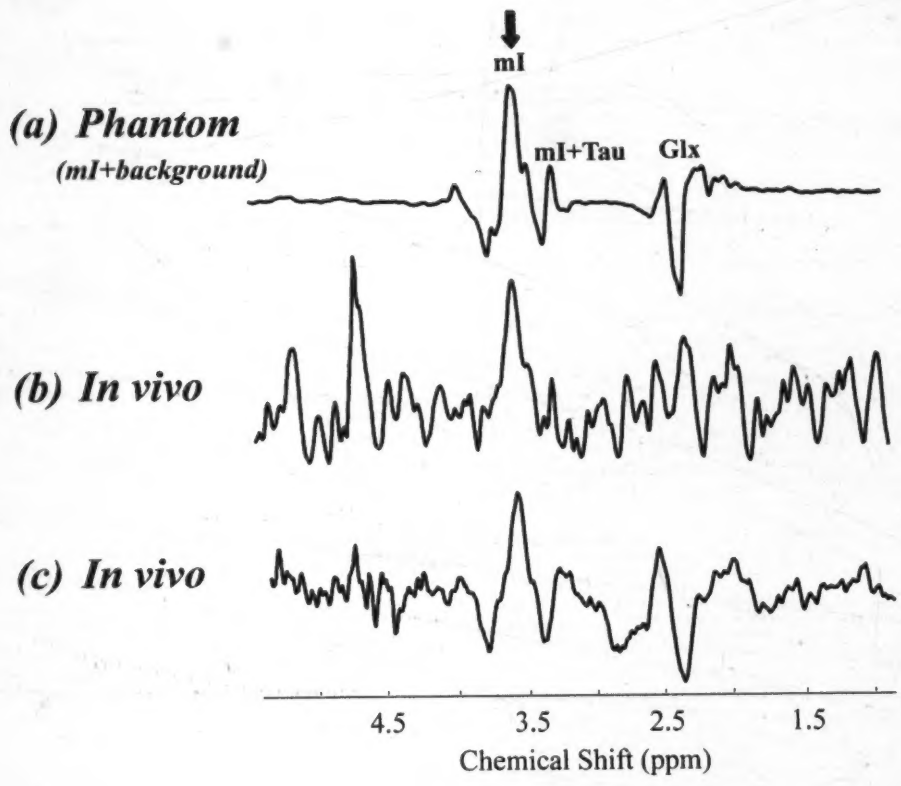

Figure 4-6 The DQ-filtered spectra of the human brain. Shown in (a) is the phantom response of mI and its background metabolites to the optimized filter. The spectrum in (b) was taken from the occipital region of the brain of a 25 yrs. old healthy male subject with a voxel size of 2.5 x 2.5 x 2.5 cm^3 and 256 averages (scan time ~ 13 min.). The spectrum in (c) was obtained from a 30 yrs. old healthy male (same brain region) with a voxel size of 3.5 x 3.5 x 3.5 cm^3 and 512 averages (scan time ~ 27 min.). In (c), the MNPQ multiplets of Glx at ~ 2.3 ppm is also identified.

4.3.2 Sources of Variability During TM Period

The sources of variability in the filtered output (both lineshape and amplitude) can be attributed mainly to the free evolution of spin systems during TM and the two TE periods.

The evolution of coherences during TEs was discussed in detail in Reference 42 for both weakly-coupled and strongly-coupled spin systems, for the latter of which

coherence transfer can take place not only during r.f. pulse irradiation but during the free evolution period as well. As the amount of ZQC just after the MQC-generating second 90° pulse is determined by the choice of TE/2 in a STEAM sequence (43), so the amount of DQC is determined by the choice of TE_1. This is illustrated in Fig. 4-7 where the snapshots of the distribution of DQCs available for the mI spin system are shown at the onset of TM period for two different TE_1 of (a) 32 ms and (b) 62 ms. Note that only *imaginary* DQC terms are included in the figure as the frequency selective third 90° pulse was determined to excite all of the spin species of mI for the maximum signal yield, in which case no *real* DQC term contributes to the final signal (see Table 4-2). Among the 15 possible DQCs, only those terms whose amplitude changes significantly between the two snapshots were indexed. The TE_1-dependence of individual DQC terms is clearly demonstrated in the figure. Note that, as in the case with ZQCs for strongly-coupled spin systems (43), the amplitude of DQC involving A and N spins, $DQC(AN)_{imag}$, can be comparable with other terms, although there is no direct coupling between these two spin species. The existence of such a term can be credited to the strong coupling interactions during TE_1, which facilitates the transfer of coherences from M spins to A and N spins (M spin is a common coupling partner of A and N spins), and subsequently gives rise to APC terms of A and N spin species. As well, due to the symmetry in the mI spin system, the amplitude of $DQC(M_1N_2)_{imag}$ and $DQC(M_2N_1)_{imag}$ are the same in the two snapshots in Fig. 4-7, and so are the amplitude of such pairs as $DQC(AN_1)_{imag}$ and $DQC(AN_2)_{imag}$, and $DQC(N_1P)_{imag}$ and $DQC(N_2P)_{imag}$.

The characteristics of the evolution of the strongly-coupled spin systems during the mixing period of a DQF sequence can be understood in line with that for STEAM. DQCs also oscillate during TM between a real and an imaginary states just as ZQCs do so in a STEAM sequence under the action of the Zeeman Hamiltonian (43). For the strongly-coupled spins, the scalar-coupling Hamiltonian allows for the transfer between ZQC and z-magnetization during the TM period of STEAM as well as transfer between ZQCs with different spin species involved.

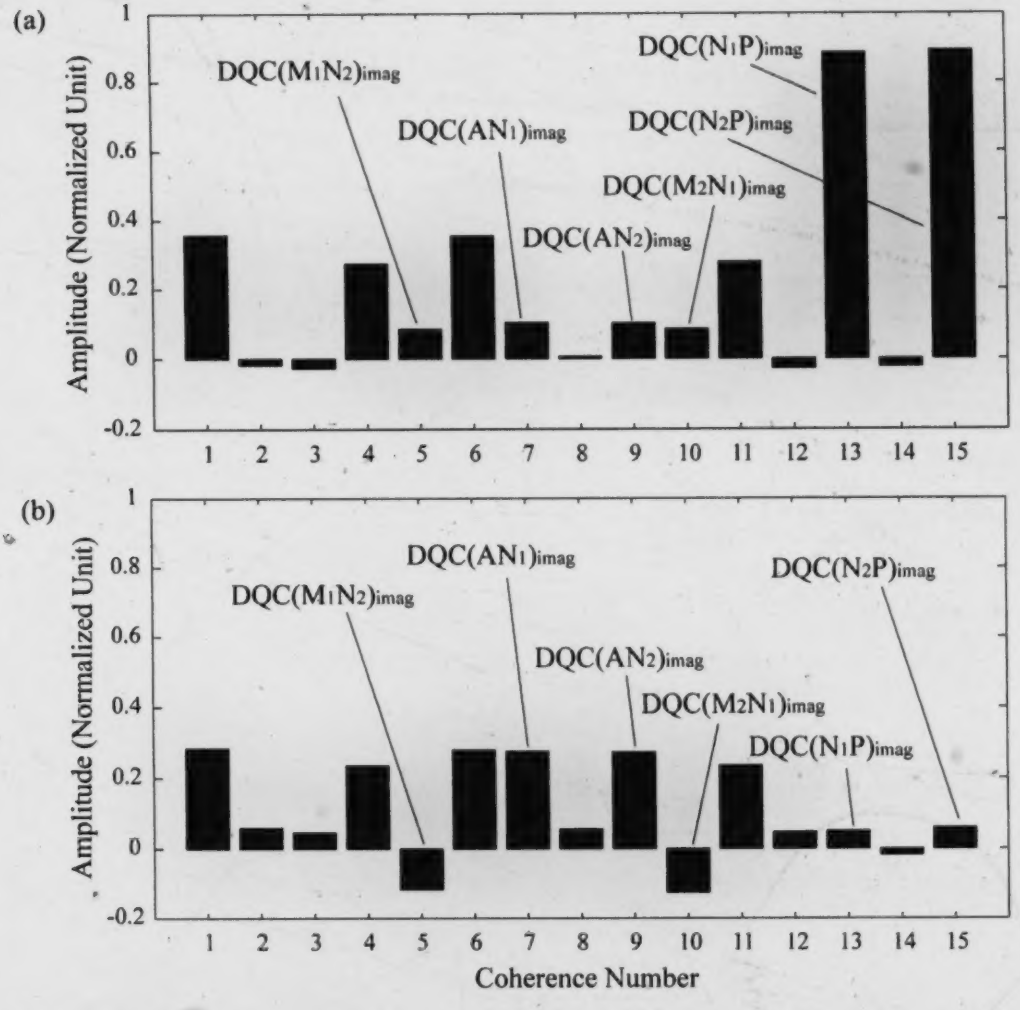

Figure 4-7 The snap shots of the distribution of DQCs just after the second 90° MQC-generating pulse at (a) TE_1 of 32 ms and (b) TE_1 of 62 ms. Among the 15 DQC terms available for the mI spin system, only those DQC terms with significant change in amoplitude between the two TE_1's are Indexed. The TE_1-dependance of each coherence term is clearly demonstrated.

In the case of a DQF sequence, however, only those transfers between different DQC terms can occur as the change in level of coherence is brought about only during the irradiation of r.f. pulses. The coupling Hamiltonian also produces the 'additional double order terms' from ordinary DQC terms, which corresponds to the creation of the 'additional zero order terms from ZQCs in a STEAM sequence (43), e.g., creation of

$[DQC(AM)]X_z$ from DQC(AM) for an AMX spin system. Illustrated in Fig. 4-8 are all such evolutions of DQCs for the mI spin system during TM.

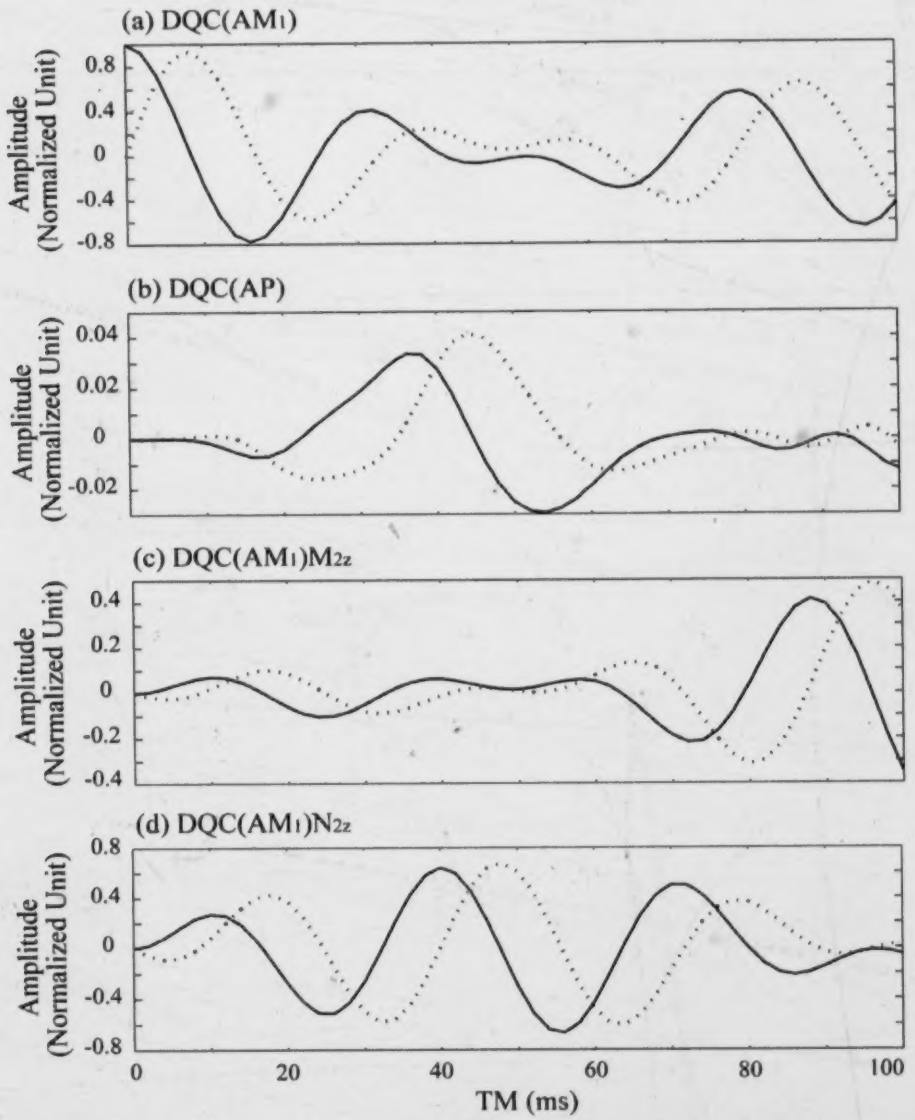

Figure 4-8 The generation and evolution of various DQCs of *myo*-Inositol during TM. With the initial state comprising only of $DQC(AM_1)_{imag}$, the oscillation between real (dotted line) and imaginary (solid line) term of $DQC(AM_1)$ is shown in (a). Also, due to the interactions between coupled spins during TM, new DQCs are produced such as DQC(AP) (b), as well as the additional double order terms such as $DQC(AM_1)M_{2z}$ (c) and $DQC(AM_1)N_{2z}$ (d). Those new coherences thus created also oscillate between real and imaginary terms.

Note that the initial state was comprised *solely* of $DQC(AM_1)_{imag}$. The creation of $DQC(AM_1)_{real}$ from $DQC(AM_1)_{imag}$ and the oscillation between these two states are shown in Fig. 4-8(a) along with the coherence transfer from $DQC(AM_1)$ to DQC(AP) in (b). Also illustrated in Figs. 4-8(c) and (d) is the production of the additional double order terms which also oscillate between a real and an imaginary state. It should be noted that the creation of such additional double order terms is one of the *signal loss* mechanisms in a DQF sequence since they are rarely inverted by the read pulse back into observable, SQ-APCs. For instance, the term, $[DQC(AM_1)_{imag}]M_{2z}$, of which the evolution during TM is shown in Fig. 4-8(c) as a solid line, is converted by the read pulse with three different excitation schemes into

$$\begin{aligned} A_xM_{1y}M_{2z} + A_yM_{1x}M_{2z} \text{ —} \quad 3^{rd}\,90^{o}{}_{x}\,(P) \quad &\rightarrow A_xM_{1y}M_{2z} + A_yM_{1x}M_{2z} \\ \text{—} \quad 3^{rd}\,90^{o}{}_{x}\,(M, N, P) \quad &\rightarrow A_xM_{1z}M_{2y} + A_yM_{1x}M_{2y} \\ \text{—} \quad 3^{rd}\,90^{o}{}_{x}\,(A, M, N, P) \quad &\rightarrow A_xM_{1z}M_{2y} + A_zM_{1x}M_{2y} \end{aligned} \qquad (4\text{-}2)$$

where the spin species excited by the pulse were specified in the parentheses and the coefficient and the sign of each coherence were suppressed. Among those six resultant terms above only $A_yM_{1x}M_{2y}$ contains SQC (¾ SQCs and ¼ triple quantum coherences). The rest of the terms are a mixture of non-observable ZQCs and DQCs. Note that, as a result of these signal loss mechanisms during TM, the maximum amplitude of the real and the imaginary DQC terms in each panel of Fig. 4-8 are not necessarily the same.

4.4 Summary and Discussion

The purpose of this study was to establish an optimal condition in the design of a DQF sequence for the detection of an important brain metabolite mI *in vivo*. The advantage of the filter sequence lies in its capability to suppress any uncoupled spin resonances, which is an important aspect in that the contamination of the target peak of mI by uncoupled Gly was unavoidable with PRESS and STEAM even after optimization.

In addition to the intrinsic poor signal yield of a DQF and a variety of sequence parameters to be optimized, the difficulty in designing the filter for mI detection is exacerbated by the complexity of the mI spin system. It was emphasized that the difference spectra method was not a practical alternative to a DQF due to the complicated evolution of the mI spin system as a function of sequence timings, which results from strong-coupling interactions. As such, the evaluation of the evolution of the mI spin system in response to a DQF sequence cannot be achieved by the conventional product operator analysis. By using numerical solutions of density matrix, the methodical optimization procedure in the design of a DQF (23) was adopted in this study. The optimization of the frequency offset of the third 90° read pulse was considered first for maximum signal yield of the target peak of mI. With initial, tentative values of the flip angle and the duration of that pulse as well as an initial TM value, a preliminary contour plot was produced, which contained information on the variation of the signal intensity of the target peak in $\{TE_1, TE_2\}$ space. As a next step, the frequency selective pulse and TM were optimized in a similar way. As the response of a coupled spin system is most sensitive to the choice of TEs, they were reoptimized upon the incorporation of the other sequence parameters thus optimized.

The performance of the optimized filter was tested both in phantom and *in vivo*, and it was shown *in vivo* that the background metabolites with coupled spins were effectively suppressed. The removal of the uncoupled Gly resonance from the target spectral region was demonstrated by considering the suppression efficiency of the filter *in vivo* for other uncoupled resonances such as water, Cr and NAA, and by comparing the phantom response of mI with and without the presence of the background metabolites.

The filter yield of the mI target peak was estimated to be ~ 15 % with respect to that obtainable with PRESS at the shortest sequence timings. To overcome the resultant poor S/N, a rather larger voxel dimension of $3.5 \times 3.5 \times 3.5$ cm^3 was necessitated with a total of 512 averages for data acquisition (scan time ~ 27 min.). As discussed in Section 4.3.2, the active coherence transfer from the signal-contributing M or N spin species to A and P spins under the strong coupling Hamiltonian followed by unwanted proliferation of

coherences into non-observable terms such as additional double order terms could be one of the mechanisms responsible for the lower filter yield of mI.

A new editing method was reported by Trabesinger et al (49), namely, a single quantum filtering. The sequence can simply be implemented by one additional 90° pulse at the first echo location in a conventional PRESS sequence. It filters out SQCs of strongly-coupled spin systems only, while suppressing those from weakly-coupled and uncoupled spins. Intuitively, the application of such a filter design may be very suitable for the mI editing, since the weakly-coupled A spin multiplets of Glx and the uncoupled Gly singlet can effectively be suppressed by the nature of the sequence. This additional degree of freedom in the sequence optimization procedure may potentially be valuable in the mI editing.

Finally, the results presented in this study are specific at 3.0 T. Due to changes in chemical shift difference (in Hz), the evolutionary picture of the spin systems of mI and its background metabolites in response to a DQF will need to be redefined at different magnetic field strengths.

4.5 References

1. R. A. Moats, T. Ernst, T. K. Shonk, and B. D. Ross, *Magn. Reson. Med.*, **32**, 110, 1994
2. B. L. Miller, R. A. Moats, T. K. Shonk, T. Ernst, S. Woolley, and B. D. Ross, *Radiology*, **187**, 433, 1993
3. B. D. Ross, S. Bluml, R. Cowan, E. Danielsen, N. Farrow and R. Gruetter, *Biophys. Chem.*, **68**, 161, 1997
4. T. Shonk and B. D. Ross, *Magn. Reson. Med.*, **33**, 858, 1995
5. R. Kreis and B. D. Ross, *Radiology*, **184**, 123, 1992
6. R. Kreis, B. D. Ross, N. A. Farrow and Z. Ackerman, *Radiology*, **182**, 19, 1992
7. T. Naegele, W. Grodd, R. Viebahn, U. Seeger, U. Klose, D. Seitz, S. Kaiser, I. Mader, J. Mayer, W. Lauchart, M. Gregor and K. Voigt, *Radiology*, **216**, 683, 2000
8. B. D. Ross, S. Jacobson, F. Villamil, J. Korula, R. Kreis, T. Ernst, T. Shonk and R. A. Moats, *Radiology*, **193**, 457, 1994
9. R. A. Moat, Y. H. Lien, D. Filippi and B. D. Ross, *Biochem. J.*, **295**, 15, 1993
10. R. Frey, D. Metzler, P. Fisher, A. Heiden, J. Scharfetter, E. Moser and S. Kasper, *J. Psyc. Res.*, **32**, 411, 1998
11. M. J. Berridge and R. F. Irvine, *Nature*, **341**, 197, 1989

12. H. Shimon, G. Agam, R. H. Belmaker, T. M. Hyde and J. E. Kleinman, *Am. J. Psyc.*, **154:8**, 1148, 1997
13. G. J. Moore, J. M. Bebchuk, J. K. Parrish, M. W. Faulk, C. L. Arfken, J. Strahl-Bevacqua and H. K. Manji, *Am. J. Psyc.*, **156:12**, 1902, 1999
14. R. H. Lenox and D. G. Watson, *Clin. Chem.*, **40:2**, 309, 1994
15. T. Michaelis, K. D. Merboldt, H. Bruhn, J. Frahm, *Radiology*, **187**, 219, 1993
16. C. G. Choi and J. Frahm, *Magn. Reson. Med.*, **41**, 204, 1999
17. H. Bruhn, G. Stoppe, J. Staedt, K. D. Merboldt, and J. Frahm, *Proc. ISMRM*, New York, 1993, p. 1543
18. K. L. Behar, D. L. Rothman, D. D. Spencer and O. A. C. Petroff, *Magn. Reson. Med.*, **32**, 294, 1994
19. U. Seeger, I. Mader, T. Nagele, W. Grodd, O. Lutz and U. Klose, *Magn. Reson. Med.*, **45**, 948, 2001
20. L. Hofmann, J. Slotboom, C. Boesch and R. Kreis, *Magn. Reson. Med.*, **46**, 855, 2001
21. H. Kim and P. S. Allen, *Proc. ISMRM*, Denver, 2000, p. 1943
22. O. W. Sorensen, G. W. Eich, M. W. Levitt, G. Bodenhausen and R. R. Ernst, *Prog. NMR Spec.*, **16**, 163, 1983
23. R. B. Thomson and P. S. Allen, *Magn. Reson. Med.*, **39**, 762, 1998
24. B. D. Ross, *NMR in Biomed.*, **4**, 59, 1991
25. D. L. Rothman, O. A. C. Petroff, K. L. Behar and R. H. Mattson, *Proc. Natl. Acad. Sci. USA*, **90**, 5662, 1993
26. R. A. de Graaf and D. L. Rothman, *J. Magn. Reson.*, **152**, 124, 2001
27. J. R. Keltner, L. L. Wald, P. J. Ledden, Y. I. Chen, R. T. Matthews, J. R. Baker, B. R. Rosen, and B. G. Jenkins, *Magn. Reson. Med.*, **39**, 651, 1998
28. J. R. Keltner, L. L. Wald, B. B. Frederick, and P. F. Renshaw, *Magn. Reson. Med.*, **37**, 366, 1997
29. H. Lei and J. Peeling, *Magn. Reson. Med.*, **42**, 454, 1999
30. M. A. McLean, A. L. Busza, L. L. Wald, R. J. Simister, G. J. Barker and S. R. Williams, *Magn. Reson. Med.*, **48**, 233, 2002
31. A. H. Wilman and P. S. Allen, *J. Magn. Reson.*, **B105**, 58, 1994
32. H. Lei and J. Peeling, *J. Magn. Reson.*, **143**, 95, 2000
33. L. A. Trimble, J. F. Shen, A. H. Wilman and P. S. Allen, *J. Magn. Reson.*, **86**, 191, 1990
34. A. H. Wilman and P. S. Allen, *J. Magn. Reson.*, **B109**, 169, 1995
35. A. H. Trabesinger, O. M. Weber, C. O. Duc, and P. Boesiger, *Magn. Reson. Med.*, **42**, 283, 1999
36. C. H. Sotak, D. M. Freeman, and R. E. Hurd, *J. Magn. Reson.*, **78**, 355, 1988
37. L. Jouvensal, P. G. Carlier, and G. Bloch, *Magn. Reson. Med.*, **36**, 487, 1996
38. A. H. Wilman and P. S. Allen, *J. Magn. Reson.*, **B107**, 25, 1995
39. J. C. Lindon, D. J. Baker, R. D. Farrant and J. M. Williams, *Biochem. J.*, **233**, 275, 1986
40. K. L. Behar and T. Ogino, *Magn. Reson. Med.*, **17**, 285-303, 1991
41. G. B. Matson, *Magn. Reson. Imag.*, **12**, 1205, 1994
42. R. B. Thomson and P. S. Allen, *Magn. Reson. Med.*, **41**, 1162, 1999
43. R. B. Thomson and P. S. Allen, *Magn. Reson. Med.*, **45**, 955, 2001

44. R. R. Ernst, G. Bodenhausen and A. Wokaun, *Principles of nuclear magnetic resonance in one and two dimensions*, Oxford Science Publications, 1997
45. P. J. Hore, *J. Magn. Reson.*, **55**, 283, 1983
46. G. A. Morris and R. Freeman, *J. Magn. Reson.*, **29**, 433, 1978
47. R. Kreis, T. Ernst and B. D. Ross, *J. Magn. Reson.*, **B102**, 9, 1993
48. S. W. Provencher, *Magn. Reson. Med.*, **30**, 672, 1993
49. A. H. Trabesinger, D. C. Mueller and P. Boesiger, *J. Magn. Reson.*, **145**, 237, 2000

CHAPTER 5

A Strategy For the Spectral Filtering of *Myo*-Inositol and Other Strongly-Coupled Spins

5.1 Introduction

Proton nuclear magnetic resonance (NMR) spectroscopy provides a non-invasive method of extracting biochemical information from the brain. However, the proton spins of many of the key brain metabolites are *strongly*-coupled, as, for example, in glutamate (Glu), glutamine (Gln), and *myo*-inositol (mI). This strong coupling gives rise to complex multiplet spectra which, at field strengths acceptable for clinical use, can overlap; change with sequence timing; make target metabolite discrimination from background difficult; and therefore degrade quantification.

Spectral-editing methods offer a realistic opportunity to suppress the background and mitigate the overlap, but in doing so they also introduce their own difficulties. For example, based upon their ability to differentiate between coupled and uncoupled spins, double quantum filters (DQF) have frequently been proposed as a means of clarifying spectral complexity in in-vivo NMR (1-12). Nonetheless, the outcome has often been disappointing. One reason for the disappointment arises when the targeted coupled-spin metabolite and its overlapping background are both coupled-spin multiplets. Both target and background are therefore likely to pass through the filter, which then fails to isolate the target. The principal goal of this paper is to demonstrate the selective suppression of coupled-spin multiplets.

A second difficulty with a DQF is its low intrinsic signal yield (the signal intensity stripped of its transverse decay). The yield of a DQF is routinely assumed to be lower than that of the unedited single-voxel methods, such as the double-spin-echo

(PRESS) (13, 14) or the stimulated echo (STEAM) (15). This is not, however, always the case, because coupled-spin coherence proliferation also occurs with PRESS and STEAM sequences. In previous work we have demonstrated that in the {TE_1, TE_2} space for PRESS (16) and the {TE, TM} space for STEAM (17), the yield of *strongly*-coupled resonances can be a very irregular function that can sink below that of a DQF (9). Before being able to make a choice for a filter strategy over the unfiltered PRESS or STEAM, it is therefore essential to know the relative target yields from all sequences, as well as their efficacy for background suppression. Moreover, if the irregular yield behaviour is not known prospectively for both a target metabolite and its background, the choice of sequence parameters may be markedly sub-optimal for the discrimination and measurement of the target metabolite. The ability to calculate the yield (and the lineshape) were therefore instrumental in the prospective optimization of the filter design presented here.

The purpose of the paper is therefore to demonstrate tools that not only facilitate the elimination from the spectrum of weakly-coupled, as well as uncoupled spins, but which also provide the flexibility for partially suppressing one *strongly*-coupled spin species relative to another. In short it significantly enhances target to background isolation. Such isolation is only valuable, however, if, as demonstrated below in the example of mI, the signal to noise ratio (S/N) of the isolated target is maintained, in spite of reduced yield and transverse relaxation.

A pulse sequence, designed to differentiate between *strongly*-coupled and the *weakly*-coupled spins was also proposed recently by Trabesinger et al (18). Based on the isolation of *strongly*-coupled single quantum coherences (SQC) it provided greater background suppression than the basic DQF. However, (as the authors themselves point out) the filtering mechanism of this sequence relies solely on the phase of a 90° pulse and is vulnerable to instabilities and phase errors of the r.f. pulses. In contrast, the alternative method proposed here is based on the isolation of *strongly*-coupled zero quantum coherence (ZQC) and longitudinal magnetization. Because it employs both r.f. phase orthogonality and gradient filtering it is more robust at suppressing signals from

uncoupled and *weakly*-coupled spins. In addition, it also provides the flexibility to adjust the relative discrimination of different *strongly*-coupled spin systems by adjustment of its timing parameters.

The isolation of the mI peak in the vicinity of 3.6 ppm provides a particularly appropriate example for testing the proposed filter. This is because, in-vivo, the quantification of mI is hindered by the uncoupled resonance from glycine (Gly) at 3.55 ppm; the *weakly*-coupled A multiplets of the AMNPQ spin systems of Glu and Gln (collectively referred to as Glx) at 3.78 ppm, and the *strongly*-coupled A_2B_2 multiplet of taurine (Tau) at 3.35 ppm. The in-vivo spectrum in this region is also contaminated by a broad macromolecular signal (19-21) and the glucose (Glc) resonances between 3.4 and 3.8 ppm. Because its low concentration is distributed over several multiplets, the Glc contamination was neglected. Neither were the macromolecules prospectively included in the numerical evaluation of the optimum sequence design. The sequence parameters were, nonetheless, chosen such as to minimize any macromolecular signal.

In the following paragraphs we outline first the logic and operational mechanisms of the sequence, secondly the means of testing the sequence operation experimentally with phantoms is explained, prior to providing an in-vivo demonstration of its efficacy. A preliminary report of this work (22) was presented recently.

5.2 Theory

5.2.1 The Sequence and the Multiple Quantum Filter Mechanism

When a generic multiple quantum filter (MQF) sequence of three coherent 90° pulses is applied to a *weakly*-coupled metabolite spin system, the sequence gives rise to the even orders of multiple quantum coherence (MQC), each one of which can be isolated by appropriate gradient filtering (23). This is the conventional sequence for observing ZQC. However, it is not adept at distinguishing the ZQC (or the gradient-insensitive longitudinal magnetization), from different coupled-spin systems or from the

longitudinal magnetization of uncoupled spins. Alternatively, if the phase of the second 90° pulse in the MQF is made orthogonal to that of the first pulse, the sequence produces only odd orders of MQC from *weakly*-coupled spins and might not therefore be expected to produce ZQC. In contrast, however, the spins of *strongly*-coupled metabolites experience polarization transfer in the first inter-pulse interval (18, 24), which leads to additional terms in the density operator that *can* be turned into ZQC by the orthogonal phase disposition of the first two pulses. The combination of r.f. phase orthogonality followed by a strong dephasing gradient in the second inter-pulse (mixing) period, therefore enables the proposed technique to suppress all uncoupled and *weakly*-coupled spin coherences, while at the same time maintaining ZQC and longitudinal magnetization from *strongly*-coupled spins only.

The proposed filter sequence is shown in Fig. 5-1 together with a comparative illustration of the coherence evolution through the sequence for an *un*coupled spin, I; for the A spin of a *weakly*-coupled spin pair, AX; and for the A spin of a *strongly*-coupled spin pair designated AB (24). The corresponding and symmetric evolutions of the X spin and of the B spin are omitted for clarity. Although the coherence evolution of these simpler systems cannot be taken literally for the larger spin systems of Glu, Gln, mI and Tau, it clearly illustrates the mechanism. The key illustrative point of Fig. 5-1 is that the *strongly*-coupled A spin transverse terms, A_x and A_yB_z, prior to the second 90° pulse, are overwhelmingly brought about in the first inter-pulse interval by the *strong*-coupling Hamiltonian acting on the B spin transverse term B_y which is created by the ^1H excitation pulse. They do not arise from A_y. A_x and A_yB_z are subsequently transformed by the second orthogonal pulse into gradient-insensitive A_z and $[A_yB_x]_{ZQC}$ respectively. No gradient insensitive terms arise from either *weakly*-coupled or *un*coupled spins following the second 90° pulse and therefore the application of a filter gradient during the TM period will not only remove the *un*coupled and *weakly*-coupled terms, but it will also remove all higher orders of MQC from the *strongly*-coupled spins. In contrast to a generic MQF, the absence of a second, refocusing filter gradient after the third 90° pulse in the sequence proposed here, prevents any terms other than the gradient insensitive

terms, i.e. the A_z and $[A_yB_x]_{ZQC}$ of the *strongly*-coupled spins, leading to observable signal during the acquisition period.

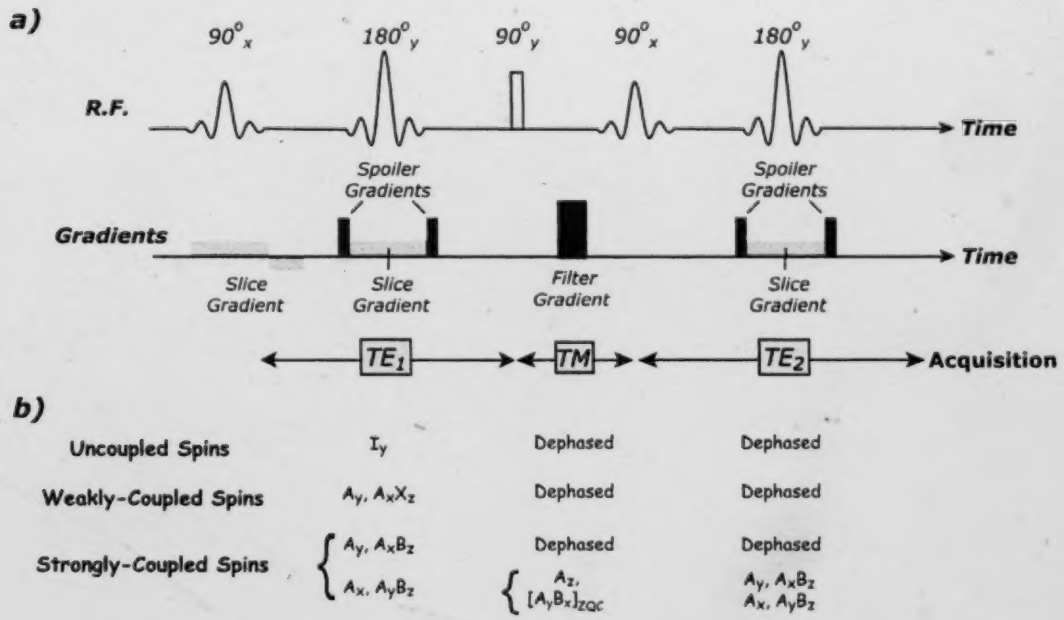

Figure 5-1 A schematic illustration of a multiple quantum filter sequence including (a) the pulses and the timing definitions and (b) a representative listing made for each coupling category of the evolution of coherence terms during the individual timing periods.

5.2.2 Outline of Analysis to Optimize mI Observation at ~ 3.6 ppm

Between 3.2 ppm and 3.9 ppm in the proton spectrum from brain, the principal background metabolite resonances interfering with the observation of mI arise from the uncoupled Gly (3.55 ppm), the *weakly*-coupled A multiplets of the Glx AMNPQ spin system (~ 3.78 ppm) and the *strongly*-coupled A_2B_2 system of Tau (~ 3.35 ppm). In addition, there is a broad macromolecular baseline hump. The sequence proposed here is designed, first, to eliminate Gly and Glx signals using r.f. phase orthogonality coupled to filtering with gradient dephasing, secondly, to suppress Tau by optimizing the inter-pulse

intervals and thirdly to ensure a cumulative echo time sufficient to complete the decay of the macromolecular signal. The spectrum of the six observable protons of mI, designated as an AM_2N_2P spin system (25) at 3.0 T in Fig. 5-2, is dominated by a band at ~ 3.6 ppm, for which the M_2N_2 *strongly*-coupled, double pair is primarily responsible.

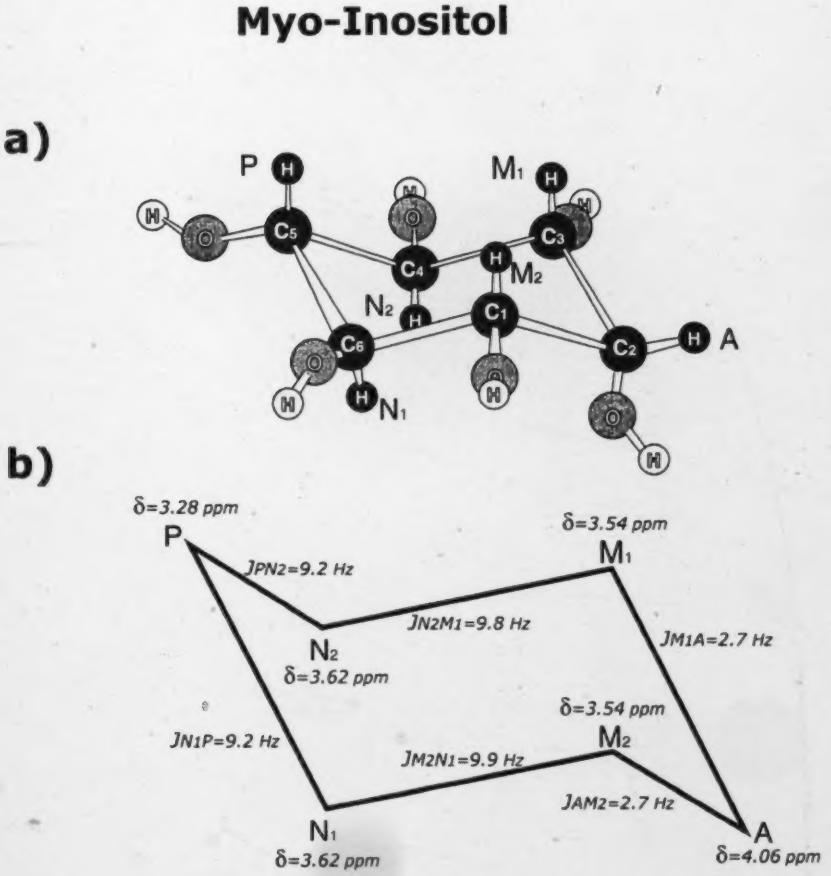

Figure 5-2 A diagram illustrating the mI molecule together with schematic of the chemical shift values, δ ppm, and the coupling configuration, including individual interaction strengths, *J* Hz.

For a full description of the response of mI to an arbitrary pulse sequence, a total of 4096 coherence terms needs to be followed. Even using a restricted set for the M_2N_2 subgroup, the still-large number of terms, together with the *strong*-coupling, precludes

manual, product-operator analysis. Alternatively, numerical methods of solving the equation of motion of the density operator (9, 16, 17, 26, 27) provide a practical way of tracking the large number of coherence terms through a pulse sequence.

To calculate the spin system response, it is necessary to solve the Liouville-von Neumann equation (28),

$$\frac{d}{dt}\rho(t) = -i[H(t), \rho(t)] \tag{5-1}$$

for the time-dependent density operator of the spin system, $\rho(t)$, where H is the Hamiltonian under which the evolution takes place. For an N spin, I = 1/2, system the density operator $\rho(t)$ can be expressed as a weighted sum of the complete set (2^{2N}) of product operator basis terms (28), the weighting coefficients reflecting the temporal evolution of each term. The Hamiltonian used in our calculations included, in addition to the Zeeman interaction, the r.f. pulses, the gradient pulses, the different chemical shielding interactions and the several scalar coupling interactions. No approximations were made for weak coupling. For time-independent Hamiltonians, Eq. (5-1) has a solution,

$$\rho(t) = U(t)\rho(0)U^{-1}(t) \tag{5-2}$$

where $U(t) = exp(-i\,Ht)$. The solutions can therefore be obtained by matrix multiplication alone, if the exponential operators are expressed as matrices. When H corresponds to a diagonal matrix, $U(t)$ can be expressed as a diagonal matrix of exponential elements. Otherwise, H needs to be diagonalized by means of a unitary matrix, V, and the resulting exponential operator transformed with the same unitary matrix, so that

$$\rho(t) = V\exp(-i\,H_{diag}t)V^{-1}\,\rho(0)\,V\exp(i\,H_{diag}t)V^{-1} \tag{5-3}$$

where $H_{diag} = V^{I} H V$, and the unitary matrix V is formed from the eigenvectors of H. When H is not time independent, for example when shaped r.f. pulses are modelled, its time evolution can be subdivided into short discrete time elements, within each of which time independence of the Hamiltonian can be assumed.

In the algorithm, each pulse sequence is treated as a series of independent contiguous time segments, each having its own Hamiltonian. Terms in the density operator can be evaluated at any stage during the sequence, or the acquisition period, by successive matrix multiplication according to Eq. (5-3). For the gradient term in the Hamiltonian there exists a spatial distribution as well as a temporal evolution, giving rise to multiple evolution operators for each time segment or sub-segment in which the gradient is applied. The gradient evolution operators for each time sub-segment were collected in a storage matrix that enabled their effects to be combined efficiently irrespective of whether the ultimate FID or a mid-sequence density operator term was required. For selective pulses, the r.f. envelope was divided into 7.5 μs time sub-segments and the gradient induced frequency distribution was typically incremented to give rise to a 0.1 mm spatial resolution. Such a resolution enabled the 90% to 10% roll-off of the 90° pulse to be captured over 30 to 40 spatial intervals. The temporal evolution of any of the various coherences or of the ultimate transverse magnetization emerging from the sequence can easily be evaluated from the trace of the product of the density operator with the corresponding coherence or magnetization operator. Because the method of solution accommodates Hamiltonians that change relatively slowly with time, the influence of practical slice selective pulses can be calculated and contrasted with that of a hard-pulse approximation.

A total of 384 SQC species can potentially contribute to the overall mI spectrum through their time evolution in the acquisition period. They are illustrated schematically in Fig. 5-3(a) at the onset of the acquisition period following the proposed filter sequence. However, the target peak of mI at ~ 3.6 ppm is dominated by far fewer than this. Although the 3.6 ppm band of the mI spectrum arises mainly from the four M and N spins, it is dominated by little more than 12% of their 256 SQC terms.

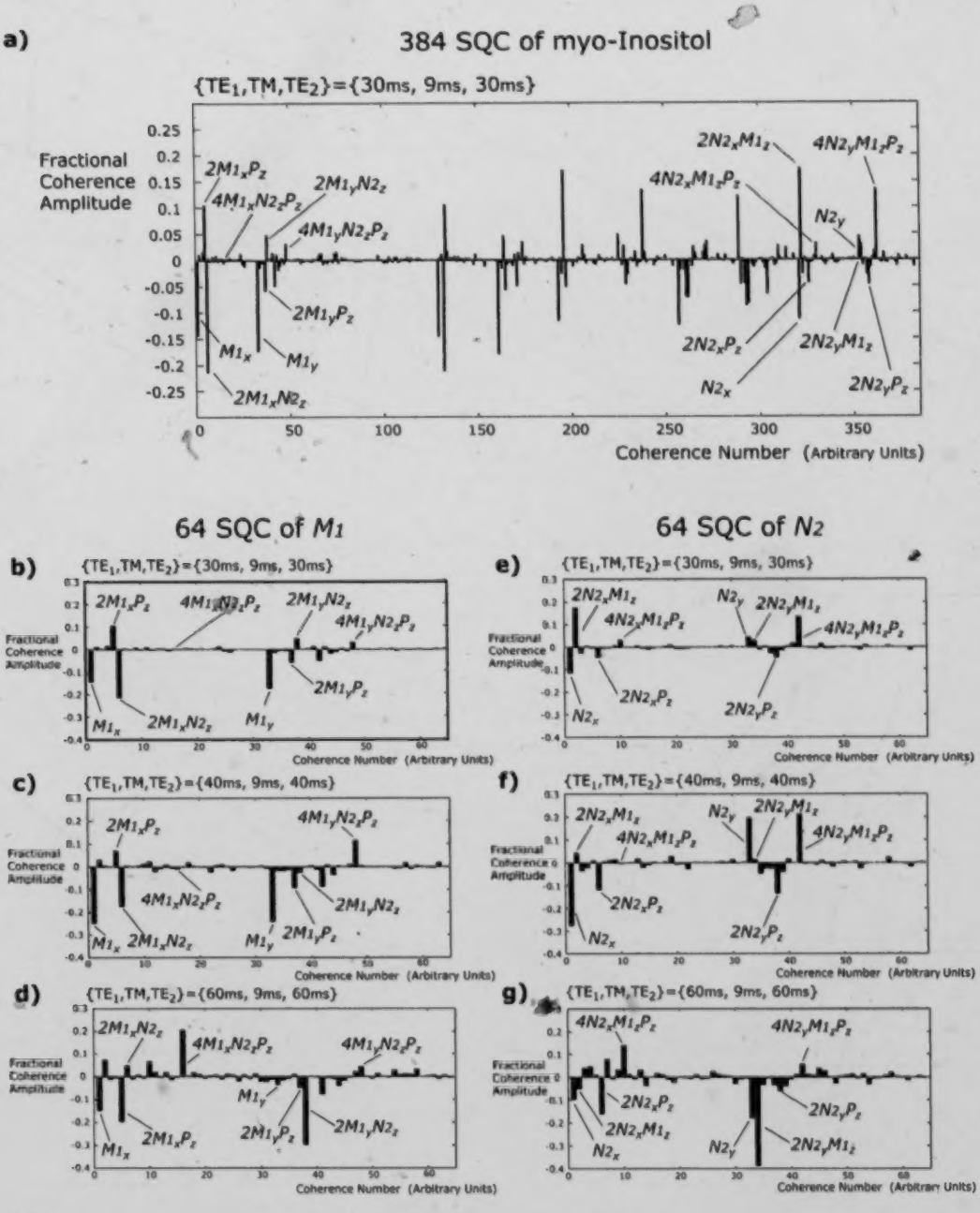

Figure 5-3 Specific-time snap-shots of the relative amplitudes of various coherences of the mI spin system. These snap-shots correspond to the onset of acquisition in the symmetric echo-time filters where {TE_1, TM, TE_2} are respectively {30 ms, 9 ms, 30 ms}, {40 ms, 9 ms, 40 ms} and {60 ms, 9 ms, 60 ms}. The coherence number labels are arbitrary, but the important coherences are labeled by name. The fractional amplitude scale represents for each coherence term the proportion of its maximum value.

For example, when the sequence has symmetric echo-times, Figs. 5-3(b) to 5-3(g) illustrate that of the 64 M_1 SQC and the 64 N_2 SQC (there also exists a corresponding 128 SQC from the M_2 and N_1 spins) the echo-time dependence is dominated by the changes in no more than an eighth of these terms, namely, the terms actually labeled in Figs. 5-3(b) to 5-3(g). It is also clear from Figs. 5-3(b) to 5-3(g) that significant changes of both the amplitude and sign of the key terms can occur with small changes in echo time. It must also be borne in mind that the lineshape of each of these SQC contributions differs one from another, and that the overall response can be represented by their weighted sum, where weighting factors correspond to the amplitudes of the SQC terms at the onset of acquisition, e.g., the amplitudes shown in Fig. 5-3. Using only the eight major terms for each of the four M and N spins, Fig. 5-4 demonstrates the close agreement between the numerically calculated response to the proposed filter and the corresponding experimental, phantom lineshape of the 3.6 ppm band. Notwithstanding, this close agreement with experiment arising from a restricted set of SQC terms, the ultimate comparison of experiment and theory for the optimized filter (shown in Fig. 5-7) made use of the full set of SQC terms.

To predict the optimal filter timings that suppress *strongly*-coupled Tau (but not mI), one must also evaluate, in response to the filter, and relative to mI, the dominating coherences for producing the Tau signal during acquisition. Because of symmetries in the A_2B_2 spin system just one of the four Tau spins, i.e., the A_1 spin, is sufficient to illustrate how these timing choices minimize the relative Tau signal. Three periods, namely, TE_1, TM and TE_2, are available for manipulating the relative strengths of the Tau and the mI signals. A key characteristic of the filter is that it specifically limits the terms that survive TM to longitudinal magnetization and to ZQC. The first step in suppressing Tau was therefore to minimize at the end of TE_1, the precursors of the Tau TM survivors.

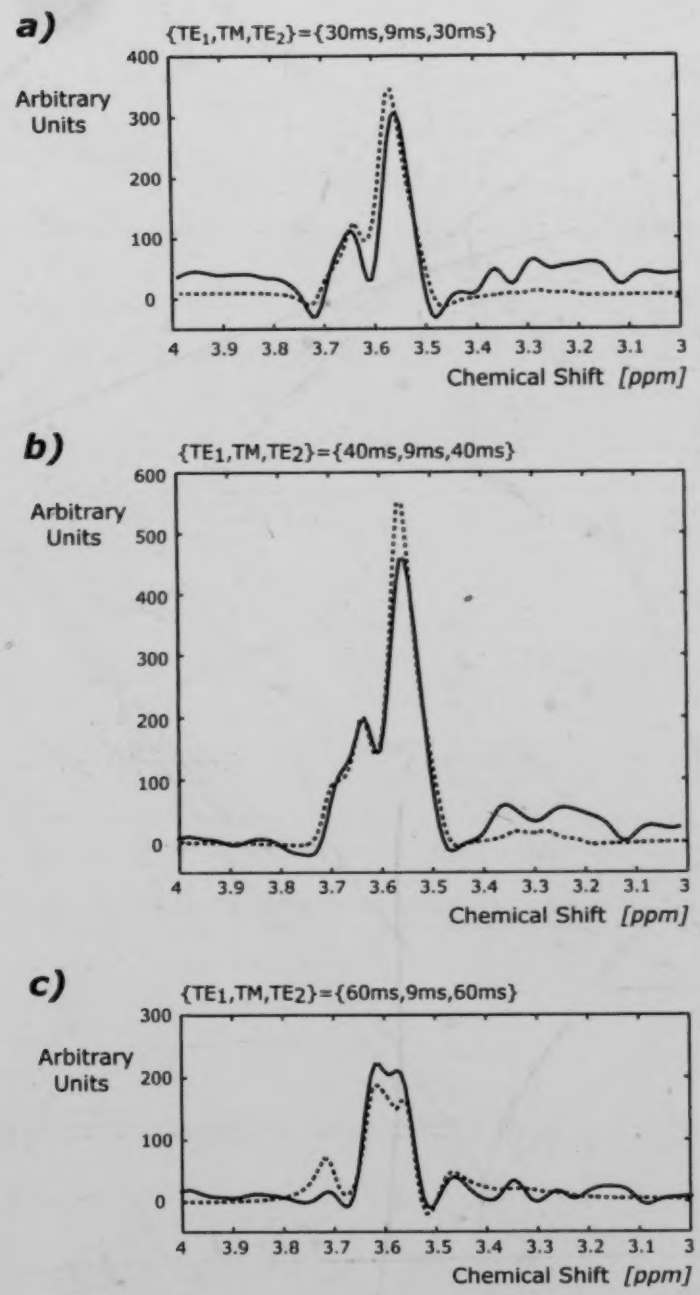

Figure 5-4 A comparison of the experimental phantom lineshapes of mI (solid lines) with the corresponding lineshapes (dashed lines) calculated using only the eight principal SQC terms of the M and N spins of mI. The comparisons are illustrated for three symmetric filters with $TE_1 = TE_2 = 30$ ms, 40 ms, and 60 ms respectively. The mixing time TM = 9 ms for all three filters.

The left side of Fig. 5-5 illustrates the evolution, during TE_1, of the precursor terms of TM survivors that could ultimately give rise to the emergence of the principal four of the 16 A_1 spin SQC terms, namely, A_{1x}, A_{1y}, $2A_{1x}B_{1z}$, and $2A_{1y}B_{1z}$, at the onset of acquisition.

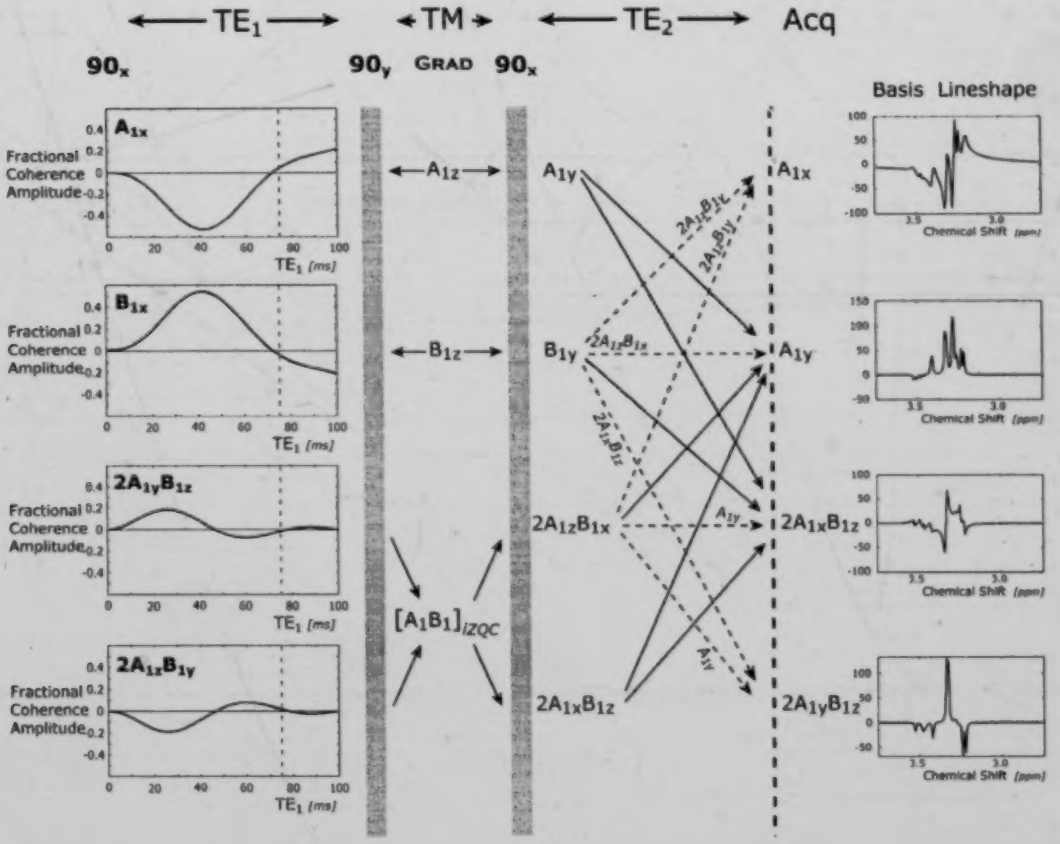

Figure 5-5 An evolutionary chart of representative coherence pathways for defining the Tau spectral response to the filter sequence. The temporal variation shown for TE_1, illustrates the most appropriate value of TE_1 for minimizing the gradient insensitive terms in the mixing time, TM, e.g., the longitudinal magnetization and the imaginary zero quantum coherence. The pathways shown under TE_2 illustrate the proliferation of coherences due to the *strong*-coupling interaction and emphasize the multi-source nature of the SQC giving rise to the lineshape components.

Clearly $TE_1 \sim 75$ ms emerges as a candidate for minimizing the TM survivors of Tau that is also consistent with the length of time needed for a significant decay of the

macromolecular signal. However, as emphasized later, these evolution curves are only a guide, and the acid test of suppression is the weighted summing of the basis lineshapes during acquisition. TM itself gives rise to very little evolutionary change and it was made just long enough (9 ms) to accommodate the selective pulse and the filter gradient. The second active step was to explore the adjustment of TE_2 to minimize the emergence of Tau SQC relative to mI SQC in the second echo period. The TE_2 period of Fig. 5-5 illustrates the proliferation of coherences after the third 90° pulse, emphasizing that due to the *strong*-coupling interaction transverse A magnetization can even arise from transverse B terms, e.g. A_{1x} and $2A_{1x}B_{1z}$ from either B_{1y} or $2A_{1z}B_{1x}$. However, in contrast to the TE_1 evolution, no clear minimum in the evolution of Tau SQC arises at acceptably short TE_2. The mI SQC are similarly slowly varying functions of TE_2. For example, if TE_2 varies from 30 ms to 50 ms, the mI intensity declines by ~ 30%, whereas Tau increases by ~ 10%. We therefore chose to maximize mI SQC at the onset of acquisition and at the shortest TE_2 consistent with this. During acquisition, each of the Tau SQC terms present at the onset will contribute its own basis lineshape to the overall Tau response, and it will do so in proportion to the amplitude of that term at the onset. The amplitude of each term at the onset is the sum over all its source pathways. The basis lineshapes for the representative SQC of the A_1 spin are shown in Fig. 5-5. The weighted sum of all major contributing Tau SQC, when compared to the corresponding sum for mI, leads to the prediction for optimum editing discrimination of an asymmetric filter with timings $\{TE_1, TM, TE_2\} = \{75 \text{ ms}, 9 \text{ ms}, 30 \text{ ms}\}$.

5.3 Methods

5.3.1 The Pulse Sequence

The first 90° pulse was a spatially-selective sinc pulse (3 ms long and ~ 3900 Hz in bandwidth) which was optimized to minimize the spatial extent of the tip-angle transition region (29). Because of its crucial role in generating MQC's, the second 90° pulse was chosen to be a rectangular, hard pulse, with as short a duration as possible (250 μs), thereby minimizing intra-pulse coherence evolution. This was made possible at 128

MHz using an 8 kW r.f. amplifier (Herley Industries Inc, Lancaster, PA). The importance of keeping this pulse short increases when *strongly*-coupled spins are involved, because of their rapid coherence transfer (16, 17). The third 90° pulse (the read pulse) was a frequency selective sinc-Gaussian pulse, optimized to excite uniformly all metabolite peaks upfield from the water resonance. The two 180° chemical shift refocusing pulses were also spatially selective (3.5 ms duration and 1200 Hz bandwidth) and similar in design to the initial 90° pulse. The phases of both the second and the third 90° pulses were carefully calibrated relative to that of the excitation pulse (see section 4.2.3). The length and amplitude of each slice-selection gradient was set to give rise to an excited voxel of $3 \times 3 \times 3$ cm^3 for both phantom and in-vivo experiments. To remove unwanted signals resulting from the incomplete refocusing that stems from the tip-angle profile of the nominal 180° pulses, these pulses were encapsulated within a pair of spoiler gradients of 2 ms duration and 20 mTm^{-1} amplitude. The filter gradient during TM (5 ms, 20 mTm^{-1}) was applied at the magic angle to enhance the suppression of residual water signal arising from the demagnetizing dipole-dipole interaction between water molecules (30). All r.f. pulses were phase-cycled (16 steps) to eliminate unwanted coherences which may have arisen from outside the volume of interest (31).

5.3.2 Spectroscopy

Four 6-cm diameter spherical aqueous phantoms were used to evaluate the sequence design. Each chemical was dissolved in distilled water. For all phantoms pH was adjusted to 7.1 ± 0.1 using hydrochloride and sodium hydroxide. The first, (phantom #1) contained only mI (50mM) and was used to confirm the numerically-determined timing variability of the mI response (Fig. 5-4). To verify the sequence discrimination of *strongly*-coupled spins from *un*coupled and *weakly*-coupled spins (Fig. 5-6), phantom #2 was prepared containing mI (with both *strongly*- and *weakly*-coupled spins) and creatine (Cr), in a 5:1 concentration ratio, with mI again at 50 mM. Thirdly, to represent the coupled-spin metabolites appearing in the proton spectrum of normal brain between 3.0 ppm and 4.0 ppm, phantom #3 was manufactured with mI, Glu, Gln, Gly, Tau and Cr in the relative concentrations, 1 : 1.3 : 0.6 : 0.2 : 0.5 : 1.1 respectively (20, 32, 33), and with

mI at 50 mM to maintain consistency with phantoms #1 and #2. The experimental performance of the filter was initially evaluated by comparing the responses of the phantoms to PRESS and to a series of three, symmetric-echo-time sequences, namely, {30 ms, 9 ms, 30 ms}, {40 ms, 9 ms, 40 ms} and {60 ms, 9 ms, 60 ms} in {TE_1, TM, TE_2} space. A fourth phantom, identical to phantom #3 in all respects except that Gly was removed, was used to demonstrate that the presence of Gly is clearly observable in the PRESS spectrum. All chemicals (purity ≥ 98%) were purchased from Sigma Chemical Co. (St. Louis, USA) except for Cr (ICN Biomedicals, Inc, Aurora, USA).

The in-vivo performance of the optimized filter was tested on a total of six volunteers (three males and three females). One of the results is shown in Fig. 5-7 (a 30 yr-old female volunteer). For all in-vivo experiments the spectra were acquired from a 3 x 3 x 3 cm^3 volume of the occipital lobe, over which ~ 6 Hz shim was obtained.

All experiments were carried out at 3.0 T in an 80-cm bore magnet (Magnex Scientific PLC, Abingdon, UK), using a home-built 28-cm i.d. quadrature birdcage coil for both transmission and reception. The spectrometer control was provided by an SMIS console (Surrey Medical Imaging Systems PCL, Guilford, UK). All phantom spectra were acquired with 32 averages (scan time < 2 min.) and subjected to a line broadening of ~ 6 Hz to produce correspondence with in-vivo spectra. In-vivo the number of averages and scan time were increased to 256 and < 13 min., respectively. For all experiments the repetition time (TR) was set to 3 s.

5.4 Results

The first objective was to demonstrate that the theoretical model correctly predicted the response of both *coupled* and *uncoupled* metabolite spin systems to the proposed filter. The second was to optimize this filter for the discrimination of mI from its contaminating background of *strongly*-coupled, *weakly*-coupled and *uncoupled* spins.

The multiplet resonances of mI close to 3.6 ppm can be roughly grouped into two closely neighboring bands, one designated α at ~ 3.54 ppm and the other, β, at ~ 3.62 ppm. These bands, which are resolvable at 3.0 T, display significantly different echo time dependences, not only in response to either the STEAM or the PRESS sequence, but also in response to the proposed filter sequence. This difference in response gives rise to lineshape and peak frequency variations in single voxel spectroscopy at 1.5 T which have not to our knowledge been reported. With the proposed filter at 3.0 T they provide a critical test of the numerical modeling, the efficacy of which is demonstrated in Fig. 5-4.

The ability of the filter to remove *uncoupled* and *weakly*-coupled resonances is shown in Fig. 5-6, where the response of phantom #2 to both PRESS and the proposed filter is illustrated. In phantom #2, Cr provides two uncoupled resonances, one at 3.0 ppm (methyl) and one at 3.9 ppm (methylene), whereas mI provides both a *weakly*-coupled resonance (A spin) at 4.06 ppm, as well as the band of *strongly*-coupled resonances around 3.6 ppm. Although all these resonances are present in the PRESS spectrum, all but the *strongly*-coupled signals are shown by Fig. 5-6 to be eliminated at all the echo-time combinations of the proposed filter.

The response of a portfolio of brain metabolites in the appropriate relative concentrations (20, 32, 33) both to a symmetric version of the proposed filter and to a symmetric PRESS sequence is illustrated in Fig. 5-6. There are two PRESS spectra shown in the right column of Fig. 5-6. They are presented to emphasize the clear demonstration at 3.0 T, of Gly adding to the α band of mI. Moreover, in the 3.0 T PRESS spectra the substantial spectral overlap of all resonances is clearly apparent, whereas only the *strongly*-coupled resonances of mI, Glx (at ~ 2.3 ppm) and Tau are able to penetrate the filter. The weakly-coupled A spins of Glx at ~ 3.75 pm are suppressed by the filter. The difference in echo-time sensitivities of the different strongly-coupled spins are also demonstrated in Fig. 5-6.

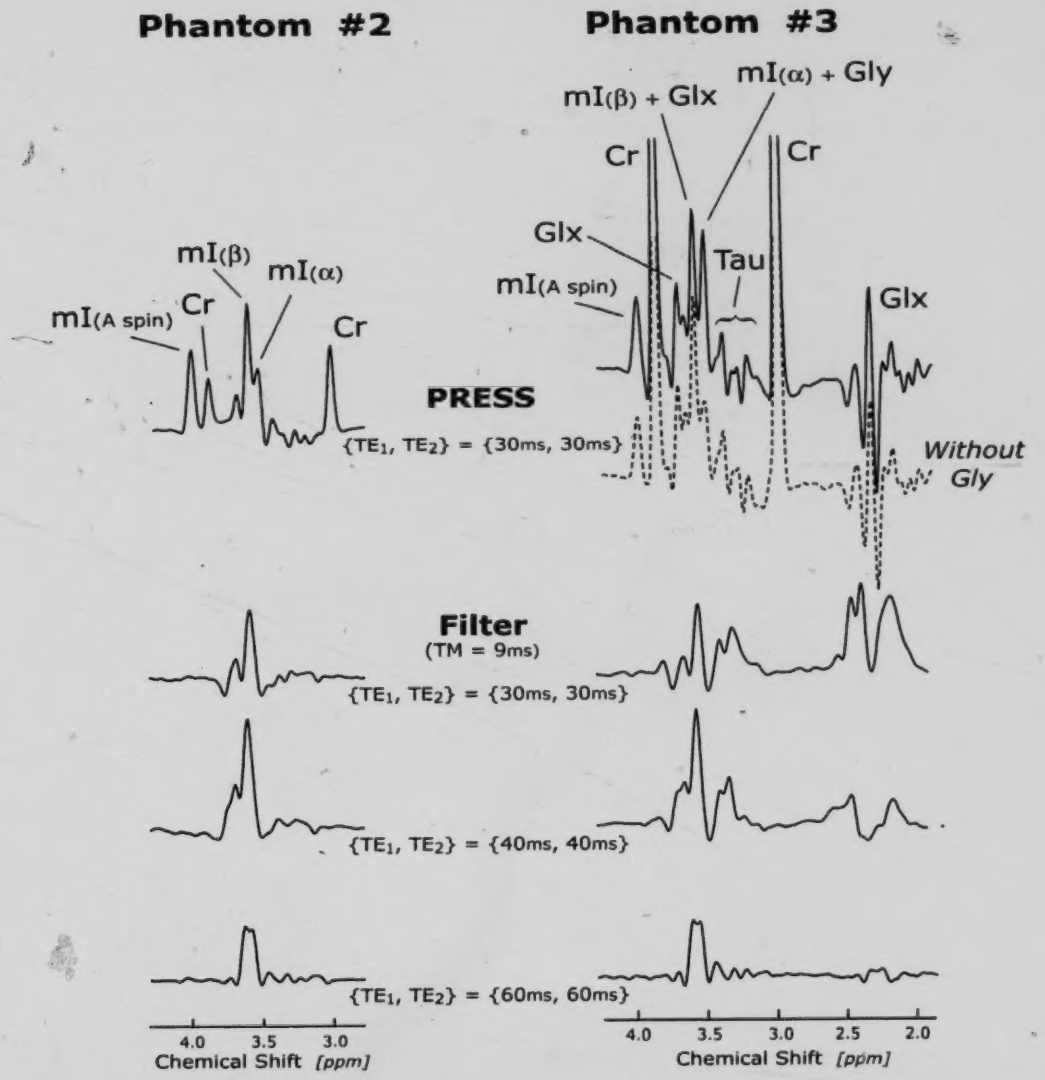

Figure 5-6 A comparison of the experimental phantom responses to a symmetric PRESS sequence {$TE_1 = TE_2 = 30$ ms} and to three symmetric filters with $TE_1 = TE_2 =$ 30 ms, 40 ms, and 60 ms respectively, and with a mixing time TM = 9 ms for all three filters. The column of spectra of the first phantom illustrated, namely, phantom #2, demonstrates the elimination of uncoupled and weakly-coupled resonances by the filter, as well as the non-singular TE dependence of the lineshape and its intensity. The second column, illustrating the spectra of phantom #3, demonstrates the elimination of *un*coupled and *weakly*-coupled background resonances of metabolites found in brain, as well as the suppression of Tau relative to mI. In comparison with the dashed spectrum of the supplemental phantom #3 (not containing Gly), the spectrum of the original phantom #3 strikingly illustrates the marked addition of the Gly resonance to the resonance of mI.

The performance of the optimized asymmetric filter, both on phantoms and in-vivo, is demonstrated in Fig. 5-7, by comparison with the corresponding asymmetric PRESS sequence.

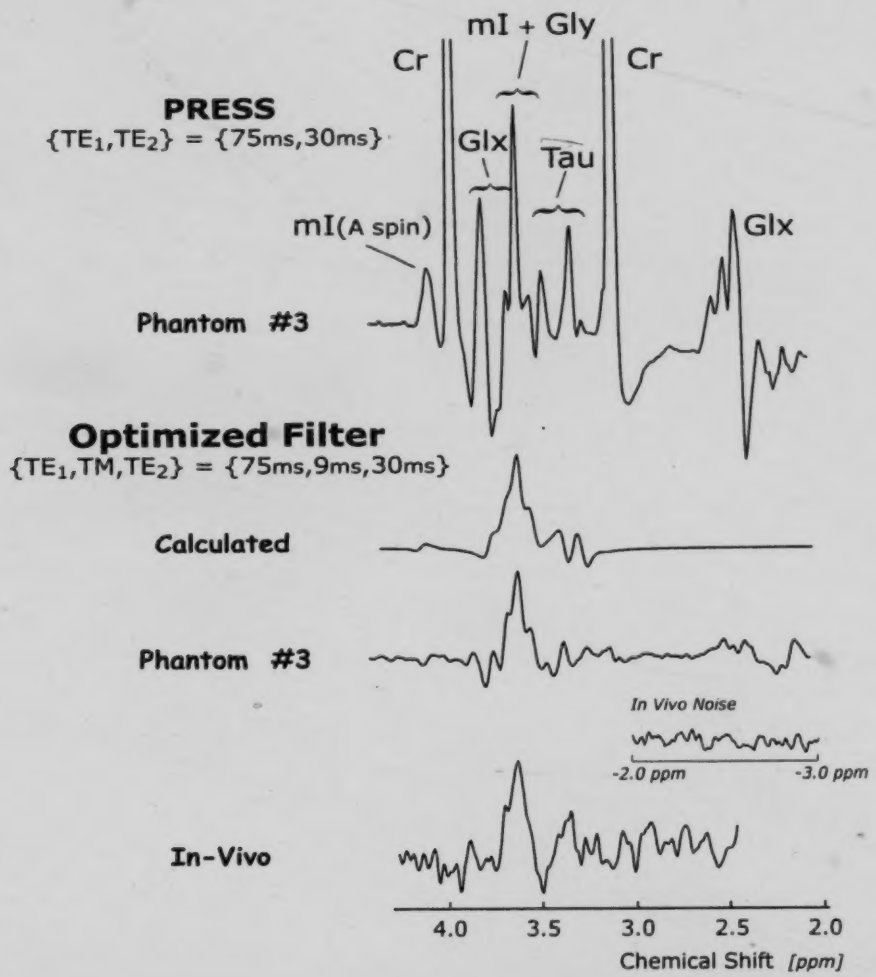

Figure 5-7 A comparison of spectral responses intended to establish the efficacy of the optimized filter in vivo. As a baseline spectrum, the response of the phantom of brain metabolites, namely, phantom #3, to a PRESS sequence correspondingly timed to the optimized filter is used. Because the timings are changed, this PRESS spectrum is different from that of Fig. 5-6. Tabulated below the PRESS spectrum are the responses to the optimized filter. First is that calculated for mI itself, second is that from phantom #3, and third is the in-vivo spectrum. The in-vivo spectrum between 3.5 ppm and 2.5 ppm displays residual background signals from metabolites with *strongly*-coupled spins, most notably the aspartate group of NAA, that were not included in phantom #3. The true noise level is represented by an insert panel of the baseline between -2 ppm and -3 ppm.

The phantom response to PRESS is quite different from that shown in Fig. 5-6 because of the difference and asymmetry of the echo times between the two figures. The close correspondence of both the lineshape and the spectral discrimination, between the calculated filter performance, that using phantoms, and that obtained in-vivo from the occipital cortex of a human brain is well demonstrated by Fig. 5-7.

5.5 Discussion

The prospective design of sequence parameters for both the preservation and the isolation of signal from a target metabolite is a valuable asset in brain spectroscopy. This is because many key brain metabolites contain *strongly*-coupled proton spins that give rise to an overlapping multiplet spectrum. The sequence proposed herein is superior to conventional DQFs, not only because it has the ability to suppress *weakly*-coupled spins along with *uncoupled* spins, but because it can also selectively discriminate between species of *strongly*-coupled spins by suppressing one relative to another. It is also more robust than a previously proposed filter for *strongly*-coupled spins (18) due to the reinforcement of phase-sensitive coherence selection with gradient filtering. The design strategy was demonstrated with a sequence whose goal was the isolation of mI at ~ 3.6 ppm. In-vivo, mI gives rise to a large resonance band at ~ 3.6 ppm that is severely corrupted, both by neighboring metabolite resonances (particularly co-resonant Gly) and also by a broad macromolecular band that effectively produces a sloping baseline (19-21). As a result of this sloping baseline, short echo-time PRESS or STEAM at 3.0 T show an adjacent Glx peak at ~3.8 ppm of comparable height to that of mI at 3.6 ppm, and the Cr methylene peak comparable in height to its methyl peak instead of in a 2:3 ratio (see Fig. 3-10(a)). The sequence proposed here avoids the macromolecular baseline artifact by extending the overall echo time beyond 100 ms. It eliminates background signal from *uncoupled* (Gly) and *weakly*-coupled (Glx) proton spins by coherence filtering and it differentially suppresses background signal from metabolites with *strongly*-coupled protons e.g. (Tau), by using appropriate echo times identified from the calculated coherence evolutions of the respective metabolites.

The principal justification for the filter is the suppression of background resonances sufficiently to enable target metabolite quantification to take place unambiguously. To assess the filter design and performance critically it was necessary, first, to use experimental phantom spectra (Figs. 5-4, 5-6 and 5-7), because the density matrix calculations included only metabolite spins and not the macromolecular spin that can also contribute to the spectral background in vivo. In anticipation of a macromolecular signal, the filter timings were chosen to ensure that the macromolecular transverse decay ran its course. To quantify background metabolite contamination, the calculated spectra corresponding to phantom # 3 predict a signal to background area ratio, S/B, of ~ 4.2 between 3.4 ppm and 3.75 ppm for the optimized filter, whereas for the correspondingly-timed PRESS sequence S/B ~ 0.8, i.e., a gain of a factor of 5 in favour of the filter. The optimization of the filter, which itself eliminated Glx and Gly, reduced the Tau intensity to 30% of that returned by the equivalently timed PRESS sequence. At these longer echo times, where the macromolecular background has decayed, calculated spectra, phantom spectra and in vivo spectra are all in close agreement (Fig. 5-7) and the numerical values of S/B from calculated spectra hold in vivo. Although there is also close agreement at short echo-times between calculated and phantom spectra for both PRESS and STEAM sequences, it would not be meaningful to compare calculated and phantom measures of S/B with in-vivo measures of S/B. This is because in vivo, at short echo times, the major distortion arises from the macromolecular signal, notwithstanding the ~ 10% contribution from unedited Gly (much greater at longer echo times) to the intensity of the α peak of the mI band in normal brain.

Of comparable importance to the minimization of background is an understanding of the actual yield of the target metabolite itself, in response to the pulse sequence employed. Yield (the signal intensity stripped of its transverse decay) is an essential (but sometimes neglected) element in the accurate determination of metabolite concentration from the spectrum. For coupled spins, the signal intensity evolution is not governed by T_2 alone, as it is for *un*coupled spins satisfying the vector model. It is also governed by the proliferation of coherences that originate with the spin-system coupling and that give rise to variations in yield that can be sensitive and irregular functions of sequence

parameters. Irregular variations in yield occur independently of whether the signals arise from PRESS, or STEAM or a filter sequence. This difference in the determinants of signal-intensity evolution between coupled and uncoupled spins can lead to quite misleading concentration estimates, if a direct ratio of coupled to uncoupled signal intensities is used, e.g., mI with the acetyl resonance of N-acetyl aspartate (NAA). Only if the mI to NAA yield ratio is known can the concentration be determined from the signal intensity ratio. The inability to calculate yield for a PRESS or STEAM acquisition is therefore no less an impediment to representative concentration estimates than is the absence of the internal "standard" singlet resonances in a multiple quantum filter spectrum. To quantify metabolites when multiple quantum filters are used, at least two options are available. The first, if a singlet resonance is preferred as an internal "standard", would be to track the evolution of the uncoupled spins through the filter sequence and then, following the filtered-signal acquisition, add a supplementary sequence to bring back the uncoupled-spin signal. Such a strategy was published several years ago (34). Alternatively, the intensity of a coupled resonance, not thought to be involved in the pathology and that has not been suppressed as part of the contaminating background of the target metabolite, could be used so long as all relative yields and lineshapes in the filtered spectrum were calculated. A similar strategy was adopted to estimate GABA concentration changes due to vigabatrin administration in normal volunteers (35).

To put into perspective the price paid in target-signal yield to achieve the optimum S/B, we note first, that the short-echo-time PRESS sequence $\{TE_1, TE_2\} = \{18$ ms, 16 ms$\}$ has an mI yield of only 70% of that of a 90^o - Acquire sequence (36). When the PRESS timing corresponds to that of the optimized filter proposed here, the yield is reduced to ~ 20%. By comparison, the maximum signal yield of mI for the proposed filter occurs at $\{TE_1, TM, TE_2\} = \{50$ ms, 9 ms, 30 ms$\}$ and is calculated to be ~ 25%. For optimal background suppression however, i.e., $\{TE_1, TM, TE_2\} = \{75$ ms, 9 ms, 30 ms$\}$, the yield drops to 15%. Thus in terms of yield and S/B, the optimized filter produces 75% of the equivalent PRESS sequence, but is five times better in background discrimination. Viewing this result in the light of S/N considerations, the optimized filter

gives a peak signal that is ~ 5 times the peak to peak noise at 3.0 T (S/N ~ 12, using the standard deviation of the noise).

The result and optimal sequence parameters presented in this paper are clearly dependent on the field strength. Deviations from the weak-coupling limit will be more marked at lower field strengths, and although this will provide a better signal yield for a *strongly*-coupled target resonance at 1.5 T, it will also impede the suppression of the resonances from metabolites whose proton coupling might be a better approximation to the weak-coupling limit at 3.0 T.

5.6 References

1. C. L. Dumoulin and D. Vatis, *Magn. Reson. Med.*, **3**, 282, 1986
2. C. H. Sotak, D. M. Freeman, and R. E. Hurd, *J. Magn. Reson.*, **78**, 355, 1988
3. L. A. Trimble, J. F. Shen, A. H. Wilman, and P. S. Allen, *J. Magn. Reson.*, **86**, 191, 1990
4. A. H. Wilman and P. S. Allen, *J. Magn. Reson.*, **B105**, 58, 1994
5. A. H. Wilman and P. S. Allen, *J. Magn. Reson.*, **B109**, 169, 1995
6. L. Jouvensal, P. G. Carlier, and G. Bloch, *Magn. Reson. Med.*, **36**, 487, 1996
7. J. L. Keltner, L. L. Wald, B. B. Frederick, and P. F. Renshaw, *Magn. Reson. Med.*, **37**, 1997
8. J. R. Keltner, L. L. Wald, P. J. Ledden, Y. I. Chen, R. T. Matthews, J. R. Baker, B. R. Rosen, and B. G. Jenkins, *Magn. Reson. Med.*, **39**, 651, 1998
9. R. B. Thomson and P. S. Allen, *Magn. Reson. Med.*, **39**, 762, 1998
10. A. H. Trabesinger, O. M. Weber, C. O. Duc, and P. Boesiger, *Magn. Reson. Med.*, **42**, 283, 1999
11. H. Lei and J. Peeling, *J. Magn. Reson.*, **143**, 95, 2000
12. M. A. McLean, A. L. Busza, L. L. Wald, R. J. Simister, G. J. Barker, and S. R. Williams, *Magn. Reson. Med.*, **48**, 233, 2002
13. P. A. Bottomley, *US Patent,* **4(480)**, 228, 1984
14. R. J. Ordidge, M. R. Bendall, R. E. Gordon, and A. Connelly, *Magnetic resonance in biology and medicine,* McGraw-Hill, 1985. p387
15. J. Frahm, K. D. Merboldt, and W. Hanicke, *J. Magn. Reson.*, **72**, 502, 1987
16. R. B. Thomson and P. S. Allen, *Magn. Reson. Med.*, **41**, 1162, 1999
17. R. B. Thomson and P. S. Allen, *Magn. Reson. Med.*, **45**, 955, 2001
18. A. H. Trabesinger, D. C. Mueller, and P. Boesiger, *J. Magn. Reson.*, **145**, 237, 2000
19. K. L. Behar, D. L. Rothman, D. D. Spencer, and O. A. C. Petroff, *Magn. Reson. Med.* **32**, 294, 1994
20. S. W. Provencher, *Magn. Reson. Med.*, **30**, 672, 1993
21. L. Hofmann, J. Slotboom, C. Boesch, and R. Kreis, *Magn. Reson. Med.*, **46**, 855, 2001

22. H. Kim, J. M. Wild, and P. S. Allen, *Proc. ISMRM,* Glasgow, 2001, p. 621
23. A. Bax, P. G. de Jong, A. F. Mehlkopf, and J. Smidt, *Chem. Phys. Lett.*, **69**, 567, 1980
24. L. E. Kay and R. E. D. McClung, *J. Magn. Reson.*, **77**, 258, 1988
25. K. L. Behar, and T. Ogino, *Magn. Reson. Med.*, **17**, 285, 1991
26. K. Young, V. Govindaraju, B. J. Soher, and A. A. Maudsley, *Magn. Reson. Med.*, **40**, 812, 1998
27. K. Young, B. J. Soher, and A. A. Maudsley, *Magn. Reson. Med.*, **40**, 816, 1998
28. R. R. Ernst, G. Bodenhausen, and A. Wokaun, *Principles of Nuclear Magnetic Resonance in One and Two Dimensions*, Clarendon Press, 1987
29. G. B. Matson, *Magn. Reson. Imag.*, **12**, 1205, 1994
30. W. Richter, S. Lee, W. S. Warren, and Q. He, *Science*, **267**, 654, 1995
31. J. Hennig, *J. Magn. Reson.*, **96**, 40, 1992
32. R. Kreis, T. Ernst, B. D. Ross, *J. Magn. Reson.*, **B102**, 9, 1993
33. B. D. Ross, *NMR in Biomed.*, **4**, 59, 1991
34. A. H. Wilman, M. Astridge, R. E. Snyder, and P. S. Allen, *J. Magn. Reson., 109(B)*, 202, 1995
35. C. C. Hanstock, N. J. Coupland, and P. S. Allen, *Magn. Reson. Med.*, **48**, 617, 2002
36. H. Kim and P. S. Allen, *Proc. ISMRM*, Denver, 2000, p. 1943

CHAPTER 6

In Search of the Complete Set of Optimum Sequence Parameters in the Design of MQF in In-Vivo ^{1}H MRS

6.1 Introduction

A Multiple quantum filter (MQF) has been used for the detection of brain metabolites with coupled-spins for its effective background suppression (1-9). Among the choice of the level of coherences to be filtered out, which depends on the number of spins in the spin system, zero quantum and double quantum coherence (ZQC and DQC, respectively) filtering are preferred for their relatively higher sensitivity. Despite its higher sensitivity than double quantum filter (DQF) by a factor of 2 in principle, the use of a zero quantum filter (ZQF) is limited when uncoupled spin resonances are present in a targeted spectral region, due to its nature of being permeable to those uncoupled spins.

In order to make the application of these sophisticated filtering techniques more feasible in an in-vivo study where both the intrinsic poor signal yield of the filter sequences and the low concentrations of cerebral metabolites need to be dealt with simultaneously, a continuous effort has been made to improve the performance of MQFs, starting from the incorporation of spatial localization into the filter design (10, 11). In addition, the first and the second echo times (TE_1 and TE_2, respectively), which can deviate from the conventional 1/2J for the production of maximum anti-phase coherences (APCs) before the irradiation of multiple quantum coherence (MQC)-generating 90° pulse (12), must be optimized along with the flip-angle (13) and the duration (1) of the third nominal 90° read pulse that converts MQCs back into APCs as well as the frequency selectivity of that pulse for maximum coherence transfer into the target peak. Moreover, the directional adjustment of filter gradient(s) needs to be considered for additional water suppression (1).

For maximum signal yield of even-order MQFs, it has previously been assumed that the phase of the MQC-generating second 90° pulse (MQ-pulse) needs to be tuned identical to that of the first 90° excitation pulse, regardless of the degree of scalar coupling of a spin system (2-4). For odd-order filtering, it has also been assumed that the MQ-pulse should be 90° out-of-phase with the excitation pulse, i.e., a phase of y if the excitation pulse has a phase of x. However, as was demonstrated in Reference *14*, by changing the phase, φ, of the MQ-pulse from x to y, the conventional ZQF becomes capable of generating coherences that arise during TE_1 solely from strong-coupling interactions.

In this report we first examine the physical significance of the phase of the MQ-pulse through both analytical and numerical analysis, secondly, extend its concept to the DQF, and finally propose that to obtain the best discrimination of a strongly-coupled spin system from its background, the phase of the MQ-pulse needs to be incorporated into the portfolio of sequence parameters that must be optimized, i.e., TEs, TM, the flip angle, θ, and duration of the nominal 90° read pulse, as well as frequency selectivity of that pulse (Fig. 6-1).

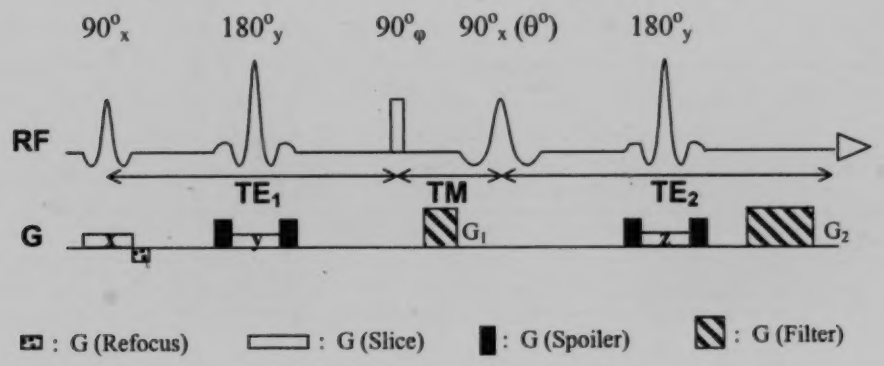

Figure 6-1 A simplified diagram of a generic multiple quantum filter sequence. The second $90°_{\varphi}$ MQC-generating pulse and the filter gradient during TM play a key role in the filtering mechanism. The third (nominal) 90° frequency-selective read pulse excites all metabolite ppm ranges upfield from water. The second filter gradient G_2 is set to 0 for a ZQF and to $2 \times G_1$ for a DQF.

The optimization of the phase of the MQ-pulse allows us not only to distinguish strongly-coupled spins from weakly-coupled and uncoupled spins (14), but it also allows us to differentiate between different strongly-coupled spin systems, an objective that was approached previously through the optimization of sequence timings (14). This is a significant point, because at 3.0 T and even higher fields, the majority of the spin systems of key brain metabolites fall into the strong-coupling regime, e.g., aspartate (Asp; ABX spin system), glutamate (AMNPQ), glutamine (AMNPQ) (Glu and Gln, respectively and Glx for both), glutathione (GSH; ABX and AM_2PQ), myo-Inositol (mI; AM_2N_2P), aspartate group of N-acetylaspartate (NAA; ABX) and taurine (Tau; A_2B_2) (15, 16).

6.2 Methods

6.2.1 Theory

In order to examine the physical significance of the phase of the MQ-pulse, density operators, $\rho(t)$'s, of a strongly-coupled AB spin system of citrate (Cit) were calculated with the phase of that pulse, φ, as a variable. All calculations were based on the Cartesian product operators that were derived from the spherical basis set used in Reference *17*.

Upon the use of the full J-coupling Hamiltonian, H_J (= $2\pi J_{AB}(A_zB_z + A_xB_x + A_yB_y)$), just after the first spin-echo period (just before the MQ-pulse), the density operator takes the form of

$$\begin{aligned}\rho(TE_1^-) = {} & A_x\cdot S_1 + A_y\cdot W_2^+ + 2A_xB_z\cdot W_1^+ + 2A_yB_z\cdot S_2 \\ & - B_x\cdot S_1 + B_y\cdot W_2^+ + 2B_xA_z\cdot W_1^+ - 2B_yA_z\cdot S_2 \end{aligned} \qquad (6\text{-}1a)$$

where

$$\begin{aligned} W_1^{\pm} = {} & -\sin(\pi J\cdot t)\,\{\cos^2(\Lambda\cdot t/2) + [(\delta\omega/\Lambda)^2 - (\pi J/\Lambda)^2]\sin^2(\Lambda\cdot t/2)\} \\ & \pm (\pi J/\Lambda)\sin(\Lambda\cdot t)\cos(\pi J\cdot t), \end{aligned}$$

$$W_2^{\pm} = \cos(\pi J\cdot t)\,\{\cos^2(\Lambda\cdot t/2) + [(\delta\omega/\Lambda)^2 - (\pi J/\Lambda)^2]\sin^2(\Lambda\cdot t/2)\}$$
$$\pm (\pi J/\Lambda)\sin(\Lambda\cdot t)\sin(\pi J\cdot t),$$
$$S_1 = -2(\delta\omega/\Lambda)(\pi J/\Lambda)\sin^2(\Lambda\cdot t/2)\sin(\pi J\cdot t),$$
$$S_2 = 2(\delta\omega/\Lambda)(\pi J/\Lambda)\sin^2(\Lambda\cdot t/2)\cos(\pi J\cdot t),$$

and

$$\Lambda = [(\delta\omega)^2 + (\pi J)^2]^{1/2},\ \delta\omega = (\omega_A - \omega_B)/2,\ t = TE_1. \qquad (6\text{-}1b)$$

Upon using the weak-coupling approximation where the J-coupling Hamiltonian reduces to $H_J^{weak} = 2\pi J_{AB}(A_zB_z)$, the coefficients in Eq. (6-1b) simplifies to $W_1^{\pm} \sim -\sin(\pi J\cdot TE_1)$ and $W_2^{\pm} \sim \cos(\pi J\cdot TE_1)$, while $S_1 = S_2 \sim 0$, thereby leaving

$$\rho(TE_1^-)^{weak} = A_y\cdot W_2^+ + 2A_xB_z\cdot W_1^+ + B_y\cdot W_2^+ + 2B_xA_z\cdot W_1^+$$
$$= A_y\cdot\cos(\pi J\cdot TE_1) - 2A_xB_z\cdot\sin(\pi J\cdot TE_1) + B_y\cdot\cos(\pi J\cdot TE_1) - 2B_xA_z\cdot\sin(\pi J\cdot TE_1), \qquad (6\text{-}2)$$

which is a familiar form for a weakly-coupled two-spin system just after the first spin-echo period. Comparison of Eqs. (6-1a) with (6-2) clearly shows that the coherence terms such as A_x, $2A_yB_z$, B_x and $2B_yA_z$ are produced solely from strong-coupling interactions during TE_1 (14, 18). In fact, those are the terms that are observable with Trabesinger et al's single quantum filter (SQF) (18). In contrast, the rest of the terms in Eq. (6-1a) such as A_y, $2A_xB_z$, B_y and $2B_xA_z$ are produced from both weak- and strong-coupling interactions. For instance, A_y at the end of the first spin-echo period, is produced not only from the initial A_y term through the weak-coupling interaction, which is created by the first excitation pulse, but from initial B_y through coherence transfer under the strong-coupling interaction as well (the second term in $W_2^{\pm}$ in Eq. (6-1b)). That is, the second terms in $W_1^{\pm}$ and $W_2^{\pm}$ originate from the strong-coupling interaction through coherence transfer. In further calculations, coherence terms that originate from those strong-coupling specific terms can be identified by tracing the coefficients S_1 and S_2.

6.2.1.1 ZQF

Just after the MQ-pulse in a ZQF sequence, the density operator becomes

$$\rho(TE_1^+)_{ZQF} \sim A_z[S_1 \cdot \sin(\varphi) - W_2^+ \cdot \cos(\varphi)] - B_z[S_1 \cdot \sin(\varphi) + W_2^+ \cdot \cos(\varphi)] + 2(A_xB_y - A_yB_x)[S_2 \cdot \sin(\varphi)], \quad (6\text{-}3a)$$

which reduces upon using the weak-coupling approximation to

$$\rho(TE_1^+)_{ZQF}^{weak} \sim -(A_z + B_z) \cdot \cos(\pi J \cdot TE_1) \cdot \cos(\varphi). \quad (6\text{-}3b)$$

Since longitudinal magnetizations also contribute to the signal of a ZQF, they are also included in Eqs. (6-3a) and (6-3b). The change in the level of coherence by the MQ-pulse is reflected in the argument of trigonometric functions, i.e., φ and $-\varphi$ ($\cos(\varphi)$ being expanded into $\frac{1}{2}[\cos(\varphi) + \cos(-\varphi)]$) in Eq. (6-3a), originating from the change in the level of coherence of $-1 \rightarrow 0$ and of $+1 \rightarrow 0$, respectively (19). The φ-dependence of those coherence terms in Eq. (6-3a) are shown in Fig. 6-2(a) (dotted line) where $TE_1 = 30$ ms, $\delta\omega = 15.36\pi$ and $J_{AB} = 15.4$ Hz were used. The calculated results using numerical methods (1) are also shown in the same panel (solid line). None of those terms show a monotonic decay in response to varying φ. For instance, A_z has its maximum amplitude at $\varphi \sim 50^\circ$ and the minimum amplitude of B_z appears at $\varphi = 40^\circ$, while the amplitude of the ZQC term, $2(A_xB_y - A_yB_x)$, increases as a function of $\sin(\varphi)$. Eqs. (6-3a) and (6-3b) show that for a conventional ZQF with the phase of the MQ-pulse tuned to x, the ZQ-filtered signal of a two-spin system (both AX and AB spin systems) originates from z-magnetizations only (none from ZQC). However, as the phase of the MQ-pulse is tuned away from x, ZQCs that originate exclusively from the strong-coupling interaction during TE_1 (14) also take part in the ZQ-filtered signal of the AB system. Note that in Eq. (6-3a) the S's, which are the coefficients of the coherence terms produced solely from strong-coupling interactions during TE_1, are coupled to a sine function whereas the W's are coupled to a cosine function. This means that the φ-dependent curve of final signal will

be a combined function of cos(φ) and sin(φ) whose weighting factors are S's and W's, respectively, which are functions of sequence timings.

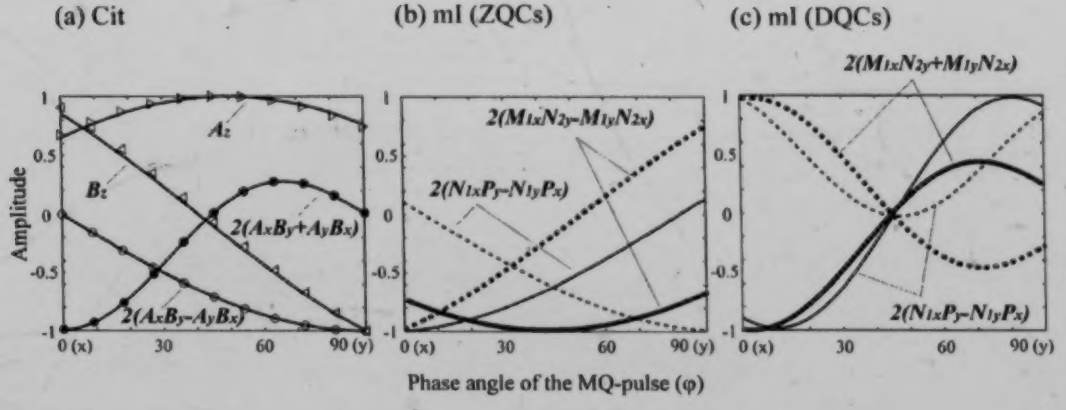

Fig. 6-2 The φ-dependence of the representative coherence terms of citrate and *myo*-Inositol just after the MQ-pulse. Shown in (a) are the calculated response of z-magnetization A_z and B_z of Cit to varying phase of the MQ-pulse after a TE_1 period of 30 ms. Also shown in the same panel are DQC term $2(A_xB_y + A_yB_x)$ and ZQC term $2(A_xB_y - A_yB_x)$ of Cit. In (b), the φ-dependence of the two representative ZQCs of mI are illustrated with TE_1 of 30 ms (solid lines) and 60 ms (dotted lines). Shown in (c) is the φ-dependence of the two representative DQCs of mI with TE_1 of 50 ms (solid lines) and 80 ms (dotted lines). Unlike for Cit shown in (a), the DQCs of mI can have non-zero values at φ = 90°. A step size of 2° was used for the numerical calculations and 9° for analytic solutions. Each curve was normalized to its own maximum amplitude.

For instance, for $TE_1 = TE_2$, the signal of A-spin (2.54 ppm) of Cit, S_{Ay}, is calculated by taking the coefficient of A_y at the onset of acquisition to be

$$\begin{aligned} S_{Ay} \sim\ & \cos(\varphi)\cdot(W_2^{+})^2 + \sin(\varphi)\cdot< S_1\cdot\ [\ \{(\delta\omega/\Lambda)^2 + (\pi J/\Lambda)^2\cdot\cos(2\Lambda\cdot TM)\}\cdot W_2^{-} \\ & + \{(\pi J/\Lambda)\cdot\sin(2\Lambda\cdot TM)\}\cdot W_1^{-}\ ] \\ & + S_2\cdot\ [\ \{\cos(2\Lambda\cdot TM)\}\cdot W_1^{-} \\ & - \{(\pi J/\Lambda)\cdot\sin(2\Lambda\cdot TM)\}\cdot W_2^{-}\ ] >. \end{aligned} \qquad (6\text{-}4)$$

At certain phase angles of 0°, 30° and 90°, Eq. (6-4) can be arranged as $S_A(\varphi = 0^\circ) = S_A(W_2^+)$, $S_A(\varphi = 45^\circ) = S_A(W_2^+, S_1, S_2)$ and $S_A(\varphi = 90^\circ) = S_A(S_1, S_2)$. Therefore, the physical consequence of rotating the phase of the MQ pulse is that it controls the proportion of the two groups of coherence terms with different origins in the final signal, one being produced during TE_1 from both weak- and strong-coupling interactions obeying cos(φ), and the other arising exclusively from the strong-coupling interaction obeying sin(φ). The net φ-dependent curve of signal is ultimately determined in combination with W's and S's, which are weighting factors of cos(φ) and sin(φ), and are functions of sequence timings. In general a combination curve of sine and cosine function can exhibit various shapes depending on their weighting factors. For example, a monotonic decaying curve will be obtained when the weighting factor of the cosine function is dominant over that of the sine function, or monotonous increasing when vice versa. When the two weighting factors are comparable to each other, the maximum can occur at an intermediate phase angle. For example, when $TE_1 = TE_2 = 30$ ms, TM = 9 ms, $\delta\omega = 15.36\pi$ and J = 15.4 Hz in Eq. (6-4), the coefficient of cos(φ) and sin(φ) are 0.43 and 0.48, respectively. Therefore, at these sequence timings, the maximum signal (area of spectrum) of the A-spin of Cit will take place at an intermediate phase angle.

According to Eqs. (6-3a) and (6-3b), the φ-dependence of coherence terms is determined by the change in the level of coherence brought about by the MQ-pulse. Therefore, an analytic solution for the φ-dependence of other weakly-coupled spin systems can simply be derived. For example, using Eq. [4] of Reference *12* and including z-magnetization as in Eq. (6-3a), the density operator for the X_3 doublet of Lac (a weakly-coupled AX_3 spin system) can be written just after the MQ-pulse in a ZQF as

$$\rho(TE_1^+)_{ZQF} \rightarrow \{(X_z)\cdot\cos(\pi J\cdot TE_1) - (A_xX_y - A_yX_x)\cdot\sin^3(\pi J\cdot TE_1)\}\cdot\cos(\varphi) \qquad (6\text{-}5)$$

where $X_\mu = X_{1\mu} + X_{2\mu} + X_{3\mu}$ and μ = x, y, or z. Therefore the φ-dependent response of the X_3 doublet of the AX_3 spin system of Lac just after the MQ-pulse is identical to that of AX spin system as in Eq. (6-3b), which is a simple decay as a function of cos(φ),

regardless of the choice of TE_1. Note that as described in Eq. [4] of Reference *12* and also in Eq. (6-5) in this report, the absence of ZQC in a conventional ZQF experiment is specific to a two-spin system.

Likewise, just after the MQ-pulse, the density operator for an uncoupled spin with varying phase of the MQ-pulse is simply

$$\rho(TE_1^{+}) = I_z \cdot \cos(\varphi), \tag{6-6}$$

which shows that the ZQ-filter signal of an uncoupled spin will decay as a function of $\cos(\varphi)$ irrespective of sequence timings. Thus, as was demonstrated in Reference *14*, when a target metabolite includes a strongly-coupled spin system, ZQF with the phase of the MQ-pulse tuned to y can be as useful as DQF even with the presence of uncoupled spin resonance in the target spectral region.

Due to the absence of net ZQC at $\varphi = 0^{\circ}$, which is specific to a two-spin system, i.e., no net ZQC is produced from $2A_xB_z$ and $2B_xA_z$, which are APCs available for both weakly- and strongly-coupled spin systems, Eq. (6-3a) does not contain sufficient information on an analytic form of the φ-dependence of ZQCs. For better understanding of the φ-dependence of coherences, more complicated strongly-coupled spin systems need to adopted such as an ABC spin system, for which the analytic solutions are yet to be found. Nonetheless, for more complicated strongly-coupled spin systems the φ-dependence of ZQCs may be generalized by including W's coupled to $\cos(\varphi)$ in addition to S's coupled to $\sin(\varphi)$ (n.b.: here W's and S's are coefficients of APCs available for both weakly- and strongly-coupled spin systems, and for strongly-coupled spin systems, respectively, such as those in Eq. (6-1a)), similar to that of longitudinal magnetization in Eq. (6-3a) and, in conformation with that of the X_3 doublet of Lac in Eq. (6-5). Clearly, since no *even*-order MQC is created by the y-phased ($\varphi = 90^{\circ}$) MQ-pulse from APCs available for weakly-coupled spins (such as $2A_xX_z$, $4A_yM_zX_z$, $8A_xM_zQ_zX_z$, etc., present at the end of the TE_1 period), the existence of terms such as W's coupled to $\sin(\varphi)$ is

excluded. As well, the existence of terms such as S's coupled to cos(φ) is not significant in terms of the origin of the filtered signal at φ = 90°. Although due to active coherence transfer during the TM and TE_2 periods, each MQC term cannot directly be related to the final filtered signal, Fig. 6-2(b) illustrates the numerically calculated (1) φ-dependence of the ZQCs of mI, $2(M_{1x}N_{2y} - M_{1y}N_{2x})$ and $2(N_{1x}P_y - N_{1y}P_x)$ with a TE_1 of 30 ms (solid lines) and 60 ms (dotted lines). Both MN- and NP-pairs are strongly-coupled. The evolution curve of $2(M_{1x}N_{2y} - M_{1y}N_{2x})$ at TE_1 = 30 ms and at 60 ms takes a form similar (with opposite sign) to that of A_z and B_z of Cit shown in Fig. 6-2(a), respectively. The evolution curve of $2(N_{1x}P_y - N_{1y}P_x)$ can be identified as - cos(φ) at TE_1 = 30 ms and - sin(φ) at TE_1 = 60 ms just like the $2(A_xB_y - A_yB_x)$ term of Cit in panel (a). In particular, the φ-dependence of the $2(N_{1x}P_y - N_{1y}P_x)$ term at those two different TE_1's clearly demonstrates that the analytic form of that φ-dependence contains both cos(φ) and sin(φ) whose weighting factors (W's and S's) are sequence timing dependent.

6.2.1.2 DQF

Just after the MQ-pulse, the density operator for DQFs becomes

$$\rho(TE_1^+)_{DQF} \sim 2(A_xB_x - A_yB_y)(1/2)\{W_1^+\cdot[\sin(\varphi) + \sin(3\varphi)]\} - 2(A_xB_y + A_yB_x)(1/2)\{W_1^+\cdot[\cos(\varphi) + \cos(3\varphi)]\}. \quad (6\text{-}7)$$

The change in the level of coherence brought about by the MQ-pulse is reflected in the arguments of the trigonometric functions, i.e., φ and 3φ, originating from the change in the level of coherence of + 1 → + 2, and of - 1 → + 2, respectively. Although it is not converted by the third 90° read pulse into observable SQCs, $2(A_xB_x - A_yB_y)$ is retained in Eq. (6-7) since it evolves under the chemical-shift Hamiltonian during TM into $2(A_xB_y + A_yB_x)$, which is then converted into observable SQCs. Thus, following a non-zero TM period, the function, sin(3φ) + sin(φ), will also take effect in the φ-dependence of $2(A_xB_y + A_yB_x)$.

The φ-dependence of $2(A_xB_y + A_yB_x)$ in Eq. (6-7) is shown in Fig. 6-2(a) as a dotted line where TE_1 = 30 ms, $\delta\omega = 15.36\pi$ and J_{AB} = 15.4 Hz. The numerically calculated one is also shown in the same panel as a solid line. The minimum amplitude of the term occurs at $\varphi = 45^\circ$ and 90°. Note that the coefficient S_2 is not involved in Eq. (6-7), i.e., no DQC is produced from the strong-coupling specific APCs in the AB spin system, and that both real and imaginary DQC terms become null at $\varphi = 90^\circ$.

Further calculation leads, for $TE_1 = TE_2$, to

$$S_{real} = (1/2)(W_1^+)^2\{\sin(2\varpi TM)[\sin(\varphi) + \sin(3\varphi)] - \cos(2\varpi TM)[\cos(\varphi) + \cos(3\varphi)]\} \quad (6\text{-}8a)$$

and

$$S_{mag} = (S_{real}^2 + S_{imag}^2)^{1/2} = \cos(\varphi)\cdot(W_1^+)^2 \quad (6\text{-}8b)$$

where S_{real} and S_{mag} denotes signal in real and in magnitude mode, respectively, and $\varpi = (\omega_A + \omega_B)/2$. As discussed above, Eq. (6-8a) includes $(\sin(\varphi) + \sin(3\varphi))$-dependence. Upon substitution with $\varphi = 0^\circ$ and for a specific TM, Eq. (6-8a) reduces to Eq. [1] in Reference *20*, which is a solution for the AB spin system of Cit in response to a conventional DQF. According to Eq. (6-8b), the DQ-filtered signal of the AB spin system measured by the area under the spectrum in magnitude mode will decay as a function of $\cos(\varphi)$ and becomes null at $\varphi = 90^\circ$ regardless of the choice of the sequence timings.

As no DQC term is produced from the strong-coupling specific APCs irrespective of the phase angle of the MQ-pulse, the AB spin system we adopted here is equivalent to a weakly-coupled AX spin system in terms of the φ-dependence of DQCs and consequently falls short of providing for general information on the φ-dependence of DQCs of strongly-coupled spin systems. For more complicated *weakly-coupled* spin system such as that of Lac whose deviation from the weak-coupling approximation is negligible, the φ-dependence of DQC terms such as $2(A_xX_{1y} + A_xX_{1y})$ (imaginary

component) and $2(A_xX_{1x} - A_yX_{1y})$ (real component) are identical to those of AB (or AX) spin system in Eq. (6-7), all of which become null at $\varphi = 90^\circ$ (results not shown). In contrast, however, for more complicated *strongly-coupled* spin systems such as mI, DQC terms can have a non-zero amplitude even at $\varphi = 90^\circ$. Using numerical methods, this is illustrated in Fig. 6-2(c) where the φ-dependence of the representative DQCs, $2(M_{1x}N_{2y} + M_{1y}N_{2x})$ and $2(N_{1x}P_y + N_{1y}P_x)$, of mI are shown at TE_1 of 50 ms (solid lines) and 80 ms (dotted lines). For a ZQF in the previous section, the two functions, $\cos(\varphi)$ and $\sin(\varphi)$, were used as a basis set for the description of the φ-dependence of ZQCs of strongly-coupled spin systems and the non-zero amplitude of their ZQCs at $\varphi = 90^\circ$ was explained. A feasible analytic form of the φ-dependence of DQCs of strongly-coupled spin systems, however, cannot be inferred from Eq. (6-7) in the similar fashion, since the two functions, $(\sin(\varphi) + \sin(3\varphi))$ and $(\cos(\varphi) + \cos(3\varphi))$, in the equation become null simultaneously at $\varphi = 90^\circ$. Nonetheless, since it is certain that no *even*-order MQC can be produced by the y-phased ($\varphi = 90^\circ$) MQ-pulse from APCs available for weakly-coupled spins, the existence of DQCs with non-zero amplitude at $\varphi = 90^\circ$ such as $2(M_{1x}N_{2y} + M_{1y}N_{2x})$ and $2(N_{1x}P_y + N_{1y}P_x)$ of mI can be regarded as specific to strongly-coupled spin systems.

6.2.2 Experiments

A total of six 6-cm diameter spherical phantoms were produced individually for Cit, Tau, Glu, Gln and mI as well as for Lac. Each chemical was dissolved in distilled water. Although it is not found in the human brain, Cit was used to verify analytic calculations. All phantom concentrations were maintained at 50 mM. In addition, a mixed phantom was made containing creatine (Cr), glycine (Gly), Tau, Glu, Gln and mI at relative physiological concentrations of the normal human brain (21, 22) with the mI concentration normalized to 50 mM. For all phantoms pH was adjusted to 7.1 ± 0.1 using hydrochloride and sodium hydroxide. All chemicals (purity $\geq$ 98%) were purchased from Sigma Chemical Co. (St. Louis, USA) except for Cr (ICN Biomedicals, Inc, Aurora, USA).

All experiments were carried out in a 3.0 T Magnex, 80 cm bore magnet with a SMIS spectrometer console. The first 90° pulse is an optimized sinc pulse of 3 ms duration and 4000 Hz bandwidth. A rectangular, hard pulse was chosen for the MQ-pulse with a duration of 250 μs. The third 90° read pulse was a numerically optimized sinc-Gaussian pulse with a duration of 5 ms. The two 180° chemical-shift refocusing pulses were numerically optimized sinc-like pulses of 3.5 ms duration and 1200 Hz bandwidth. The phases of both the second and the third 90° pulses were carefully calibrated (see section 4.2.3). In order to remove unwanted signals, each 180° pulses was sandwiched by a pair of spoiler gradients with a duration of 2 ms and an amplitude of 20 mTm^{-1}. The filter gradients during TM (5 ms, 20 mTm^{-1}) and TE_2 (for DQF only, with its duration twice as long as the first filter gradient) were applied at the magic angle to facilitate the suppression of residual water signal resulting from the demagnetizing dipole-dipole interaction between water molecules (23).

Since the purpose of the study was to demonstrate the effect of varying φ, the φ dependence was determined at several representative, symmetric TEs ($\{TE_1,TE_2\}$) in ms and all other sequence parameters were kept fixed, i.e., repetition time (TR) = 3 s, TM = 9 ms and the third 90° read pulse was tuned to excite between 1.0 ppm and 4.5 ppm as an additional water suppression strategy. For all experiments, a voxel size of 3 × 3 × 3 cm^3 were used. A total of 32 averages were taken with a spectral bandwidth of 2500 Hz and 2048 data points for acquisition.

As no reference singlet is available in DQ-filtered spectra, phase correction cannot be made consistently to individual spectra to be compared. As a consequence, the area (or maximum amplitude) of spectra measured in real mode, which is very sensitive to phase correction, can be misleading. This difficulty is also encountered in ZQF experiments due to gradual decay of the singlet resonance as a function of the phase of the MQ-pulse. Therefore, all spectra were obtained in magnitude mode, $((\text{real})^2 + (\text{imaginary})^2)^{1/2}$, for proper comparison of total areas of the spectra at different sequence timings, and the areas thus measured were used as signal intensity. All φ-dependence

curves were plotted based on these areas and each curve was normalized to the maximum signal at each pair of sequence timings used.

6.3 Results

Fig. 6-3 shows the φ-dependence of Cit in response to the ZQF at {TE_1 = 30 ms, TM = 9 ms, TE_2 = 30 ms}. In Eq. (6-5), which is the signal of the A-spin in real mode, the coefficient of cos(φ) and sin(φ) are 0.43 and 0.48, respectively. As discussed above, since the weighting factors of cos(φ) and sin(φ) are comparable to each other in this case, the maximum signal of the A-spin occurs at an intermediate phase angle. (54° among the spectra shown in Fig. 6-3(a)). When measured in magnitude mode, the total area of Cit increases as a function of the phase of the MQ-pulse, φ.

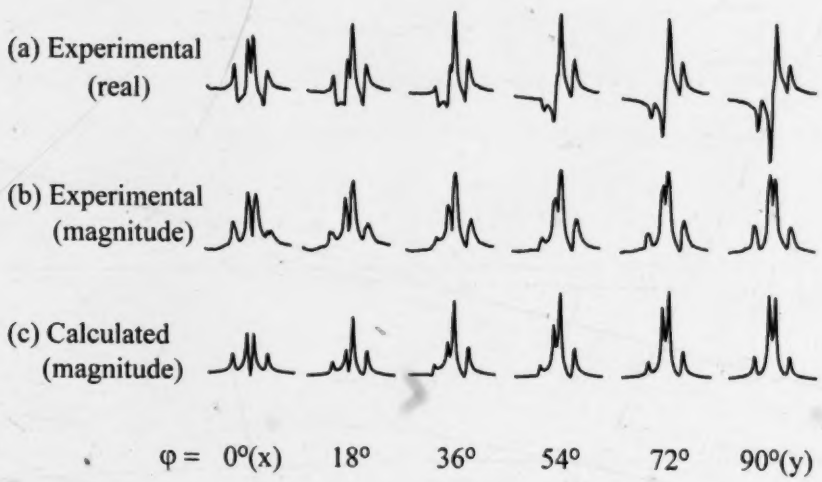

Figure 6-3 The response of the strongly-coupled AB system of Cit to ZQF at {TE_1 = 30 ms,TE_2 = 30 ms} with varying phase of the MQ-pulse. As the phase angle of the pulse is tuned from the conventional phase angle of 0° to 90°, the Cit signal is enhaced as shown in (a) in real mode and in (b) in magnitude mode. Also shown in (c) are the calculated spectra in magnitude mode using numerical methods.

In Fig. 6-4, the φ dependence of uncoupled Cr (methyl group at ~ 3.0 ppm) and weakly-coupled Lac are illustrated in response to the ZQF at {TE_1 = 30 ms, TM = 9 ms,

TE_2 = 30 ms}. As shown in Eqs. (6-6) and (6-7), the signal of uncoupled Cr and weakly-coupled Lac decay as a function of cos(φ). Despite its better signal yield over the DQF by a factor of two in principle, the conventional ZQF has been less popular in its application *in vivo* for its incapability to suppress uncoupled spin resonances. However, when the phase is adjusted to y, this problem can be resolved, thereby rendering its usage more feasible. The fact that the residual signal of Lac observed at φ = 90° is negligible means that the deviation of the evolution of the spin system from the weak-coupling approximation is not significant (14, 18).

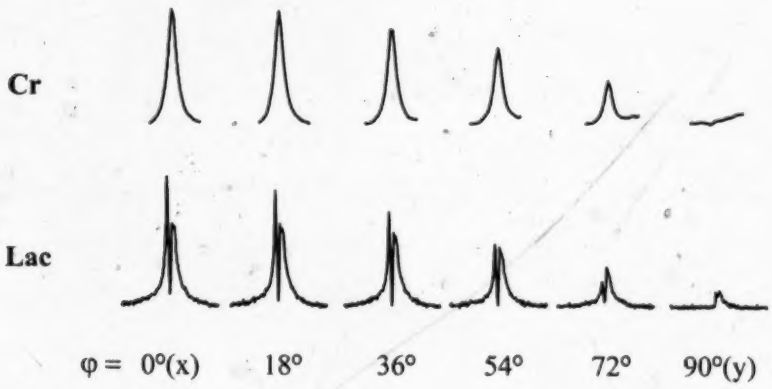

Figure 6-4 The response of uncoupled Cr (methyl group) at ~ 3.0 ppm and weakly-coupled Lac (methyl group) at ~ 1.3 ppm to varying phase of the MQ-pulse to ZQF at {TE_1 = 30 ms, TE_2 = 30 ms}. As the phase of the pulse is tuned from the conventional x-phase towards y-phase, signal decays monotonically for both metabolites.

Fig. 6-5 compares the φ-dependence of (a) Cit (b) Tau and (c) mI (strongly-coupled 2-, 4- and 6-spin system, respectively) in response to ZQF and DQF sequences at several representative symmetric echo times, {TE_1, TE_2}. In (a), the DQ-filtered signal of Cit at {30, 30} (curve #1) decays as φ approaches 90° as described in Eq. (6-8b). In contrast to the response of uncoupled or weakly-coupled spins, whose signal decays monotonically as φ increases to 90°, the signal response from strongly-coupled spins can be enhanced with respect to that with the conventional phase of φ = 0° as φ is increased. For instance, curve #2 in Fig. 6-5(a), which corresponds to the experimental results for Cit with ZQF at {30,30} shown in Fig. 6-3 illustrate that varying the phase of the MQ-

pulse from x to y results in approximately 20 % enhancement in the filter yield at the same sequence timings. Signal enhancement is also observed in curves #3, #4, #10 and #12-14. Fig. 6-5 also illustrates that the amount of increase or decrease in signal within the same spin system depends on the choice of $\{TE_1, TE_2\}$, e.g., between curves #2 vs. #3, #5 vs. #7, #6 vs. #8. In particular, comparison between curves #9 and #10, and between curves #11 and #14 clearly demonstrate sequence timing dependent response of spin systems to varying φ, which results in ~ 50% increase or decrease of signal yield at the same sequence timings. Fig. 6-5 also illustrates that any maximum or minimum in the enhanced signal can appear at an angle intermediate between 0° and 90° (curve #4, #12, #13), thereby emphasizing the need to optimize φ.

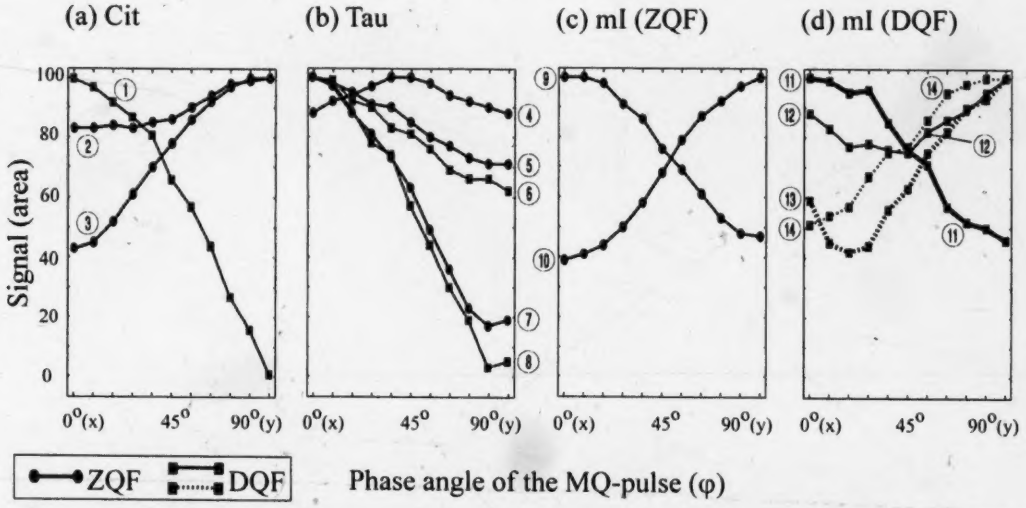

Figure 6-5 The φ-dependence of the strongly-coupled spin systems of citrate, taurine and *myo*-Inositol in ZQF and DQF experiments at various representative, symmetric sequence timings. Unlike those of uncoupled and weakly-coupled, the response of strongly-coupled spin systems ((a) Cit, (b) Tau and (c)-(d) mI) are diverse depending on the spin systems and the sequence timings. The filter and sequence timings ($\{TE_1,TE_2\}$ in ms) corresponding to the responsive curves are as follows: curve #1. DQF {30,30}, 2. ZQF {30,30}, 3. ZQF {40,40}, 4. ZQF {40,40}, 5. ZQF {30,30}, 6. DQF {40,40}, 7. ZQF {60,60}, 8. DQF {80,80}, 9. ZQF {30,30}, 10. ZQF {60,60}, 11. DQF {30,30}, 12. DQF {50,50}, 13. DQF {80,80} and 14. DQF {70,70}. All the spectra were obtained in magnitude mode and then the areas were measured as signal intensity.

The optimization of φ can be useful for differentiating even between strongly-coupled spin systems. For instance, the response of Cit, Tau and mI to ZQF at {30, 30} are all different as shown in curves #2 (Cit; ~ 20 % increase), #5 (Tau; ~ 30% decrease) and #9 (mI; ~ 50% decrease). Finally, the $\{TE_1, TE_2\}$ dependence of the φ rate of change of the signal from either a ZQF or a DQF sequence reflects the fact that the strongly-coupling evolution during TE_1 determines the end points of the φ-dependence (14).

As was demonstrated in Figs. 6-4 and 6-5, because the response of metabolites to the phase rotation depends upon both spin systems and sequence timings, the phase of the MQ-pulse can be used as an additional sequence parameter to be optimized for more efficient design of a MQF for a target metabolite.

A practical example of taking advantage of the extra contrast mechanism achieved by φ-optimization is given first for the discrimination of mI (~ 3.6 ppm) from strongly-coupled Tau (~ 3.35 ppm) and uncoupled Gly (~3.55 ppm) using a ZQF sequence at {60, 60} and a DQF sequence at {80, 80} as illustrated in Figs. 6-6(a) and 6-6(b), respectively. For the conventional ZQF with the phase of the MQ-pulse tuned into x, the uncoupled Gly passes through the filter and subsequently it contaminates mI target multiplet (Fig. 6-6(a)). Moreover, due to the significant amount of signal from Tau at this timing, the contamination of mI is more severed. Therefore, when a conventional ZQF is used, {60, 60} is not a good choice for mI detection. However, as φ is varied towards 90° (y), Gly will automatically be removed as demonstrated in Fig. 6-4 and Eq. (6-7), and, at this specific sequence timing, the strongly-coupled Tau signal is also lost (curve #7 in Fig. 6-5(b)). On the other hand, the target signal of mI is enhanced by a factor of more than 2 (curve #10 in Fig. 6-5(c)). Therefore, at $\varphi = 90°$ the initially contaminated mI signal by a mixture of Tau and Gly can effectively be edited with its lineshape and amplitude matching that obtained from the phantom containing mI only. The advantage of incorporating the rotation of the phase of the MQ-pulse for mI editing can also be seen in a DQF experiment taken at {80, 80} as shown in Fig. 6-6(b), in which case no contamination from uncoupled Gly is possible.

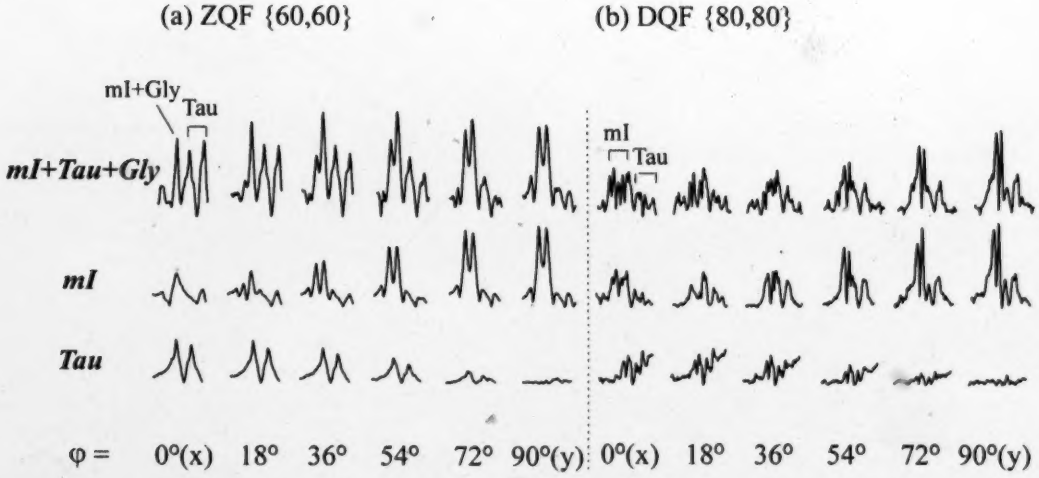

Figure 6-6 The practical example of the optimization of the phase of the MQ-pulse for the discrimination of mI from Tau. In a ZQF experiment at {60,60} (a), the initial signal of mI at $\varphi = 0°$ is contaminated by interfering background signal from Tau and Gly. However, as φ approaches 90°, the mI signal is enhanced, while that of Tau is effectively suppressed at the specific sequence timings. As a result, the lineshape and the signal amplitude of mI obtained from a phantom with a mixture of mI + Tau + Gly (top row) converges into those from mI only (middle row). Also shown in (b) are the experimental results with DQF taken at {80,80}. Similarly to (a), the optimization of φ results in both signal enhancement for mI and suppression for the neighboring Tau signal.

Again, as the phase of the MQ-pulse approaches 90° the signal from Tau is suppressed as in the curve #8 in Fig. 6-5(b), while that of mI is enhanced via its minimum value at $\varphi = 18°$ as in curve #13 in Fig. 6-5(c). In this way, optimizing the phase of the MQ-pulse can provide another window for spectral editing within the same sequence timing.

Another example of incorporating phase rotation into sequence optimization is given with the optimization of the MNPQ multiplet (2.0 - 2.5 ppm) of Glu against that of Gln. This is illustrated in Fig. 6-7 using (a) ZQF at {40, 40} and (b) DQF {50, 50}. In both Figs. 6-7(a) and 6-7(b), the initial spectra taken at $\varphi \doteq 0°$ from a mixture of Glu and Gln are dominated by Gln. However, as the phase of the MQ-pulse approaches 90°, a significant amount of signal from Glu is still retained, while that of Gln is effectively suppressed. As a result the lineshape and the signal amplitude of Glu+Gln complex

converge into those from the pure Glu phantom. As in this example, even in the case where the signal from a target (Glu) and a background metabolite (Gln) are both decaying as a function of φ, the contrast provided by the difference in the rate of signal decay can be useful for the purpose of spectral editing.

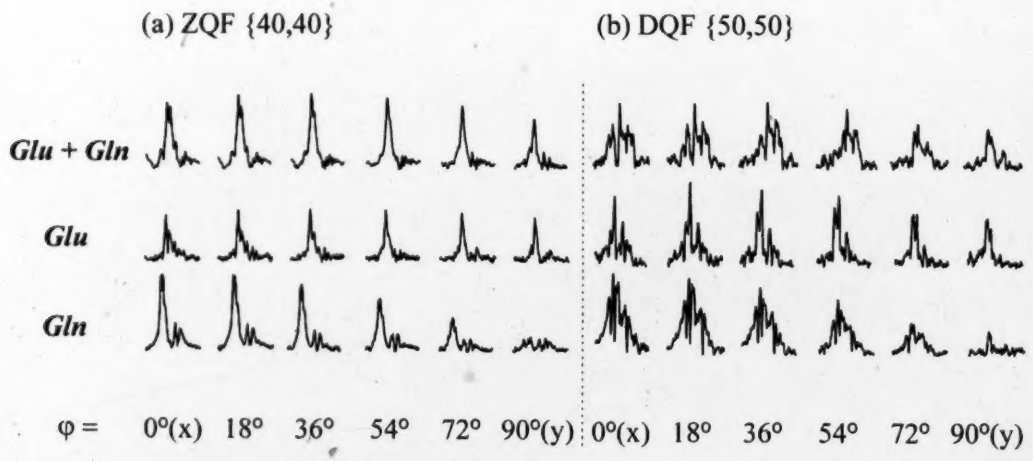

Figure 6-7 The practical example of the optimization of the phase of the MQ-pulse for the discrimination of Glu from that of Gln. In response to both (a) ZQF at {40,40} and (b) DQF at {50,50}, the MNPQ multiplet (~ 2.0-2.5 ppm) of Glu is severely comtaminated at the initial phase angle of $\varphi = 0^{\circ}$ due to the interference of that of Gln (top rows). However, by taking advantage of the φ-dependence of Glu (middle rows) different from that of Gln (bottom rows) at the specific sequence timings, the spectral integrity of Glu can remarkably be improved in both ZQF and DQF experiments.

These examples clearly illustrate the efficacy of incorporating φ into the optimization procedure in the design of MQFs, even for Glu and Gln whose spectral characteristics are hardly distinguishable from each other due to the similarity of their molecular structures. It is obvious in these examples that the phase rotation provides for an additional spectral editing mechanism *over and above the use of* $\{TE_1, TE_2\}$.

6.4 Summary and Discussion

This report demonstrates, by means of the mI and Glu discrimination problem, the potential role of optimizing the phase dependence of the MQ-pulse as an additional

sequence parameter to be varied. Unlike uncoupled and weakly-coupled spin systems, the response of the strongly-coupled ones to the varying phase of the MQ-pulse shows diverse patterns depending on the spin systems and on the choice of sequence timings. Therefore, this technique is useful not only for discriminating strongly-coupled spin systems from uncoupled and weakly-coupled ones, but also for differentiating between different strongly-coupled spin systems. In addition, the inherent problem of a conventional ZQF being unable to suppress uncoupled spin resonances can be resolved by tuning the phase of the MQ-pulse to y, thereby rendering its in-vivo application more flexible.

The strongly-coupled AB spin system of Cit adopted in this study was not a sufficient model in itself for the general description of the physical mechanism of the φ-dependence of strongly-coupled spin systems. For the analytic solution for the response of the AB model to a ZQF, no ZQC is produced from APC terms that are created commonly in both weakly- and strongly-coupled spin systems after the TE_1 period. For a DQF, no general information was given from the AB model as to the φ-dependence of the DQCs originating from strong-coupling specific APC terms. Therefore, for a general discussion on the φ-dependence of coupled spin systems, analytic solutions of more complicated strongly-coupled spin system are required such as for an ABC model, for which the evolution equations of coherences in response to NMR pulse sequences are yet to be found. Nevertheless, for the φ-dependence of strongly-coupled spin systems in response to the ZQF, a generalized analytic solution was proposed in terms of two basis functions, cos(φ) and sin(φ), by resorting to the analytic solutions for the AX_3 spin system of Lac. By doing so it was inferred that, for a ZQF, tuning the phase of the MQ-pulse allows the control of the proportion of the two different kinds of coherence terms in the final filter output, i.e., one created during the preparation period from both weak- and strong-coupling interactions and the other exclusively from strong-coupling interactions, each of which is then coupled to cos(φ) and sin(φ), respectively, upon the exertion of the MQ-pulse. Since the weighting factors of these basis functions, namely W's and S's, are sequence timing dependent, the net φ-dependent curve of filtered signal can exhibit various patterns. As such, an optimum phase of the MQ-pulse for spectral editing purpose

can be found even at an intermediate angle. For a DQF, in contrast to weakly-coupled spin systems for which no even-order MQC is produced by the y-phased MQ-pulse, the existence of strong-coupling specific DQCs was illustrated using numerical methods with the representative DQC terms of mI and their sequence timing dependent amplitude modulation was also demonstrated in phantom experiments.

The different φ-dependence of MNPQ multiplets of Glx demonstrated in both ZQF and DQF experiments may be due mainly to the difference in the degree of coupling, $J/\Delta\delta$ (J: coupling-constant, $\Delta\delta$: chemical-shift difference between coupled spins in Hz), between MN-pairs, and between PQ-pairs, of those two spin systems, which ultimately leads to different sequence-timing dependence of coherences that are responsible for the filtered signal. As in the coupling network of Glx (24) shown in Fig. 6-8(a), the difference in $J/\Delta\delta$ results from the difference in chemical-shift rather than from the difference in coupling-constant. Due to active coherence transfer in the course of evolution of strongly-coupled spin systems during TM (25) and TE_2 (26), for instance, the SQCs of P- or Q-spins at the onset of acquisition period that contribute to the PQ multiplets of Glx (2.3-2.5 ppm) can have different coherence pathways. Based on Fig. 6-8(a), various ZQCs consisting of different spin species can evolve into the SQCs of P- or Q-spins, such as ZQC(PQ), ZQC(MP) and ZQC(NP). In addition to these ZQC terms, even ZQC(MN) can contribute to the PQ multiplets via the form of ZQC(MP) or ZQC(NP). As a result, the TM-dependence of the SQCs of P- or Q-spin of Glu at the onset of acquisition period can be significantly different from that of Gln as the oscillation frequencies of ZQC(MN) and ZQC(PQ) of Glu are significantly different from those of Gln. Since coherence transfer is active during TE_2 as well, the choice of TE_2 period also influences the amount of final filter output of Glx. Although in this example the degree of coupling of PQ-pair of Glu is larger than that of Gln ($J/\Delta\delta(PQ) \sim 8.3$ for Glu and ~ 5.5 for Gln), $J/\Delta\delta$ alone cannot be considered as an absolute measure of the amount of residual signal from strong-coupling interaction at $\varphi = 90^{\circ}$.

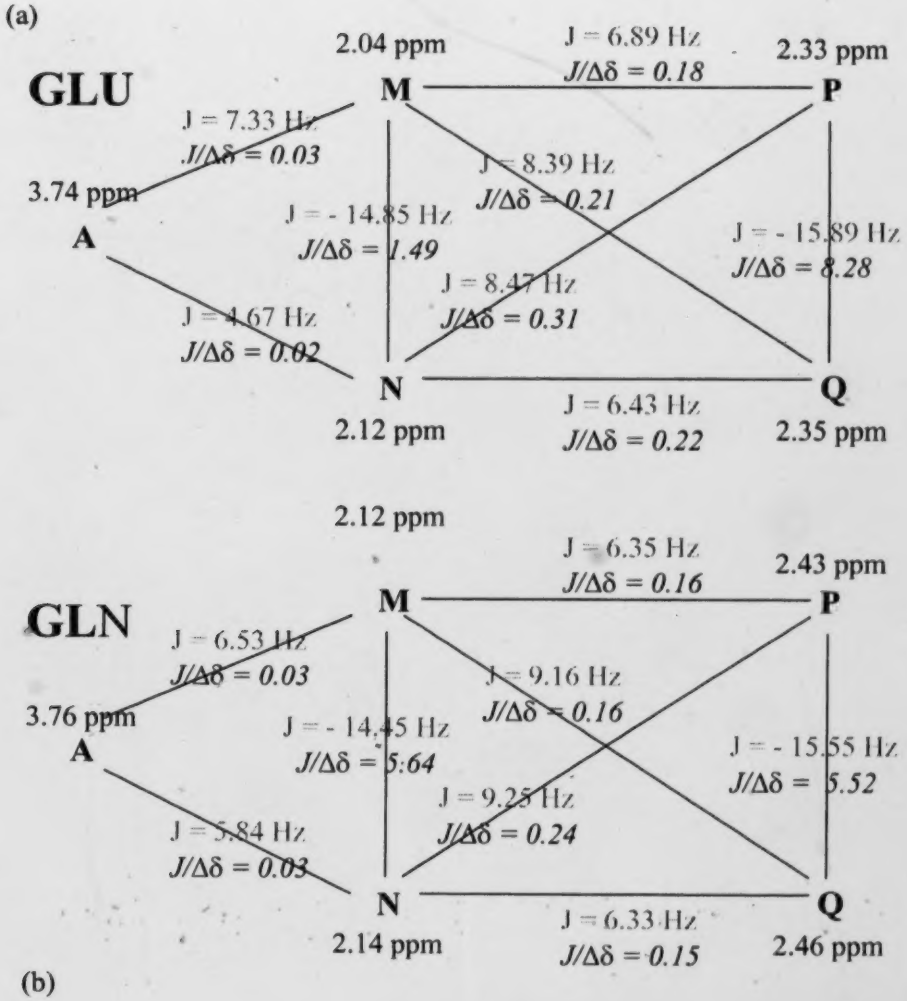

Figure 6-8 The coupling networks of Glx spin systems and the J/Δδ-dependent oscillation amplitude of strong-coupling specific APCs of an AB spin system. In (a) the coupling networks of AMNPQ spin systems of Glx are shown along with chemical-shifts, J-constants and J/Δδ between coupled spins. In (b) the oscillation amplitude of the APC terms, which are created during a TE_1 period, is illustrated as a function of the degree of coupling, J/Δδ.

For instance, for a strongly-coupled AB spin system, the amount of APC terms, $2A_yB_z$ and $2B_yA_z$ in Eq. (6-1), which are specific to strong-coupling interaction and are to be maximally converted into ZQC by the MQ-pulse tuned at $\varphi = 90^o$, is coupled to the coefficient S_2 whose oscillation amplitude is proportional to the term, $(\delta\omega/\Lambda)(\pi J/\Lambda)$ (see Eq. (6-1b)). This can be rewritten in terms of degree of coupling, $J/\Delta\delta$, as $(J/\Delta\delta)/[1+(J/\Delta\delta)^2]$. As illustrated in Fig. 6-8(b), the amplitude of this quantity is proportional to $J/\Delta\delta$ only for $J/\Delta\delta \leq 1$ and beyond that range it is *inversely* proportional. Therefore for an AB spin system whose $J/\Delta\delta$ is larger than unity, the degree of coupling by itself cannot be taken as a means of determining the amount of residual signal. In fact, the decaying rate of the MNPQ signal of Glu in response to φ-rotation is faster than that of Gln at $\{TE_1 = 70$ ms, $TE_2 = 70$ ms$\}$ with ZQF.

In conclusion, this methodology will find application whenever the target metabolite contains strongly-coupled spins. It provides another means by which we can control the relative acquisition period magnitudes of the coherences that originate from uncoupled, weakly- and strongly-coupled spins at the end of the TE_1 evolution period. Thus, in the MQF sequence the MQ-pulse itself possesses filtering capability that works based on the degree of coupling in addition to the filter gradients that perform filtering based on the level of coherence. Since the responses of the various metabolites to the φ dependence are different, it also expands the toolbox for differentiating between metabolites with strongly-coupled spins.

6.5 References

1. R. B. Thomson and P. S. Allen, *Magn. Reson. Med.*, **39**, 762, 1998
2. J. R. Keltner, L. L. Wald, B. B. Frederick, and P. F. Renshaw, *Magn. Reson. Med.*, **37**, 366, 1997
3. J. R. Keltner, L. L. Wald, P. J. Ledden, Y. I. Chen, R. T. Matthews, J. R. Baker, B. R. Rosen, and B. G. Jenkins, *Magn. Reson. Med.*, **39**, 651, 1998
4. A. H. Trabesinger, O. M. Weber, C. O. Duc, and P. Boesiger, *Magn. Reson. Med.*, **42**, 283, 1999
5. A. A. de Graaf, P. R. Luyten, J. A. den Hollander, W. Heindel, and W. M. M. J. Bovee, *Magn. Reson. Med.*, **30**, 231, 1993
6. A. H. Trabesinger and P. Boesiger, *Magn. Reson. Med.*, **45**, 708, 2001

7. J. Shen, D. L. Rothman, and P. Brown, *Magn. Reson. Med.*, **47**, 447, 2002
8. M. A. McLean, A. L. Busza, L. L. Wald, R. J. Simister, G. J. Barker, and S. R. Williams, *Magn. Reson. Med.*, **48**, 233, 2002
9. J. Shen, D. C. Shungu, and D. L. Rothman, *Magn. Reson. Med.*, **41**, 35, 1999
10. G. C. McKinnon and P. Boesiger, *Magn. Reson. Med.*, **8**, 355, 1988
11. M. A. Thomas, H. P. Hetherington, D. J. Meyerhoff, and D. B. Twieg, *J. Magn. Reson.*, **93**, 485, 1991
12. J. F. Shen and P. S. Allen, *J. Magn. Reson.*, **92**, 398, 1991
13. J. F. Shen and P. S. Allen, *J. Magn. Reson.*, **90**, 606, 1990
14. H. Kim, J. M. Wild, and P. S. Allen, *Proc. ISMRM*, Glasgow, 2001, p. 621
15. K. L. Behar, and T. Ogino, *Magn. Reson. Med.*, **17**, 285, 1991
16. R. A. de Graaf and D. L. Rothman, *Concepts Magn. Reson.*, **13**, 32, 2001
17. L. E. Kay and R. E. D. McClung, *J. Magn. Reson.*, **77**, 258, 1988
18. A. H. Trabesinger, D. C. Mueller, and P. Boesiger, *J. Magn. Reson.*, **145**, 237, 2000
19. G. Bodenhausen, H. Kogler, and R. R. Ernst, *J. Magn. Reson.*, **58**, 370, 1984
20. A. H. Willman and P. S. Allen, *J. Magn. Reson.*, **B105**, 58, 1994
21. R. Kreis, T. Ernst, B. D. Ross, *J. Magn. Reson.*, **B102**, 9, 1993
22. S. W. Provencher, *Magn. Reson. Med.*, **30**, 672, 1993
23. W. Richter, S. Lee, W. S. Warren, and Q. He, *Science*, **267**, 654, 1995
24. V. Govindaraju, V. J. Basus, G. B. Matson, and A. A. Maudsley, *Magn. Reson. Med.*, **39**, 1011, 1998
25. R. B. Thomson and P. S. Allen, *Magn. Reson. Med.*, **45**, 955, 2001
26. R. B. Thomson and P. S. Allen, *Magn. Reson. Med.*, **41**, 1162, 1999

CHAPTER 7

Conclusion

7.1 Summary

In the previous chapters, various spectral editing techniques were used to maximize the spectral integrity of the target signal. In Chapter 3, PRESS and STEAM sequences were optimized for mI detection where the editing efficiency relied mainly on the concentration and the T_2 of mI relative to those of Gly. To remove that variability arising from the overlapping Gly singlet in the quantification of the target metabolite, a conventional DQ-filtering technique was used in Chapter 4. In Chapter 5, the efficacy of a MQF was shown to be further enhanced by uncovering the filtering capability of the MQC-generating pulse based on the degree of coupling in addition to the conventional filtering based on the order of coherences. A detailed discussion was given in Chapter 6 on the physical consequences and the potential role of optimizing the MQC-generating pulse in the design of a MQF whereby the MQF parameter space was extended to include a total of seven sequence parameters.

7.2 Product Operator Formalism and Numerical Methods

Considering the complicated evolution of both the spin system of a target metabolite and those of a group of background metabolites in response to each variable, the optimization of a MQF is not trivial. Therefore, as was demonstrated throughout this thesis, the incorporation of numerical methods in the *sequence optimization* is essential. Although its application is limited due to the large amount of calculation, the physical insight provided by the conventional product operator approach cannot be underestimated in the *sequence development*. Therefore, combined with numerical methods, the product operator formalism is valuable asset in spectral editing techniques.

7.3 LC Model -An Alternative to Spectral Editing ?

In contrast to spectral editing techniques, metabolite quantification may be achieved in much simpler way by line-fitting methods based on *a priori* knowledge, of which the efficacy relies solely on post-data processing rather than sequence optimization. For instance, the LC model (1), a commonly used method for metabolite quantification, claims to extract results as refined as spectral editing methods from a cluttered mixture of resonance lines. It models an in-vivo spectrum as a linear combination of a basis set which is formed by spectra of all component metabolites obtained *in vitro* with all sequence parameters fixed identical to those used for *in vivo* data acquisition.

To avoid possible errors arising from different transverse relaxation rate amongst resonances and to minimize signal loss of coupled spins resulting from J-evolution, the shortest-STEAM-strategy is the most popular choice for the post-data processing method. However, as was illustrated in chapter 3, the amount of signal from macromolecules can be comparable to that from metabolites at the short sequence timings. For this reason, an accurate definition of baseline is crucial to the precision of the LC model in metabolite quantification. The measurement precision may drop drastically if a spectral region of interest to be modeled involves a metabolite whose only resonance resides in that region of the spectrum, e.g., Gly. Moreover, even with all the sequence parameters kept constant, spectra taken *in vivo* are far more vulnerable to baseline contamination by unwanted signal than those acquired from spherical phantom solutions, thereby exacerbating the difficulty of defining baseline in the LC model. The contaminated baseline may still be adjustable in the LC model by comparing resonances from a metabolite in that spectral region with those from the same metabolite in a different region of a spectrum, but this is not the case with Gly. Modeling in-vivo spectra taken at long sequence timings to minimize macromolecule contamination is still subject to uncertainty due to different T_2's of overlapping metabolites. Incorporating the metabolite-nulling technique into the modeling of in-vivo spectra may improve the efficacy of the LC model (2).

7.4 Spectral Editing vs. LC Model at Higher Fields

As field strength increases, the efficacy of both the spectral editing method and the LC model may be further improved. As for the LC model, since the line-fitting is carried out with spectra taken at short sequence timings, a better spectral resolution at a higher field can reduce measurement errors. In this context, the performance of the LC model will *always* be proportional to the field strength at which data is acquired. As for the spectral editing methods, an improved spectral resolution is also in line with an improved frequency selectivity of editing pulses, which is one of the essential parts of the spectral editing techniques.

Compared in Fig. 7-1 is the calculated response of mI and its background metabolites to a 90°-acquire experiment at three different magnetic field strengths of 3.0 T, 4.7 T and 7.0 T where the line broadening was assumed to be a linear function of a field strength starting from 6 Hz, which can easily be attained at 3.0 T for a 3×3×3 cm^3 voxel located in the human brain. The spectral dispersion at higher fields may not appear as drastic as one might anticipate. The spectral resolution amongst the resonances of those metabolites in the spectra can be further enhanced dependent upon the relative concentration ratio of the metabolites and shim values. However, it should also be noted that the linearly varying linewidth assumed in Fig. 7-1 could be attained only if the magnetic susceptibility effect arising from field inhomogeneity of an imperfect magnet is *completely* removed by shimming as was claimed in Reference *3*. Thus, the spectral resolution at higher fields can be even worse. This may also imply the limitation of the line-fitting techniques such as the LC model.

A better spectral resolution and improved signal to noise ratio at higher fields will certainly be beneficial for spectral editing techniques as well. However, unlike the line-fitting methods, the editing techniques do not necessarily require *higher* fields for a better outcome. Rather, the optimal field strength may differ from one target spin system to another. This is due to the fact that in spectral editing methods the desired spectral discrimination of a target metabolite from its contaminants is achieved mainly by taking

advantage of different evolution of the spin systems in response to a pulse sequence rather than by the natural spectral dispersion at higher fields, and that the overall evolutionary picture of the spin systems at higher fields does not necessarily alter in favor of a better spectral discrimination of the target spin system.

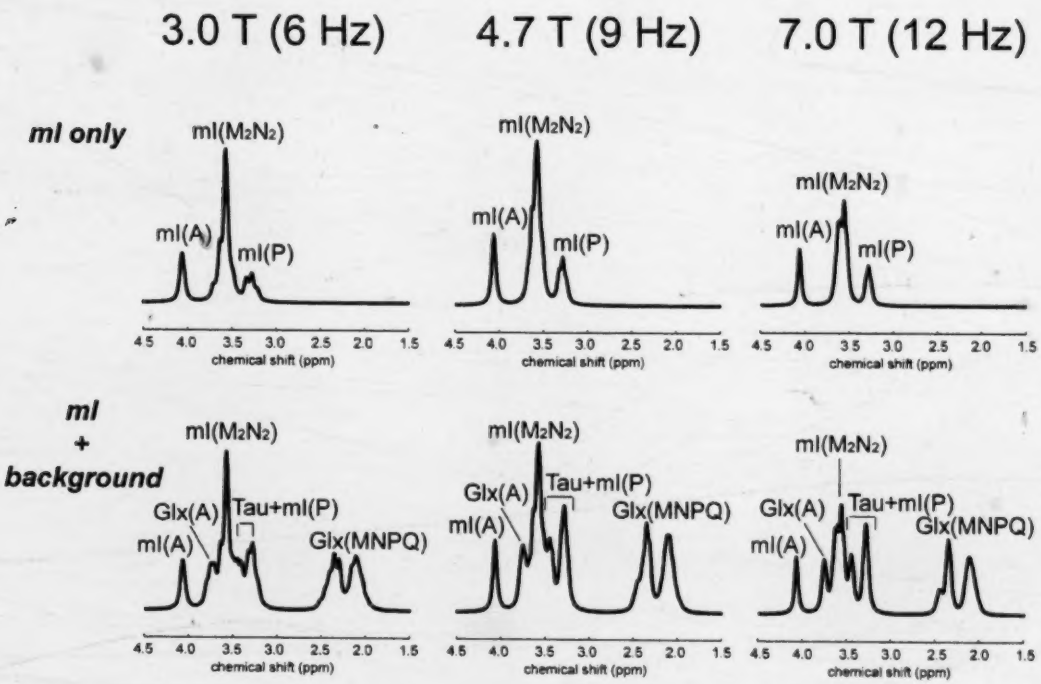

Figure 7-1 The calculated spectra of mI and its background metabolites in response to a 90°-acquire sequence at 3.0 T, 4.7 T and 7.0 T. The linewidth of all spectra was adjusted proportionally to the field strengths. The spectra on top row includes mI only whereas those on the bottom row includes its background metabolites as well according to their relative concentration ratio in normal human brain. Even at 7.0 T with a linewidth of ~ 12 Hz, the central multiplet of mI still overlaps with Tau and the A multiplets of Glx.

It will remain as a fascinating task in in-vivo MRS to compare the performance of those two distinct methods of metabolite quantification at different field strengths, one literally freezing any evolution of spins and modeling the lines of resonances based on

a priori knowledge, and the other leaving them to evolve and singling out one set of sequence parameters in the maze of choices in the parameter space of a pulse sequence via product operator analysis and numerical methods.

7.5 References

1. S. W. Provencher, *Magn. Reson. Med.*,**30**, 672, 1993
2. R. A. de Graaf and D. L. Rothman, *Concepts Magn. Reson.*, **13**, 32, 2001
3. I. Tkac, P. Andersen, G. Adriany, H. Merkle, K. Ugurbil, and R. Gruetter, *Magn. Reson. Med.*,**46**, 451, 2001

APPENDIX 1

Bloch Equations

A magnetic moment vector μ in static $\mathbf{B_o}$ is subject to a torque, τ. Starting with a classical equation of

$$\tau = d\mathbf{L}/dt = \mu \times \mathbf{B_o} \qquad \text{(A1-1)}$$

where $\mathbf{L}$ is an angular momentum vector, $\mu = \gamma \hbar \mathbf{L}$ in this case and "×" is vector product. Therefore,

$$d\mu/dt = \gamma \hbar \mu \times \mathbf{B_o} \qquad \text{(A1-2a)}$$

or

$$d\mathbf{M}/dt = \gamma \hbar \mathbf{M} \times \mathbf{B_o} \qquad \text{(A1-2b)}$$

for the magnetic moment in a unit volume. Therefore,

$$dM_x/dt = \gamma \hbar B_o M_y,\ dM_y/dt = -\gamma \hbar B_o M_x,\ dM_z/dt = 0. \qquad \text{(A1-3)}$$

Including transversal and longitudinal relaxation, T_2 and T_1, respectively, Eq. (A1-3) can be modified into

$$\begin{aligned} dM_x/dt &= \gamma \hbar B_o M_y - M_x/T_2\ , \\ dM_y/dt &= -\gamma \hbar B_o M_x - M_y/T_2, \\ dM_z/dt &= (M_o - M_z)/T_1 \end{aligned} \qquad \text{(A1-4)}$$

where M_o is a net magnetic moment in a unit volume at the equilibrium state.

In a rotating frame with the angular frequency of ω_o, Eq. (A1-4) takes the form of

$$dM_x/dt = \hbar\omega_\cdot M_y - M_x/T_2 , \qquad \text{(A1-5a)}$$

$$dM_y/dt = \hbar\omega_\cdot M_x - M_y/T_2, \qquad \text{(A1-5b)}$$

$$dM_z/dt = (M_o - M_z)/T_1 \qquad \text{(A1-5c)}$$

where $\omega_\cdot$ is the precession frequency of the magnetization vector in a rotating frame and $\omega_\cdot = \omega_{r.f.} - \omega_o$. Letting $M_{xy} = M_x + iM_y$, then, (A1-5a) + (A1-5b) × i gives

$$dM_{xy}/dt = \hbar\omega_\cdot iM_y - M_{xy}/T_2 = -(1/T_2 - \hbar\omega_\cdot i)M_{xy} \qquad \text{(A1-6a)}$$

$$dM_z/dt = (M_o - M_z)/T_1 \qquad \text{(A1-6b)}$$

Using boundary conditions, $M_{xy}(0) = M_o$ and $M_z(0) = 0$, Eqs. (A1-6a) and (A1-6b) has a solution of

$$M_{xy} = M_o\exp(-t/T_2)\exp(i\hbar\omega_\cdot t) \qquad \text{(A1-7a)}$$

and

$$M_z = M_o\{1-\exp(-t/T_1)\}, \qquad \text{(A1-7b)}$$

respectively. In particular, on-resonance, Eq. (A1-7a) reduces merely into

$$M_{xy} = M_o\exp(-t/T_2). \qquad \text{(A1-8)}$$

APPENDIX 2

Eigenvalues and Eigenvectors of Spin Operators

For a unit vector $\mathbf{n} = (\sin\theta\cos\phi, \sin\theta\sin\phi, \cos\theta)$ in the polar coordinate, i.e., θ being an angle between z-axis and the unit vector, and ϕ being an angle between x-axis and the projection of the unit vector onto the xy-plane,

$$\begin{aligned}\mathbf{S}\cdot\mathbf{n} &= (\hbar/2)\boldsymbol{\sigma}\cdot\mathbf{n} \\ &= (\hbar/2)\{\sigma_x n_x + \sigma_y n_y + \sigma_z n_z\} \\ &= (\hbar/2)\begin{pmatrix} \cos\theta & \exp(-i\phi)\sin\theta \\ \exp(i\phi)\sin\theta & -\cos\theta \end{pmatrix}. \end{aligned} \tag{A2-1}$$

The eigenvalue of $\mathbf{S}\cdot\mathbf{n}$ can be found by solving a determinant equation

$$|\mathbf{S}\cdot\mathbf{n} - \lambda\mathbf{1}| = 0 \tag{A2-2}$$

where λ is an eigenvalue and $\mathbf{1}$ is a unit vector. From Eq. (A2-2), it can be found that the eigenvalue, λ, of the spin operator $\mathbf{S}$ is $\pm\,\hbar/2$, irrespective of the direction along which $\mathbf{S}$ is measured.

The corresponding eigenvectors, $\mathbf{u}_+ = \begin{pmatrix} u1 \\ u2 \end{pmatrix}$ for $\lambda = \hbar/2$ can be found by solving,

$$(\hbar/2)\begin{pmatrix} \cos\theta - 1 & \exp(-i\phi)\sin\theta \\ \exp(i\phi)\sin\theta & -\cos\theta - 1 \end{pmatrix}\begin{pmatrix} u1 \\ u2 \end{pmatrix} = 0. \tag{A2-3}$$

Therefore,

$$\mathbf{u}_+ = \begin{pmatrix} \exp(-i\phi/2)\cos(\theta/2) \\ \exp(i\phi/2)\sin(\theta/2) \end{pmatrix}. \qquad \text{(A2-4a)}$$

Similarly,

$$\mathbf{u}_- = \begin{pmatrix} -\exp(-i\phi/2)\sin(\theta/2) \\ \exp(i\phi/2)\cos(\theta/2) \end{pmatrix}. \qquad \text{(A2-4b)}$$

for $\lambda = -\hbar/2$. Therefore, for S_z, when $\mathbf{n} = (0, 0, 1)$,

$$\mathbf{u}_+ = \begin{pmatrix} 1 \\ 0 \end{pmatrix} \text{ and } \mathbf{u}_- = \begin{pmatrix} 0 \\ 1 \end{pmatrix}. \qquad \text{(eigenvectors of } S_z\text{)} \quad \text{(A2-5a)}$$

Likewise, for S_x and S_y, when $\mathbf{n} = (1, 0, 0)$ and $\mathbf{n} = (0, 1, 0)$, respectively,

$$\mathbf{u}_+ = (1/\sqrt{2})\begin{pmatrix} 1 \\ 1 \end{pmatrix} \text{ and } \mathbf{u}_- = (1/\sqrt{2})\begin{pmatrix} -1 \\ 1 \end{pmatrix}, \text{ (eigenvectors of } S_x\text{)} \quad \text{(A2-5b)}$$

and

$$\mathbf{u}_+ = (1/\sqrt{2})\begin{pmatrix} 1 \\ i \end{pmatrix} \text{ and } \mathbf{u}_- = (1/\sqrt{2})\begin{pmatrix} -1 \\ i \end{pmatrix}. \text{ (eigenvectors of } S_y\text{)} \quad \text{(A2-5c)}$$

APPENDIX 3

Rotation of Spin Operators

In Quantum mechanics, the rotation of the spin operator S around z-axis by θ is expressed in terms of exponential operators such as $\exp(-i\theta S_z/\hbar)$, which can be written as

$$\begin{aligned}\exp(-i\theta S_z/\hbar) &= \exp(-i\theta\sigma_z/2) \\ &= 1 + (-i\theta\sigma_z/2) + (-i\theta\sigma_z/2)^2/(2!) + (-i\theta\sigma_z/2)^3/(3!) + \cdots\cdots \\ &= 1 - (\theta/2)^2/(2!) + \cdots\cdots \\ &\quad - i\sigma_z\{(\theta/2) - (\theta/2)^3/(3!) + \cdots\cdots\} \\ &= \mathbf{1}\cdot\cos(\theta/2) - i\sigma_z\cdot\sin(\theta/2) \qquad \text{(A3-1a)}\end{aligned}$$

where σ_z is the Pauli matrix and **1** is a unit matrix. Similarly,

$$\exp(i\theta S_z/\hbar) = \mathbf{1}\cdot\cos(\theta/2) + i\sigma_z\cdot\sin(\theta/2). \qquad \text{(A3-1b)}$$

Using Eq. (A3-1), $\exp(-i\theta S_z/\hbar)S_x\exp(i\theta S_z/\hbar)$ can also be written as

$$\begin{aligned}&\exp(-i\theta S_z/\hbar)S_x\exp(i\theta S_z/\hbar) \\ &\quad = (\hbar/2)[\mathbf{1}\cdot\cos(\theta/2) - i\sigma_z\cdot\sin(\theta/2)]\sigma_x[\mathbf{1}\cdot\cos(\theta/2) + i\sigma_z\cdot\sin(\theta/2)] \\ &\quad =\end{aligned}$$

$$(\frac{\hbar}{2})\begin{pmatrix}\cos(\frac{\theta}{2}) - i\sin(\frac{\theta}{2}) & 0 \\ 0 & \cos(\frac{\theta}{2}) + i\sin(\frac{\theta}{2})\end{pmatrix}\begin{pmatrix}0 & 1 \\ 1 & 0\end{pmatrix}\begin{pmatrix}\cos(\frac{\theta}{2}) + i\sin(\frac{\theta}{2}) & 0 \\ 0 & \cos(\frac{\theta}{2}) - i\sin(\frac{\theta}{2})\end{pmatrix}$$

$$= \left(\frac{\hbar}{2}\right)\begin{pmatrix} 0 & \cos(\theta) - i\sin(\theta) \\ \cos(\theta) + i\sin(\theta) & 0 \end{pmatrix}$$

$$= \cos(\theta)\cdot S_x + \sin(\theta)\cdot S_y, \qquad \text{(A3-2a)}$$

and similarly,

$$\exp(-i\theta S_z/\hbar)S_y\exp(i\theta S_z/\hbar) = -\sin(\theta)\cdot S_x + \cos(\theta)\cdot S_y. \qquad \text{(A3-2b)}$$

APPENDIX 4

Louville-von Newman Equation

An element of density matrix, ρ can be written as

$$<p \mid \rho \mid q> = c_p c_q^* \qquad \text{(A4-1)}$$

where "*" means complex conjugate. Then,

$$\partial(<p \mid \rho \mid q>)/\partial t = (\partial c_p/\partial t)c_q^* + c_p(\partial c_q^*/\partial t). \qquad \text{(A4-2)}$$

Using Time-dependent Schrödinger's equation,

$$\mathbf{H}\psi = i\hbar(\partial\psi/\partial t) \qquad \text{(A4-3)}$$

where **H** is a Hamiltonian of the system. Defining ψ as $\psi = \sum_n c_n \mid n >$, then

$$\sum_n c_n \mathrm{H} \mid n > = i\hbar \sum_n (\partial c_n/\partial t) \mid n > . \qquad \text{(A4-4)}$$

Taking <m| on each side of Eq. (A4-4),

$$\sum_n c_n < m \mid \mathrm{H} \mid n > = i\hbar \sum_n (\partial c_n/\partial t) < m \mid n > .$$

$$= i\hbar(\partial c_m/\partial t) \qquad \text{(A4-5)}$$

where the orthogonality condition of basis vectors, $\delta_{mn} = <m \mid n>$, was used. From Eq. (A4-5), it can be found that

$$(\partial c_p/\partial t) = (1/i\hbar)\sum_n c_n < p \mid H \mid n > \qquad \text{(A4-6a)}$$

and

$$(\partial c_q^*/\partial t) = (-1/i\hbar)\sum_n c_{n^*} < n \mid H \mid q > . \qquad \text{(A4-6b)}$$

Then, Eq. (A4-2) can be written as

$$\partial(<p \mid \rho \mid q>)/\partial t = (1/i\hbar)\sum_n c_n c_{q^*} < p \mid H \mid n > + (-1/i\hbar)\sum_n c_p c_{n^*} < n \mid H \mid q >$$

$$= (1/i\hbar) < p \mid [H, \rho] \mid q > \qquad \text{(A4-7)}$$

where Eq. (A4-1) and the completeness theorem were used, "[ ]" is the commutation operator. Finally, from Eq. (A4-7),

$$\partial\rho/\partial t = i/\hbar\,[\rho, H]. \qquad \text{(A4-8)}$$

APPENDIX 5

Evolution of Coherences under Gradient Pulses

The gradient Hamiltonian, $\boldsymbol{H}_G$, can be expressed as

$$\boldsymbol{H}_G = -\gamma\hbar\,\mathbf{G}\cdot\mathbf{r}I_z \qquad \text{(A5-1)}$$

where **G** is a gradient vector and **r** is a displacement vector measured from the isocenter of the magnet. The solution of the Louville-von Newman equation, then, takes the form of

$$\rho(t) = \exp(i\gamma\mathbf{G}\cdot\mathbf{r}I_z t)\rho(0)\exp(-i\gamma\mathbf{G}\cdot\mathbf{r}I_z t). \qquad \text{(A5-2)}$$

With $\rho(0) = I_y$ assumed,

$$\partial\rho/\partial t = \gamma\mathbf{G}\cdot\mathbf{r}\{\exp(i\gamma\mathbf{G}\cdot\mathbf{r}I_z t)\cdot I_x\cdot\exp(-i\gamma\mathbf{G}\cdot\mathbf{r}I_z t)\} \qquad \text{(A5-3a)}$$

and

$$\begin{aligned}\partial^2\rho/\partial t^2 &= -(\gamma\mathbf{G}\cdot\mathbf{r})^2\{\exp(i\gamma\mathbf{G}\cdot\mathbf{r}I_z t)\cdot I_y\cdot\exp(-i\gamma\mathbf{G}\cdot\mathbf{r}I_z t)\}\\ &= -(\gamma\mathbf{G}\cdot\mathbf{r})^2\rho. \qquad \text{(A5-3b)}\end{aligned}$$

Therefore, evaluation of Eq. (A5-2) reduces to solving a second-order homogeneous differential equation in Eq. (A5-3b), which has a general solution of

$$\rho(t) = C_1\exp(i\gamma\mathbf{G}\cdot\mathbf{r}t) + C_2\exp(-i\gamma\mathbf{G}\cdot\mathbf{r}t). \qquad \text{(A5-4)}$$

Using the boundary conditions,

$$\rho(0) = I_y \qquad \text{(A5-5a)}$$

and

$$\partial\rho(0)/\partial t = \gamma\mathbf{G}\cdot\mathbf{r}I_x, \qquad \text{(A5-5b)}$$

then,

$$C_1 = (I_y - iI_x)/2 = (1/2i)I_+ \qquad \text{(A5-6a)}$$

and

$$C_2 = (I_y + iI_x)/2 = (-1/2i)I_- . \qquad \text{(A5-6b)}$$

Therefore, from Eq. (A5-4),

$$\rho(t) = (1/2i)\{I_+\exp(i\gamma\mathbf{G}\cdot\mathbf{r}t) - I_-\exp(-i\gamma\mathbf{G}\cdot\mathbf{r}t)\}. \qquad \text{(A5-7)}$$

Since the initial state, $\rho(0)$, which can also be written in terms of raising and lowering operators as $\rho(0) = I_y = (1/2i)(I_+ - I_-)$,

$$I_+ \xrightarrow{\gamma Grt\cdot I_z} I_+\exp(i\gamma\mathbf{G}\cdot\mathbf{r}t) \qquad \text{(A5-8a)}$$

and

$$I_- \xrightarrow{\gamma Grt\cdot I_z} I_-\exp(-i\gamma\mathbf{G}\cdot\mathbf{r}t). \qquad \text{(A5-8b)}$$

For a DQC term, I_+S_+, created from a two-spin system, IS, since $[I_+, S_+] = 0$,

$$I_+S_+ \xrightarrow{\gamma Grt\cdot I_z} \xrightarrow{\gamma Grt\cdot S_z} I_+S_+\exp(2i\gamma\mathbf{G}\cdot\mathbf{r}t), \qquad \text{(A5-9)}$$

which shows that gradient pulses encode coherences according to their order of coherence.

APPENDIX 6a

Transformation Equations (Weak-Coupling Approximation)

Under r.f. pulses (right-hand side rotation)

$$I_x \xrightarrow{-\gamma B_1 t \cdot I_x} I_x$$

$$I_y \xrightarrow{-\gamma B_1 t \cdot I_x} I_y\cos(-\gamma B_1 t) + I_z\sin(-\gamma B_1 t)$$

$$I_z \xrightarrow{-\gamma B_1 t \cdot I_x} I_z\cos(-\gamma B_1 t) - I_y\sin(-\gamma B_1 t)$$

$$I_x \xrightarrow{-\gamma B_1 t \cdot I_y} I_x\cos(-\gamma B_1 t) - I_z\sin(-\gamma B_1 t)$$

$$I_y \xrightarrow{-\gamma B_1 t \cdot I_y} I_y$$

$$I_z \xrightarrow{-\gamma B_1 t \cdot I_y} I_z\cos(-\gamma B_1 t) + I_x\sin(-\gamma B_1 t) \qquad \text{(A6a-1)}$$

Under chemical-shift (right-hand side rotation)

$$I_x \xrightarrow{\omega t \cdot I_z} I_x\cos(\omega_1 t) + I_y\sin(\omega_1 t)$$

$$I_y \xrightarrow{\omega t \cdot I_z} I_y\cos(\omega_1 t) - I_x\sin(\omega_1 t)$$

$$I_z \xrightarrow{\omega t \cdot I_z} I_z \qquad \text{(A6a-2)}$$

Under scalar-coupling (right-hand side rotation)

$$I_{1x} \xrightarrow{2\pi J t \cdot I_{1z}I_{2z}} I_{1x}\cos(\pi J t) + 2I_{1y}I_{2z}\sin(\pi J t)$$

$$I_{1y} \xrightarrow{2\pi J t \cdot I_{1z}I_{2z}} I_{1y}\cos(\pi J t) - 2I_{1x}I_{2z}\sin(\pi J t)$$

$$I_{1z} \xrightarrow{2\pi J t \cdot I_{1z}I_{2z}} I_{1z}$$

$$2I_{1x}I_{2z} \xrightarrow{2\pi Jt \cdot I_{1z}I_{2z}} 2I_{1x}I_{2z}\cos(\pi Jt) + I_{1y}\sin(\pi Jt)$$

$$2I_{1y}I_{2z} \xrightarrow{2\pi Jt \cdot I_{1z}I_{2z}} 2I_{1y}I_{2z}\cos(\pi Jt) - I_{1x}\sin(\pi Jt)$$

$$2I_{1x}I_{2x} \xrightarrow{2\pi Jt \cdot I_{1z}I_{2z}} 2I_{1x}I_{2x}$$

$$2I_{1x}I_{2y} \xrightarrow{2\pi Jt \cdot I_{1z}I_{2z}} 2I_{1x}I_{2y}$$

$$2I_{1y}I_{2x} \xrightarrow{2\pi Jt \cdot I_{1z}I_{2z}} 2I_{1y}I_{2x}$$

$$2I_{1y}I_{2y} \xrightarrow{2\pi Jt \cdot I_{1z}I_{2z}} 2I_{1y}I_{2y}$$

$$2I_{1z}I_{2z} \xrightarrow{2\pi Jt \cdot I_{1z}I_{2z}} 2I_{1z}I_{2z} \qquad \text{(A6a-3)}$$

APPENDIX 6b

Transformation Equations for a Strongly-Coupled AB Spin System

Defining $\boldsymbol{H}^{weak}$ and $\boldsymbol{H}^{strong}$ as

$$\boldsymbol{H}^{weak} = \hbar \cdot \varpi \cdot (A_z + B_z) + 2\pi J_{AB} \hbar\, (A_z B_z)$$
$$\boldsymbol{H}^{strong} = \hbar \cdot \delta\omega \cdot (A_z - B_z) + 2\pi J_{AB} \hbar\, (A_x B_x + A_y B_y) \qquad \text{(A6b-1)}$$

where $\varpi = (\omega_A + \omega_B)/2$, $\delta\omega = (\omega_A - \omega_B)/2$ and $\Lambda = [(\delta\omega)^2 + (\pi J)^2]^{1/2}$, the transformation equations under $\boldsymbol{H}^{weak}$ for a strongly-coupled AB spin system are

$$A_x \xrightarrow{H^{weak} t} A_x\{\cos(\pi Jt)\cos(\varpi t)\} + A_y\{\cos(\pi Jt)\sin(\varpi t)\} - 2A_xB_z\{\sin(\pi Jt)\sin(\varpi t)\} + 2A_yB_z\{\sin(\pi Jt)\cos(\varpi t)\}$$

$$A_y \xrightarrow{H^{weak} t} - A_x\{\cos(\pi Jt)\sin(\varpi t)\} + A_y\{\cos(\pi Jt)\cos(\varpi t)\} - 2A_xB_z\{\sin(\pi Jt)\cos(\varpi t)\} - 2A_yB_z\{\sin(\pi Jt)\sin(\varpi t)\}$$

$$2A_xB_z \xrightarrow{H^{weak} t} - A_x\{\sin(\pi Jt)\sin(\varpi t)\} + A_y\{\sin(\pi Jt)\cos(\varpi t)\} + 2A_xB_z\{\cos(\pi Jt)\cos(\varpi t)\} + 2A_yB_z\{\cos(\pi Jt)\sin(\varpi t)\}$$

$$2A_yB_z \xrightarrow{H^{weak} t} - A_x\{\sin(\pi Jt)\cos(\varpi t)\} - A_y\{\sin(\pi Jt)\sin(\varpi t)\} - 2A_xB_z\{\cos(\pi Jt)\sin(\varpi t)\} + 2A_yB_z\{\cos(\pi Jt)\cos(\varpi t)\}. \qquad \text{(A6b-2)}$$

The evolution equations for the spin B can be derived in a symmetric consideration.

Under H^{strong}, they are

$$A_x \xrightarrow{H^{strong}t} A_x\{\cos(\Lambda t)\} + A_y\{(\delta\omega/\Lambda)\sin(\Lambda t)\} - 2B_yA_z\{(\pi J/\Lambda)\sin(\Lambda t)\}$$

$$A_y \xrightarrow{H^{strong}t} - A_x\{(\delta\omega/\Lambda)\sin(\Lambda t)\} + A_y\{\cos(\Lambda t)\} + 2B_xA_z\{(\pi J/\Lambda)\sin(\Lambda t)\}$$

$$2A_xB_z \xrightarrow{H^{strong}t} - B_y\{(\pi J/\Lambda)\sin(\Lambda t)\} + 2A_xB_z\{\cos(\Lambda t)\} + 2A_yB_z\{(\delta\omega/\Lambda)\sin(\Lambda t)\}$$

$$2A_yB_z \xrightarrow{H^{strong}t} B_x\{(\pi J/\Lambda)\sin(\Lambda t)\} - 2A_xB_z\{(\delta\omega/\Lambda)\sin(\Lambda t)\} + 2A_yB_z\{\cos(\Lambda t)\}. \quad \text{(A6b-3)}$$

For the B spin, the transformation equations can be found in a symmetric way except those terms with $\delta\omega$, for which they are anti-symmetric. For instance,

$$B_x \xrightarrow{H^{strong}t} B_x\{\cos(\Lambda t)\} - B_y\{(\delta\omega/\Lambda)\sin(\Lambda t)\} - 2A_yB_z\{(\pi J/\Lambda)\sin(\Lambda t)\}. \quad \text{(A6b-4)}$$